TESIS DE LA UNIVERSIDAD DE ZARAGOZA

2019

63

Julen Munárriz Tabuenca

Computational Catalysis of Homogenous and Heterogeneous Systems: New Insights into the Activation of Small Molecules

Departamento
Química Física

Director/es
POLO ORTIZ, VICTORIANO

ISSN 2254-7606

Prensas de la Universidad
Universidad Zaragoza

ISSN 2254-7606

Universidad Zaragoza
1542

Tesis Doctoral

COMPUTATIONAL CATALYSIS OF HOMOGENOUS AND HETEROGENEOUS SYSTEMS: NEW INSIGHTS INTO THE ACTIVATION OF SMALL MOLECULES

Autor

Julen Munárriz Tabuenca

Director/es

POLO ORTIZ, VICTORIANO

UNIVERSIDAD DE ZARAGOZA

Química Física

2019

Universidad Zaragoza
1542

Facultad de Ciencias
Universidad Zaragoza

Ph.D. Thesis

Computational Catalysis of Homogenous and Heterogeneous Systems:

New Insights into the Activation of Small Molecules

Julen Munárriz Tabuenca

Supervised by Dr. Víctor Polo Ortiz

Zaragoza

2018

Computational Catalysis of Homogenous and Heterogeneous Systems: New Insights into the Activation of Small Molecules

Memoria presentada por Julen Munárriz Tabuenca, graduado en Química y Máster Europeo en Química Teórica y Modelización Computacional, para optar al grado de Doctor en Ciencias, en el programa de Doctorado en Química Física.

Esta tesis doctoral se presenta en la modalidad de tesis por compendio de publicaciones, e incluye siete artículos que se encuentran recogidos en revistas científicas con un índice de impacto incluido en la relación de revistas del *Journal of Citations Reports*. Las publicaciones que forman parte de la tesis son las siguientes:

1. *Understanding the reaction mechanism of the oxidative addition of ammonia by (PXP)Ir(I) complexes: the role of the X group.*
   Julen Munárriz, Ederley Velez, Míguel Ángel Casado, Víctor Polo.
   Physical Chemistry Chemical Physics. **2018**, *20*, 1105–1113.

2. *A well-defined NHC-Ir(III) catalyst for the silylation of aromatic C–H bonds: substrate survey and mechanistic insights.*
   Laura Rubio-Pérez, Manuel Iglesias, Julen Munárriz, Víctor Polo, Vincenzo Passarelli, Jesús Julián Pérez-Torrente, Luis Antonio Oro.
   Chemical Science **2017**, *8*, 4811–4822.

3. *A highly efficient Ir-catalyst for the solventless dehydrogenation of formic acid: the key role of an N-heterocyclic olefin.*
   Amaia Iturmendi, Manuel Iglesias, Julen Munárriz, Victor Polo, Vincenzo Passarelli, Jesús J. Pérez Torrente, Luis A. Oro.
   Green Chemistry, **2018**, *20*, 4875–4879.

4. *Efficient preparation of carbamates by Rh-catalysed oxidative carbonylation: unveiling the role of the oxidant.*
   Amaia Iturmendi, Manuel Iglesias, Julen Munárriz, Victor Polo, Jesús J. Pérez Torrente, Luis A. Oro.
   Chemical Communications, **2017**, *53*, 404–407.

5. Analysis of the Magnetic Entropy in Oxygen Reduction Reactions Catalysed by Manganite Perovskites.
   José Gracia, Julen Munárriz, Víctor Polo, Ryan Sharpe, Yunzhe Jiao, J. W. (Hans) Niemantsverdriet, Tingbin Lim.
   ChemCatChem **2017**, *9*, 3358–3363.

6. *Principles determining the activity of magnetic oxides for electron transfer reactions.*
   José Gracia, Ryan Sharpe, Julen Munárriz.
   Journal of Catalysis **2018**, *361*, 331–338.

7. *On the Role of Ferromagnetic Interactions in Highly Active Mo-based Catalysts for Ammonia Synthesis.*
   Julen Munárriz, Víctor Polo, José Gracia.
   ChemPhysChem **2018**, *19*, 2843–2847.

Victoriano Polo Ortiz, Profesor Titular de la Facultad de Ciencias en el Departamento de Química Física de la Universidad de Zaragoza,

CERTIFICA:

Que la presente Memoria titulada *"Computational Catalysis of Homogenous and Heterogeneous Systems: New Insights into the Activation of Small Molecules"* ha sido realizada en el Departamento de Química Física de la Universidad de Zaragoza bajo mi dirección y autoriza su presentación para que sea calificada como Tesis Doctoral en la modalidad de compendio de publicaciones.

Zaragoza, a 12 de noviembre de 2018.

Fdo. Dr. Victoriano Polo Ortiz

A mis padres

y a mi hermano

Resumen

Esta Tesis Doctoral se ubica en el contexto del estudio teórico y computacional de catalizadores, tanto homogéneos como heterogéneos, para la fijación de moléculas pequeñas, en concreto N_2, O_2, CO, NH_3, HCOOH e hidrosilanos, empleando DFT. Estos procesos presentan un gran interés en investigación química, ya que un conocimiento en profundidad de los mismos facilitaría el diseño racional de nuevos catalizadores más activos y respetuosos con el medio ambiente. A continuación se presenta un resumen de los procesos estudiados.

En el campo de la catálisis homogénea, se estudiaron cuatro procesos químicos diferentes, catalizados por complejos organometálicos de Rh e Ir:

i) Fijación de amoniaco mediante complejos de Ir con ligandos de tipo pincer. En particular, se estudiaron los factores cinéticos y termodinámicos que afectan a la actividad del catalizador. Para ello, se emplearon diferentes métodos para el estudio del enlace químico, como IQA y la ELF.
ii) La sililación de enlaces C–H aromáticos mediante un complejo bien definido de Ir(III)–NHC. Se propuso un mecanismo de reacción completo mediante cálculos computacionales. Asimismo, se realizaron una serie de experimentos que apoyan dicho mecanismo. Los resultados obtenidos revelaron el papel clave de los grupos directores presentes en el sustrato en el control de la selectividad del proceso.
iii) El empleo de hidrógeno molecular como vector energético. En particular, se estudió el proceso de deshidrogenación de ácido fórmico para generar H_2 catalizado por un compuesto de Rh–NHO muy activo. Los estudios computacionales permitieron proponer un mecanismo de reacción plausible, que está de acuerdo con las barreras energéticas determinadas experimentalmente.
iv) La alcoxicarbonilación de alcoholes y aminas con CO para preparar carbamatos. El proceso está catalizado por un complejo de Rh y requiere le acción de un oxidante ($KHSO_5$). El estudio teórico realizado permitió proponer un mecanismo de reacción y determinar el papel clave del oxidante.

Con respecto a la catálisis heterogénea, se abordó la propuesta de nuevos descriptores de la actividad catalítica basados en las propiedades magnéticas del catalizador y los reactivos. Los diferentes procesos estudiados se resumen a continuación:

v) Las reacciones de reducción de oxígeno (ORR) y de evolución de oxígeno (OER) catalizadas por materiales basados en perovskitas. En concreto, es analizaron las propiedades magnéticas de diferentes catalizadores derivados de $LaMnO_3$. Los resultados mostraron la importancia de tener en cuenta la entropía electrónica y la fase magnética del catalizador. Basándonos en estos resultados, se propusieron una serie de reglas para el diseño de nuevos catalizadores heterogéneos derivados de óxidos metálicos magnéticos para ORR y OER. Finalmente, estas reglas se emplearon en el diseño de un nuevo catalizador para OER basado en la perovskita $LaFeO_3$.
vi) Los principios previamente presentados se ampliaron al estudio de procesos de fijación de N_2 catalizados por nitruros de Mo. Los resultados muestran la validez de la aplicación del momento magnético del molibdeno como descriptor de la actividad catalítica.

Abstract

This Ph.D. Thesis is devoted to the theoretical and computational study of homogeneous and heterogeneous catalysts for the activation of small molecules, namely N_2, O_2, CO, NH_3, HCOOH and hydrosilanes, using DFT methodologies. These processes have a great interest in current chemical research, as their in-depth knowledge paves the way to the rational design of new environmentally respectful and active catalysts. A summary of the different reactions considered is presented below.

Within the field of homogeneous catalysis, four different chemical processes catalysed by Rh- or Ir-based organometallic complexes were considered:

i) Ammonia fixation by Ir-complexes that bear different pincer ligands. In particular, we studied the thermodynamic and kinetic factors that can affect the catalytic activity. For that, different methods for the study of chemical bonds, such as IQA and the ELF, were applied.
ii) The silylation of aromatic C–H bonds by means of a well-defined and highly active Ir(III)–NHC catalyst. A detailed computational study of the reaction mechanism was performed. This mechanism was experimentally supported by different stoichiometric experiments. The results revealed the key role of the directing groups in the substrate for controlling the reaction selectivity.
iii) The use of molecular hydrogen as an energy vector. In particular, we considered the formic acid dehydrogenation process to yield H_2 catalysed by a very active Ir–NHO complex. The performed studies allowed to propose a plausible reaction mechanism that is in agreement with the activation energy experimentally determined.
iv) The alcoxycarbonylation of alcohols and amines with CO to yield carbamates. The process is catalysed by a Rh-complex and requires the presence of an oxidant ($KHSO_5$). The theoretical study allowed to propose a reaction mechanism, as well as to unravel the role of the oxidant.

With respect to heterogeneous catalysis, we addressed the proposal of novel catalytic descriptors on the basis of orbital physics and the magnetic properties of the catalyst and the reagent. The considered processes are the following.

v) The oxygen reduction reaction (ORR) and the oxygen evolution reaction (OER) catalysed by perovskite-based materials. Specifically, the magnetic features of different catalysts based on $LaMnO_3$ were analyzed. The results showed the importance of taking into account the electronic entropy and the catalyst magnetic phase. On the basis of these results, a set of rules for the design of heterogeneous catalysts for ORR and OER based on magnetic metal oxides was proposed. Finally, these guidelines were applied to the design of a novel catalyst for OER based on a $LaFeO_3$ composition.
vi) The previous principles were extended to N_2 fixation catalysed by different Mo-nitrides. The results provided strong evidence on the application of the Mo magnetic moment as a descriptor for the catalysts activity towards N_2 fixation.

TABLE OF CONTENTS

INTRODUCTION

Current chemical research is not only based on chemical intuition and trial-error approaches for the design and synthesis of novel molecules and materials. On the contrary, increasingly sophisticated methodologies have been developed to help the efficient and sustainable development of novel chemical processes. Within this new way of proceeding, Theoretical and Computational Chemistry (TCC) has become a popular discipline, as it is able to provide rigorous models and concepts that allow to understand, design and control novel experiments and complex syntheses, thus going beyond extrapolation and induction from empirical data.[1]

The main goal of Theoretical and Computational Chemistry is the understanding of the inherent link between microscopic properties and observable chemical behaviour.[2,3] As previously stated, the knowledge of this relation is not only important from an academic point of view, but also from a practical way. As Kurt Lewin said, *"There is nothing more practical than a good theory"*. The in-depth understanding of the relationship between the chemical structure and the macroscopic behaviour holds the key for the rational design of new synthetic routes leading to compounds with target properties in good yields and from an environmental-friendly point of view.[4,5] Due to its valuable contributions and its enormously high potential in chemical research, during the last decades, TCC has spread to all the branches of knowledge related to Chemistry, as Physics, Materials Science and Biochemistry.[6]

One can consider that Quantum Mechanics were born between 1925 and 1927, when Schrödinger, Heisenberg and Dirac proposed (independently) a novel theory for studying the behaviour and dynamics of microscopic systems. In this way, they set a new paradigm for the treatment of *"very small"* systems, of the size of electrons and individual atoms; overcoming, at least partially, the limitations of classical mechanics. Nonetheless, the equations that arose presented a great complexity, and could only be solved analytically for the hydrogen atom. For that reason, some approximated methods for solving them were developed, the best known probably being the Hartree-Fock one.[7] During the next decades, following the successive developments of more efficient and increasingly powerful computers and mathematical methods, Quantum and Computational Chemistry enormously grew up, becoming more and more powerful in the study of increasingly complex chemical systems.[8]

Probably, the most celebrated milestone of TCC took place in the 1960s, when Hohenberg, Kohn and Sham proposed their well-known theorems, in which they proved that the external potential, and hence the total energy, of a given non-degenerate system is a functional of the electron density, $\rho(r)$. Consequently, energies and other properties of the system can be directly obtained from the electron density, leading to the development of Density Functional Theory (DFT).[9] Thanks to it, the application of Quantum Mechanics extended from a dozen of atoms to much bigger systems.

In principle, DFT is an exact theory. However, the analytical expression of the functional that links the electron density with the external potential is only partially known, as it lacks the exchange-correlation term $E_{xc}[\rho]$. For that reason, different approximate methodologies with increasing complexity have been developed, leading to the appearance of Density Functional Approximations (DFA),[10] which will be further explained in the Methodology chapter. As expected, the mathematical complexity and the computational cost increases when increasing DFAs quality and thus the accuracy of the expected results. This process is exemplified by different rungs in the Jacob's ladder, as proposed by Perdew and co-workers (see Figure I.1).[11]

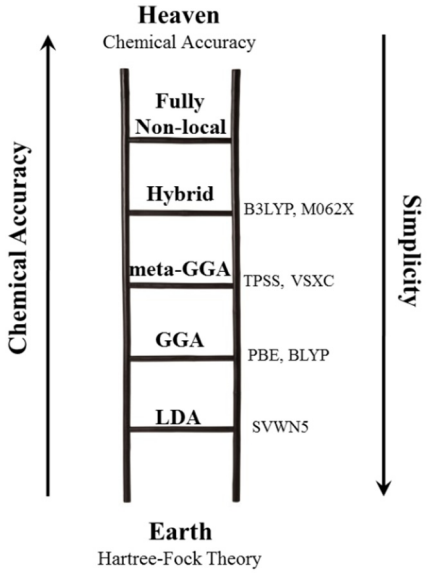

Figure I.1. Schematic representation of the Jacob's Ladder and examples of each Density Functional Approximations.

Nonetheless, a recipe for systematically improve the results accuracy while maintaining the computational cost reasonable remains unknown. These methods, in conjunction with other milestones of TCC, such as the development of hybrid QM/MM approaches, highly efficient molecular dynamics (MD) simulations or novel solvation models, have made a huge impact in current chemical research.[12] As a consequence, TCC has been awarded the Nobel Prize in several occasions, the last one being the Nobel Prize in Chemistry in 2013 to Karplus, Levitt and Warshel *"for the development of multiscale models for complex chemical systems"*.

As previously stated, the working framework of TCC allows for obtaining data at an atomic level. This information is, in most cases, not accessible experimentally. In particular, we can predict molecular spectra, characterize non-covalent enzyme-ligand interactions, and compute activation and reaction energies, among many others.[1] Within this context, Theoretical and Computational Chemistry has proven to be especially useful in the field of Catalysis.[12]

Catalysis can be defined as the process whereby a chemical reaction is accelerated due to the participation on it of a substance known as "catalyst". This species produces a change in the reaction mechanism, reducing the activation energy, and is recovered unaltered at the end of the reaction (see Scheme I.1). Catalytic processes usually classify attending to the relative phase of the reagents with respect to the catalyst. When they are in the same phase, we talk about homogeneous catalysis. On the contrary, when they are in different phases, we have heterogeneous catalysis; the chemical reaction happening at the interface in between. Since enzymatic catalysis has some points in common with both types of catalysis (the global system is homogeneous as far as the solvent influence is involved, while the reaction takes place in the interface determined by the protein active site), it is usually considered as an independent category.[13] In general terms, the main advantages of homogeneous catalysis with respect to heterogeneous one are its greater activity and selectivity, in conjunction with the requirement of softer reaction conditions. Besides that, and contrarily to what usually happens in heterogeneous catalysis, the catalytic active centres are generally well known, enhancing the facility of modulating their properties. Nonetheless, the separation and recycling of the catalyst is much more complicated for homogeneous catalysts.

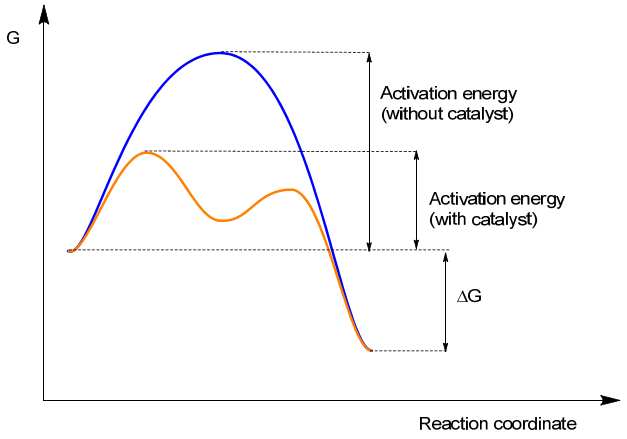

Scheme I.1. General reaction profile for a given chemical reaction with (orange) and without catalyst (blue).

The two main properties of a given catalyst are its activity and selectivity. The activity accounts for the increase in the reaction rate achieved by the catalyst. There

are many different manners of expressing it. Probably, the most used in the chemical community are the *"turnover number"* (TON) and the *"turnover frequency"* (TOF).[14]

With respect to the selectivity, one can consider that the main goal of synthetic chemistry is being able to manipulate the reagents in such a way that any functional group could be installed at the desired position of a molecule or material in the presence of other potentially reactive functional groups.[15] In this sense, catalysis plays a fundamental role, as it allows to modulate chemical reactivity, favoring a given product over all the other possible ones. In addition, catalysis allows, in some occasions, to obtain the least thermodynamically stable isomer, which could not be obtained otherwise.[16,17]

Taking into account the scope of the previous concepts, it is not surprising that catalysis is one of the fundamental supports of Green Chemistry.[18] In particular, it is especially useful for the rational design of chemical processes that reduce the use of hazardous substances, so that we can simultaneously synthetize the desired products with broad economic benefits from an environmentally respectful perspective. It also reduces the energy requirements for a given process to take place, increasing the selectivity and decreasing the necessity for separation steps (especially in heterogeneous catalysis). In addition, it limits the number of by-products, and reduces the economic cost, since only catalytic amounts of the catalysts are need.[19]

Within this context, Theoretical and Computational Chemistry has proven to be one of the key components of catalysis research; being especially suitable for reaction mechanism investigations, and, subsequently, for catalyst design.[12] In this way, current computational approaches, mainly DFT-based ones, are well-sited for performing chemical reactivity studies, predicting chemical kinetics of catalytic processes and, in general, investigating complex reacting pathways, thus providing an in-depth insight on the factors that determine why a given chemical process is favoured over all the potentially possible ones.[20]

These outstanding results have been possible thanks to the development of DFT methodologies that provide accurate results while maintaining the required computational effort reasonable. Specifically, modern TCC approaches provide computational tools able to achieve "chemical accuracy", that is, an absolute error lower than 4 kJ/mol, for relatively simple and small systems.[21] However, the enormous complexity of real catalytic systems makes necessary the use of different approximations and simplifications. For that, it is of great importance to make an adequate valance between the model systems and the characteristics of the real system, so that computational results are representative of the system.[20] In this regard, computational schemes based on optimizations carried out using standard functionals like B3LYP, in conjunction with double-zeta basis sets as well as dispersion and solvent corrections, with subsequent energy refinement using larger basis sets have

proven to be efficient for molecular systems.[22] With respect to calculations in periodic systems, required for heterogeneous catalysis modelling, approaches based on GGA+*U* approximations (especially the PBE functional), with Hubbard *U* values selected so as to reproduce experimental data, and empirical dispersion corrections are generally suited.[23]

Nonetheless, for the case of complex reactions, DFT studies alone may not be enough to provide an accurate description of the reaction mechanism. This way, it is possible to compute an apparently correct reaction mechanism that does not correlate with the experimental data. For that, if there is no possibility to test the theoretical results, there is no absolute certainty that they are correct.[24] This feature shows the importance of benchmark studies that correlate experimental and computational data, and the comparison between different computational approaches, so that we can make sure that the obtained results are *"chemically meaningful"*.[25,26]

This Doctoral Thesis is located within the previously explained context of Theoretical and Computational Chemistry applied to the understanding of catalytic reaction mechanisms, finding descriptors for predicting the catalytic activity and, in general, catalysts design. It covers the study of both, homogenous and heterogeneous catalysts for the activation of small molecules, namely hydrosilanes, ammonia, carbon dioxide, alcohols, oxygen and nitrogen. The obtained results are divided into two different chapters.

Chapter 1 focuses on the study of homogeneous catalysis mediated by Ir or Rh organometallic complexes bearing different kinds of ancillary ligands. The chapter is structured into four different sections, which are schematically presented in Scheme I.2, and are briefly presented below.

A. Ammonia activation by Ir(I)-PXP complexes. In this section, we address the analysis of the electronic factors governing NH_3 activation by means of five different Ir(I)-(PXP) complexes. The main goal of the performed analyses is the rational development of novel Ir(I) complexes bearing pincer ligands for ammonia activation. Results corresponding to this section are included in the following article:

Munárriz, J.; Velez, E.; Casado, M. A.; Polo, V. Understanding the reaction mechanism of the oxidative addition of ammonia by (PXP)Ir(I) complexes: the role of the X group. *Phys. Chem. Chem. Phys.* **2018**, *20*, 1105–1113.

B. Ir(III)-NHC catalysts for the silylation of aromatic C–H bonds. This section is devoted to the understanding of the reaction mechanism of aromatic C–H bonds silylation by means of a Ir(III)-NHC catalyst (see Scheme I.2). Special attention is

payed to unravelling the importance of directing groups in the catalyst selectivity. Results discussed in this section are published in:

Rubio-Pérez, L.; Iglesias, M.; Munárriz, J.; Polo, V.; Passarelli, V.; Pérez-Torrente, J. J.; Oro, L. A. A well-defined NHC-Ir(III) catalyst for the silylation of aromatic C–H bonds: substrate survey and mechanistic insights. *Chem. Sci.* **2017**, *8*, 4811–4822.

C. Ir(III)-NHO catalyzed solventless dehydrogenation of formic acid. This section is located within the context of molecular H_2 as an environmentally friendly energy vector. In particular, the Ir(III)-NHO catalyst presented in Scheme I.2 is able to efficiently dehydrogenate formic acid to release H_2 and CO_2, opening the door to novel routes for H_2 transport. A detailed reaction mechanism study of this process is performed with the aim of in-depth understanding the process and being able to design new catalysts. Results corresponding to this section are published in:

Iturmendi, A.; Iglesias, M.; Munárriz, J.; Polo, V.; Passarelli, V.; Pérez-Torrente, J. J.; Oro, L. A. Highly Efficient Ir-Catalyst for the Solventless Dehydrogenation of Formic Acid: The Key Role of an N-heterocyclic Olefin. *Green Chem.* **2018**, *20*, 4875–4879

D. Unveiling the role of organic oxidants on oxidative carbonylations. A detailed investigation of the reaction mechanism of the synthesis of carbamates by means of Rh(I)-catalyzed oxidative carbonylation of different alcohols and aromatic amines is performed. The reaction requires an oxidant; in particular, we selected Oxone ($KHSO_5$). In addition to proposing a reaction mechanism, especial efforts are made so as to clearly identify the effect of the oxidant within the process. The results presented in this section correspond to the following article:

Iturmendi, A.; Iglesias, M.; Munárriz, J.; Polo, V.; Pérez-Torrente, J. J.; Oro, L. A. Efficient preparation of carbamates by Rh-catalysed oxidative carbonylation: unveiling the role of the oxidant. *Chem. Commun.* **2017**, *53*, 404–407.

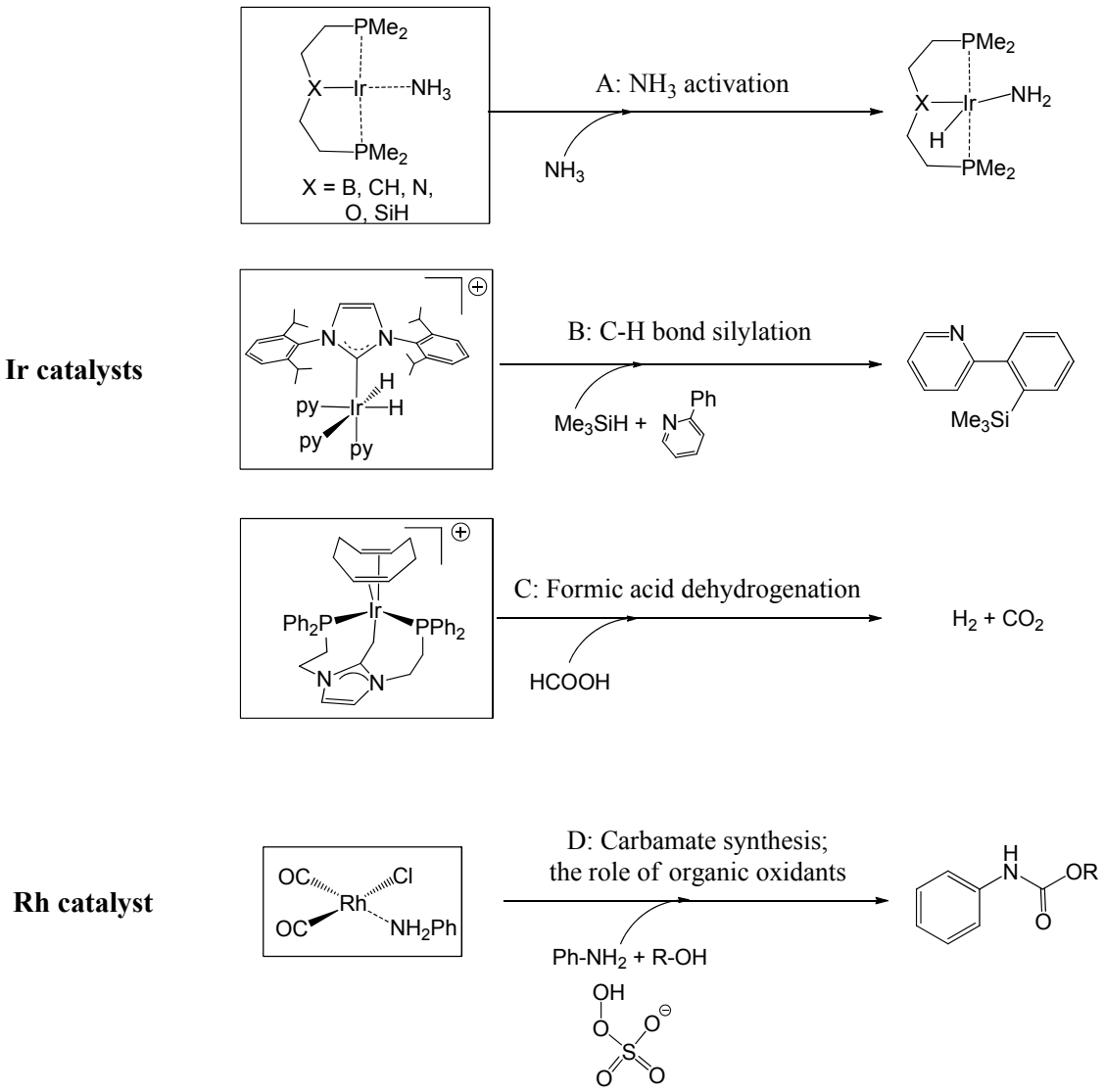

Scheme I.2. Schematic representation of the different chemical processes and catalysts considered in each section of Chapter 1.

Chapter 2 is devoted to the study of heterogeneous catalytic reactions involving small molecules, namely, O_2 and N_2. The main goal of this chapter is the determination of the importance of magnetic effects in the catalytic performance and their application to derive physically meaningful descriptors for the design of novel materials. Specifically, two different families of systems are studied. In the first section, oxygen evolution and reduction reactions (OER and ORR) catalysed by perovskite-based materials are addressed. In the second one, we explore the application of the descriptors derived from magnetic properties to explain the catalytic activity of Mo-based nitrides towards nitrogen fixation reactions to produce ammonia. The processes discussed in both sections are exemplified in Scheme I.3.

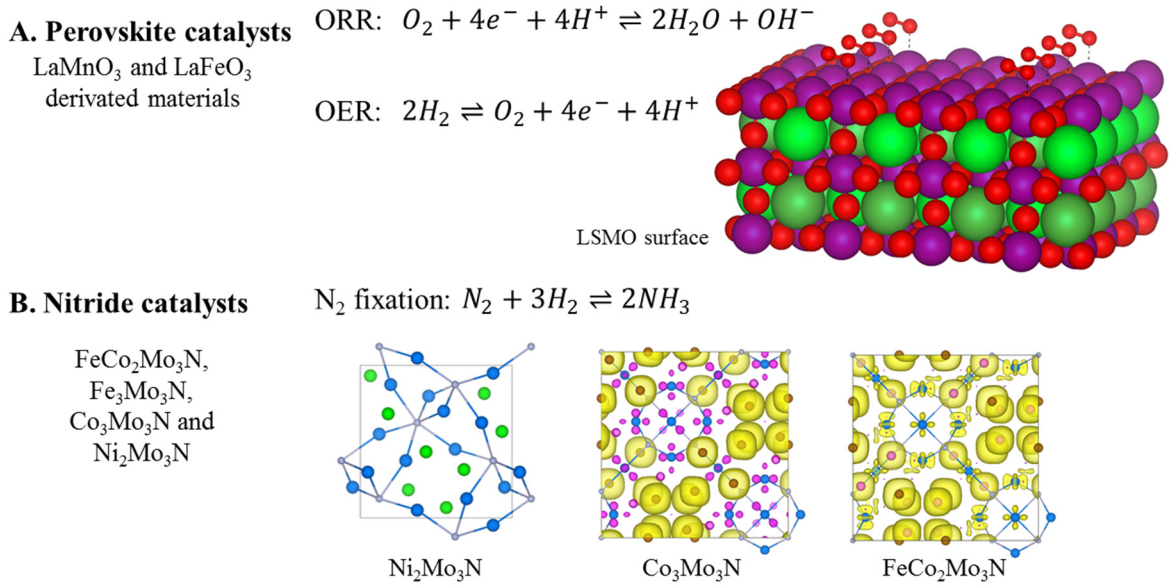

Scheme I.3. Schematic representation of the different chemical processes and catalysts considered in each section of Chapter 2.

The two sections and the three articles that constitute Chapter 2 are briefly described below.

A. Oxygen Reduction and Evolution Reactions. The main goal of this section is the in-depth investigation of the magnetic effects on Oxygen Evolution and Reduction Reactions. For that, we first analysed the effect of magnetic entropy on the catalytic performance of highly active $LaMnO_3$-based catalysts towards the Oxygen Reduction Reaction. Then, general rules for predicting the relative activity of oxide-based catalysts for OER and ORR are presented. Finally, a working example of the application of the previous rules for catalyst design is presented. Results corresponding to this section are included in the following papers:

Gracia, J.; Munárriz, J.; Polo, V. Sharpe, R.; Jiao, Y.; Niemantsverdriet, J. W. H.; Lim, T. Analysis of the Magnetic Entropy in Oxygen Reduction Reactions Catalysed by Manganite Perovskites. *ChemCatChem* **2017**, *9,* 3358–3363.

Gracia, J.; Sharpe, R.; Munárriz, J. Principles determining the activity of magnetic oxides for electron transfer reactions. *J. Catal.* **2018**, *361*, 331–338.

B. Nitrogen fixation. Within this part, we analysed the influence of magnetic structure on Mo-based nitrides for N_2 fixation, namely: Ni_2Mo_3N, Fe_3Mo_3N, Co_3Mo_3N and $FeCo_2Mo_3N$. In particular, the main goal is investigating the possibility of the application of the same principles that worked for OER and ORR to nitrogen fixation. The results presented in this section are contained in the following article:

Munárriz, J.; Polo, V.; Gracia, J. On the Role of Ferromagnetic Interactions in Highly Active Mo-based Catalysts for Ammonia Synthesis. *ChemPhysChem.* **2018**, *19*, 2843–2847.

This way, the thematic unit of this Doctoral Thesis is the theoretical and computational study of catalytic systems bearing transition metals towards the activation and functionalization of small molecules.

References

[1] Cramer, C. J. *Essentials of Computational Chemistry: Theory and Models*; Wiley-VCH: Chichster, 2014.

[2] Hoffmann, R.; Alvarez, S.; Mealli, C.; Falceto, A.; Cahill, T.J.; Zeng, T.; Manca, G. From Widely Accepted Concepts in Coordination Chemistry to Invented Ligand Fields. *Chem. Rev.* **2016**, *116*, 8173–8192.

[3] Thiel, W. Theoretical Chemistry-Quo Vadis? *Angew. Chem. Int. Ed.* **2011**, *50*, 9216–9217.

[4] Johnson, M. A. Experiment and theory in harmony. *Nat. Chem.* **2009**, *1*, 8–9.

[5] Rohmann, K.; Hölscher, M.; Leitner, W. Can Contemporary Density Functional Theory Predict Energy Spans in Molecular Catalysis Accurately Enough To Be Applicable for in Silico Catalyst Design? A Computational/Experimental Case Study for the Ruthenium-Catalyzed Hydrogenation of Olefins. *J. Am. Chem. Soc.* **2016**, *138*, 433–443.

[6] For examples see: (a) Castelli, I. E.; García-Lastra, J. M.; Thygesen, K. S.; Jacobsen, K. W. Bandgap calculations and trends of organometal halide perovskites. *Apl. Materials* **2014**, *2*, 081514. (b) Ashby, M. F. Multi-Objective Optimization in Material Design and Selection. *Acta Mater.* **2000**, *48*, 359–369. (c) Göltl, F.; Müller, P.; Uchupalanun, P.; Sautet, P.; Hermans, I. Developing a Descriptor-Based Approach for CO and NO Adsorption Strength to Transition Metal Sites in Zeolites. *Chem. Mater.* **2017**, *29*, 6434–6444. (d) Kupgan, G.; Abbott, L. J.; Hart, K. E.; Colina, C. M. Modeling Amorphous Microporous Polymers for CO_2 Capture and Separations. *Chem. Rev.* **2018**, *118*, 5488–5538. (e) Keith, T.; Frost, J. M.; Walsh, A. Ferroelectric materials for solar energy conversion: photoferroics revisited. *Energy Environ. Sci.* **2015**, *8*, 838–848. (f) Butler, K. T.; Frost, J. M.; Skelton, J. M.; Svane, K. L.; Walsh, A. Computational materials design of crystalline solids. *Chem. Soc. Rev.* **2016**, *45*, 6138–6146. (g) Steinhauser, M. O.; Hiermaier, S. A Review of Computational Methods in Materials Science: Examples from Shock-Wave and Polymer Physics. *Int. J. Mol. Sci.* **2009**, *10*, 5135–56216. (h) Curtarolo, S.; Hart, G. L. W.; Nardelli, M. B.; Mingo, N.; Sanvito, S.; Levy, O. The high-throughput highway to computational materials design. *Nat. Mater.* **2013**, *12*, 191–201. (i) Palsgaard, M.; Markussen, T.; Gunst, T.; Brandbyge, M.; Stokbro, K. Efficient Fisrt-Principles Calculation of Phonon-Assisted Photocurrent in Large-Scale Solar-Cell Devices. *Phys. Rev. Appl.* **2018**, *10*, 014026. (j) Goonie, A.; Schuschnigg, S.; Holzer, C. A Review of Multiscale Computational Methods in Polymeric Materials. *Polymers* **2017**, *9*, 16.

[7] Ramachandran, K. I.; Gopakumar, D.; Namboori, K. *Computational Chemistry and Molecular Modeling*; Springer: Berlin, Heidelberg, 2008.

[8] (a) Li, P.; Merz Jr., M. *Chem. Rev.* **2017**, *117*, 1564–1686. (b) Sevgen, E.; Giberti, F.; Sidky, H.; Whitmer, J. K.; Galli, G.; Gygi, F.; de Pablo, J. J. Hierarchical Coupling of First-Principles Molecular Dynamics with Advanced Sampling Methods. *J. Chem. Theory Comput.* **2018**, *14*, 2881–2888.

[9] (a) Hohenberg, P.; Kohn, W. Inhomogeneous electron gas. *Phys. Rev.* **1964**, *136*, B864–B871. (b) Kohn, W.; Sham, L. J. Self-consistent equations including exchange and correlation effects. *Phys. Rev.* **1965**, *140*, A1133–1138.

[10] Sharkas, K.; Toulouse, J.; Savin, A. Double-hybrid density-functional theory made rigorous. *J. Chem. Phys.* **2011**, *134*, 064113.

[11] Perdew, J. P.; Schmidt, K. Jacob's ladder of density functional approximations for the exchange-correlation energy. *AIP Conference Proceedings* **2001**, *577*, 1–20.

[12] Houk, K. N.; Liu, F. Holy Grails for Computational Organic Chemistry and Biochemistry. *Acc. Chem. Res.* **2017**, *50*, 539–543.

[13] Rothenberg, G. *Catalysis: Concepts and Green Applications*; Wiley-VCH: Chichster, 2008.

[14] Kozuch, S.; Martin, J. M. L. "Turning Over" Definitions in Catalytic Cycles. *ACS Catal.* **2012**, *2*, 2787–2794.

[15] Arndsten, B. A.; Bergman, R. G.; Mobley, T. A.; Peterson, T. H. Selective Intermolecular Carbon-Hydrogen Bond Activation by Synthetic Metal Complexes in Homogeneous Solution. *Acc, Chem. Res.* **1995**, *28*, 154–162.

[16] Hartwig, J. F. Catalyst-Controller Site-Selectivity Bond Activation. *Acc. Chem. Res.* **2017**, *50*, 549–555.

[17] Iglesias, M.; Aliaga-Lavrijsen, M.; Sanz Miguel, P. J.; Fernandez-Alvarez, F. J.; Perez-Torrente, J. J.; Oro, L. A. Preferential α□Hydrosilylation of Terminal Alkynes by Bis□N□ Heterocyclic Carbene Rhodium(III) Catalysts. *Adv. Synth. Catal.* **2015**, *357*, 350–354.

[18] Anastas, P. T.; Warner, J. C. *Green Chemistry: theory and Practice*; Oxford University Press: New York, 1998.

[19] Anastas, P. T.; Kirchhoff, M. M.; Williamson, T. C. Catalysis as a foundation pillar of green chemistry. *Appl. Catal., A* **2001**, *221*, 3–13.

[20] Pidko, E. A. Towards the balance between the reductionist and systems approaches in computational catalysis: model versus method accuracy for the description of catalytic systems. *ACS Catal.* **2017**, *7*, 4230–4234.

[21] Peterson, K. A.; Feller, D.; Dixon, A. A. Chemical accuracy in ab initio thermochemistry and spectroscopy: current strategies and future challenges. *Theor. Chem. Acc.* **2012**, *131*, 1079.

[22] Thiel, W. Computational Catalysis–Past, Present, and Future. *Angew. Chem. Int. Ed.* **2014**, *53*, 8605–8613.

[23] Capdevila-Cortada, M.; Łodziana, Z.; López, N. Performance of DFT+U Approaches in the Study of Catalytic Materials. *ACS. Catal.* **2016**, *6*, 8370–8379.

[24] Plata, R. E.; Singleton, D. A. A Case Study of the Mechanism of Alcohol-Mediated Morita Baylis–Hillman Reactions. The Importance of Experimental Observations *J. Am. Chem. Soc.* **2015**, *137*, 3811–3826.

[25] Bligaard, T.; Bullock, R.M.; Campbell, C. T.; Chen, J. G.; Gates, B. C.; Gorte, R. J.; Jones, C. W.; Jones, W. D.; Kitchin, J. R.; Scott, S. L. Toward Benchmarking in Catalysis Science: Best Practices, Challenges, and Opportunities. *ACS Catal.* **2016**, *6*, 2590–2602.

[26] Hopmann, K. H. How Accurate is DFT for Iridium-Mediated Chemistry? *Organometallics* **2016**, *35*, 3795–3807.

RESEARCH OBJECTIVES

As previously introduced, the results that constitute this Doctoral Thesis are divided into two chapters. The results corresponding to the study of homogeneous catalysis are presented in Chapter 1, whereas those involving heterogeneous catalysts are included in Chapter 2. The main research objectives are the following:

The main goal of **Chapter 1** is the understanding of the reaction mechanism of different chemical processes catalysed by Ir and Rh complexes, with special focus on the electronic factors that determine the reaction selectivity and the catalyst activity. The different processes studied and the main objectives of each study are explained below:

A. Ammonia activation by Ir(I)-PXP complexes. The main goal of this section is the understanding of the electronic features that determine the kinetics and thermodynamics of ammonia activation processes catalysed Ir(I)-PXP complexes.

B. Ir(III)-NHC catalysts for the silylation of aromatic C–H bonds. The main objectives of this section are: i) unrevealing the reaction mechanism of the silylation of aromatic C–H bonds catalysed by an Ir(III)-NHC catalyst; ii) explaining the effect of the directing groups of the substrate in the reaction selectivity.

C. Ir(III)-NHO catalyzed solventless dehydrogenation of formic acid. The main goal of this section is proposing a feasible reaction mechanism for the dehydrogenation of formic acid to yield H_2 and CO_2, catalysed a Ir(III)-NHO complex.

D. Unveiling the role of organic oxidants on oxidative carbonylations. The main objectives of this section are: i) the determination of the reaction mechanism for the synthesis of carbamates by means of the oxidative carbonylation of alcohol and amines with CO and an oxidant, catalized by a Rh(I) organometallic complex; ii) explaining the exact role of the oxidant required in these kind of processes.

The main research objective of **Chapter 2** is the understanding of the influence of magnetic interactions in heterogeneous catalysis. In particular, this dissertation focuses on chemical processes that involve the O_2 and N_2 molecules catalysed by magnetic oxides and Mo-based nitrides, respectively. The different systems under study and the specific goals are presented below:

A. Oxygen Reduction and Evolution Reactions. The main objective of this section is: i) the in-depth investigation of the influence of magnetic interactions in the catalytic activity of magnetic metal oxides (with especial focus on perovskites) towards the oxygen reduction and evolution reactions (ORR and OER); ii) the proposal of physically meaningful descriptors able to predict the relative activity of this kind of materials; iii) Apply these descriptors for the rational design of new materials with improved activity towards ORR and OER.

B. Nitrogen fixation. The main goal of this section is expanding the previous physical principles to the N_2 fixation reaction to produce ammonia catalysed by a set of Mo-based nitrides.

METHODOLOGY

A. The Schrödinger equation

The evolution in time of a given chemical system is determined by the Schrödinger equation (eq. M.1), which constitutes the cornerstone of quantum mechanics.

$$i\hbar\Psi(q,t) = \hat{H}\Psi(q,t) \tag{M.1}$$

Within eq. M.1, $\Psi(q,t)$ is the system wavefunction, which contains all the accessible information about the system, and $\hat{H}$ is the time-dependent Hamiltonian operator. This operator is expressed as the sum of two terms, the kinetic and the potential operators, and altogether, they account for the system total energy. If the system is in a stationary state the Hamiltonian does not depend on time, and the spatial and temporal parts of the wavefunction can be separated. In this way, the time-independent Schrödinger equation is obtained (eq. M.2).

$$\hat{H}\psi(q) = E\psi(q) \tag{M.2}$$

However, the great complexity of this equation makes impossible its analytical resolution, making necessary the use of different approximations and the application of numerical methods.

Probably, the most common simplification is the so-called Born-Oppenheimer approximation. It is based on the fact that nuclei mass is much higher than that of electrons. As a consequence, the kinetic energy of the nuclei can be neglected with respect to that of electrons. Their motion scales are different and both movements can be separated and studied independently. In particular, one can consider that the electrons follow the movements of the nuclei, adapting instantaneously to each nuclear configuration. Moreover, during each electron movement, the nuclear configuration is fixed. Thus, the nuclear repulsion term is constant, avoiding the need for calculating the integrals for nucleus-nucleus interactions. Within this framework, the Schrödinger equation is solved for each nuclear configuration, leading to the appearance of the concept of Potential Energy Surface (PES).[1]

In spite of the usefulness of this simplification, the exact solution of the Schrödinger equation (within this approach) is only possible for one-electron systems, such as the H_2^+ molecule. For many electron systems, such as molecules and solids, electron-electron interactions have to be evaluated, and represent a very difficult task since the interaction of N-electrons cannot be expressed as a sum of N one-electron integrals. As a result, further approximations are required.

In this regard, there are two different approaches, Density Functional Theory, which constitutes the working framework of this dissertation and will be explained below, and *ab initio* methods.[2,3] The latter aim to solve the Schrödinger equation by means of the computation of an approximate wavefunction for the system under study.[4] Unfortunately, these methods are quite computationally expensive and are only affordable for relatively small systems, of the order of 40 atoms, or even lower if metal atoms are included.

B. Density Functional Theory

Density Functional Theory (DFT) methods constitute a good compromise between accuracy and computational efficient, allowing for the study of systems bearing transition metals, bulky ligands and/or the consideration of periodic systems, such as the ones considered in this dissertation. In addition, electronic and steric effects are crucial in the determination of catalytic properties in transition metal catalysis; then, the use of small model systems is severely discouraged.[5]

Density Functional Theory was proposed by Hohenberg and Kohn in 1964.[6] This method is based on the so-called Hohenberg-Kohn theorems, which state that the ground state energy of a given system can be univocally derived from the system electron density, $\rho(\vec{r})$. Noteworthily, this approach enormously simplifies the complexity of the problem: the electron density only depends on the three spatial coordinates, independently of the number of electrons; while the wavefunction of a system of N electrons has dimension 3N.[7] Within the DFT framework, the total energy of the system is expressed as a functional of the electron density (see eq. M.3).

$$E[\rho(\vec{r})] = F[\rho(\vec{r})] + \int \rho(\vec{r})V(\vec{r})d\vec{r} \qquad \text{(M.3)}$$

In eq. M.3, $V(\vec{r})$ is the nucleus-electron potential and $F[\rho(\vec{r})]$ is a functional of the electron density. A manner for calculating $F[\rho(\vec{r})]$ was proposed by Khon and Sham in 1965.[8] This approach consists on the replacement of the multi-electronic system of interacting electrons by a fictitious one composed of non-interacting electrons in which an effective potential, $V_{eff}(\vec{r})$, is applied in such a way that the

electron density of both systems is the same. Such a system can be described by a single Slater determinant, since electrons do not interact with each other.

In such situations, eq. M.3 can be further decomposed into different terms as shown in eq. M.4.

$$F[\rho(\vec{r})] = T_S[\rho(\vec{r})] + J[\rho(\vec{r})] + E_{Ne}[\rho(\vec{r})] + E_{XC}[\rho(\vec{r})] \qquad \text{(M.4)}$$

Where $T_S[\rho(\vec{r})]$ is the kinetic energy of the electrons in the non-interacting system, $J[\rho(\vec{r})]$ is the Coulomb electron-electron repulsion energy, $E_{Ne}[\rho(\vec{r})]$ is the nucleus-electron interaction and $E_{XC}[\rho(\vec{r})]$ is the exchange-correlation energy. The latter term contains the kinetic energy of the interacting electrons, as well as exchange and correlation energies; and is the only unknown of the theory. Moreover, since electrons in the fictitious system are non-interacting, the system Hamiltonian can be expressed as a sum of one-electron Hamiltonians, yielding the Khon-Sham equations (see eqs. M.5).

$$h_i^{KS}\psi_i = \varepsilon_i\psi_i \qquad h_i^{KS} = \frac{\nabla^2}{2} + V_{eff}(\vec{r}) \qquad \text{(M.5)}$$

In eq. M.5, h_i^{KS} is the Kohn-Sham one-electron Hamiltonian, ψ_i represents the one-electron Kohn-Sham orbitals and the values of ε_i are their energies. The effective potential can be calculated according to eq. M.6.

$$V_{eff}(\vec{r}) = V(\vec{r}) + \int \frac{\rho(\vec{r}\prime)}{|\vec{r}' - \vec{r}|} d\vec{r}' + V_{XC}(\vec{r}) \qquad \text{(M.6)}$$

Where $V_{XC}(\vec{r})$ is the exchange-correlation potential, which can be computed following eq. M.7.

$$V_{eff}(\vec{r}) = \frac{\delta E_{XC}[\rho(\vec{r})]}{\delta\rho(\vec{r})} \qquad \text{(M.7)}$$

The set of equations presented in eq. M.5 have a strong resemblance with the Hartree-Fock (HF) ones. They are interrelated in the sense that each one depends on the others. Then, they can be resolved in a self-consistent way starting from a trial initial guess.

Within this framework, the only unknown of the theory is the computation of the exchange-correlation potential, $V_{XC}(\vec{r})$. As a result, approaches for estimating it have been proposed, leading to the appearance of different Density Functional Approximations (DFA). In the following lines, a brief explanation of the most common ones is provided.

Local Density Approximation (LDA)

This is the simplest approach, and assumes that the density can be treated locally as a uniform electron gas.[6] The most common functional of this type is the one developed by Vosko and co-workers.[9] This model works reasonably well for solids, but fails in systems in which the electron density changes rapidly; such as molecules. On balance, energies are quite inaccurate and LDA is not usually enough for the majority of chemical systems.

Generalised Gradient Approximation (GGA)

This method adds the electron density gradient to the calculation of the exchange-correlation potential so that it depends on the electronic density at each point (local) and on the values of nearby regions. This kind of functionals are usually split into a correlation and an exchange parts, as shown in eq. M.8.

$$E_{XC}^{GGA} = E_{X}^{GGA} + E_{C}^{GGA} \quad \text{(M.8)}$$

There exist different approaches for calculating the terms in eq. M.8. Some of them include parameters derived from experimental or high level theoretical calculations. In particular, BP86, BLYP, B97D, PBE and PW91 are examples of widely used GGA functionals are.[10-15] These functionals have proven to perform well for geometries and frequencies, among other properties. In particular, solid state calculations performed in this Doctoral Thesis employed the PBEsol functional,[16] that is, the PBE functional revised for solids. This decision was made on the basis of its ability to accurately reproduce experimental parameters of periodic systems, while keeping the computational cost reasonable.[17]

Meta Generalised Gradient Approximation (m-GGA)

These approaches also use the Laplacian of the electron density in the computation of the exchange-correlation potential. Among these functionals we can highlight the TPSS one.[18] However, any of this functionals was employed in this dissertation, as results do not improve much with respect to GGA for the kind of systems under study, while the computational effort increases significantly.

Hybrid Functionals

The “exact” exchange energy can be obtained from HF theory. This is the basis of hybrid methods, which add a percentage of the HF exchange energy to GGA scheme using an adiabatic connection method. There exist a wide number of hybrid functionals depending on the amount of HF exchange. Probably, the most popular is the B3LYP one, which is obtained as a combination of HF with LDA exchange-correlation, B88 exchange and LYP correlation functionals.[19] This functional has proven to be efficient in the calculation of molecular properties, and was the one used in the molecular calculations performed within this Doctoral Thesis. Other examples of common hybrid

functionals are wB97XD,[20] TPSSh[21] and the Minnesota suite (M06, M06-2X, M06-L and M06-HF).[22] In spite of their success in molecular systems, hybrid functionals usually underperform for solids, while the computational cost of computing HF exact exchange with plane wave basis is very high. For that, hybrid functionals were not applied in the periodic calculations performed as part of this Thesis.

The Hubbard Model

GGA methodology has limitations for the description of some chemical properties, such as the underestimation of the band gap in semiconductors, as a consequence of the DFT delocalization error. One possibility for improving the quality of the results is the use of hybrid functionals. In this case, the mixing of HF exchange (which tends to overestimate the band gap) with GGA may cancel the error and provide accurate results. However, periodic-HF methodology is prohibitively expensive when combined with plane-waves. Then, for strongly-correlated electrons, the simplest and most pragmatic approach to treat the strong on-site Coulomb interactions of localized electrons of *d* and *f* shells is the use of the so-called Hubbard approximation.[23] This approach is based on the addition of a term, the so-called Hubbard *U*, which acts as a penalty function that favors fully occupied or fully unoccupied energy levels. This way, the delocalized solutions are relatively destabilized with respect to the localized ones, with the aim of cancelling the delocalization error. Nonetheless, the choice of the *U* value is not universal, and the quality of the results critically depends on it. As a result, an adequate selection of the *U* for the systems under study is fundamental for obtaining accurate results.[24] In this dissertation GGA+*U* methodology was used for the study of periodic systems.

C. Basis sets

Wavefunctions in molecular systems are generally expressed as linear combinations of the elements of a given basis set. A *minimal basis set* is the minimum number of bases functions that are necessary to describe all the electrons of each atom that forms part of a given system. However, for an accurate description of complex molecules, the inclusion of a set of polarization functions is required. These are additional functions with higher angular momenta that provide more flexibility to the mathematical description of the system. Moreover, the addition of extra diffuse functions, helps improve results in systems with big and polarizable atoms. These are smooth functions, usually Gaussians, which describe the tail of the orbitals in regions that are far away from the nuclei.

In the molecular DFT calculations performed in Chapter 1, def2-SVP and def2-TZVP Ahlrichs basis sets were used.[25] They are Gaussian basis sets of split valence,

double zeta and triple zeta valence quality; that is, the valence shell is described by two and three sets of functions, respectively. In addition, they include a set of polarization functions. Moreover, the inner electrons are considered by means of electron core potentials (ECPs, which will be explained in the next section). The choice of these basis sets was made because these basis are defined for all the atoms, and because def2-SVP usually provides qualitatively correct results, whereas def2-TZVP allows to refine the energy results, being quite close to the DFT basis set limit.[26]

D. Periodic calculations

Bloch Theorem

The solution of the Schrödinger equation of a solid-state material is enormously more difficult than that of a molecule. If the system magnitude is, for example, of the order of magnitude of a mole, the computational problem will be enormously more demanding than that derived from any molecular system we can imagine; and the extremely high computational resources required are not available nowadays. However, one can use the translational symmetry of the system to reduce its complexity. In this regard, the Bloch Theorem is enormously useful, as it allows to reduce the problem dimension to that of a single unit cell.[27]

In particular, the Bloch Theorem *utilizes* the system translational symmetry to generate the wavefunction. This wavefunction is composed of crystal orbitals, which are also referred to as electronic bands. In an idealized perfect (*i.e.* infinite and without any impurity) periodic system, the electronic potential at a given point, $V(\vec{r})$, has the same periodicity as the crystal lattice (represented by the lattice vector, $\vec{T}$), see eq. M.9.

$$V(\vec{r} + \vec{T}) \equiv V(\vec{r}) \tag{M.9}$$

Specifically, the Bloch Theorem states that for a given wavefunction, $\psi(\vec{k}, \vec{r})$, there exists a vector $\vec{k}$, such that translation by a lattice vector $\vec{T}$ is equivalent to multiplying the wavefunction by a phase vector, as shown in eq. M.10.

$$\psi(\vec{k}, \vec{r} + \vec{T}) = e^{i\vec{k}\vec{T}}\psi(\vec{k}, \vec{r}) \tag{M.10}$$

As a result, the knowledge of $\psi(\vec{k}, \vec{r})$ at a particular point allows for determining its value for all the symmetry equivalent positions. However, the price for this simplification (the consideration of an entirely periodic potential) is the newly introduced quantum number $\vec{k}$.

The crystal orbital $\psi(\vec{k},\vec{r})$ can be further rewritten in terms of localised atomic orbitals, ϕ_j, that are centred at atomic positions, (see eq. M.11).

$$\psi(\vec{k},\vec{r}) = \sum_j \phi_j \, e^{i\vec{k}\vec{r_j}} \tag{M.11}$$

Instead of using localized atomic orbitals, it is possible to expand the crystal wavefunction in terms of plane-waves, which is the approach used in the calculations performed in this dissertation (see eq. M.12).

$$\psi(\vec{k},\vec{r}) = \sum_{\vec{g}} a_{\vec{g},\vec{k}} \, e^{i(\vec{k}+\vec{g})\vec{r_j}} \tag{M.12}$$

Where $\vec{g}$ represents the set of k-vectors that lie in the so called first Brillouin zone. Since this representation is set in the reciprocal space, $e^{i\vec{g}\vec{r}} = 1$, and $e^{i\vec{g}\vec{r}}$ has the periodicity of the real lattice. $a_{\vec{g},\vec{k}}$ are the plane-wave coefficients, which satisfy the relation $\vec{g}\cdot\vec{r} = 2\pi m$, were m is an integer. Since the number of plane-waves included in the expansion has to be finite, it is necessary to cut the expansion at some point. For that, a cutoff value is defined in such a way that plane-waves with kinetic energy higher than that of the cutoff are discarded. The kinetic energy of a given plane-wave is defined according to eq. M.13.

$$E_{cut} = \frac{\hbar^2}{2m_e}\left|\vec{k}+\vec{g}\right|^2 \tag{M.13}$$

The Reciprocal Space

The mathematical study of periodic structures is much easier upon consideration of the reciprocal space. This space accounts for the wave-vectors that fit the symmetry of the periodic structure.[28] In particular, the reciprocal-space basic vectors can be constructed from the direct-space ones, as shown in eq. M.14.

$$\overrightarrow{g_i} = 2\pi \frac{\overrightarrow{a_j}\cdot\overrightarrow{a_k}}{\overrightarrow{a_i}\cdot(\overrightarrow{a_j}\cdot\overrightarrow{a_k})} \tag{M.14}$$

Where $\overrightarrow{a_i}$ and $\overrightarrow{g_i}$ are the direct-space and reciprocal-space primitive lattice vectors, respectively. The primitive cell in the reciprocal space constitutes the so-called first Brillouin zone, also referred to as the Wigner-Seitz cell. Even though the $\vec{k}$ vector is infinite, calculations can be restricted to a discrete set of vectors in the irreducible Brillouin zones. This way, the complexity of the problem is significantly reduced.

Pseudopotentials

As previously stated, plane-waves can be used as robust and straightforward basis functions for periodic calculations. However, rapid oscillations of electrons close to the nucleus are very difficult to model by smooth plane-waves, and, as a result, the number of plane-waves required for an accurate description of these regions is

prohibitively high. Nonetheless, as long as these oscillations are suppressed, plane-waves constitute the ideal choice for periodic-boundary-conditions calculations.

Within this context, an approximation that has proven to be suitable for dealing with core oscillations is the use of pseudopotentials. The main idea behind this approach is getting rid of the nucleus oscillations by replacing the strong-electron potential by a much weaker pseudopotential. This theory is supported by two physical arguments. On the one side, it is well known that the nuclear charge that effects the valence electrons is highly screened by the core electrons. On the other side, valence electrons cannot enter the core region as a consequence of the Pauli Exclusion Principle. Then, this two opposite effects (nuclear attraction of valence electrons and Pauli repulsion between core and valence electrons) partially cancel, and as a result, a weak pseudopotential is left.[29] In addition, core electrons are not directly involved in chemical bonding. Hence, contrarily to what happens for valence electrons, considering that their electronic structure is invariant with respect to a reference calculation is a good approximation. This way, the wavefunctions of the core regions are substituted by fixed pseudo-wavefunctions that reproduce the all-electron calculations behaviour. Notice that pseudopotentials are also referred to as effective core potentials.

There are different schemes for constructing the pseudopotentials, such as the augmented plane wave (APW)[30] and the full-potential linearized augmented plane wave (FP-LAPW).[31] In this dissertation, the projector-augmented wave method (PAW) developed by Blöchl was selected[32] on the basis of its good performance in solid state quantum chemistry. Within this method, the pseudopotential immediately adapts to changes in the valence electrons as it is calculated on the fly, for each electronic configuration; thus avoiding transferability problems.

E. Dispersion interactions

Even though there is no doubt of the usefulness of DFT in chemical research, and especially in reactivity studies, it presents some drawbacks that one should know before applying it to a given system. In this regard, probably, the main problem that derives from current approximations to the exchange-correlation potential is the incomplete treatment of van der Waals (dispersion) interactions. This is especially relevant for large systems, such as the ones considered in this dissertation. In particular, bulky ligands can modulate the catalyst selectivity *via* steric hindrance or non-covalent interactions.[33]

In order to overcome this limitation, different approaches have been proposed.[34] One of them consists on the development of DFT functionals with parameters fitted to experimental data so as to account for dispersion interactions. Within this way of proceeding, the set of M06 functionals developed by Truhlar and co-workers is the most used approach.[35] Alternatively, Grimme proposed to add an energy term accounting for dispersion corrections, E_D, to the DFT-computed energy (see eq. M.15).[36] This was the selected scheme applied in this dissertation.

$$E_{DFT-D} = E_{DFT} + E_D \quad \text{(M.15)}$$

There are different approaches for calculating E_D. Among them, we selected the DFT-D3 scheme, in conjunction with the recently proposed BJ damping.[37] Within this methodology, the dispersion contribution, E_{D3BJ}, is computed according to eqs. M.16 and M.17.

$$E_{D3BJ} = \sum_{n=6,8} S_n \sum_{i,j>1}^{N} \frac{c_n^{ij}}{R_{ij}^n + (f_{dmp}(R_{ij}))^n} \quad \text{(M.16)}$$

$$f_{dmp}(R_{ij}) = \alpha_1 \sqrt{\frac{c_8^{ij}}{c_6^{ij}}} + \alpha_2 \quad \text{(M.17)}$$

Where S_n is a *n*th-order scaling factor (orders n = 6, 8) that depends on the functional, c_n^{ij} is a dispersion coefficient between atoms *i* and *j*, *N* is the total number of atoms in the system and R_{ij} is the interatomic distance. $f_{dmp}(R_{ij})$ is a damping function that rapidly decays when R_{ij} decreases (see eq. M.17), so that not to include *"ordinary"* bonds. The terms α_1 and α_2 are adjusted constants.

In all the DFT calculations performed in Chapter 1, Grimme D3BJ corrections were added (in both, single point and gradient calculations) to the DFT energy obtained by means of B3LYP functional.

F. Solvation effects

Solvent effects may play a key role in chemical reactivity. In particular, interactions between the reagents (or catalysts) and the solvent molecules can enormously affect the kinetics and selectivity of the catalytic processes.[38] A rigorous treatment of these interactions would require the use of hybrid QM/MM approaches, as well as molecular dynamics. However, these methodologies are computationally expensive and thus they are not affordable for the systems under study. There are two main approaches for addressing the solvation effects in computational catalysis in a more economic way. The first method consists on including explicit solvent molecules

in the calculation, so that specific interactions between these molecules and the reagents are considered. Nonetheless, the number of molecules required for modelling real catalytic conditions may be very high, making the calculations unaffordable for DFT methodologies. The second approach, which is the one considered in this Doctoral Thesis, is the use of implicit solvation models. Within these models, the solute is studied by means of quantum mechanics, whereas the environment is considered to be a polarizable continuum dielectric. More specifically, the model considers the formation of a cavity in a continuum solvation medium whose dielectric constant is that of the solvent. The solute is placed into this cavity, and determines its shape. Solute electrostatic interactions with the solvent polarizes the cavity, and *vice versa*. The process takes place iteratively until mutual polarizations reach self-consistency, this is the reason why this methodology is referred to as Self-Consistent Reaction Field (SCRF).[39] The total solvation energy is computed as shown in eq. M.18.

$$\Delta G_{sol} = \Delta G_{el} + \Delta G_{cav} + \Delta G_{rep} + \Delta G_{disp} \quad \text{(M.18)}$$

Where ΔG_{el} accounts for the aforementioned solute-solvent electrostatic interactions; ΔG_{cav} is the energy required for the cavity formation; ΔG_{disp} are the solvent-solute dispersion interactions and ΔG_{rep} is the solvent-solute repulsive term.

Different implicit solvation models have been proposed in the literature. Among them, in this dissertation, the Polarization Continuum Model (PCM)[40] was chosen. In particular, this model applies the Poisson-Boltzmann equation for the definition of the cavity, and is specially adequate for solvents with low dielectric constant that are non-coordinating and do not stablish specific interactions, such as hydrogen bonds, with the reagents.

G. Thermochemistry

Thermodynamic properties of the molecular systems under study were computed by means of an ideal-gas statistical thermodynamic model.[41] This model assumes that the molecules do not interact with each other and that the concentrations are those of an ideal gas under a pressure of 1 atm.

Within this framework, the total system partition function, $q(V,T)$, is expressed as a product of translational (q_t), rotational (q_t), vibrational (q_v), and electronic (q_e) partition functions, as shown in eq. M.19.

$$q(V,T) = q_t q_r q_v q_e \quad \text{(M.19)}$$

Entropic and internal energy contributions are derived from the partition function corresponding to each kind of motion. In general, within the field of

homogeneous catalysis, the model performs satisfactorily well for rotational, electronic and vibrational contributions.[42] However, the translational entropy (see eqs. M.20 and M.21) is largely overestimated. As a result, the model fails when there is a significant entropy variation, that is, when the molecularity of the process is not maintained, as it is common in the calculation of catalytic cycles.[43]

$$q_t = \left(\frac{2\pi m k_B T}{h^2}\right)^{3/2} V \tag{M.20}$$

$$S_{trans} = R[\ln(q_t) + 5/2] \tag{M.21}$$

There exist different schemes that attempt to improve translational entropy description. Among them, we can cite the one proposed by Martin and co-workers,[44] which determines the pressure required for reproducing the solvent density and applies it in the calculation, instead of the standard pressure (1 atm).

In this dissertation, we applied the approach proposed by Morokuma *et al.*[45] This approximation is based on the fact that the molecular movement in solution will be much lower than in the gas phase. As a consequence, one can consider that translational movement is "quenched" in solution, and, as a result, it is possible to assume that it is very close to zero and thus, we can neglect it. Even though this is a very simple approach, it has proven to be adequate for computing reaction mechanisms.[46]

H. Chemical Bonding

Two main tools for the study of chemical bonding were applied in this Thesis, the Electron Localization Function (ELF) and Interacting Quantum Atoms (IQA) energy decomposition scheme.

H.1 Electron Localization Function

The Electron Localization Function was introduced by Becke and Edgecombe as an attempt to measure the probability of finding an electron in the surroundings of another electron with the same spin, and thus identify "localized electrons in atomic and molecular systems".[47] Since then, it has proven to be very useful in the understanding of chemical systems. Specifically, its applications range from analysing reaction mechanisms[48] to aromaticity evaluation[49] and predicting solid state properties,[50] among many others.

One of the main strengths of the ELF is that it can be easily associated with chemical intuitive interpretations, being especially remarkable the one suggested by Savin *et al.*[51] It identifies the ELF core, χ, with a local measure of electrons local kinetic energy excess relative to the homogeneous electron gas. Then, the ELF is defined according to eq. M.22.

$$\eta(\vec{r}) = \frac{1}{1+\chi^2} \tag{M.22}$$

As shown in eq. M.22, it has the shape of a Lorentzian function whose values range from 0 ($\chi \to \infty$), to 1, ($\chi \to 0$). This way, maxima are associated with covalent bonds, lone pairs, internal atomic shells (and electron pairs in general), which correspond to situations in which local electron kinetic energy excess is minimal, and thus the ELF is maximum.

The gradient vector of the ELF, $\nabla\eta(\vec{r})$, allows to divide the Euclidean space in basins of attractors where electrons are localized. This partition generates a set of non-overlapping regions called basins. The number of connections between a given valence basin and the surrounding core basins determines the synaptic order. A monosynaptic basin corresponds to a lone pair, a disynaptic one is associated with a two-centre bond and polysynaptic basins are associated with multi-centre bonds.[52]

Basin properties can be determined by integrating over the volume associated with each basin. Hence, for obtaining electron populations, $\overline{N}(\Omega_i)$, the electron density, ρ, has to be integrated over the corresponding basin, Ω_i (see eq. M.23).

$$\overline{N}(\Omega_i) = \int_{\Omega_i} \rho(\vec{r}) d\vec{r} \tag{M.23}$$

It is interesting to highlight that this model recovers the Valence Shell Electron Pair Repulsion (VSEPR) picture of molecules and solids,[53] as the system is represented Lewis entities: core regions connected by bonds and lone pairs.

H.2 Interacting Quantum Atoms

Interacting Quantum Atoms (IQA) was introduced in 2005 as a useful tool for partitioning the total molecular energy into different components with chemical sense.[54] This approach was designed in such a way that atoms and functional groups retain their identity. In addition, the partition is rigorous and is solely derived from the system wavefunction. Hence, the results accuracy only depends on the quality of the wavefunction. On balance, IQA is a physically rigorous method, though computationally expensive.

The method has proven to be suitable for the study of chemical bonds. For example, it has been successfully applied to the study of halogen and hydrogen

bonding,[55] molecular interactions in metallic complexes,[56] steric repulsions[57] and delocalization indices.[58]

Specifically, IQA follows the classical QTAIM scheme for partitioning a molecule into topological atoms. The different contributions to the total energy are calculated using the first and second order density matrices, obtaining the total Born-Oppenheimer system energy, as shown in eq. M.24.

$$E = \sum_A T_A + V_{ee}^{AA} + V_{en}^{AA} + \sum_{A>B} V_{en}^{AB} + V_{ne}^{AB} + V_{nn}^{AB} + V_{ee}^{AB} \qquad \text{(M.24)}$$

As shown in eq. M.24, the total energy is divided into two different contributions. The first summation corresponds to the intra-atomic contribution of each atom, E_{intra}^{A} (see eq. M.25).

$$E_{intra}^{A} = T_A + V_{ee}^{AA} + V_{en}^{AA} \qquad \text{(M.25)}$$

Where T_A is the kinetic energy of electrons in atom A, V_{ee}^{AA} is the electron-electron repulsive potential energy and V_{en}^{AA} is the electron-nucleus attractive potential.

The second summation in eq. M.24 corresponds to inter-atomic energy between atoms A and B, E_{inter}^{AB} (see eq. M.26).

$$E_{inter}^{AB} = V_{nn}^{AB} + V_{ee}^{AB} + V_{en}^{AB} + V_{ne}^{AB} \qquad \text{(M.26)}$$

It includes the nucleus-nucleus, V_{nn}^{AB}, and electron-electron, V_{ee}^{AB}, repulsive energy, as well as the attractive interaction between electrons in atom A and nucleus in atom B, V_{en}^{AB}, and electrons in B with nucleus in A, V_{ne}^{AB}. Electron-electron interaction can be further divided into a classical Coulombic electrostatic interaction, V_{coul}^{AB}, and an exchange-correlation contribution, V_{XC}^{AB}. This way, the inter-atomic interaction energy can be divided into a classical electrostatic energy term, which accounts for nucleus-nucleus, electron-nucleus, nucleus-electron and Coulombic interactions (see eq. M.27) and a quantum exchange-correlation energy term, V_{XC}^{AB} (see eq. M.28).

$$V_{elec}^{AB} = V_{nn}^{AB} + V_{en}^{AB} + V_{ne}^{AB} + V_{coul}^{AB} \qquad \text{(M.27)}$$

$$E_{inter}^{AB} = V_{elec}^{AB} + V_{XC}^{AB} \qquad \text{(M.28)}$$

At this point it is important to highlight that the original IQA computation of the Coulombic term worked only within HF wavefunctions. However, it was recently improved so that it could support also B3LYP level density functional theory.[59]

I. Computational Details

The computational details for the different theoretical calculations performed along this Thesis are presented below.

I.1 Molecular calculations

All the DFT molecular calculations performed in **Chapter 1** have been performed using the Gaussian09 program package.[60] The B3LYP functional[19,61] has been employed including the D3 dispersion correction scheme developed by Grimme using the Becke-Johnson damping[28] for both, energies and gradient calculations, in conjunction with the "ultrafine" grid. The def2-SVP basis set has been selected for all atoms for geometry optimizations, performing single point calculations with the def2-TZVP basis set to refine energy results.[24] Solvent effects were included by means of the PCM model, as implemented in the Gaussian09 package.[62] In particular, the solvents considered in the different sections were: tetrahydrofuran (section B), formic acid (section C) and toluene (section D).

The nature of the stationary points has been confirmed by analytical frequency analysis, and transition states were characterized by calculation of reaction paths following the intrinsic reaction coordinate.

For chemical bond analyses in Section A, the ELF study was performed with TopMod program[63] using the corresponding monodeterminantal B3LYP-D3BJ/def2-SVP wavefunctions; in a tridimensional grid of 200 points in each direction. ELF plots of molecular structures were represented using Chimera software.[64] The IQA and QTAIM analyses were performed using the AIMAll package.[65]

I.2 Periodic calculations

All periodic calculations presented in **Chapter 2** were performed using periodic density functional theory (DFT) as implemented in the Vienna ab initio simulations package (VASP).[66] The PAW method developed by Blochl was used to represent interactions between core and valence electrons.[30] The Perdew-Burke-Ernzerhof exchange-correlation DFT functional revised for solids was used for all calculations.[67] A plane wave cutoff of 400 eV was used for all the elements. In order to properly describe on-site Coulomb interactions of localised *d* electrons, DFT+U methodology was used;[68] unless otherwise mentioned, all elements had a U value of 0. Specific details for each studied system are provided below. Images were produced with VESTA.[69]

With respect to materials studied in section A, a k-points grid of (7x7x5) was employed in the calculations of $LaMnO_3$ and $CaMnO_3$. A value of U equal 5.5 was used for Mn^{3+} octahedrons in $LaMnO_3$ and 3.0 for Mn^{4+} octahedrons in $CaMnO_3$. For intermediate compositions, which present vacancies and substitution of Ca and La by other atoms (Sr and Pb), a 2x2x1 supercell was constructed; and the U for Mn was set to 4.0. For $LaFeO_3$-based catalysts, we used a k-points grid of (4x5x3), in conjunction with U values of 4.0 for Fe and 8.0 for Nd, as reported in the literature.[70,71]

For Mo-based nitrides considered in Section B, k-points meshes of (11x11x11) were used in all cases. U values for Co and Fe are set to 2.0 and 4.0; respectively.[36]

J. References

[1] Born, M.; Oppenheimer, R. *Zur Quantentheorie der Molekeln.* In: *Annalen der Physik* **1927**, *389*, 457–484

[2] Friesner, R. A. Ab initio quantum chemistry: Methodology and applications. *Proc. Natl. Acad. Sci.* **2005**, *102*, 6648–6653.

[3] Hehre, W. J. Ab initio molecular orbital theory. *Acc. Chem. Res.* **1976**, *9*, 399–406.

[4] Helgaker, T.; Coriani, S.; Jørgensen, P.; Kristensen, K.; Olsen, J.; Ruud, K. Recent Advances in Wave Function-Based Methods of Molecular-Property Calculations. *Chem. Rev.* **2012**, *112*, 543–631.

[5] Macgregor, S. A. Computational chemistry of molecular inorganic systems. *Dalton Trans.* **2011**, *40*, 11065.

[6] Hohenberg, P.; Kohn, W. Inhomogeneous Electron Gas. *Phys. Rev. B* **1964**, *136*, 864–871.

[7] Parr, R. G.; Yang. W. *Density–Functional Theory of Atoms and Molecules, International Series of Monographs on Chemistry*; Oxford University Press: Oxford, 1989.

[8] Kohn, W.; Sham L. J. Self-Consistent Equations Including Exchange and Correlation Effects. *Phys. Rev. A* **1965**, *140*, 1133–1138.

[9] Vosko, S. H.; Wilk, L.; Nusair. M. Accurate spin-dependent electron liquid correlation energies for local spin density calculations: a critical analysis. *Can. J. Chem.* **1980**, *58*, 1200–1211.

[10] Becke, A. D. Density-functional exchange-energy approximation with correct asymptotic behaviour. *Phys. Rev. A* **1988**, *38*, 3098–3100.

[11] Perdew, J. P. Density-functional approximation for the correlation energy of the inhomogeneous electron gas. *Phys. Rev. B* **1986**, *33*, 8822.

[12] Grimme, S. Semiempirical GGA-type density functional constructed with a long-range dispersion correction. *J. Comp. Chem.* **2006**, *27*, 1787–1799.

[13] Lee, C.; Yang. W.; Parr, R. G. Development of the Colle-Salvetti correlation-energy formula into a functional of the electron density. *Phys. Rev. B* **1988**, *37*, 785–789.

[14] Cohen. M. L. Electronic structure of solids. *Phys. Rep.* **1984**, *110*, 293–309.

[15] Perdew, J. P.; Burke, k.; Ernzerhof, M. Generalized gradient approximation made simple. *Phys. Rev. Lett.* **1996**, *77*, 3865.

[16] Perdew, J. P.; Ruzsinszky, A.; Csonka, G. I.; Vydrov, O. A.; Scuseria, G. E.; Constantin, L. A.; Zhou, X.; Burke, K. Restoring the Density-Gradient Expansion for Exchange in Solids and Surfaces. *Phys. Rev. Lett.* **2008**, *100*, 136406.

[17] For examples see: (a) Zalake, P.; Ghosh, S.; Narasimhan, S.; Thomas, G. Descriptor-Based Rational Design of Two-Dimensional Self-Assembled Nanoarchitectures Stabilized by Hydrogen Bonds. *Chem. Mater.* **2017**, *29*, 7170−7182. (b) Kim, S. J.; Park, B.; Noh, S. H.; Yoon, H. S.; Oh, J.; Yoo, S.; Kang, K.; Han, B.; Jun, S. C. Carrier Scattering in Quasi-free Standing Graphene on Hexagonal Boron Nitride. *Nanoscale* **2017**, *9*, 15934−15944. (c) Peralta, D.; Chaplais, G.; Simon-Masseron, A.; Barthelet, K.; Chizallet, C.; Quoineaud, A. − A.; Pirngruber, G. D. Comparison of the Behavior of Metal-Organic Frameworks and Zeolites for Hydrocarbon Separations. *J. Am. Chem. Soc.* **2012**, *134*, 8115−8126.

[18] Tao, J. M.; Perdew, J. P.; Staroverov, V. N.; Scuseria, G. E. Climbing the density functional ladder: Nonempirical meta-generalized gradient approximation designed for molecules and solids. *Phys. Rev. Lett.* **2003**, *91*, 146401.

[19] Becke. A. D. A new mixing of Hartree-Fock and local density-functional theories. *J. Chem. Phys.* **1993**, *98*, 1372–1377.

[20] Chai, J. –D.; Head-Gordon, M. Long-range corrected hybrid density functionals with damped atom–atom dispersion corrections. *Phys. Chem. Chem. Phys.* **2008**, *10*, 6615–6620.

[21] Tao, J. M.; Perdew, J. P.; Staroverov, V. N.; Scuseria, G. E. Climbing the density functional ladder: Nonempirical meta-generalized gradient approximation designed for molecules and solids. *Phys. Rev. Lett.* **2003**, *91*, 146401.

[22] (a) Zhao, Y.; Truhlar, D. G. A new local density functional for main-group thermochemistry, transition metal bonding, thermochemical kinetics, and noncovalent interactions. *J. Chem. Phys.* **2006**, *125*, 194101. (b) Zhao, Y.; Truhlar, D. G. The M06 suite of density functionals for main group thermochemistry, thermochemical kinetics, noncovalent interactions, excited states, and transition elements: two new functionals and systematic testing of four M06-class functionals and 12 other functionals. *Theor. Chem. Acc.* **2008**, *120*, 215–241.

[23] Anderson, P. W. Localized magnetic states in metals. *Phys. Rev.* **1961**, *124*, 41–53.

[24] Capdevila-Cortada, M.; Lodziana, Z.; Lopez, N. Performance of DFT plus U Approaches in the Study of Catalytic Materials. *ACS Catal.* **2016**, *6*, 8370–8379.

[25] Weigend, F.; Ahlrichs, R. Balanced basis sets of split valence, triple zeta valence and quadruple zeta valence quality for H to Rn: Design and assessment of accuracy. *Phys. Chem. Chem. Phys.* **2005**, *7*, 3297–3305.

[26] Hopmann, K. H. How Accurate is DFT for Iridium-Mediated Chemistry? *Organometallics* **2016**, *35*, 3795–3807.

[27] Bloch, F. Über die Quantenmechanik der Elektronen in Kristallgittern. *Z. Phys.* **1928**, *52*, 555–600.

[28] Dronskowski, R. *Computational Chemitry of Solid State Materials. A Guide for Materials Scientists, Chemists, Physicists and others*; Wiley-VCH Verlag: Weinheim, 2005.

[29] Hellmann, H. A New Approximation Method in the Problem of Many Electrons. *J. Chem. Phys.* **1935**, *3*, 61.

[30] (a) Slater, J. C. Wave Functions in a Periodic Potential. *Phys. Rev.* **1937**, *51*, 846–851. (b) Loucks, T. L. A*ugmented Plane Wave Method: a Guide for Performing Electronic Structure Calculations*; Benjamin: New York, 1967.

[31] (a) Wimmer, E.; Krakauer, H., Weinert, M.; Freeman, A. J. Full-potential selfconsistent linearized-augmented-plane-wave method for calculating the electronic structure of molecules and surfaces: O_2 molecule. *Phys. Rev. B* **1981**, *24*, 864–875. (b) Weinert, M.; Wimmer, E.; Freeman, A. J. Total-energy all-electron density functional method for bulk solids and surfaces. *Phys. Rev. B* **1982**, *26*, 4571–4578.

[32] (a) Blöchl, P. E. Projector augmented-wave method. *Phys. Rev. B* **1994**, *50*, 17953–17979. (b) Kresse, G.; Joubert, D. From ultrasoft pseudopotentials to the projector augmented-wave method. *Phys. Rev. B* **1999**, *59*, 1758–1775.

[33] (a) Cort, A. D.; Mandolini, L.; Schiaffino, L. The Role of Attractive van der Waals Forces in the Catalysis of Michael Addition by a Phenyl Decorated Uranyl-Salophen Complex. *J. Org. Chem.* **2008**, *73*, 9439–9442. (b) Rodriguez-Reyes, J. C. F.; Siler, C. G.; Liu, W.; Tkatchenko, A.; Friend,

C. M.; Madix, R. J. van der Waals Interactions Determine Selectivity in Catalysis by Metallic Gold. *J. Am. Chem. Soc.* **2014**, *136*, 13333−13340.

[34] Marom, N.; Tkatchenko, A.; Rossi, M.; Gobre, V. V.; Hod, O.; Scheffler, M.; Kronik, L. Dispersion Interactions with Density-Functional Theory: Benchmarking Semiempirical and Interatomic Pairwise Corrected Density Functionals. *J. Chem, Theory Comput.* **2011**, *7*, 3944–3951.

[35] Zhao, Y.; Truhlar, D. G. A new local density functional for main-group thermochemistry, transition metal bonding, thermochemical kinetics, and noncovalent interactions. *J. Chem. Phys.* **2006**, *125*, 194101.

[36] Zhao, Y.; Schultz, N. E.; Truhlar, D. G. Design of Density Functionals by Combining the Method of Constraint Satisfaction with Parametrization for Thermochemistry, Thermochemical Kinetics, and Noncovalent Interactions. *J. Chem. Theory Comput.* **2006**, *2*, 364–382.

[37] (a) Grimme, S.; Antony, J.; Ehrlich, S.; Krieg, H. A consistent and accurate ab initio parametrization of density functional dispersion correction (DFT-D) for the 94 elements H-Pu. *J. Chem. Phys.* **2010**, *132*, 154104. (b) Johnson, E. R.; Becke, A. D. A post-Hartree–Fock model of intermolecular interactions. *J. Chem. Phys.* **2005**, *123*, 024101.

[38] Dyson, P. J.; Jessop, P. G. Solvent effects in catalysis: rational improvements of catalysis via manipulation of solvent interactions. *Catal. Sci. Technol.* **2016**, *6*, 3302–3316.

[39] Mennucci, B. Polarizable continuum model. Comput. *Mol. Sci.* **2012**, *2*, 386–404.

[40] Scalmani, G.; Frisch, M. J. Continuous surface charge polarizable continuum models of solvation. I. General formalism. *J. Chem. Phys.* **2010**, *132*, 114110.

[41] McQuarrie, D. A.; Simon, J. D. *Molecular Thermodynamic*s; University Science Books: Sausalito, 1999.

[42] Besora, M.; Vidossich, P.; LLedós, A.; Ujaque, G.; Maseras, F. Calculation of Reaction Free Energies in Solution: A Comparison of Current Approaches. *J. Phys. Chem. A* **2018**, *122*, 1392–1399.

[43] Courtemanche, M. –A.; Légaré, M. –A.; Maron, L.; Fontaine Reducing, F. –G. CO_2 to Methanol Using Frustrated Lewis Pairs: On the Mechanism of Phosphine–Borane-Mediated Hydroboration of CO_2. *J. Am. Chem. Soc.* **2014**, *136*, 10708−10717.

[44] Martin, R. L.; Hay, P. J.; Pratt, L. R. Hydrolysis of Ferric Ion in Water and Conformational Equilibrium. *J. Phys. Chem. A* **1998**, *102*, 3565−3573.

[45] Tanaka, R.; Yamashita, M.; Chung, L. W.; Morokuma, K.; Nozaki, K. Mechanistic Studies on the Reversible Hydrogenation of Carbon Dioxide Catalyzed by an Ir-PNP Complex. *Organometallics* **2011**, *30*, 6742–6750.

[46] Julián, A.; Guzmán, J.; Jaseer, E. A.; Fernández-Alvarez, F. J.; Royo, R.; Polo, V.; García-Orduña, P.; Lahoz, F. J.; Oro. Mechanistic Insights on the Reduction of CO_2 to Silylformates Catalyzed by Ir-NSiN Species. *Chem. Eur J.* **2017**, *23*, 11898−11907.

[47] Becke, A.D.; Edgecombe, K.E. A simple measure of electron localization function in atomic and molecular systems. *J. Chem. Phys*. **1900**, *92*, 5397−5403.

[48] Polo, V.; Andres, J.; Slawomir, B.; Domingo, L.R.; Silvi, B. Understanding Reaction Mechanisms in Organic Chemistry from Catastrophe Theory Applied to the Electron Localization Function Topology. *J. Phys. Chem. A* **2008**, *112*, 7128–7136.

[49] (a) Poater, J.; Duran, M.; Sola, M.; Silvi, B. Theoretical Evaluation of Electron Delocalization in Aromatic Molecules by Means of Atoms in Molecules (AIM) and Electron Localization Function (ELF) Topological Approaches. *Chem. Rev.* **2005**, *105*, 3911–3947. (b) Boldyrev A.I. All-Metal Aromaticity and Antiaromaticity. *Chem. Rev*. **2005**, *105*, 3716–3757.

[50] Marques, M.; Ackland, G.J.; Lundegaard, L.F.; Stinton, G.; Nelmes, R. J.; McMahon, M.I.; Contreras-Garcia, J. Potassium under Pressure: A Pseudobinary Ionic Compound. *Phys. Rev. Lett.* **2009**, *103*, 115501.

[51] Savin, A.; Jepsen, O.; Flad, J.; Andersen, L. K.; Preuss, H.; von Schnering, H. G. Electron localization in solid-state structures of the elements: The diamond structure. *Angew. Chem. Int. Ed. Engl.* **1992**, *31*, 187–188.

[52] Silvi, B. The synaptic order: a key concept to understand multicenter bonding. *J. Mol. Struct.* **2002**, *614*, 1–3.

[53] Gillespie, R.J.; Nyholm, R.S. Inorganic stereo-chemistry. *Quart. Rev.* **1957**, *11*, 339–380.

[54] Blanco, M. A.; Pendás, A. M.; Francisco, E. Interacting Quantum Atoms: A Correlated Energy Decomposition Scheme Based on the Quantum Theory of Atoms in Molecules. *J. Chem. Theory Comput.* **2005**, *1*, 1096–1109.

[55] (a) Synzgantseva, O. A.; Tognetti, V.; Joubert, L. On the Physical Meaning of Halogen Bonds: A QTAIM Study. *J. Phys. Chem. A* **2013**, *117*, 8969–8980. (b) Guevara-Vela, J. M.; Chavez-Calvillo, R.; Garcia-Revilla, J.; Hernandez-Trujillo, J.; Christiansen, O.; Francisco, E.; Pendas, A. M.; Rocha-Rinza, T. Hydrogen-Bond Cooperative Effects in Small Cyclic Water Clusters as Revealed by the Interacting Quantum Atoms Approach. *Chem. Eur. J.* **2013**, *19*, 14304–14315.

[56] Cukrowski, I.; de Lange, J. H.; Mitoraj, M. Physical Nature of Interactions in Zn-II Complexes with 2,2'-Bidyridyl: Quantum Theory of Atmos in Molecules (QTAIM), Interacting Quantum Atoms (IQA), Noncovalent Interactions (NCI), and Extended Transition State Coupled with Natural Orbitals for Chemical Valence (ETS-NOCOV) Comparative Studies. *J. Phys. Chem. A* **2014**, *118*, 623–637.

[57] Pendas, A. M.; Blanco, M. A.; Franco, E. Steric Repulsions, Rotation Barriers, and Stereoelectronic Effects: A Real Space Perspective. *J. Comput. Chem.* **2009**, *30*, 98–109.

[58] Pendas, A. M.; Blanco, M. A.; Francisco, E. Chemical fragments in real space: Definitions, properties, and energetic decompositions. *J. Comput. Chem.* **2007**, *28*, 161–184.

[59] Maxwell, P.; Pendas, A. M.; Popelier, P. L. A. Extension of the interacting quantum atoms (IQA) approach to B3LYP level density functional theory (DFT). *Phys. Chem. Chem. Phys.* **2016**, *18*, 20986–21000.

[60] Frisch, M. J.; Trucks, G. W.; Schlegel, H. B.; Scuseria, G. E.; Robb, M. A.; Cheeseman, J. R.; Scalmani, G.; Barone, V.; Mennucci, B.; Petersson, G. A.; Nakatsuji, H.; Caricato, M.; Li, X.; Hratchian, H. P.; Izmaylov, A. F.; Bloino, J.; Zheng, G.; Sonnenberg, J. L.; Hada, M.; Ehara, M.; Toyota, K.; Fukuda, R.; Hasegawa, J.; Ishida, M.; Nakajima, T.; Honda, Y.; Kitao, O.; Nakai, H.; Vreven, T.; Montgomery Jr., J. A.; Peralta, J. E.; Ogliaro, F.; Bearpark, M.; Heyd, J. J.; Brothers, E.; Kudin, K. N.; Staroverov, V. N.; Kobayashi, R.; Normand, J.; Raghavachari, K.; Rendell, A.; Burant, J. C.; Iyengar, S. S.; Tomasi, J.; Cossi, M.; Rega, N.; Millam, J. M.; Klene, M.; Knox, J. E.; Cross, J. B.; Bakken, V.; Adamo, C.; Jaramillo, J.; Gomperts, R.; Stratmann, R. E.; Yazyev, O.; Austin, A. J.; Cammi, R.; Pomelli, C.; Ochterski, J. W.; Martin, R. L.; Morokuma, K.; Zakrzewski, V. G.; Voth, G. A.; Salvador, P.; Dannenberg, J. J.; Dapprich, S.; Daniels, A. D.; Farkas, Ö.; Foresman, J. B.; Ortiz, J. V; Cioslowski, J.; Fox, D. J. Gaussian, Inc., Wallingford CT, 2009.

[61] (a) Lee, C. T.; Yang, W. T.; Parr, R. G. Development of the Colle-Salvetti correlation-energy formula into a functional of the electron density. *Phys. Rev. B* **1988**, *37*, 785–789.

[62] Tomasi, J.; Mennucci, B.; Cammi, R. Quantum Mechanical Continuum Solvation Models. *Chem. Rev.* **2005**, *105*, 2999–3093.

[63] Noury, S.; Krokidis, X.; Fuster, F.; Silvi, B. Computational tools for the electron localization function topological analysis. *Comput. Chem.* **1999**, *23*, 597–604.

[64] (a) Pettersen, E. F.; Goddard, T. D.; Huang, C. C.; Couch, G. S.; Greenblatt, D. M.; Meng, E. C.; Ferrin, T. E. UCSF Chimera--a visualization system for exploratory research and analysis. *J. Comput Chem.* **2004**, *25*, 1605–1612. (b) Goddard, T. D.; Huang, C. C.; Ferrin, T. E. Visualizing density maps with UCSF Chimera. *J. Struct. Biol.* **2007**, *157*, 281–287.

[65] Keith, T. A. AIMAll (Version 17.01.25), TK Gristmill Software, Overland Park KS, USA, 2017.

[66] (a) Kresse, G.; Hafner, J. Ab initio molecular dynamics for liquid metals. *Phys. Rev. B* **1993**, *47*, 558–561. (b) Kresse, G.; Hafner, J. Ab initio molecular-dynamics simulation of the liquid-metal–amorphous-semiconductor transition in germanium. *Phys. Rev. B* **1994**, *49*, 14251–14269. (c) Kresse, G.; Furthmüller, J. Efficient iterative schemes for ab initio total-energy calculations using a plane-wave basis set. *Phys. Rev. B* **1996**, *54*, 11169–11186.

[67] Perdew, J. P.; Ruzsinsky, A.; Csonka, G. I.; Vydrov, O. A.; Scuseria, G. E.; Constantin, L. A.; Zhou, X.; Burke, K. Restoring the Density-Gradient Expansion for Exchange in Solids and Surfaces. *Phys. Rev. Lett.* **2008**, *100*, 136406.

[68] Dudarev, S. L.; Botton, G. A.; Savrasov, S. Y.; Humphreys, C. J.; Sutton, A. P. Electron-energy-loss spectra and the structural stability of nickel oxide: An LSDA+U study. *Phys. Rev. B* **1998**, *57*, 1505–1509.

[69] Momma, K.; Izumi, F. VESTA 3 for three-dimensional visualization of crystal, volumetric and morphology data. *J. Appl. Crystallogr.* **2011**, *44*, 1272–1276.

[70] Wang, L.; Maxisch, T.; Ceder, G. Oxidation energies of transition metal oxides within the GGA + U framework. *Phys. Rev. B* **2006**, *73*, 195107.

[71] Bouadjemi, B.; Bentata, S.; Abbad, A.; Benstaali, W. Ab-initio study of optoelectronic and magnetic properties of the orthorhombic $NdMnO_3$ perovskite. *Solid State Commun.* **2015**, 207, 9–15.

CONTRIBUTIONS

The applicant contribution to each of the articles that constitute this Doctoral Thesis is explained in the two following chapters. As previously introduced, the results and discussion corresponding to homogeneous catalysis are in Chapter 1, while those involving heterogeneous catalysts correspond to Chapter 2.

Chapter 1:

HOMOGENEOUS CATALYSIS

A. Ammonia activation by Ir(I)-PXP complexes

A.1 Introduction and objectives

One of the topics of most interest in state-of-the-art chemical research is the development of novel organometallic complexes for effective ammonia N–H bond activation. Such a milestone would open the door towards new processes allowing the efficient synthesis of nitrogenated compounds, such as fertilizers and drugs.[1] Nonetheless, it is a difficult task since ammonia tends to coordinate to metallic centres by the lone pair (forming stable Werner complexes) instead of by the N–H bond, thus hindering the activation process. For this reason, it is not surprising that the number of ammonia activation processes reported in the literature is scarce.[2] In spite of this situation, some Iridium-based complexes bearing PXP pincer ligands in conjunction with Ir(I) metallic centres, Ir(I)-(PXP) (X = CH, Ph, and SiMe), able to carry out the oxidative addition of ammonia have recently been described (see Scheme 1A.1).[3] This promising results show that the correct combination of ligands and metal centres can activate ammonia *via* oxidative addition. As a result, the partner amido compounds, M–NH_2, are obtained, as shown in Scheme 1A.1.

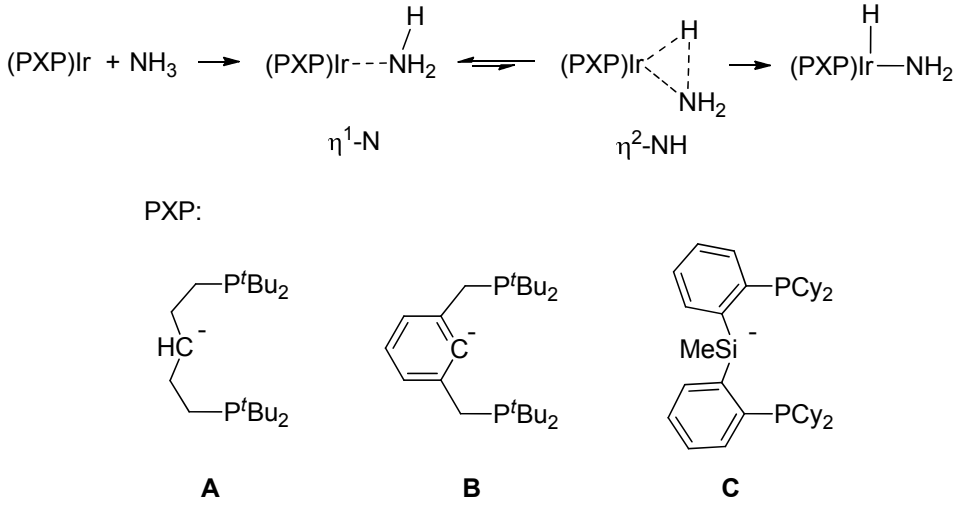

Scheme 1A.1. Oxidative addition of ammonia to Ir(PXP) complexes and proposed pincer ligands.

Given this situation, the in-depth understanding of the electronic factors controlling oxidative addition is of great importance for the synthesis of novel complexes able to effectively activate ammonia N–H bond. In this regard, some authors have proposed that thermodynamics and kinetics of oxidative addition are favored by the use of ligands with strong electron-donating properties.[4] On the contrary, others have proposed that electron-withdrawing ligands are better for this kind of processes.[5] In this line, Goldman *et al.* recently reported that *sigma* donation of X groups in *trans*-$(PH_3)_2IrX$ complexes disfavors the thermodynamics of oxidative addition of C–H and N–H bonds.[6]

Within this context, this section of the Doctoral Thesis focuses on the understanding of the electronic principles governing the kinetics and thermodynamics of oxidative addition of ammonia N–H bond to different Ir(I) complexes bearing pincer ligands with different functional groups in the position *trans* to the NH_3 molecule (see Scheme 1A.2).

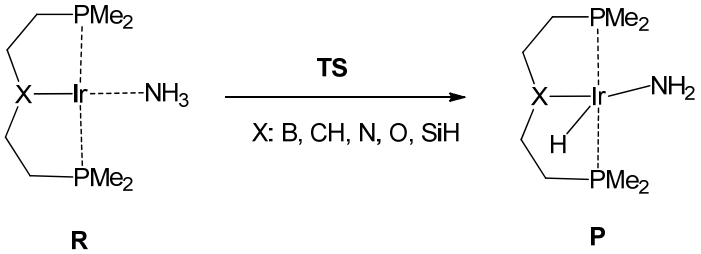

Scheme 1A.2. Oxidative addition processes and Ir(I)-PXP complexes studied.

Different theoretical approaches are available for this kind of studies. Among them, we can highlight the study of the Electron Localization Function (ELF), which allows for the identification of electron pairs, thus recovering "Lewis entities" as lone pairs and two-electron chemical bonds from a Valence Shell Electron Pair Repulsion Theory perspective.[7] Integration of the electron density inside the different ELF basins allows for the quantification of the number of electrons belonging to each lone pair or bond. Moreover, the study of the ELF along a reaction pathway, known as Bonding Evolution Theory (BET), is especially suited for the identification of electronic rearrangements that take place as the chemical reaction proceeds. In this way, representative and chemically intuitive *"curly arrows"* diagrams can be drawn.[8] Over the years, this methodology has proven to be very useful when elucidating reaction mechanisms for organic,[9] organometallic[10] and biochemical[11] reactions. Then, the BET allows for identifying the main chemical events happening along ammonia activation, such as N–H bond breaking and the formation of Ir–H and Ir–N bonds.

The previous approach was complemented by an analysis of the interaction between Ir and the X group. For that, we chose Interacting Quantum Atoms (IQA) energy decomposition scheme in its extension to B3LYP.[12,13] This method divides the

total energy into different components from the topological partition defined by the Quantum Theory of Atoms in Molecules (QTAIM), as explained in the Methodology chapter. In addition, an analysis of Molecular Orbitals (MO) was performed in order to determine the importance of the *trans*-effect in the stability of the reagents and hence on the thermodynamics of the process.[6] We accomplished these results by means of Natural Bond Orbitals (NBO) charge analysis and Wiberg Bond Order (BO) determination.

This way, this section of the Doctoral Thesis focused on:

(i) Unravel the electronic rearrangements that take place along the reaction pathway of N–H bond oxidative addition into Ir(I)-(PXP) complexes.

(ii) Determine the role of the X group on the process kinetics and thermodynamics.

A.2 Results and Discussion

The different analyses performed in this part of the dissertation are presented below.

A.2.1 Activation and reaction energies for Ir(I)-(PXP) complexes towards NH_3

For the sake of simplicity, the five Ir(I)-(PXP) complexes considered in the study were numerated from **1** to **5**, as shown in Scheme 1A.3.

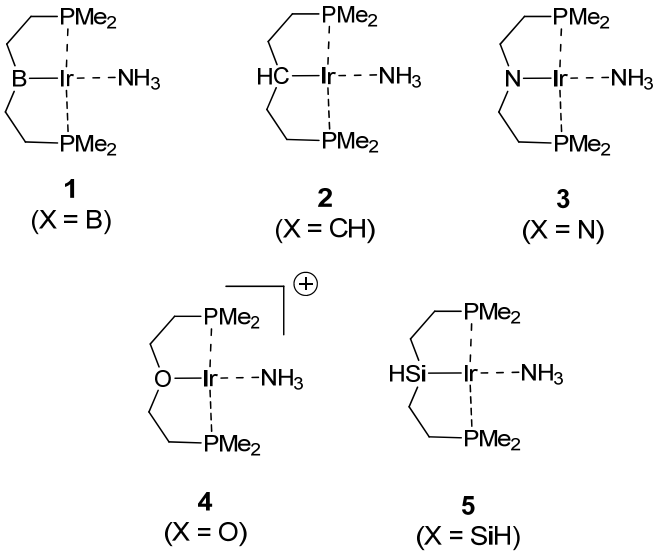

Scheme 1A.3. Nomenclature applied to the complexes under study.

Analysis of the DFT computed activation and reaction energies for N–H oxidative addition clearly showed the critical role played by the X group in both, reaction kinetics and thermodynamics. Energy values for the different complexes, as well as some selected distances and BO are presented in Table 1A.1.

Table 1A.1. Relative energy with respect to the reagent (in kcal·mol^{-1}), geometric distances, NBO atomic charges and Wiberg bond order indexes for, reagents (R), transition structures (TS) and products (P) for complexes **1-5**.

complex	structure	ΔE (kcal·mol^{-1})	d(Ir–N)	d(Ir–X)	q(Ir)	q(X)	BO Ir–N	BO Ir–X
1 (X=B)	R	0.0	2.382	2.023	-0.76	0.65	0.21	0.88
	TS	27.4	2.183	2.059	-0.68	0.61	0.57	0.89
	P	-9.9	2.015	2.027	-0.67	0.72	0.80	0.89
2 (X=CH)	R	0.0	2.267	2.124	-0.62	-0.42	0.29	0.56
	TS	21.9	2.18	2.134	-0.5	-0.46	0.57	0.56
	P	-4.8	1.998	2.145	-0.51	-0.34	0.87	0.70
3 (X=N)	R	0.0	2.185	2.072	-0.55	-0.68	0.37	0.53
	TS	18.2	2.174	2.049	-0.46	-0.68	0.54	0.54
	P	-1.1	1.981	2.131	-0.39	-0.66	0.91	0.62
4 (X=O)	R	0.0	2.089	2.164	-0.39	-0.55	0.52	0.33
	TS	29.9	2.036	2.173	-0.31	-0.56	0.78	0.32
	P	5.2	1.922	2.244	-0.25	-0.56	1.10	0.27
5 (X=SiH)	R	0.0	2.309	2.322	-0.88	1.10	0.26	0.82
	TS	25.5	2.17	2.366	-0.78	1.06	0.57	0.76
	P	-6.8	2.011	2.323	-0.83	1.26	0.84	0.75

Interestingly, the activation energies range from values that are affordable at room temperature, 18.2 kcal·mol^{-1} for X = N and 21.9 kcal·mol^{-1} for X = CH, to others that would require higher temperatures, 25.5 kcal·mol^{-1} for X = SiH, 27.4 kcal·mol^{-1} for X = B and 29.9 kcal·mol^{-1} for X = O. These results show that the Lewis acid character of the X group do not correlate with the activation energy, since the two stronger Lewis acids, X = N and X = O have the lowest and the highest activation energy, respectively.

Results presented in Table 1A.1 also demonstrate that the thermodynamics of the oxidative addition is strongly influenced by the nature of the X group. Some processes are exothermic, with ΔE = -9.9 kcal·mol^{-1} for X = B, -6.8 kcal·mol^{-1} for X = SiH, and -4.8 kcal·mol^{-1} for X = CH. On the contrary, others are endothermic, with ΔE = 1.1 kcal·mol^{-1} for X = CH and 5.2 kcal·mol^{-1} for X = O. Complex **4** (X = O), the only cationic one, presents the largest activation and reaction energies. However, when one compares neutral complexes, it is noteworthy that the ones having the largest activation energy (**1** and **5**) are also those that have the most favorable thermodynamics. This

feature suggests that the oxidative addition reaction follows an anti-Hammond behavior and that the transition structure and the product are very dissimilar.

A.2.2 Analysis of *trans*-influence

The differences in the reaction thermodynamics of the different complexes were analyzed by means of the evaluation of the *trans*-influence exerted by the X group. Following the previous work of Goldman *et al.*[6] the Ir–N distance in the reagent, that is, the one in *trans* to X, was employed as a descriptor for evaluating the *trans*-influence exerted by this group. As previously proposed, longer distances were obtained for less electronegative groups (X = B and SiH), pointing towards a higher *trans*-influence exerted by less electronegative ligands. These results are in agreement with the more exothermic character of the reactions involving complexes **1** and **5** (X = B and SiH). Since the *trans*-effect in the reagent for these complexes is higher, they are more destabilized and, as a consequence, the reaction is more favorable. Interestingly, we found a good linear correlation (R^2 = 0.980) between the Ir–N distance in the reagent and the reaction energy, as shown in Figure 1A.1. This fact confirms the use of the Ir–N distance as a descriptor for the *trans*-influence.

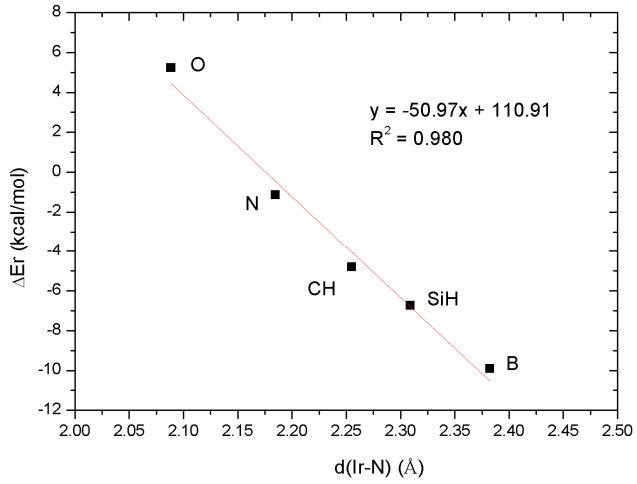

Figure 1A.1. Representation of the reaction energy (in kcal·mol^{-1}) as a function of the Ir–N distance in the reagent. Linear regression fitting is shown in red.

Besides, the previous findings are in agreement the previous results reported by Ziegler *et al.*[14] On the basis of molecular orbital analysis of d^8-square-planar complexes, they proposed that there is an inverse relation between the electronegativity of the X atom and the stability of the reagent (see Scheme 1A.4). According to this analysis, the HOMO of the square-planar complex would be the mainly formed by the combination of the HOMO of ammonia and the LUMO of the fragment that results from the de-coordination of NH_3. Within this fragment, the main contributions to the

LUMO come from the $5d_z^2$ atomic orbital of Ir and the $2p_z$ of X ($3p_z$ for X = SiH). Hence, more electronegative atoms, as X= O, and N, would present more stable LUMO orbitals in the fragment, and thus the mixture with the HOMO of ammonia would be higher, yielding more stable complexes.

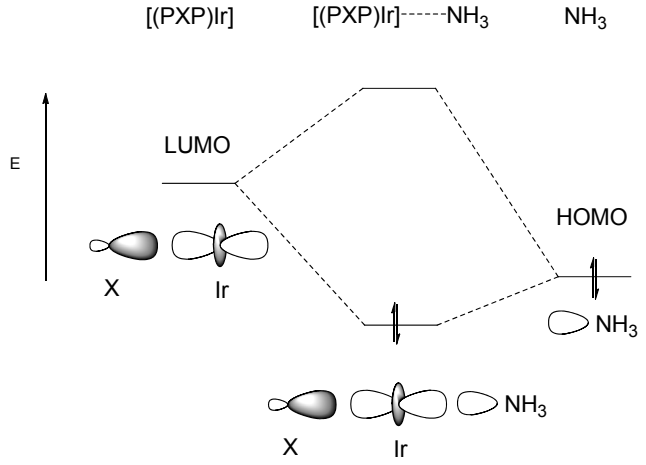

Scheme 1A.4. Molecular Orbital representation for the (PXP)Ir–NH_3 interaction.

Moreover, Ir–N distances substantially decrease when going from the reagent to the transition structure, and even more in the product. This results points towards some degree of double bond, Ir=N, in the product. This is also supported by high Wiberg Bond Orders in the product, of the order of 0.8–1.1 for all complexes, (see Table 1A.1). They are similar to those reported for metal carbenes, [M=C].[15] On the contrary, the Ir–X distance barely changes along the reaction.

A.2.2 Analysis of Ir-X classical electrostatic interaction

As previously explained, IQA approach expresses the total energy as the sum of atomic contributions, as defined by the QTAIM topological partition. In particular, the total system energy is provided as a sum of intra-atomic (E_{intra}^{A}) contributions for each atom plus the inter-atomic interaction energy between each pair of atoms (E_{inter}^{AB}). This contribution is further divided into a classical electrostatic interaction term (V_{cl}^{AB}) and a non-classical exchange-correlation one (V_{XC}^{AB}), which addresses for quantum mechanical effects.[12,13] These two terms can be associated with the character of ionic and covalent bond, respectively. Hence, the relative magnitude of both terms can be used for characterizing a given chemical bond.

Following the previous scheme, IQA was used for evaluating the magnitude and the characteristics of Ir–X interaction for the five metallic complexes. Results show that the energy term that most significantly changes along the oxidative addition

process is the classical electrostatic one (V_{cl}^{Ir-X}). The value of V_{cl}^{Ir-X} for reagent (R), transition structure (TS) and product (P) for each system is provided in Figure 1A.2.

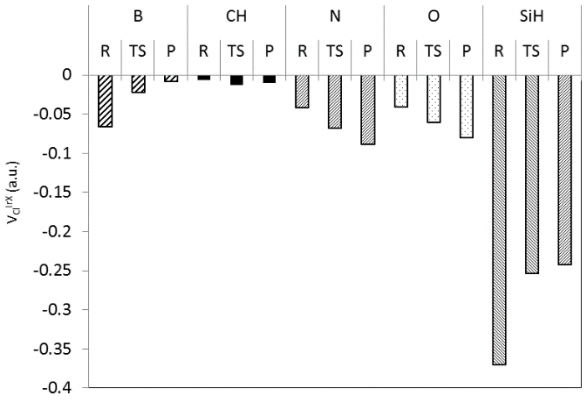

Figure 1A.2. V_{cl}^{Ir-X} interaction energy values (in a.u.) for reagent (R), transition structure (TS) and product (P) for the five complexes under study.

These results can be used to rationalize the difference in the process kinetics for the five complexes under study. Noteworthy, there are two well-differentiated trends. On the one hand, the groups bearing more electronegative atoms, (X = N and O, complexes **3** and **4**), present V_{cl}^{Ir-X} values that are increasingly negative (more stabilizing) as the reaction proceeds. This way, classical electrostatic stabilization in the TS is higher than that in R. This feature is in agreement with the lower energy barrier obtained for these complexes, as the transition structure is stabilized with respect to the reagent. On the contrary, for the least electronegative groups, (X = B and SiH, complexes **1** and **5)** the magnitude of V_{cl}^{Ir-X} reduces upon going from R to TS. The transition structure is thus destabilized with respect to the reagent and the energy barriers are higher. In the middle, we find the case of complex **2** (X = CH), with classical electrostatic contributions very similar for the reagent and the transition state, and an intermediate energy barrier.

Inspection of atomic charges supports these findings (see Table 1A.1). Within complexes **1** and **5** (X = B and SiH), the X atoms have a neat positive charge, whereas the Ir has a significantly negative charge in R; this charge being much lower in absolute value in the TS as consequence of oxidation. Then, the classical electrostatic interaction, which is strongly dependant on atomic charges, reduces as the reaction proceeds. On the contrary, Ir atoms have a neat positive charge for complexes **2**, **3** and **4**, while X groups have a negative charge that barely changes when evolving from R to TS. This way, V_{cl}^{Ir-X} is more favourable in the transition structure than in the reagent. This fact is the reason why the energy barrier is lower for these complexes. These results further support the findings derived from the BET, which points towards the

metal oxidation takes place before the transition state. This analysis will be explained in the following section.

A.2.3 Bonding Evolution Theory analysis

The ELF was used for analysing the electronic structure of the stationary points (reagent, transition structure and product) of the different systems from a Lewis-like perspective. In all cases, similar results were obtained, hence, discussion will be made on the basis of complex **2** (see Figure 1A.3). The ELF analysis revealed that initially, the Ir–N bond, V(Ir,N), can be characterized as a single bond (with a population of 1.88 e^-). As the reaction proceeds, this population significantly increases, being 3.27 e^- in the transition structure and 3.65 e^- in the product (~4 e^-). This result, in conjunction with the planarity of the Ir-NH_2 moiety, points towards the presence of, at least, some double bond character in Ir–N bond. Hence, the Ir(III) product would be better described as the combination of two resonance forms involving a single and a double Ir–N bond, as shown in Scheme 1A.5.

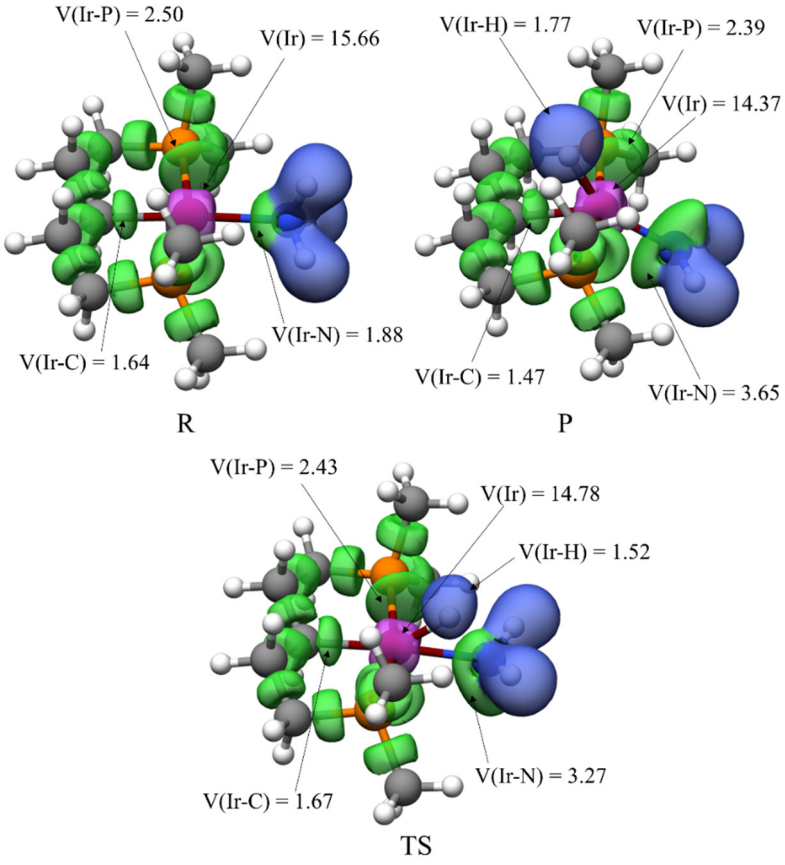

Figure 1A.3. ELF representation (isovalue = 0.8) and electron density integrated along the ELF basins of the reagent (R), transition structure (TS) and product (P) for complex **2**, X = CH. Core basins are shown in purple, hydrogenated in blue and disynapthic in green. Some hydrogen basins have been omitted for the sake of simplicity.

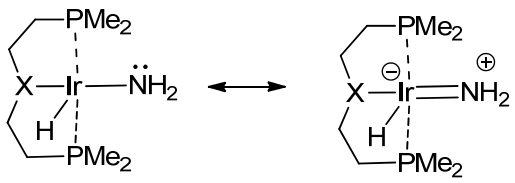

Scheme 1A.5. Proposed resonance forms for the oxidative addition product.

It is also important to note that the N–H bond in ammonia, V(N,H) with 1.98 e, breaks to form a Ir–H bond, V(Ir,H), with 1.77 e^- (corresponding to a single bond). Another relevant feature is that the population in the monosynaptic Ir basin, V(Ir), sharply decreases from R (15.66 e^-) to TS (14.78 e^-), while it keeps almost constant from TS to P (14.37 e^-). This fact provides strong evidence that the metal oxidation takes place before the transition state. Finally, it is worth mentioning that V(Ir,X) and both V(Ir,P) basins decrease their population as the oxidative addition proceeds, as expected due to their donor properties.

In order to obtain more insight into the electronic rearrangements that take place in ammonia oxidative addition into Ir(I)-(PXP) complexes, the evolution of the ELF topology and the integrated basin populations were analyzed by means of Bonding Evolution Theory. Similar qualitative results were obtained for all complexes. As a consequence, the discussion is performed in terms of complex **2** (X = CH); the most relevant differences with other complexes will be explained afterwards. The evolution of ELF basins and populations along the reaction pathway for complex **2** is shown in Figure 1A.4a.

The first turning point, *i.e.* a change in the ELF topology, corresponds to the break of the N–H bond, as shown by the first vertical line in Figure 1A.4a. As a result, the V(N,H) basin transforms into a monosynaptic V(H) basin carrying an electronic population of ~2 e^-. This fact indicates that the hydrogen atom is transferred as a hydride and the process takes place before reaching the transition state. The second turning point in the ELF topology also happens before the transition state. It corresponds to the merging of the V(H) basin with the iridium monosynaptic V(Ir) one, to yield a disynaptic (hydrogen) V(Ir,H) basin. This process represents the formation of the Ir–H bond. Noteworthy, within this structure second stability domain (SSD), SSD-II, the oxidation of the metal centre from Ir(I) to Ir(III) takes place. This observation is supported by the sudden decrease in V(Ir) population at the begging of SSD-II. Along SSD-III the geometrical reorganization of the complex occurs. All the relevant chemical events (Ir oxidation, N–H bond breaking and Ir–H bond formation) happen before the transition state, as exemplified in Scheme 1A.6.

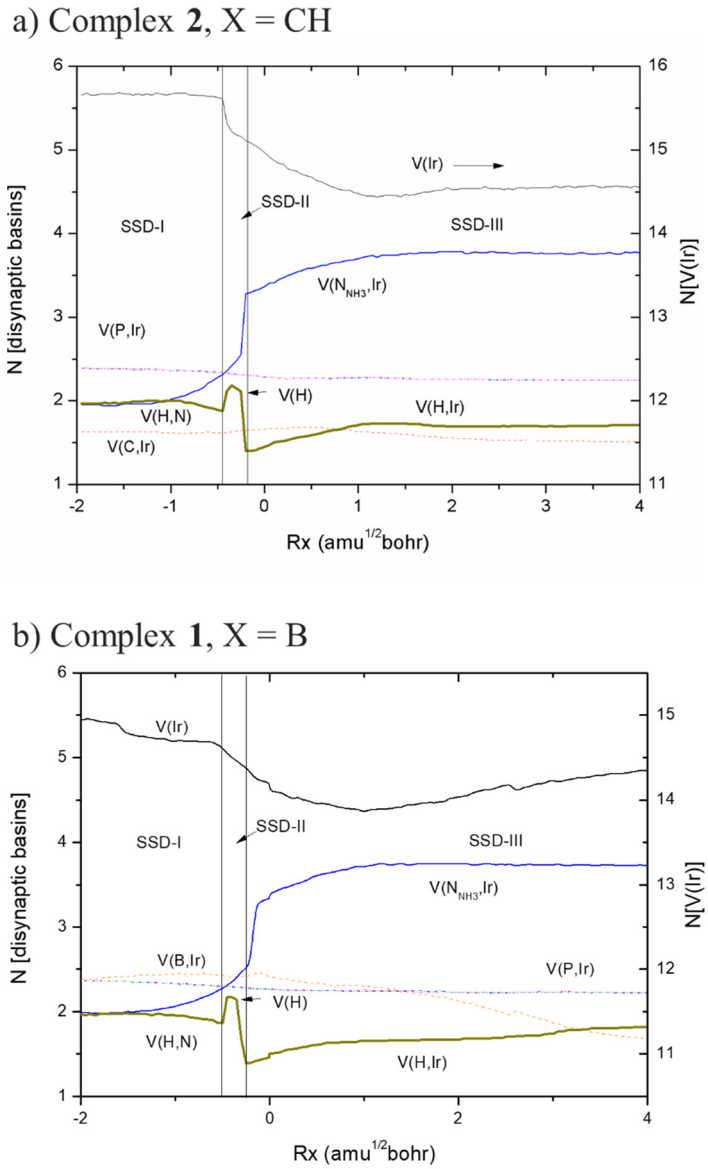

Figure 1A.4. Integrated electron populations within more relevant ELF basins along the reaction pathway of a) X= CH, complex **2**, and b) X = B, complex **1**. Bifurcation points separating different structure stability domains are shown by the presence of vertical lines. Basin populations is expressed in electrons; V(Ir) values being shown in the right axis.

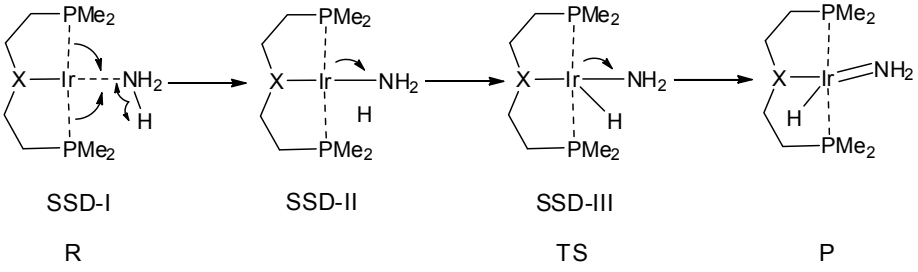

Scheme 1A.6. Representation of the proposed electronic rearrangements taking place in the oxidative addition of ammonia to Ir(I)-(PXP) complexes.

Even though the chemical events for all the complexes under study are qualitatively similar, there are some relevant differences for complexes **1** and **5**, (X = B, SiH). They can be exemplified by comparison with the BET results for complex **1**, see Figure 1A.4b. First of all, the V(P,Ir) population remains almost constant along the whole process in for complex **2** (X = CH, Figure 1.4a), whereas in complex **1** (X = B, Figure 1.4b) this population reduces from ~2.5 to ~1.5 e^- along SSD-III. At the same time, V(Ir) population significantly increases for complexes **1** and **5**, whereas it keeps roughly constant in SSD-III for the other systems. This fact is explained by the highest σ-donor character of PBP and PSiP ligands, since they are able to donate electron density to the oxidized metal.

A.3 Summary

In this section, the electronic factors that govern ammonia N–H bond activation by means of oxidative addition to five different Ir(I)-(PXP) complexes have been studied. The main findings are summarized in the following key points:

(a) Oxidative addition of ammonia into Ir(I)-(PXP) complexes does not follow the Hammond postulate. This is due to the fact that the chemical events taking place in the proximities of the transition state are very dissimilar, as pointed out by means of Bonding Evolution Theory analysis.

(b) The BET revealed that there are two main chemical events within this kind of processes; both taking place before the transition state. The first one is ammonia slippery and N–H bond activation. The second one corresponds to hydrogen transfer (as a hydride) to the Ir centre, forming the Ir–H bond upon metal oxidation from Ir(I) to Ir(III). It is also remarkable to note that for better σ-donor ligands (the ones bearing less electronegative groups, X = B and SiH), there is significant electron density transfer from the Ir–X bond to Ir electron pairs.

(c) There is a correlation between the *trans*-influence exerted by the X group in the reagent and the thermodynamics of the process. In particular, less electronegative groups present a greater *trans*-influence, thus destabilizing the reagent and presenting more favorable reaction energies.

(d) Activation energies strongly depend on the type of pincer ligand. In particular, more electronegative ligands have lower activation energies. This feature was rationalized in terms of IQA energy decomposition analysis and atomic charges evaluation.

B. Ir(III)-NHC catalysts for the silylation of aromatic C-H bonds

B.1 Introduction and objectives

The synthesis of organosilicon compounds, that is, organic derivatives bearing Si atoms, is at the forefront of current chemical research. This situation is a consequence of their highly desirable properties, being very useful in different branches of chemistry and technology. Moreover, silicon reactants are non-toxic, relatively cheap and can be easily functionalized into a variety of derivate molecules by means of a number of organic transformations.[16] More concretely, they are important in modern organic synthesis, especially as building blocks for complex molecules and as monomers for silicon polymers.[17] Conjugated organosilicon compounds have even more interest, since they are also attractive *per se*, owing to their numerous and promising applications in organic electronics and photonics.[18,19]

From a clean and sustainable perspective, the synthesis of organosilicon compounds by the catalytic silylation of C–H bonds represents a highly atom- and step-efficient alternative. Given this situation, the silylation of (hetero)arenes is an especially promising process, not only due to their widespread presence in nature, and thus its inexpensive character; but also to the high interest of the organosilicon-derivative products. These reactions are typically divided into two groups: intermolecular and intramolecular. The former requires the prefunctionalization of the arene, to yield an intermediate in which a hydrosilane group is incorporated into the molecule. Then, through a second reaction step, the C–H bond silylation happens, yielding the final product.[20] Intermolecular reactions can be further classified into directed and undirected. Catalytic directed processes need for the presence of a coordinating group in the substrate that is able to coordinate to the catalyst.[21] This interaction should leave a C–H bond in the proximities of the active site, thus favoring the silylation of this bond over the others. Within this type of processes, the selectivity is easier to modulate, since rational election of the substrate can be used to select the C–H bond to be silylated.[22] On the contrary, non-directed reactions employ substrates that do not present any coordinating group able to interact with the metal centre. As a consequence, the selectivity is much more difficult to control.

Quite surprisingly, the majority of the processes described in the literature for the catalytic silylation of C–H bonds employ commercial precursors to generate the catalysts *"in situ"*; and very little attention has been paid to the development of well-defined catalysts.[23] In this regard, it is also remarkable the small number of catalysts for deshydrogenative silylation bearing ancillary NHC ligands reported hitherto;[24] especially taking into account the enormous success of this kind of ligands in homogeneous catalysis.[25]

Within this context, this section of the Doctoral Thesis focuses on the study of the reaction mechanism of a recently reported NHC-Ir(III) complex for the catalytic silylation of aromatic C–H bonds, synthesized in the research group. The complex, $[Ir(H)_2(IPr)(py)_3][BF_4]$ (py = pyridine, IPr = 1,3-bis-(2,6-diisopropylphenyl)imidazol-2-ylidene), constitutes a well-defined catalyst (see Scheme 1B.1) that is able to efficiently and selectively catalyze intermolecular silylation reactions involving substrates with directing groups. In particular, the catalyst proved to be adequate for a wide range of (hetero)arenes, as well as with a number of hydrosilanes, including Et_3SiH, Ph_2MeSiH, $PhMe_2SiH$, Ph_3SiH and elusive $(EtO)_3SiH$. Besides, the catalytic reaction worked with and without the presence of a hydrogen acceptor (norbornene, NBE). For the sake of simplicity, the catalyst, $[Ir(H)_2(IPr)(py)_3]^+$, will be referred to as **1**, as shown in Scheme 1B.1; all the other reaction intermediates and transitions structures will be named by following the number sequence.

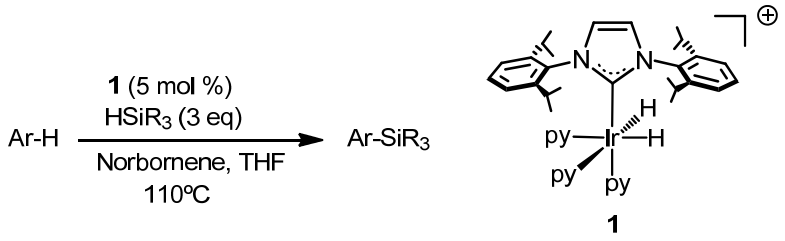

Scheme 1B.1. Schematic representation of the C–H silylation reaction, catalyst under study (**1**) and experimental conditions.

Mechanistic studies of these kind of processes are scare, being mainly limited to the experimental one reported by Hartwig *et al.*[26] on a Rh(I) catalyst for the silylation for the C–H bond in arenes and the theoretical work of Murata *et al.*[27] on a Rh catalyst for the silylation of C(sp^3)–H bonds. Another relevant mechanistic proposal is that of Mashima and co-workers,[24] who studied a similar process using a Ir(III)-complex. Nonetheless, the proposed mechanism was made just on the basis of NMR measurements and author's chemical intuition.

This situation encouraged us to perform an in-depth DFT mechanistic study of the aforementioned catalytic cycle. Theoretical calculations were performed by means of state-of-the-art DFT, as explained in the Methodology chapter. The main aims of the computational studies were:

(i) Unravel the reaction mechanism for the proposed process.
(ii) Determine the rate- and selectivity-determining steps.
(iii) Evaluate and understand the effect of directing groups for reaction selectivity.
(iv) Quantify the importance of the hydrogen acceptor for the reaction kinetics and thermodynamics.

B.2 Results and Discussion

Theoretical calculations were performed using Me_3SiH as a model for the hydrosilane, and 2-phenylpyridine for the heteroarene. For the hydrogen acceptor, we employed the experimental reagent, NBE, as well as for the Ir(III)-catalyst (complex **1**). More specific details about the calculations are provided in Methodology chapter. Results concerning the different processes under study are to be explained bellow.

B.2.1 Directed reaction in the presence of a hydrogen acceptor

The proposed reaction mechanism is presented in Figure 1B.1. The first part of the mechanism (intermediates **1** to **4**) involves the dehydrogenation of **1** to yield a Ir(I) square-planar complex, **4**, able to undertake cyclometallation with the organic substrate. The first step within this part of the catalytic cycle is the ligand exchange between a pyridine in **1** and the hydrogen acceptor, NBE, yielding complex **2**. Then, this intermediate can undergo a migratory insertion of the olefin double bond into one of the Ir–H bonds *via* transition structure **TS23**; this requiring to overcome an energy barrier of 19.0 $kcal \cdot mol^{-1}$. As a result, an alkyl intermediate, **3**, is formed. The remaining hydride ligand in **3** can then undergo a reductive elimination to yield norbornane (NBA, the hydrogenation product of NBE) and the corresponding reduced Ir(I) square-planar complex, intermediate **4**. This process needs to surmount an energy barrier of 21.0 $kcal \cdot mol^{-1}$ (taking **1** as a reference), determined by transition structure **TS45**. On balance, the dehydrogenation process is exergonic, presenting a ΔG of -15.2 $kcal \cdot mol^{-1}$.

The second part of the catalytic cycle consists on the oxidation of the Ir atom in **4** from Ir(I) to Ir(III) to recover the original catalyst and yield the organosilicon final product. The first step involves the ligand exchange between a pyridine and the heteroarene (the organic substrate, 2-phenylpyridine), yielding intermediate **5** (5.1 $kcal \cdot mol^{-1}$ higher in energy than **4**). Notice that, to the substrate (2-phenylpyridine) has a N atom that can coordinate to the metallic centre, acting as a directing group. As a result, only one hydrogen atom lies on the proximities of the metal. Then, only this position can be silylated, thus explaining the high reaction selectivity towards the 2'-position; this observation is in agreement with experimental results (see Scheme 1B.2). Afterwards, **5** undergoes the oxidative addition of the aromatic C–H bond at the 2'-position to yield **6** (-27.0 $kcal \cdot mol^{-1}$), a Ir(III) metallacycle. Noteworthy, C–H oxidative addition into the metal centre is a barrierless process, the energy decreases homogeneously when approaching the substrate. De-coordination of the pyridine ligand and coordination of the hydrosilane yields intermediate **7** (-8.9 $kcal \cdot mol^{-1}$), which then undergoes σ-complex assisted metathesis (σ-CAM) between the hydrosilane Si–H bond and Ir–C bond in intermediate **7**.[28]

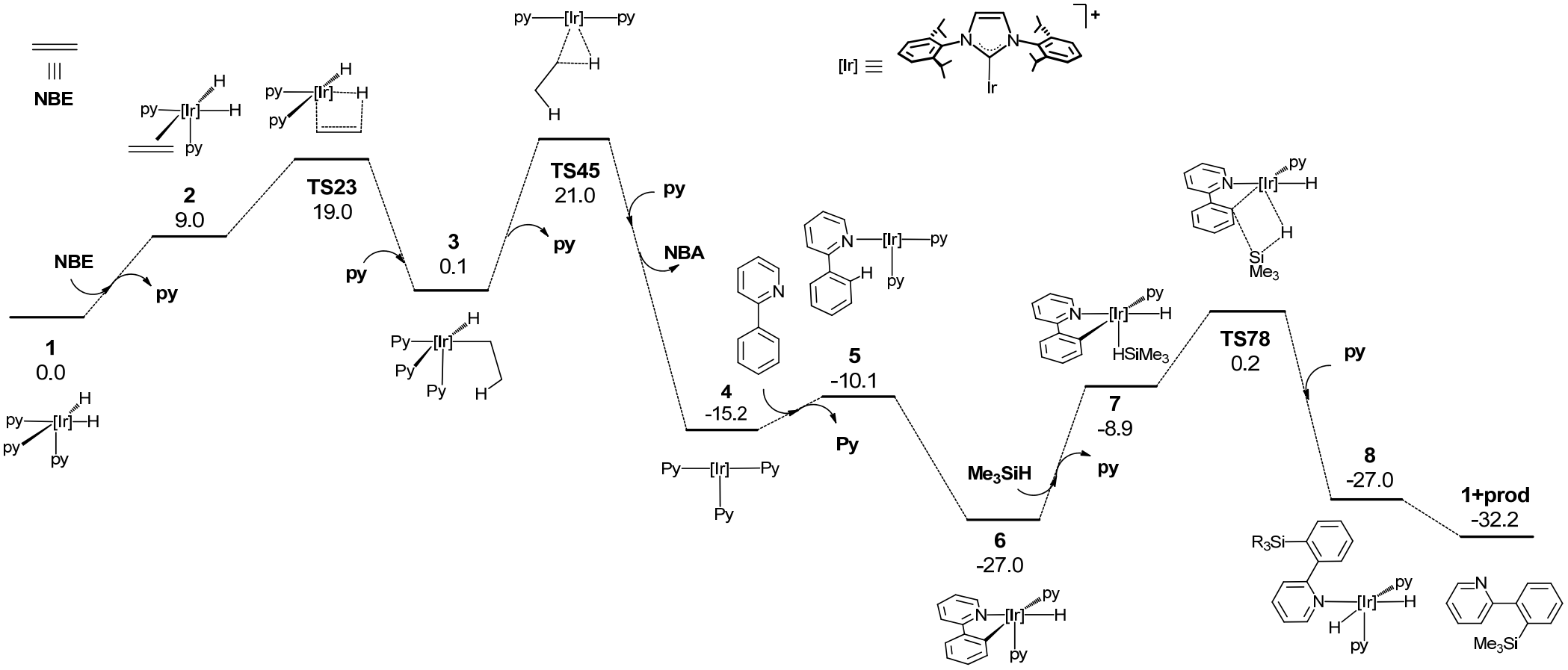

Figure 1.B1. DFT calculated Gibbs Energy profile (kcal·mol^{-1}) at 110 ºC for the directed C–H bond silylation of arenes in the presence of a hydrogen acceptor.

This process is determined by transition structure **TS78**; requiring to surmount an energy barrier of 27.2 kcal·mol^{-1} (from intermediate **6**). As a result, de Ir(III) dihydride intermediate, structure **8**, is obtained.

Finally, upon de-coordination of the organosilane (the final product), the original catalyst (complex **1**) is regenerated, closing the cycle. On balance, the process is highly exergonic (-32.2 kcal·mol^{-1}); and the effective energy span is 27.2 kcal·mol^{-1}, according to the model proposed by Kozuch and co-workers.[29] This barrier is determined by intermediate **6** and transition structure **TS78**.

Alternative mechanisms involving Ir(V) intermediates were explored; however, no stationary points for these kind of intermediates were found. Consequently, we the existence of Ir(V) species within the catalytic cycle was discarded, as proposed by Mashima *et al.*[24]

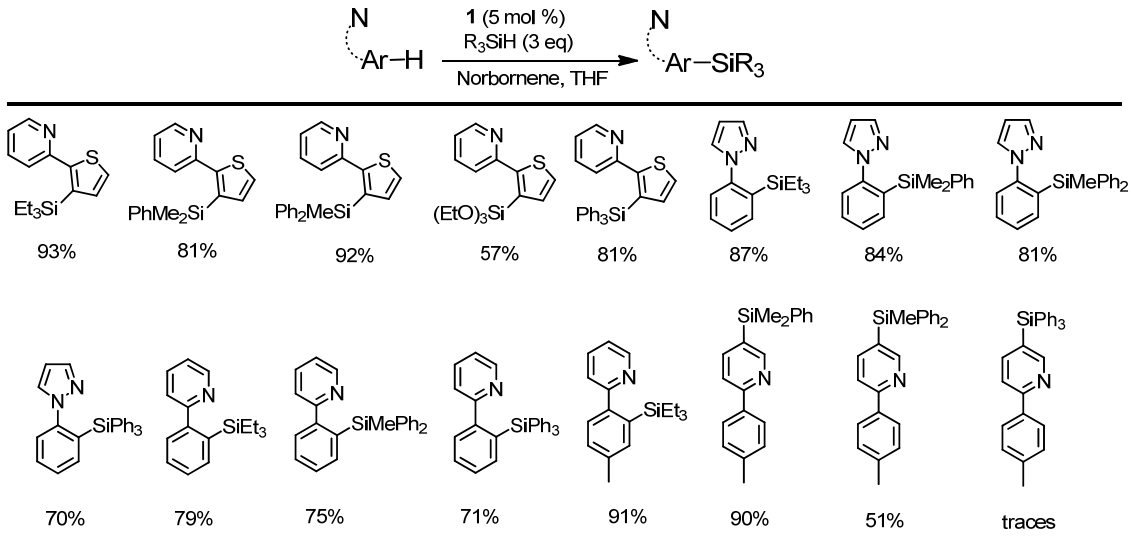

Scheme 1B.2. Experimental yields for the directed silylation of C–H aromatic bonds in the 2'-position.

B.2.2 Directed reaction without hydrogen acceptor

Reaction mechanism for the directed silylation process was also computed in the absence of hydrogen acceptor. Results are shown in Figure 1B.2. In this case, the only possibility for the dehydrogenation of **1** is the thermic dehydrogenation. This way, **1** directly transforms into **4'** (equivalent to intermediate **4** in Figure 1B.1) through a direct reductive elimination of H_2. Noteworthy, the process is very endergonic and no transition state was found. The energy landscape between **1** and **4'** being continuous; as previously proposed in some catalytic reaction involving similar organometallic species.[30]

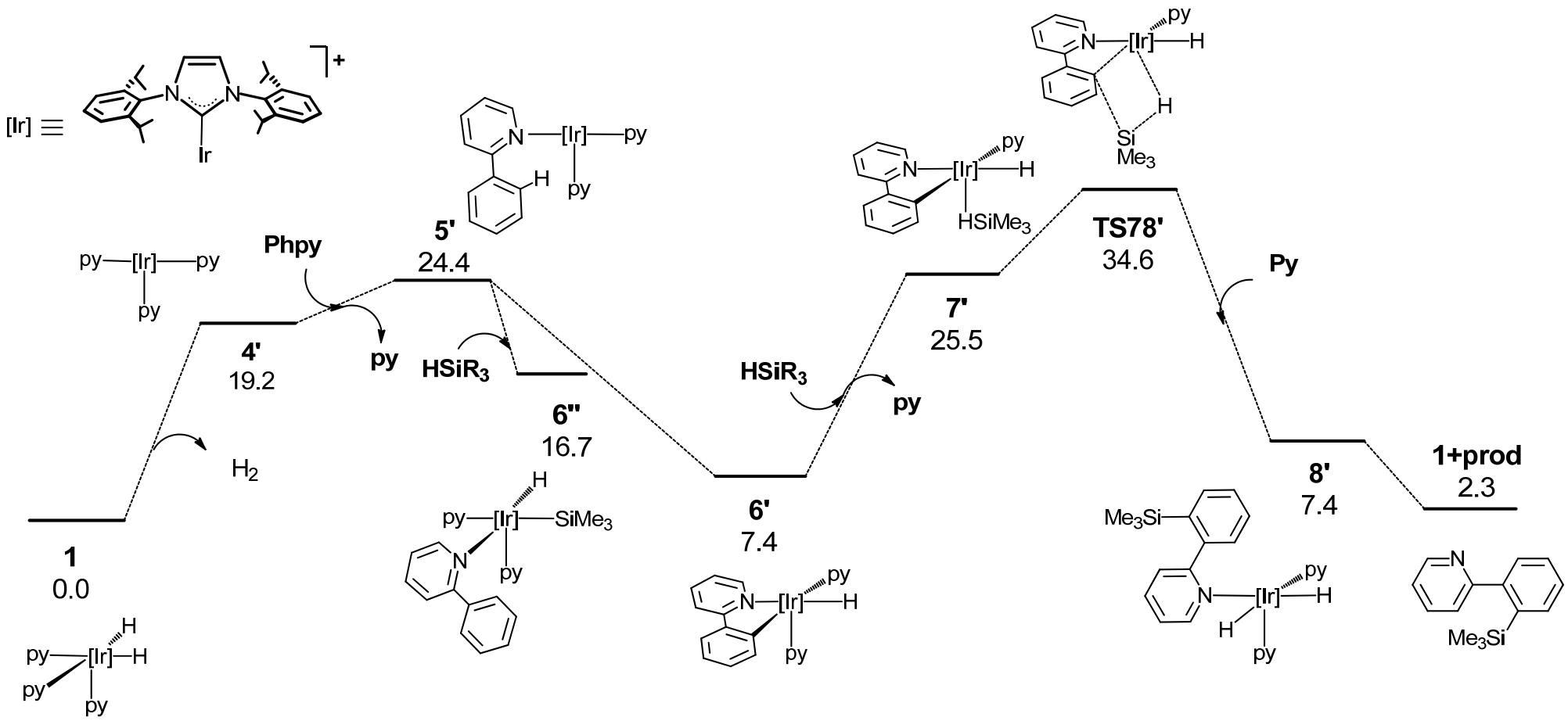

Figure 1B.2. DFT calculated Gibbs Energy profile (kcal·mol^{-1}) at 110 ºC for the directed C–H bond silylation of arenes without hydrogen acceptor.

The second part of the catalytic cycle is formally equivalent to the one proposed in the presence of a hydrogen acceptor. However, direct evolution of molecular hydrogen instead of NBE hydrogenation results into a significantly less favoured process in thermodynamic terms. In particular, ΔG for the acceptorless process is 2.3 kcal·mol^{-1}, 34.5 kcal·mol^{-1} higher than that corresponding to the reaction in the presence of NBE.

Interestingly, the reaction energy difference between both processes is approximately equal to the hydrogenation enthalpy of norbornane (33.2 kcal·mol^{-1}),[31] this fact proving strong evidence on the consistency of the theoretical results. The process kinetics is also affected by the absence of hydrogen-acceptor. In particular, a significantly higher energy span was found for the acceptorless process, 34.6 kcal·mol^{-1} (7.4 kcal·mol^{-1} higher than that corresponding to the process in the presence of NBE). This result is a consequence of the fact that olefin hydrogenation is more favourable than direct H_2 reductive elimination; then, in this situation, all the reaction profile is displaced to higher energies. However, it does not affect the cycle starting point (intermediate **1**), as it appears in the cycle before the hydrogenation processes.

The rate determining transition state remains the same as for the previous process (**TS78**'), while the rate limiting structure is now intermediate **1**. The difference in kinetics and thermodynamics between both processes is in agreement with the worse reaction yields experimentally obtained in the absence of NBE.

B.2.3 Non-directed reaction

In order to study the directing group effect in the reaction selectivity, the C–H oxidative addition step (**5** → **6** in Figure 1B.1, the selectivity determining step), was computed for the de-coordination of the N atom in the pyridine-derived organic substrate. Proceeding this way, we simulated the non-directed processes. Results for the non-directed oxidative addition of C–H into the metallic centre are reported in Figure 1B.3. For the sake of clarity, the energies of the different transition structures are computed with respect to intermediate **5**.

Contrarily to directed oxidative addition, the process presented an energy barrier in all cases. Specifically, an energy barrier of 5.8 kcal·mol^{-1} was found for the fixation of the C–H bond in *ortho* (**TS-*o***), 6.8 for the *para* position (**TS-*p***), and 8.0 for the *meta* one (**TS-*m***). As a consequence of the proximity between transition structures, there is an energy difference of only 1.0 kcal·mol^{-1} between transition structures leading to silylation in *ortho* and *para*. Then, an energy mixture between both products would be obtained in a situation in which the N atom of 2-phenylpyridine does not coordinate to the Ir centre. Hence, these results confirm that coordination of the

directing group in the substrate is necessary for explaining the high reaction selectivity, as previously proposed by Morokuma *et al.*[32]

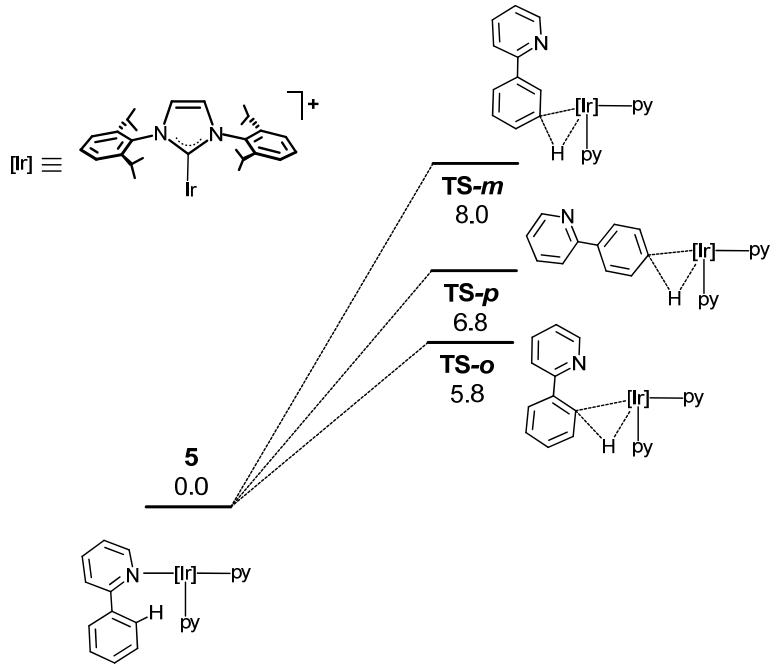

Figure 1B.3. DFT calculated Gibbs Energy profile at 110 ºC for the non-directed aromatic C–H bond oxidative addition.

B.2.4 Reactivity studies

Several stoichiometric reactivity studies were performed for confirming the aforementioned catalytic cycle proposal. The different reactions carried out are explained in the following lines.

Reactivity of complex 1

The reaction of the well-defined catalyst **1** at room temperature with 1 equivalent of different organic substrates, with and without hydrogen acceptor afforded the corresponding cyclometalated complex, that is, intermediate **6** (see Scheme 1B.3).* The straightforward formation of intermediate **6** (the resting state of the proposed cycle) in the presence of NBE at room temperature provides strong evidence about the validity of the proposed mechanism. On the one hand, the formation of **6** in the absence of hydrosilane points towards the fact that this complex is not necessary in the first steps of the catalytic cycle. In addition, the high stability and subsequent isolation of complex **6** supports the previous result of it being the most stable intermediate in the

* All the complexes resulting from stoichiometric reactions were isolated as air stable solids and characterized on the basis of NMR and X-ray diffraction studies.

catalytic cycle. Besides, the reaction takes place at room temperature, which is in agreement with the energy barrier found for the first part of the catalytic cycle, 21.0 kcal·mol^{-1} (see Figure 1B.1, structures **1** – **6**).

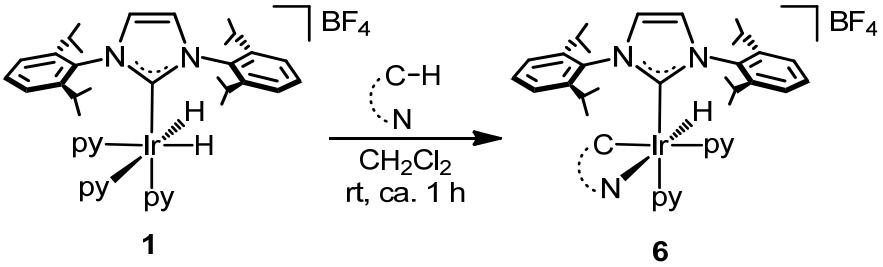

Scheme 1B.3. Stoichiometric reaction between complex **1** and a heteroarene to yield intermediate **6**.

Reactivity of cyclometalated complexes

The addition of up to three equivalents of Me_3SiH to a solution of complex **6** at room temperature yielded the starting complex. This observation is in agreement with the high energy barrier for the σ-CAM process (27.2 kcal·mol^{-1}) and the experimental requirements of at least 110 ºC for the reaction to take place with good yields. Moreover, isolation of **6** (and derivative complexes bearing similar aromatic ligands) and subsequent reaction with Me_3SiH at 110ºC under the same experimental conditions as those employed in catalytic studies, yielded the organosilicon product with good yields.

Finally, complex **9**, which is structurally related to **1** but bears a non-labile $PPhMe_2$ group instead of a pyridine in the *trans* position to the carbene ligand, was also tested as a catalyst (see Scheme1B.4). However, no silylated product was obtained. This fact can be explained on the basis of ligand lability; since pyridine is a labile ligand, it easily de-coordinates, allowing hydrosilane coordination and ulterior activation (**6** → **7** in Figure 1B.1). On the contrary, $PPhMe_2$ does not de-coordinate, thus, there is not any vacancy available for the hydrosilane to coordinate to the metallic centre.

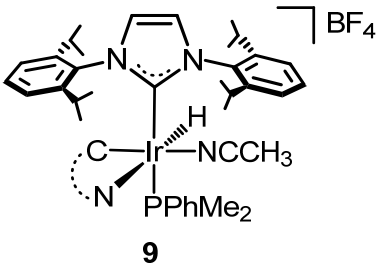

Scheme 1B.4. Schematic structure of complex **9**.

Use of deuterated hydrosilanes

The catalytic reaction was performed using **1** as a catalyst and a deuterated hydrosilane, $PhMe_2SiD$. Interestingly, no deuterium was observed in the organosilicon product; this observation is in agreement with theoretical predictions. In particular, the hydrosilane reacts through a σ-CAM mechanism in which the Si–H(D) and Ir–C bonds break and C–Si and Ir–H(D) bonds form. As a result, the D atom would be transferred to the Ir and not to the organic product, as pointed out by the reactivity study.

B.3 Summary

In this section, the reaction mechanism of a well-defined Ir(III)-NHC catalyst for the silylation of aromatic C–H bonds has been studied. A summary of the main conclusions is presented below:

(a) A reaction mechanism consistent with experimental data for the catalytic sililation of aromatic C–H bonds by a well-defined Ir(III)-NHC complex has been proposed. Theoretical calculations point towards a Ir(III)/Ir(I) reaction mechanism in which the lability of pyridine ligands is crucial for the silane activation.

(b) Reaction thermodynamics is significantly different depending on whether the reaction is carried out with or without a hydrogen acceptor. In particular, ΔG values of -32.2 and 2.3 $kcal \cdot mol^{-1}$ were obtained for both processes, respectively.

(c) An energy barrier of 27.2 $kcal \cdot mol^{-1}$ was obtained for the directed silylation in the presence of a hydrogen acceptor; this energy barrier is 34.6 $kcal \cdot mol^{-1}$ when no hydrogen acceptor is employed. Moreover, the silane σ-bond metathesis was found to be the rate determining reaction step (for both processes).

(d) The high reaction selectivity is explained on the basis of the directing groups present in the organic substrates. These groups coordinate to the Ir centre, thus leaving only one C–H bond in the proximities of the catalyst active centre.

(e) The mechanistic proposal was supported by means of specific reactivity experiments.

C. Ir(III)-NHO catalyzed solventless dehydrogenation of formic acid

C.1 Introduction and objectives

During the last decades, global energy requirements have enormously increased as a consequence of the rapidly growing world population in conjunction with extensive industrialization. Within this context, the current energy economy based on fossil fuels presents several problems; one of the most important being fossil fuel depletion. The use of this kind of fuels also involves a number of environmental concerns, especially, climate change associated with CO_2 emissions. Given this situation, there is an evident need to find renewable, environmentally clean and economically beneficial alternative energy generation sources.[33] In this regard, hydrogen use as an energy vector stands as a very promising alternative energy carrier. In particular, it is able to accumulate a lot of chemical energy per mass unit, *i.e.* 120 $kJ \cdot g^{-1}$, about three times that of petroleum;[34] being also very abundant on Earth. Moreover, there is a number of hydrogen production alternatives, some of them being environmentally friendly, such as the use of bio-oil and thermochemical water splitting; thus making it a readily accessible product.[35] In addition, the chemical energy accumulated in the chemical bonds of H_2 molecules can be released by means of different *green* processes, such as electrochemical combustion in fuel cells, obtaining only water as a by-product.[36]

Nonetheless, the use of hydrogen as an energy vector displays several drawbacks; the main of them are its storage and transportation. Hydrogen storage methods are usually classified into two different categories: physical and chemical. Physical methods are those that involve molecular H_2, existing three main possibilities depending on whether hydrogen is stored as compressed gaseous hydrogen, as liquid hydrogen or adsorbed on high-surface-area materials, such as organic polymers and zeolites. Unfortunately, this kind of storage is very expensive and inefficient, making necessary the search for alternatives.[37] In chemical methods, hydrogen is stored as hydridic or protonic hydrogen forming part of different compounds. These compounds can be solids, such as metal hydride alloys, borohydrides, aminides and ammonia-borane; or liquids, such as hydrazine, alcohols and formic acid. Then, upon transportation, hydrogen is liberated in a second step by thermic or catalysed decomposition of the partner carrier.[38] These methods have proven to be quite promising in hydrogen transport, constituting a strong alternative for avoiding problems related with physical storage.[39]

In this sense, the use of formic acid (FA) has several advantages: it presents a high kinetic stability at room temperature, as well as a low toxicity, especially when compared with other alternatives, such as amine-boranes and methanol. In addition, its

energy density is higher than that of the majority of the liquid organic hydrogen carriers. Moreover, CO_2 can be hydrogenated to FA, and then stored for further hydrogenation upon H_2 release; thus rendering a carbon-neutral cycle of storage.[40] The solventless dehydrogenation of FA presents additional advantages, since it reduces the reaction mixture volume, increasing the process energy density. It also avoids the problems caused by volatile organic solvents that can deactivate the electrodes in fuel cells.

Several organometallic active catalysts for catalytic FA dehydrogenation have been reported in the literature.[41] However, the great majority of these processes take place in solution, and the examples of homogeneous catalysts operating in pure FA reported hitherto are scarce.[42]

Following the previous research line, we proposed a highly active Ir(III)-catalyst for FA solventless dehydrogenation bearing an N-heterocyclic olefin (NHO) ligand. In particular, $[Ir(PCP)(COD)]BF_4$, (PCP = 1,3-bis(2-(diphenylphosphanyl)ethyl)-2-methyleneimizazoline, COD = 1,5-ciclooctadiene),[43] which will be referred to as complex **1** (see Scheme 1C.1).

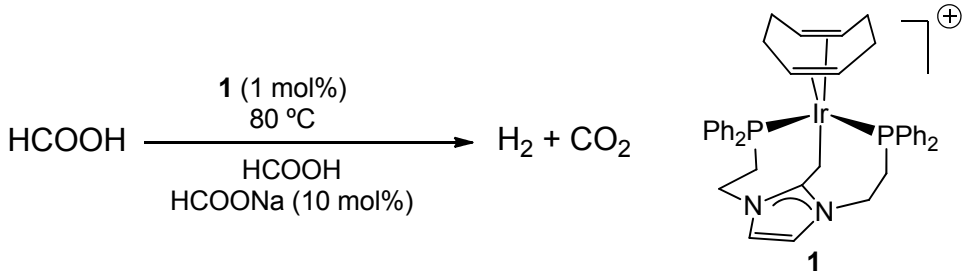

Scheme 1C.1. Studied FA dehydrogenation reaction, experimental conditions and catalyst (complex **1**).

Mechanistic investigations on this kind of processes reported in the literature has mainly focused on Ru-,[44] Fe-,[45] Rh-,[46] and Ir-based catalysts.[47] The key feature of the previous mechanisms is the way in which CO_2 is released, existing two main proposals: β-hydride elimination and hydride abstraction, as shown in Scheme 1C.2.[48]

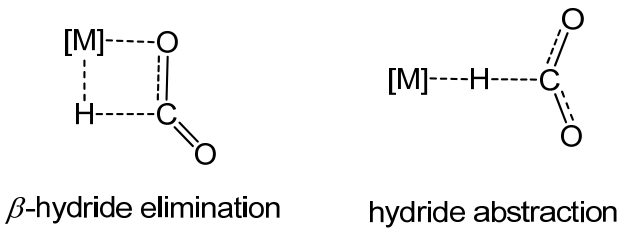

Scheme 1C.2. Schematic representation of transition states for CO_2 release *via* β-hydride elimination and hydride abstraction in FA dehydrogenation processes.

Within this context, we performed an in-depth computational study of the Ir(III) –NHO-catalyzed FA dehydrogenation reaction depicted in Scheme 1C.1. Specifically, we focused on:

(i) Proposing a reasonable reaction mechanism.
(ii) Identifying the way in which CO_2 and H_2 are released.

C.2 Results and Discussion

Theoretical calculations were performed using complex **1** as the starting structure. Specific details about the calculations are provided in Methodology chapter.

C.2.1 Reaction mechanism for FA dehydrogenation

The mechanistic proposal for FA dehydrogenation on the basis of theoretical calculations is presented in Figure 1C.1. The first step involves a ligand exchange between the COD and a FA molecule in complex **1**, yielding intermediate **2**. Subsequently, O–H bond of FA is activated through transition structure **TS23**. The process requires to overcome an energy barrier of 13.1 kcal·mol^{-1}. As a result, the Ir centre is oxidized from Ir(I) to Ir(III), yielding a mono-hydride bearing a coordinated formate ($HCOO^-$) ligand (intermediate **3**) with a relative energy of -2.9 kcal·mol^{-1}. Another molecule of FA can coordinate to the vacant left by O–H bond activation, producing intermediate **4**. This intermediate can further evolve, *via* deprotonation, to intermediate **5**, which is 2.0 kcal·mol^{-1} more stable than **3**. The next step is the formation of CO_2, by means of a β-hydride elimination process, *via* transition structure **TS36**. For reaching **TS36**, a formate ligand in **5** has to de-coordinate, since an additional coordination vacancy is needed for the hydrogen atom of the other formate to coordinate to the metal (see Figure 1C.1). As previously stated, two main mechanisms for CO_2 release have been proposed in the literature: β-hydride elimination and hydride abstraction.[48] Remarkably, in this case, the β-hydride elimination was the lowest-in-energy possibility, 8.0 kcal·mol^{-1} more favourable than hydride abstraction. As a result, a dihydride intermediate is produced, intermediate **6**. This intermediate can stabilize (4.1 kcal·mol^{-1}) upon coordination of the formate ligand, yielding intermediate **7**. Notice that this intermediate was experimentally detected and isolated, as it will be explained in the next section.

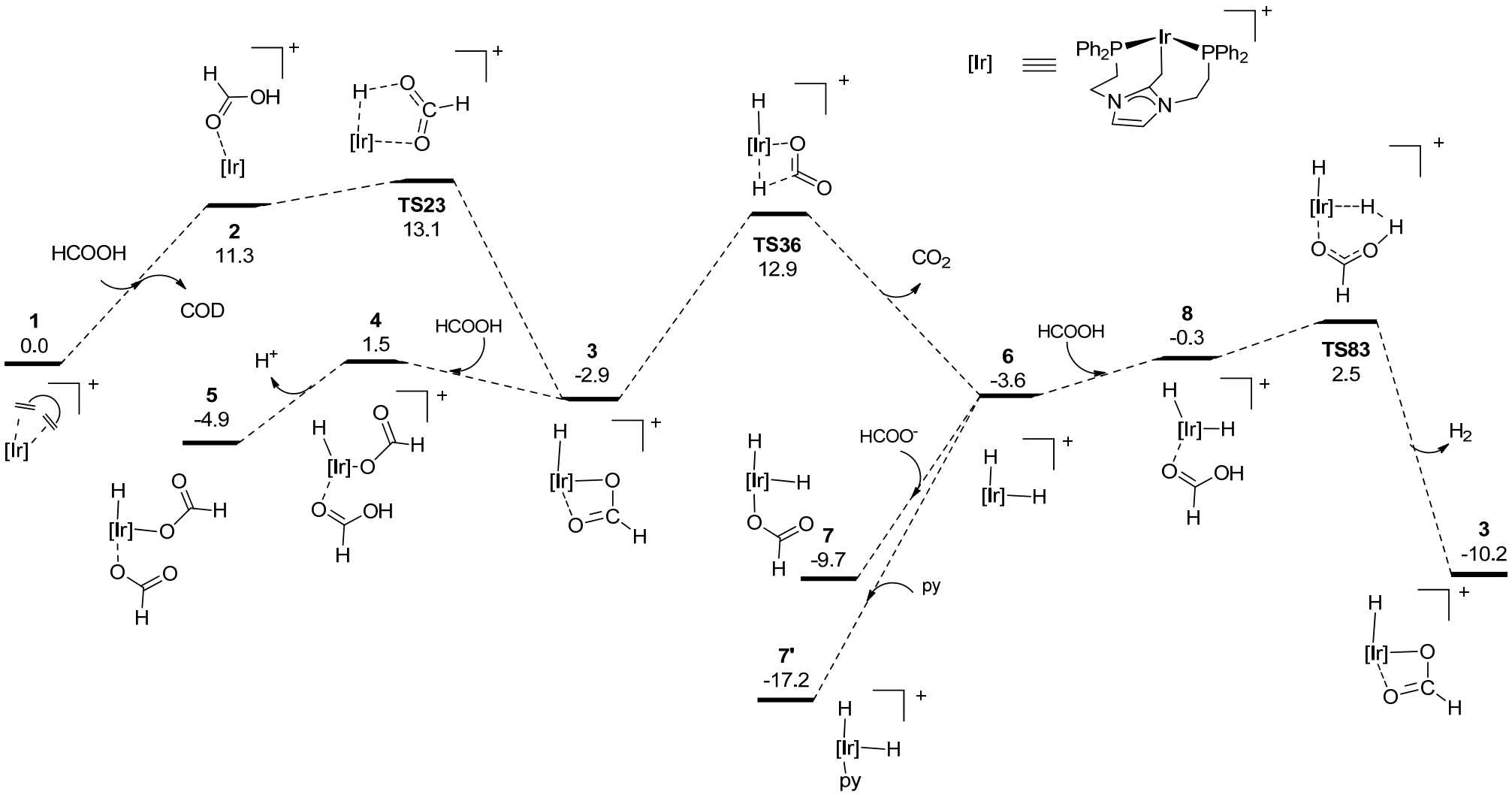

Figure 1C.1. DFT calculated Gibbs Energy profile (kcal·mol^{-1}) for FA dehydrogenation at 80ºC.

The final reaction step consists on the release of H_2 through an intramolecular protonation of a hydride ligand in **7**. For that, a ligand exchange between a formate ligand and a FA is required, yielding intermediate **8**, *via* dihydride intermediate **6**. The process is dictated by transition structure **TS83**, and involves the protonation of a hydride ligand by the acid hydrogen of FA. Interestingly, intermolecular protonation of hydride ligands by FA has extensively been suggested in the literature.[48,49] However, in this case, the coordination vacancy in **6** allows for the coordination of a FA molecule.

As a result, protonation proceeds through an intramolecular mechanism. Upon H_2 release, intermediate **3** is recovered.

This way, intermediate **3** constitutes the active species that will start subsequent catalytic cycles. On balance, ΔG for the whole process (activation and catalysis) equals -10.2 kcal·mol^{-1}, this value being -7.3 kcal·mol^{-1} if only the catalytic cycle is considered. The energy span for FA dehydrogenation corresponds to the CO_2 release step, and is 17.8 kcal·mol^{-1}. This value is obtained by the energy difference between intermediate **5** and transition structure **TS36**.

Remarkably, even though the starting pre-catalyst is an Ir(I) complex, all the catalytic steps are carried out by complexes in which Ir is in a formal oxidation state of III.

C.2.2 Reactivity studies

Several reactivity studies were performed with the aim of further confirming the reaction mechanistic proposal made on the basis of theoretical calculations. The different experiments and the derived conclusions are explained below.

Intermediates detection and isolation

According to the mechanistic proposal (see Figure 1C.1), intermediate **7** is the most stable intermediate appearing in the catalytic cycle, constituting a resting state. Then, it may be possible to experimentally detect it.

As an attempt to do so, **1** was dissolved in CH_2Cl_2 with 4 equivalents of FA at 50 ºC (lower than the 80 ºC considered in the theoretical calculations) in the presence of traces of water. As a result, a dihydride complex is formed, as detected by NMR measurements. However, this species decomposed during the isolation process. When a large excess of pyridine (ca. 20 equivalents) was added to the previous solution, a new dihydride complex, **7'**, of stoichiometry $[Ir(H)_2(PCP)(py)]BF_4$ was detected. This compound could be isolated and its structure was determined by X-ray diffraction methods (see Scheme 1C.3). The energy of this intermediate was calculated, being 7.5 kcal·mol^{-1} more stable than intermediate **7** (see Figure 1C.1). Moreover, addition of an excess of 3,5-dimethylpirydine to a solution of **7'** yielded

the structurally related complex **7''**, illustrating the facile access to this coordination site.

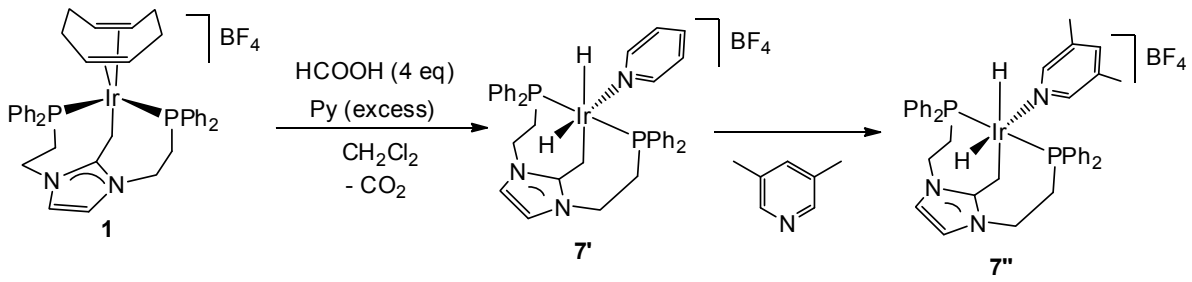

Scheme 1C.3. Synthesis and structure of complexes **7'** and **7''**.

The previous experiment confirms the relatively stable nature of intermediate **7** and derivative complexes, thus providing strong evidence of it being a resting state in the catalytic cycle of FA dehydrogenation.

Activation energy determination

Activation energies were experimentally determined by carrying the reaction at different temperatures between 60 and 90 ºC and applying the well-known Arrhenius equation (see Figure 1C.2). An activation energy of 19.9 ± 0.8 kcal·mol^{-1} was obtained for reactions taking place in the presence of catalytic amounts of water (30 mol%). The activation energy under strictly anhydrous conditions was 24.5 ± 1.8 kcal·mol^{-1}.

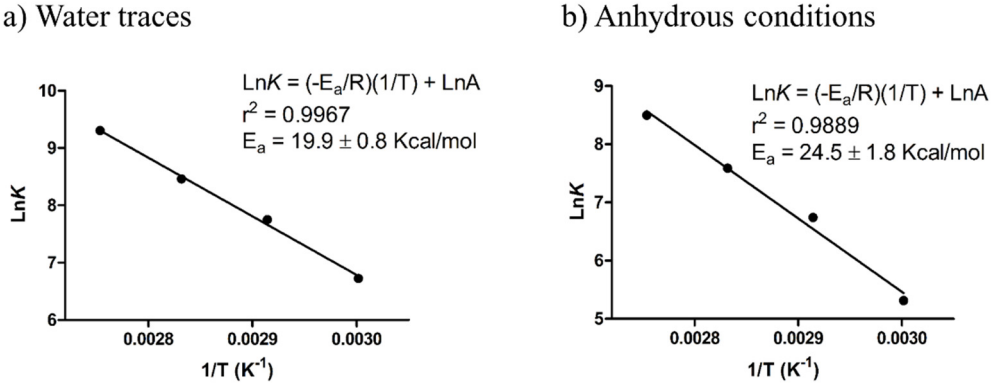

Figure 1C.2. Arrhenius plot for the dehydrogenation of FA using complex **1**, a) in the presence of water; b) in the absence of H_2O. A reaction order of 1 with respect to the catalyst was considered in the activation energy calculations.

Remarkably, these values are significantly lower than those reported by FA dehydrogenation in the absence of catalyst: about 48.5 kcal·mol^{-1} and with significant formation of CO and H_2O.[50] This comparison highlights the relevance of the catalyst herein reported.

The experimental activation energies are also in qualitative agreement with the computationally predicted ones (17.8 kcal·mol^{-1}), taking into account the inherent limitations of DFT methodology to quantitatively predict energy barriers. In addition, in this particular case, the system under study is particularly difficult to model by static calculations, as it can be strongly influenced by the acid-base equilibrium established between FA and formate molecules.

C.3 Future work perspectives

As stated in the last section, the presence of catalytic amounts of water has a positive effect on FA dehydrogenation rates. Further investigation on the effect of water in the reaction rate showed that an increase on water concentration from 0 mol% to 150 mol% (with respect to FA) resulted in progressive increase in the catalytic activity, evaluated by means of the Turnover Frequency (TOF), as shown in Figure 1C.3. In addition, the catalyst was stable in water. In this regard, it constitutes, to the best of our knowledge, the only catalyst hitherto reported able to work in water and under solventless conditions.

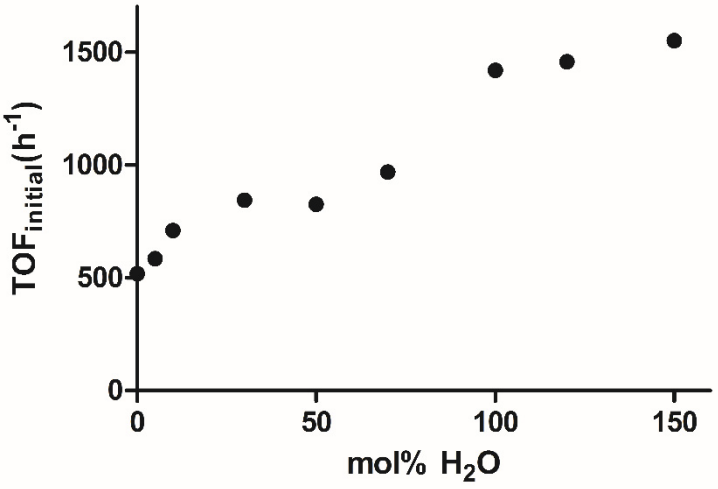

Figure 1C.3. Effect of H_2O addition on FA dehydrogenation rate, evaluated by means of the initial TOF. Quantities of water (in mol%) are referred to FA.

As depicted in Figure 1C.3, the increment in the water concentration increases the reaction rate until a plateau is reached at a concentration close to 30 mol%. Then, the catalyst activity keeps constant until 50 mol%, and then, there is a sharp rise on the catalytic activity. Then, another plateau appears at a concentration of 100 mol%, and no significant rate increase is observed upon further increment of water. We proposed this intricate behaviour to be a consequence of the combination of different effects: the role played by H_2O molecules in the dissociation equilibrium of FA, the stabilization

of different reaction intermediates by means of hydrogen bonding, and the effect of the different solvation spheres of water in FA and reaction intermediates accessibility.

However, we were unable to propose an alternative mechanism by means of DFT calculations that address the role of water on the reaction rate. In particular, we investigated the effect on water molecules as proton shuttles in the rate determining transition state (**TS36**). Nonetheless, it did not lower the energy barrier.

This way, in future works, we expect to be able to unravel the effect of H_2O on the reaction mechanism. In particular, we will explore other possibilities such as transition state stabilization by means of hydrogen bonding and the cooperative effects of several water molecules involved in second-sphere hydrogen bonding.[51]

C.4 Summary

Within this part of the Doctoral Thesis, the reaction mechanism of formic acid dehydrogenation under solventless conditions by means of a highly active Ir–NHO catalyst has been studied. The main conclusions are presented below:

(a) A catalyst pre-activation step is required. Within this step, the Ir(I) pre-catalyst is oxidized to an Ir(III) active species.

(b) There is no change in the oxidation state of the metal during the whole catalytic cycle, remaining as Ir(III) in all the reaction steps.

(c) The effective energy span of the catalytic cycle is 17.8 $kcal \cdot mol^{-1}$, and corresponds to CO_2 release through a β-hydride elimination process. This value is in qualitative agreement with the experimentally determined one.

(d) A dihydride intermediate was proposed as a resting state in the catalytic cycle. This species was experimentally identified and crystallized.

(e) Catalyst activity increased in the presence of water. We proposed this effect to be a consequence of hydrogen bonding and solvation effects. However, further investigations that take into account the role of the pH in catalysis are required for an in-depth understanding of this behaviour.

D. Unveiling the role of organic oxidants on oxidative carbonylations

D.1 Introduction and objectives

Carbamates ($R_1OCONR_2R_3$) are organic functional groups that formally derive from carbamic acid (see Scheme 1D.1). They are very important in current chemical research due to their widespread applications in different processes. In particular, they are highly relevant as functional groups with interest *"per se"* in medicinal chemistry, drug design and agrochemicals.[52] Besides, they have a number of applications as auxiliary groups in a variety of chemical transformations. More specifically, they are frequently used as protecting groups for amines, thus being important intermediates in synthetic chemistry.[53]

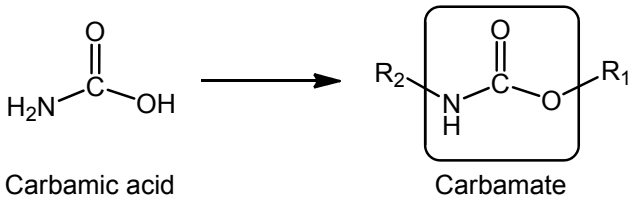

Scheme 1D.1. Schematic representation of a carbamate as a derivate of carbamic acid.

Classic procedures for the synthesis of carbamates typically involve the use of phosgene or its derivatives as a source of carbon monoxide, in conjunction with the corresponding amines and alcohols.[54] There also exist other more environmentally friendly alternatives that use different stoichiometric reagents such as azides,[55] isocyanates[56] and carbonates.[57] More recently, some catalytic processes involving the use of CO_2 as the source of carbon have been reported. However, these approaches are still scarce.[58] Interestingly, important advances have been achieved in Pd- and Au-catalyzed preparation of carbamates under carbon monoxide atmosphere.[52b,59,60] Nonetheless, given the excellent performance of Rh catalysts in oxidative carbonylation processes,[61] it is surprising that they have barely been applied to the catalytic synthesis of carbamates.

This situation motivated us to in-depth study the activity of commercially available Rh complexes towards the synthesis of carbamates starting from carbon monoxide and a set of amines and alcohols under mild conditions. In order to keep the process as environmentally respectful, as well as to investigate the effect of organic oxidants in synthetic chemistry, Oxone (potassium peroxymonosulfate, $KHSO_5$) was chosen as the oxidant. Different Rh-catalysts were subjected to an initial test, selecting $[Rh(\mu\text{-}Cl)(COD)]_2$ for further in-depth catalytic studies (see Scheme 1D.2). With respect to the reaction scope, good yields were obtained when different aromatic amines were subjected to reaction with a variety of primary and secondary alcohols.

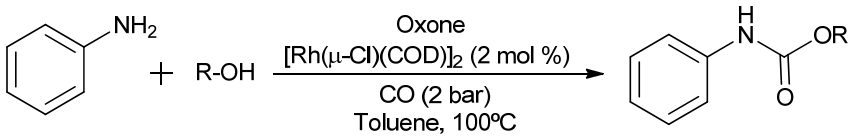

Scheme 1D.2. Oxidative carbonylation of aniline with different alcohols and experimental conditions.

The mechanistic knowledge of oxidative couplings catalysed by Rh complexes, such as the carbamates synthesis presented in Scheme 1D.2, is scarce. Theoretical studies are mainly limited to the study of Rh(III) complexes as catalysts and $Cu(OAc)_2$ as the oxidant.[62] More recently, persulfates have also proven to be efficient oxidants for the alkoxycarbonylation of C–H bonds when applied in combination with Rh(I) catalysts.[6] Up to now, two different mechanisms have been proposed for the oxidant role within this kind of Rh(I)-catalysed processes (see Scheme 1D.3).[64,65]

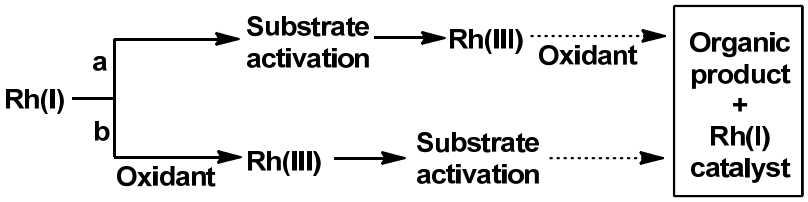

Scheme 1.D3. Mechanistic proposals reported in the literature for oxidative carbonylation of C–H bonds catalyzed by Rh(I)-complexes.

Encouraged by the lack of knowledge on this type of oxidations, an in-depth theoretical study of the reaction mechanism of the aforementioned Rh(I)-catalysed synthesis of carbamates was performed. Theoretical calculations payed special attention to unravel the role of the organic oxidant (Oxone). More specifically, the goals of the study are:

(i) Determining the reaction mechanism for the synthesis of carbamates catalysed by Rh(I) complexes using commercially available alcohols, amines and carbon monoxide in the presence of organic oxidants.
(ii) Establishing the rate determining steps of the catalytic cycle.
(iii) Revealing the role of organic oxidants in this kind of processes.

D.2 Results and Discussion

As previously stated, commercial [Rh(μ-Cl)(COD)]$_2$ pre-catalyst was used for the oxidative carbonylation of amines and alcohols. NMR studies showed that when this species is put in contact with the reagents (aniline and a alcohol) in a CO atmosphere at temperatures up to 50 ºC (the reaction needs about 100 ºC to proceed), only [Rh(Cl)(CO)$_2$(aniline)] is observed. As a result, this complex, which will be referred to as complex **1**, was taken as the catalytic active species for the theoretical calculations. Methanol (MeOH) was employed as a model for the alcohol and aniline (NH_2Ph) for the amine; the oxidant (Oxone, $KHSO_5$) and the catalyst ([Rh(Cl)(CO)$_2$(aniline)], (**1**) were considered in their totality. More details about the computational details are provided in the Methodology chapter. The proposed reaction mechanism will be explained below.

C.2.1 Reaction mechanism and role of the organic oxidant

According to the performed computational study, the first part of the reaction mechanism involves the action of the organic oxidant, oxidizing Rh(I) to Rh(III), in agreement with the previous proposal of Li and co-workers (see Figure 1D.1).[65]

Two related pathways for the oxidation of **1** were considered, shown with blue and red lines, respectively. The first one (blue) involves the direct oxidation of ([Rh(Cl)(CO)$_2$(aniline)]. For that, in a first step, the oxidant establishes a hydrogen bond with one of the hydrogen atoms in the amine, yielding intermediate **2**, with the same relative energy. Then, the oxidation of the complex takes place through a concerted mechanism in which Oxone deprotonates the amine while oxidizing the metal from Rh(I) to Rh(III) by transference of a hydroxyl group, *via* **TS23**. This process requires to surmount an energy barrier of 21.7 kcal·mol^{-1}. As a result, a Rh(III) octahedral intermediate, **3**, is formed and $KHSO_4$ is liberated. This process is significantly favourable form a thermodynamic point of view, with ΔG equals -16.2 kcal·mol^{-1}. Then, due to the higher basicity of aniline with respect to methanol, there is a hydrogen transfer from the alcohol to the deprotonated base (*via* **TS34**). This process yields intermediate **4**, a Rh(III) complex bearing the activated alcohol, with a relative energy of -22.8 kcal·mol^{-1} (6.6 kcal·mol^{-1} more stable than **3**). On balance, the process requires to overcome an energy barrier of 21.7 kcal·mol^{-1}, affordable under the experimental working conditions (100 ºC).

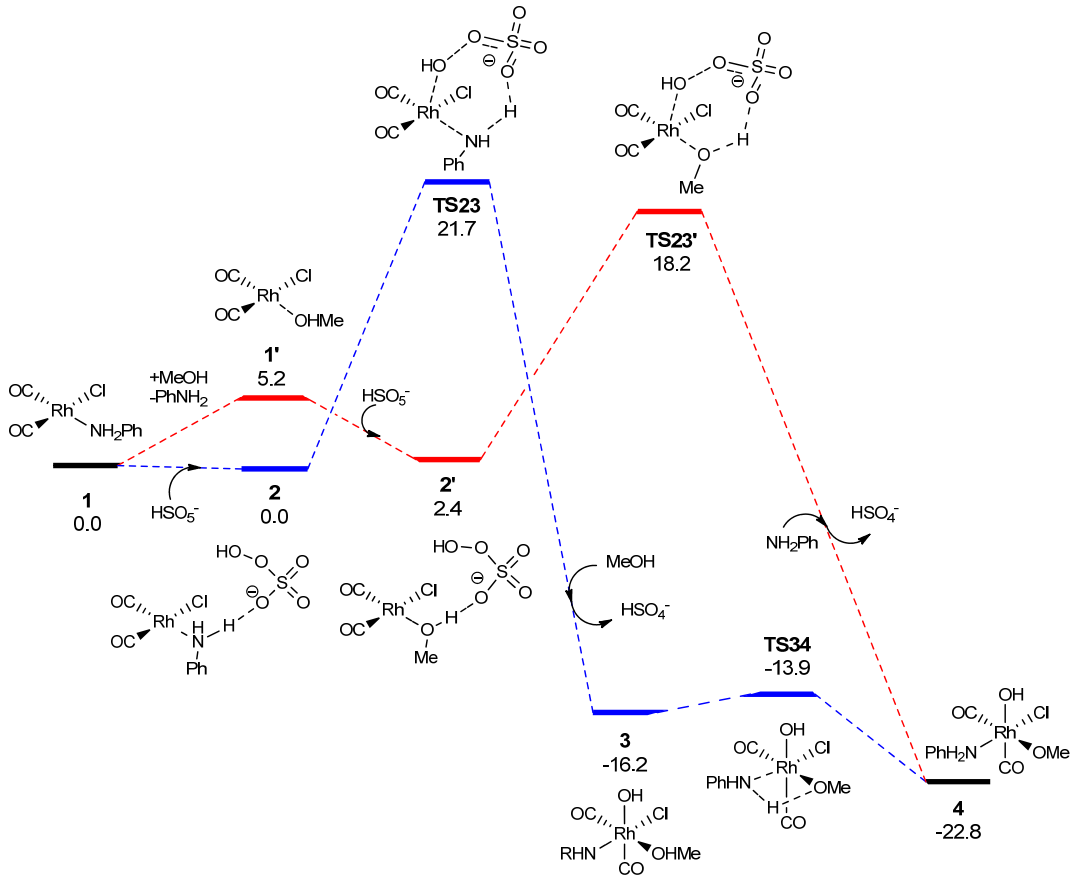

Figure 1D.1. DFT calculated Gibbs Energy profile (in kcal·mol^{-1}) at 100 ºC for the first part of the Rh-catalyzed oxidative carbonylation of amines.

Alternatively, the oxidant can deprotonate the alcohol (red lines). For that, there has to be a ligand exchange between the amine and the alcohol, yielding **1'**, 5.2 kcal·mol^{-1} less stable than **1**. Afterwards, Oxone forms a hydrogen bond interaction with the hydroxylic hydrogen of the alcohol, producing intermediate **2'**. Then, the metal oxidation from Rh(I) to Rh (III) takes place through a concerted process in which the alcohol is deprotonated and $KHSO_4$ is released. This process involves transition structure **TS23'** (see Figure 1D.2), which is formally equivalent as **TS23**, but deprotonating the alcohol instead of the amine. The energy barrier is lower in this case (18.2 kcal·mol^{-1} *vs* 21.7 kcal·mol^{-1}). Thus, this pathway is expected to be the preferred one. This way, structure **4** is produced without the need for any intermediate transformation.

On balance, the oxidation process is thermodynamically favourable (-22.8 kcal·mol^{-1}), and the activation energy barrier is 18.2 kcal·mol^{-1} for the lower-in-energy pathway.

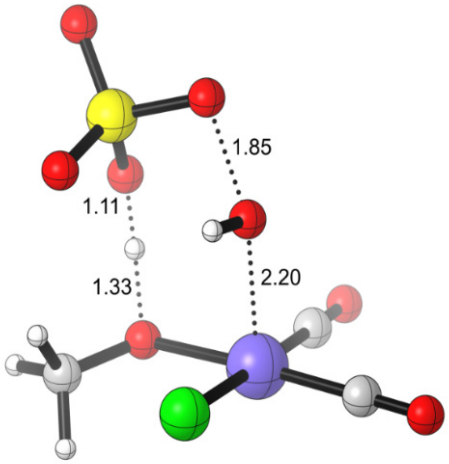

Figure 1D.2. DFT-optimized structure for transition structure **TS23'** and selected distances (in Å).

The second part of the catalytic cycle (shown in Figure 1D.3) consists on the carbonylation of the activated Rh(III) complex. The presence of the hydroxyl ligand in **4** allows for the deprotonation of the amine *via* **TS45**, surmounting an energy barrier of 8.1 kcal·mol^{-1}. The resulting intermediate, **5**, bears the two deprotonated reagents (the alcohol and the amine), and an aquo ligand. Ligand exchange between the former ligand and a CO molecule yields intermediate **6**, which is 3.4 kcal·mol^{-1} more stable. This intermediate can easily undergo carbonylation of the amido ligand *via* **TS67**, requiring to overcome an energy barrier of 11.0 kcal·mol^{-1}. As a result, intermediate **7** is formed. This process is significantly favorable from a thermodynamic point of view (**7** is 19.1 kcal·mol^{-1} more stable than **6**).

The final step is the reductive elimination of the carbamoyl (RNHC(O)–) and alkoxo (RO–) ligands in **7** to yield the final product (the carbamate). This process proceeds through transition structure **TS78**, surmounting an energy barrier of 14.3 kcal·mol^{-1}. As a result, a Rh(I) intermediate, **8**, is formed. The substitution of a CO ligand by an amine regenerates the original Rh(I) catalyst. Remarkably, this step is strongly exergonic, the product being 48.3 kcal·mol^{-1} more stable than the previous intermediate (**7**).

On balance, the process is highly exergonic, with ΔG equals -78.2 kcal·mol^{-1}, and the energy span is 23.0 kcal·mol^{-1} (determined by the energy difference between intermediate **4** and transition structure **TS67**).[29]

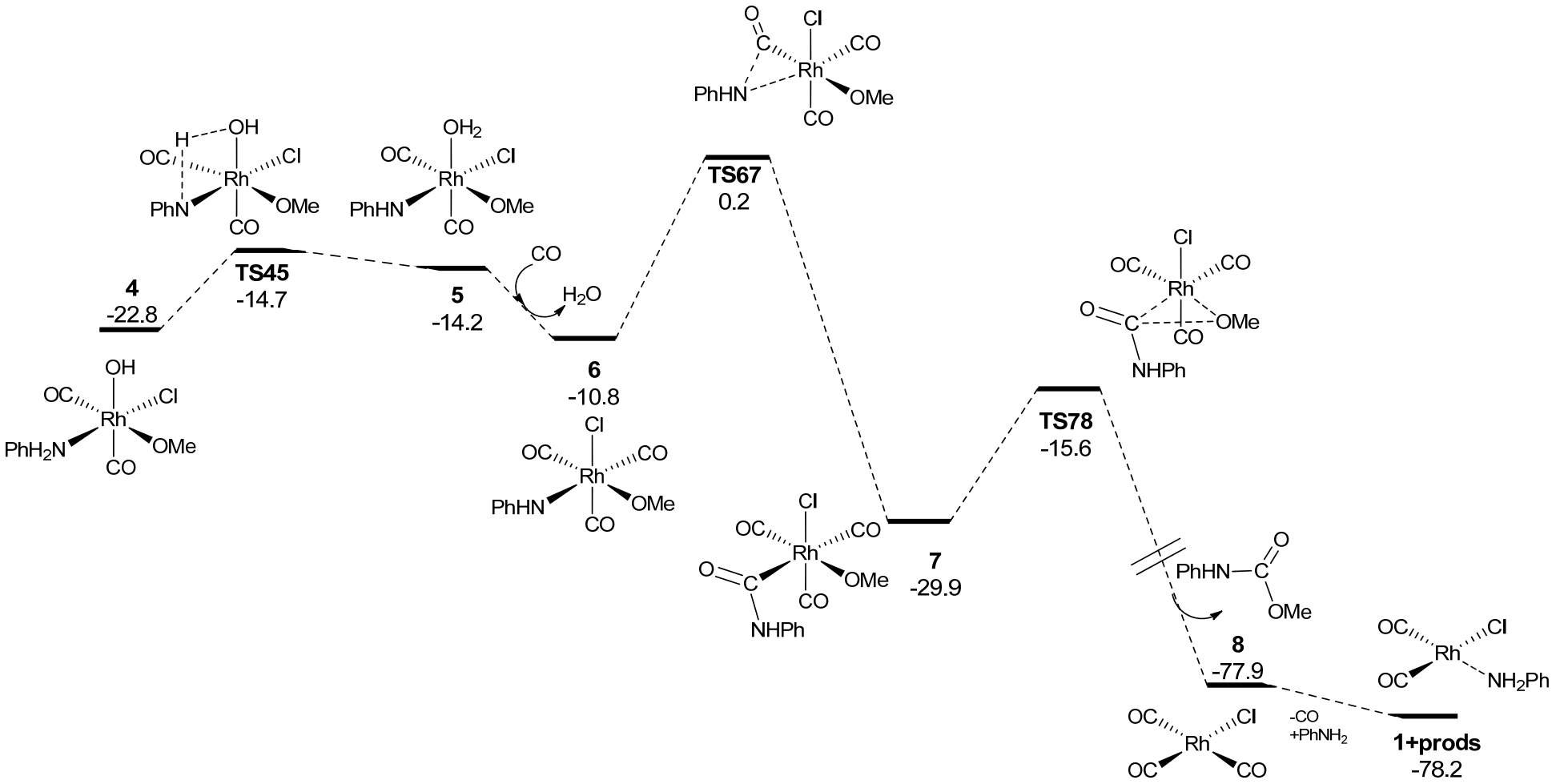

Figure 1D.3. DFT calculated Gibbs Energy profile (in kcal·mol^{-1}) at 100 ºC for the second part of the Rh-catalyzed oxidative carbonylation of amines.

D.2.2 Reactivity studies

The relatively low energy span found for the reaction (23.0 kcal·mol^{-1}) seems not be consistent whit the required experimental temperature of 100 ºC. However, we believe that the high required temperatures are a consequence of the almost negligible solubility of Oxone in toluene (the solvent) at room temperature, making necessary to heat the reaction mixture for it to dissolve, at least partially. In order to demonstrate this suggestion, the reaction was carried out in the presence of a phase transfer catalyst. In particular, 4 mol% of tetrabutylammonium tetrafluoroborate was added, which acts as a surfactant that solubilizes Oxone. As a result, the reaction proceeded at 50 ºC (with some alcohol oxidation by-products). This fact demonstrates that the reaction rate is limited by the oxidant solubility, as proposed on the basis of theoretical calculations.

D.3 Summary

In this section, the reaction mechanism of the synthesis of carbamates by means of oxidative carbonylation catalyzed by commercial Rh(I) complexes has been studied. Special attention was paid to the role and way of action of the organic oxidant. The main findings are the following:

(a) Oxidative carbonylation preparation of carbamates proceeds by means of a Rh(I)/Rh(III) reaction mechanism.

(b) The organic oxidant (Oxone) plays a dual role. On the one hand it deprotonates the alcohol (or the amine) and, on the other hand, it oxidizes the metal centre from Rh(I) to Rh(III). This process takes place through a concerted mechanism.

(c) The process presents an energy span of 23.0 kcal·mol^{-1}, and is very favourable from a thermodynamic point of view, with ΔG equals -78.2 kcal·mol^{-1}.

(d) The reaction rate was limited by the solubility of the oxidant.

E. References

[1] Kinkernberg, J. L.; Hartwig, J. F. Catalytic organometallic reactions of ammonia. *Angew. Chem. Int. Ed.* **2011**, *50*, 86–95.

[2] For examples see: (a) Velez, E.; Betoré, M. P.; Casado, M. A.; Polo, V. N–H Activation of Ammonia by [{M(μ-OMe)(cod)}$_2$] (M = Ir, Rh) Complexes: A DFT Study. *Organometallics* **2015**, *34*, 3959–3966. (b) Álvarez, M.; Álvarez, M.; Fructos, M. R.; Urbano, J.; Pérez, P. J. Copper-induced ammonia N–H functionalization. *Dalton Trans.* **2016**, *45*, 14628–14633. (c) Margulieux, G. W.; Bezdek, M. J.; Turner, Z. R.; Chirik, P. J. Ammonia Activation, H_2 Evolution and Nitride Formation from a Molybdenum Complex with a Chemically and Redox Noninnocent Ligand. *J. Am. Chem. Soc.* **2017**, *139*, 6110–6113.

[3] (a) Zhao, J.; Goldman, A. S.; Hartwig, J. F. Oxidative addition of ammonia to form a stable monomeric amido hydride complex. *Science* **2005**, *307*, 1080–1082. (b) Morgan, E.; MacLean, D. F.; McDonald, R.; Turculet, L. Rhodium and Iridium Amido Complexes Supported by Silyl Pincer Ligation: Ammonia N−H Bond Activation by a [PSiP]Ir Complex. *J. Am. Chem. Soc.* **2009**, *131*, 14234–14236.

[4] (a) Su, M. D.; Chu, S. Y. Theoretical Study of Oxidative Addition and Reductive Elimination of 14-Electron d^{10} ML_2 Complexes: A ML_2 + CH_4 (M = Pd, Pt; L = CO, PH_3, L_2 = PH‘$_2CH_2CH_2PH_2$) Case Study. *Inorg. Chem.* **1998**, *37*, 3400–3406. (b) Fazaeli, R.; Ariafard, A.; Jamshidi, S.; Tabatabie, E. S.; Pishro, K. A. Theoretical studies of the oxidative addition of PhBr to $Pd(PX_3)_2$ and $Pd(X_2PCH_2CH_2PX_2)$ (X = Me, H, Cl). *J. Organomet. Chem.* **2007**, *692*, 3984–3993.

[5] (a) Su, M. D.; Chu, S. Y. C−F Bond Activation by the 14-Electron $M(X)(PH3)_2$ (M = Rh, Ir; X = CH_3, H, Cl) Complex. A Density Functional Study. *J. Am. Chem. Soc.* **1997**, *119*, 10178–10185. (b) Diggle, R. A.; Macgregor, S. A.; Whittlesey, M. K. Ability of N-Heterocyclic Carbene Ligands to Promote Intermolecular Oxidative Addition Reactions at Unsaturated Ruthenium Centers. *Organometallics* **2004**, *23*, 1857–1865.

[6] Wang, D. Y.; Choliy, Y.; Haibach, M. C. Hartwig, J. F.; Krogh-Jespersen, K.; Goldman, A. S. Assessment of the Electronic Factors Determining the Thermodynamics of “Oxidative Addition” of C–H and N–H Bonds to Ir(I) Complexes. *J. Am. Chem. Soc.* **2016**, *138*, 149–163.

[7] Silvi, B.; Savin, A. Classification of chemical bonds based on topological analysis of electron localization functions. *Nature*, **1994**, *371*, 683–686.

[8] Polo, V.; Andrés, J.; Berski, S.; Domingo, L. R.; Silvi, B. Understanding Reaction Mechanisms in Organic Chemistry from Catastrophe Theory Applied to the Electron Localization Function Topology. *J. Phys. Chem. A* **2008**, *112*, 7128–7136.

[9] González-Navarrete, P.; Andrés. J.; Berski, S. How a Quantum Chemical Topology Analysis Enables Prediction of Electron Density Transfers in Chemical Reactions. The Degenerated Cope Rearrangement of Semibullvalene. *J. Chem. Phys. Lett*. **2012**, *3*, 2500–2505.

[10] Nizovtsev, A. S. Activation of C-H bond in methane by Pd atom from the bonding evolution theory perspective. *J. Comput. Chem.* **2013**, *34*, 1917–1924.

[11] Viciano, I.; González-Navarrete, P.; Andrés, J.; Marti, S. Joint Use of Bonding Evolution Theory and QM/MM Hybrid Method for Understanding the Hydrogen Abstraction Mechanism via Cytochrome P450 Aromatase. *J. Chem. Theory Comput.* **2015**, 11, 1470–1480.

[12] Blanco, M. A.; Pendas, A. M.; Francisco, E. Interacting Quantum Atoms: A Correlated Energy Decomposition Scheme Based on the Quantum Theory of Atoms in Molecules *J. Chem. Theory Comput.* **2005**, *1*, 1096–1109.

[13] Maxwell, P.; Pendas, M. A.; Popelier, P. L. A. Extension of the interacting quantum atoms (IQA) approach to B3LYP level density functional theory (DFT). *Phys. Chem. Chem. Phys.* **2016**, *18*, 20986–21000.

[14] Mitoraj, M. P.; Zhu, H.; Michalak, A.; Ziegler, T. On the origin of the trans-influence in square planar d8-complexes: A theoretical study. *Int. J. Quantum Chem*. **2009**, *109*, 3379–3386.

[15] Frenking, G.; Sola, M.; Vyboishcikov, S. F. Chemical bonding in transition metal carbene complexes. *J. Organomet. Chem.* **2005**, *680*, 6178–6204.

[16] (a) Marciniec, B.; Pietraszuk, C.; Knownacki, I.; Zaidlewicz, M. *Comprehensive Organic Functional Group Transformations*; Elsevier: Oxford, 2005. (b) Ojima, I. *The Chemistry of Organic Silicon Compounds*; Wiley: New York, 1989. (c) Luh, T. –Y.; Liu, S. –T. *The Chemistry of Organic Silicon Compounds*; Wiley: Chichester, 2003.

[17] (a) Nakao, Y.; Hiyama, T. Silicon-based cross-coupling reaction: an environmentally benign version. *Chem. Soc. Rev.* **2011**, *40*, 4893–4901. (b) Corriu, R. J. P.; Gerbier, P.; Guerin, C.; Henner, B. J. L.; Jean, A.; Mutin, P. H. Organosilicon polymers: pyrolysis chemistry of poly[(dimethylsilylene)diacetylene]. *Organometallics* **1992**, *11*, 2507–2513.

[18] Ponomarenko, S. A.; Kirchmeyer, S. *Silicon Polymers*; Springer-Verlag: Heidelberg, 2010.

[19] For examples see: (a) Lin, J. –J.; Liao, W. –S.; Huang, H. –J.; Wu, F. I.; Chang, C. –H. A Highly Efficient Host/Dopant Combination for Blue Organic Electrophosphorescence Devices. *Adv. Funct. Mater.* **2008**, *18*, 485–491. (b) Bin, J. –K.; Cho, N. –S.; Hong, J. –I. New Host Material for High-Performance Blue Phosphorescent Organic Electroluminescent Devices. *Adv. Mater.* **2012**, *24*, 2911–2915. (c) Leung, M. K.; Yang, W. –H.; Chuang, C. –N.; Lee, J. –H.; Lin, C. –F.; Wei, M. K.; Liu, Y. –H. 1,3,4-Oxadiazole Containing Silanes as Novel Hosts for Blue Phosphorescent Organic Light Emitting Diodes. *Org. Lett.* **2012**, *14*, 4986–4989.

[20] (a) Su, B.; Hartwig, J. F. Ir-Catalyzed Enantioselective, Intramolecular Silylation of Methyl C–H bonds. *J. Am. Chem. Soc.* **2017**, *139*, 12137–12140. (b) Kuznetsov, A.; Gevorgyan, V. General and Practical One-Pot Synthesis of Dihydrobenzosiloles from Styrenes. *Org. Lett.* **2012**, *14*, 914–917.

[21] (a) Hirano, K.; Miura, M. A lesson for site-selective C–H functionalization on 2-pyridones: radical, organometallic, directing groups and steric controls. *Chem. Sci.* **2018**, *9*, 22–32. (b) Schaufelberger, F.; Timmer, B. J. J.; Ramström, O. Resolving a Reactive Organometallic Intermediate from Dynamic Directing Group Systems by Selective C–H Activation. *Chem. Eur. J.* **2018**, *24*, 101–104.

[22] (a) Tobisu, M.; Ano, Y.; Chatani, N. Rhodium-Catalyzed Silylation of Aromatic Carbon–Hydrogen Bonds in 2-Arylpyridines with Disilane. *Chem.–Asian J.* **2008**, *3*, 1585–1591. (b) Kanyiva, K. S.; Juninobu, Y.; Kanai, M. Palladium-Catalyzed Direct C–H Silylation and Germanylation of Benzamides and Carboxamides. *Org. Lett.* **2014**, *16*, 1968–1971.

[23] (a) Oyamaga, J.; Nishura, M.; Hou, Z. Scandium-Catalyzed Silylation of Aromatic C–H Bonds. *Angew. Chem. Int. Ed.* **2011**, *50*, 10720–10723. (b) Fang, H.; Guo, L.; Zhang, Y.; Yao, W.; Huang, Z. A Pincer Ruthenium Complex for Regioselective C–H Silylation of Heteroarenes. *Org. Lett.* **2016**, *18*, 5624–5627.

[24] Choi, G.; Tsurufi, H.; Mashima, K. Hemilabile N-Xylyl-N′-methylperimidine Carbene Iridium Complexes as Catalysts for C–H Activation and Dehydrogenative Silylation: Dual Role of N-Xylyl Moiety for ortho-C–H Bond Activation and Reductive Bond Cleavage. *J. Am. Chem. Soc.* **2013**, *135*, 13149–13161.

[25] (a) Nolan, S. P. *N-Heterocyclic Carbenes in Synthesis*; Wiley-VCH: Weinheim, 2006. (b) Cazin, C. S. J.*Catalysis by Metal Complexes*, Springer Science+Business Media: New York, 2011. (c) Muller-Janssen, D.; Schlepphorst, C.; Glorius, F. Privileged chiral N-heterocyclic carbene ligands for asymmetric transition-metal catalysis. *Chem. Soc. Rev.* **2017**, *46*, 4845–4854.

[26] Cheng, C.; Hartwig, J. F. Mechanism of the Rhodium-Catalyzed Silylation of Arene C–H Bonds. *J. Am. Chem. Soc.* **2014**, *136*, 12064–12072.

[27] Kon, K.; Suzuki, H.; Takada, K.; Kohari, Y.; Namikoshi, T.; Watanabe, S.; Murata, M. Site-Selective Aliphatic C−H Silylation of 2-Alkyloxazolines Catalyzed by Ruthenium Complexes. *ChemCatChem* **2016**, *8*, 2202–2205.

[28] Perutz, R. N.; Sabo-Etienne, S. The sigma-CAM Mechanism: sigma complexes as the basis of sigma-bond metathesis at late-transition-metal centers. *Angew. Chem. Int. Ed. Engl.* **2007**, *46*, 2578–2592.

[29] Kozuch, S.; Shaik, S. How to Conceptualize Catalytic Cycles? The Energetic Span Model. *Acc. Chem. Res.* **2011**, *44*, 101–110.

[30] (a) Rubio-Pérez, L.; Iglesias, M.; Castarlenas, R.; Polo, V.; Pérez-Torrente, J. J.; Oro, L. A. *ChemCatChem* **2014**, *6*, 3192–3199. (b) Maseras, F.; Lledós, A.; Clot, E.; Eisenstein, O. *Chem. Rev*. **2000**, *100*, 601–636.

[31] McQuillin, F. J.; Baird, M. S., *Alicyclic Chemistry, Cambridge Texts in Chemistry and Biochemistry*; Cambridge University Press: Cambridge, 1983.

[32] Matsubara, T.; Koga, N.; Musaev, D. G.; Morokuma, K. Density Functional Study on Activation of *ortho*-CH Bond in Aromatic Ketone by Ru Complex. Role of Unusual Five-Coordinated d^6 Metallacycle Intermediate with Agostic Interaction. *J. Am. Chem. Soc.* **1998**, *120*, 12692–12693.

[33] (a) Huber, G. W.; Iborra, S.; Corma, A. Synthesis of Transportation Fuels from Biomass: Chemistry, Catalysts, and Engineering. *Chem. Rev.* **2006**, *106*, 4044–4098. (b) Simil, V. *Energy at the Crossroads, Global Perspectives and Un-certainties*; MIT Press: Cambridge, 2003. (c) Navlani-García, M.; Mori, K.; Kuwahara, Y.; Yamashita, H. Recent strategies targeting efficient hydrogen production from chemical hydrogen storage materials over carbon-supported catalysts. *NPG Asia Mater.* **2018**, *10*, 277–292.

[34] Sartbaeva, A.; Kuznetsov, V. L.; Wells, S. A.; Edwards, P. P. Hydrogen nexus in a sustainable energy future. *Energy Environ. Sci.* **2008**, *1*, 79–85.

[35] (a) Dincer, I.; Acar, C. review and evaluation of hydrogen production methods for better sustainability. *Int. J. Hydrog. Energy.* **2015**, *40*, 11094–11111. (b) Chattanathan, S. A.; Adhikari, S.; Abdoulmoumine, N. *Renew. Sust. Energy Rev.* **2012**, *16*, 2366–2372. (c) Singh, R.; Dutta, S. A review on H_2 production through photocatalytic reactions using TiO_2/TiO_2-assisted catalysts. *Fuel* **2018**, *220*, 607–620.

[36] (a) Rand, D. A. J.; Dell, R. M. *Hydrogen Energy-Challenges and Prospects*; RSC Publishing: Cambridge, 2008. (b) Steele, B. C. H.; Heinzel, A. Materials for fuel-cell technologies. *Nature* **2001**, *414*, 345–352.

[37] Eberle, U.; Felderhoff, M.; Schüth, F. Chemical and physical solutions for hydrogen storage. *Angew. Chem. Int. Ed.* **2009**, *48*, 6608–6630.

[38] Dalebrook, A. F.; Gan W.; Grasemann, M.; Moret, M.; Laurenczy, G. Hydrogen storage: beyond conventional methods. *Chem. Commun.* **2013**, *49*, 8735–8751.

[39] Preuster, P.; Wasserscheid, P. Liquid Organic Hydrogen Carriers (LOHCs): Toward a Hydrogen-free Hydrogen Economy. *Acc. Chem. Res.* **2017**, *50*, 74–85.

[40] (a) Singh, A. K.; Singh, S.; Kumar, A. Hydrogen energy future with formic acid: a renewable chemical hydrogen storage system. *Catal. Sci. Technol.* **2015**, 6, 12–40. (b) Eppinger, J.; Huang, K. –W. Formic Acid as a Hydrogen Energy Carrier. *ACS Energy Lett.* **2017**, *2*, 188–195. (c) Mondelli, C.; Puértolas, B.; Ackermann, M.; Chen, Z.; Pérez-Ramírez, J. Enhanced Base-Free Formic Acid Production from CO_2 on Pd/g-C_3N_4 by Tuning of the Carrier Defects. *ChemSusChem* **2018**, *11*, 2859–2869.

[41] Sordakis, K.; Tang, C.; Vogt, L. K.; Junge, H.; Dyson, P. J.; Beller, M.; Laurency, G. Homogeneous Catalysis for Sustainable Hydrogen Storage in Formic Acid and Alcohols. *Chem. Rev.* **2018**, *118*, 372-433.

[42] (a) Oldenhof, S.; de Bruin, B.; Lutz, M.; Siegler, M. A.; Patureau, F. W.; van der Vlugt, J. I.; Reek, J. N. H. Base-Free Production of H_2 by Dehydrogenation of Formic Acid Using An Iridium–bisMETAMORPhos Complex. *Chem. Eur. J.* **2013**, *19*, 11507-11511. (b) Cohen, S.; Borin, V.; Schapiro, I.; Musa, S.; De-Botton, S.; Belkova, N. V.; Gelman, D. Ir(III)-PC(sp^3)P Bifunctional Catalysts for Production of H2 by Dehydrogenation of Formic Acid: Experimental and Theoretical Study. *ACS Catal.* **2017**, *7*, 8139–8146. (c) Celaje, J. J. A.; Lu, Z.; Kedzie, E. A.; Terrile, N. J.; Lo, J. N.; Williams, T. J. A prolific catalyst for dehydrogenation of neat formic acid. *Nat. Commun.* **2016**, *7*, 11308.

[43] (a) Iglesias, M.; Iturmendi, A.; Sanz Miguel, P. J.; Polo, V.; Pérez-Torrente, J. J.; Oro, L. A. Tuning PCP–Ir complexes: the impact of an N-heterocyclic olefin. *Chem. Commun.* **2015**, *51*, 12431–12434. (b) Iturmendi, A.; García, N.; Jaseer, E. A.; Munárriz, J.; Sanz Miguel, P. J.; Polo, V.; Iglesias, M.; Oro, L. A. N-Heterocyclic olefins as ancillary ligands in catalysis: a study of their behaviour in transfer hydrogenation reactions. *Dalton Trans.* **2016**, *45*, 12835–12845.

[44] Fellay, C.; Yan, N.; Dyson, P. J.; Laurenczy, G. Selective Formic Acid Decomposition for High-Pressure Hydrogen Generation: A Mechanistic Study. *Chem. Eur. J.* **2009**, *15*, 3752–3760.

[45] (a) Boddien, A.; Mellmann, D.; Gärtner, F.; Jackstell, R.; Junge, H.; Dyson, P. J.; Laurenczy, G.; Ludwig, R.; Beller, M. Efficient Dehydrogenation of Formic Acid Using an Iron Catalyst. *Science* **2011**, *333*, 1733–1736. (b) Yang, X. Mechanistic insights into iron catalyzed dehydrogenation of formic acid: b-hydride elimination vs. direct hydride transfer. *Dalton Trans.* **2013**, *42*, 11987–11991. (c) Zell, T.; Butschke, B.; Ben-David, Y.; Milstein, D. Efficient Hydrogen Liberation from Formic Acid Catalyzed by a Well-Defined Iron Pincer Complex under Mild Conditions. *Chem. Eur. J.* **2013**, *19*, 8068–8072.

[46] Jongbloed, L. S.; de Bruin, B.; Reek, J. N. H.; Lutz, M.; van der Vlugt, J. I. Reversible cyclometalation at Rh^I as a motif for metal–ligand bifunctional bond activation and base-free formic acid dehydrogenation. *Catal. Sci. Technol.* **2016**, *6*, 1320–1327.

[47] (a) Fukuzumi, S.; Kobayashi, T.; Suenobu, T. Unusually Large Tunneling Effect on Highly Efficient Generation of Hydrogen and Hydrogen Isotopes in pH-Selective Decomposition of Formic Acid Catalyzed by a Heterodinuclear Iridium-Ruthenium Complex in Water. *J. Am.*

Chem. Soc. **2010**, *132*, 1496–1497. (b) Fernández-Álvarez, F. J.; Iglesias, M.; Oro, L. A.; Polo, V. CO*2* Activation and Catalysis by Iridium Complexes. *ChemCatChem* **2013**, *5*, 3481–3494. (c) Li, J.; Li, J.; Zhang, D.; Liu, C. DFT Study on the Mechanism of Formic Acid Decomposition by a Well-Defined Bifunctional Cyclometalated Iridium(III) Catalyst: Self-Assisted Concerted Dehydrogenation via Long-Range Intermolecular Hydrogen Migration. *ACS Catal.* **2016**, *6*, 4746–4754.

[48] Iglesias, M.; Oro, L. A. Mechanistic Considerations on Homogeneously Catalyzed Formic Acid Dehydrogenation. *Eur. J. Inorg. Chem.* **2018**, 2125–2138.

[49] For examples see: (a) Abura, T.; Ogo, S.; Watanabe, Y.; Fukuzumi, S. Isolation and Crystal Structure of a Water-Soluble Iridium Hydride: A Robust and Highly Active Catalyst for Acid-Catalyzed Transfer Hydrogenations of Carbonyl Compounds in Acidic Media. *J. Am. Chem. Soc.* **2003**, *125*, 4149–4154. (b) Boddien, A.; Loges, B.; Gärtner, F.; Torbog, C.; Fumini, K.; Junge, H.; Ludwig, R.; Beller, M. Iron-Catalyzed Hydrogen Production from Formic Acid. *J. Am. Chem. Soc.* **2010**, *132*, 8924–8934. (c) Matsunami, A.; Kayaki, Y.; Ikariya, T. Enhanced Hydrogen Generation from Formic Acid by Half-Sandwich Iridium(III) Complexes with Metal/NH Bifunctionality: A Pronounced Switch from Transfer Hydrogenation. *Chem. Eur. J.* **2015**, *21*, 13513–13517.

[50] Ruelle, P.; Kesselring, U. W.; Nam-Tam, H. Ab initio quantum-chemical study of the unimolecular pyrolysis mechanisms of formic acid. *J. Am. Chem. Soc.* **1986**, *108*, 371–375.

[51] (a) Leung, K.; Rempe, S. B. Ab Initio Molecular Dynamics Study of Formate Ion Hydration. *J. Am. Chem. Soc.* **2004**, *126*, 344–351. (b) Dyson, P. J.; Jessop, P. G. Solvent effects in catalysis: rational improvements of catalysts via manipulation of solvent interactions. *Catal. Sci. Technol.* **2016**, *6*, 3302–3316.

[52] (a) Ghosh, A. K.; Brindisi, M. Organic Carbamates in Drug Design and Medicinal Chemistry. *J. Med. Chem.* **2015**, *58*, 2895–2940. (b) Darvesh, S.; Darvesh, K. V.; McDonald, R. S.; Mataija, D.; Walsh, R.; Mothana, S.; Lockridge, O.; Martin, E. Carbamates with Differential Mechanism of Inhibition Toward Acetylcholinesterase and Butyrylcholinesterase. *J. Med. Chem.* **2008**, *51*, 4200–4212.

[53] Merzouk, A.; Guibé, F.; Loffet, A. On the use of silylated nucleophiles in the palladium catalysed deprotection of allylic carboxylates and carbamates. *Tetrahedron Lett.* **1992**, *33*, 477–480.

[54] (a) Unger, T. A. *Pesticides Synthesis Book*; Noyes Publications: New Jersey, 1996. (b) Babad, H.; Zeiler, A. G. Chemistry of phosgene *Chem Rev.* **1973**, *73*, 75–91. (c) Eckert, H.; Forster, B. Triphosgene, a Crystalline Phosgene Substitute. *Angew. Chem. Int. Ed. Engl.* **1987**, *26*, 894–895. (d) Rahmathullah, S. M.; Hall, J. E.; Bender, B. C.; McCurdy, D. R.; Tidwell, R. R.; Boykin, D. W. Prodrugs for Amidines: Synthesis and Anti-Pneumocystis carinii Activity of Carbamates of 2,5-Bis(4-amidinophenyl)furan. *J. Med. Chem.* **1999**, *42*, 3994–4000.

[55] Scriven, E. F. V.; Turnbull, K. Azides: their preparation and synthetic uses. *Chem. Rev.* **1988**, *88*, 297–368.

[56] Raspoet, G.; Nguyen, M. T.; McGarraghy, M.; Hegarty, A. F. The Alcoholysis Reaction of Isocyanates Giving Urethanes: Evidence for a Multimolecular Mechanism, *J. Org. Chem.* **1998**, *63*, 6878–6885.

[57] Salvatore, R. N.; Ladger, J. A.; Jung, K. W. An efficient one-pot synthesis of N-alkyl carbamates from primary amines using Cs_2CO_3. *Tetrahedron Lett.* **2001**, *42*, 6023–6025.

[58] (a) Alba, M.; Choi, J. C.; Sakakura, T. Nickel-catalyzed dehydrative transformation of CO2 to urethanes. *Green Chem.* **2004**, *6*, 524–525. (b) Peterson, S. L.; Stucka, S. M.; Dinsmore, C. J. Parallel Synthesis of Ureas and Carbamates from Amines and CO2 under Mild Conditions. *Org. Lett.* **2010**, *12*, 1340–1343.

[59] Shi, F.; Deng, Y. First gold(I) complex-catalyzed oxidative carbonylation of amines for the syntheses of carbamates. *Chem. Commun.* **2001**, *0*, 443–444.

[60] Guan, Z. –H.; Lei, H.; Chen, M. Ren, Z. –H.; Bai, Y.; Wanga, Y. –Y. Palladium-Catalyzed Carbonylation of Amines: Switchable Approaches to Carbamates and N,N′-Disubstituted Ureas. *Adv. Synth. Catal.* **2012**, *354*, 489–496.

[61] (a) Liu, B.; Hu, F.; Shi, B. –F. Recent Advances on Ester Synthesis via Transition-Metal Catalyzed C–H Functionalization. *ACS Catal.* **2015**, *5*, 1863–1881. (b) Iturmendi, A.; Sanz Miguel, P. J.; Popoola, S. A.; Al-Saadi, A. A.; Iglesias, M.; Oro, L. A. Dimethylphosphinate bridged binuclear Rh(I) catalysts for the alkoxycarbonylation of aromatic C–H bonds. *Dalton Trans.* **2016**, *45*, 16955–16965.

[62] For examples see: (a) Quiñones, N.; Seoane, A.; García-Fandiño, R.; Mascareñas, J. L.; Gulías, M. Rhodium(III)-catalyzed intramolecular annulations involving amide-directed C–H activations: synthetic scope and mechanistic studies. *Chem. Sci.* **2013**, *4*, 2874–2879. (b) Davies, D. L.; Ellul, C. E.; Macgregor, S. A.; McMullin, C. L. Experimental and DFT Studies Explain Solvent Control of C–H Activation and Product Selectivity in the Rh(III)-Catalyzed Formation of Neutral and Cationic Heterocycles. *J. Am. Chem. Soc.* **2015**, *137*, 9659–9669. (c) Funes-Ardoiz, I.; Maseras, F. Cooperative Reductive Elimination: The Missing Piece in the Oxidative-Coupling Mechanistic Puzzle. *Angew. Chem. Int. Ed.* **2016**, *55*, 2764–2767. (d) Wang, N.; Li, B.; Song, H.; Xu, S.; Wang, B. Investigation and Comparison of the Mechanistic Steps in the $[(Cp^*MCl_2)_2]$ ($Cp^*=C_5Me_5$; M=Rh, Ir)-Catalyzed Oxidative Annulation of Isoquinolones with Alkynes. *Chem. – Eur. J.* **2013**, *19*, 358–364.

[63] Liu, B.; Hu, F.; Shi, B. –F. Recent Advances on Ester Synthesis via Transition-Metal Catalyzed C–H Functionalization. *ACS Catal.* **2015**, *5*, 1863–1881.

[64] Guan, Z. –H.; Ren, Z. –H.; Spinella, S. M.; Yu, S.; Liang, Y. –M.; Zhang, X. Rhodium-Catalyzed Direct Oxidative Carbonylation of Aromatic C−H Bond with CO and Alcohols. *J. Am. Chem. Soc.* **2009**, *131*, 729–733.

[65] Lang, R.; Wu, J. L.; Shi, L. J.; Xia, C. G.; Li, F. W. Regioselective Rh-catalyzed direct carbonylation of indoles to synthesize indole-3-carboxylates. *Chem. Commun.* **2011**, *47*, 12553–12555.

Chapter 2:

HETEROGENEOUS CATALYSIS

A. Oxygen Reduction and Evolution Reactions

A.1 Introduction and objectives

The advanced fossil fuels depletion, in conjunction with the need for reducing the environmental pollution and constructing a geopolitically stable economy, has resulted in great efforts to develop new clean and sustainable energy technologies.[1] Given this situation, oxygen electrocatalysis, *i. e.* Oxygen Reduction Reaction (ORR, eqs. 2.1 and 2.2, depending on whether water or hydrogen peroxide is obtained) and Oxygen Evolution Reaction (OER, eq. 2.3), plays a key role in renewable fuels development.[2,3] In particular, these reactions are essential in a variety of relevant processes, such as water electrolysis,[4] direct solar water splitting[5] and fuel cells.[6-9] Among the last, bifunctional ORR/OER metal-air batteries are of particular interest. Within this kind of devices, oxygen molecules are produced during discharge (ORR), while the reverse process takes place upon charge (OER), see Scheme 2A.1.[6,10]

$$O_2 + 4e^- + 4H^+ \rightleftharpoons 2H_2O \quad (2.1)$$

$$O_2 + 2e^- + 2H^+ \rightleftharpoons H_2O_2 \quad (2.2)$$

$$2H_2O \rightleftharpoons O_2 + 4H^+ + 4e^- \quad (2.3)$$

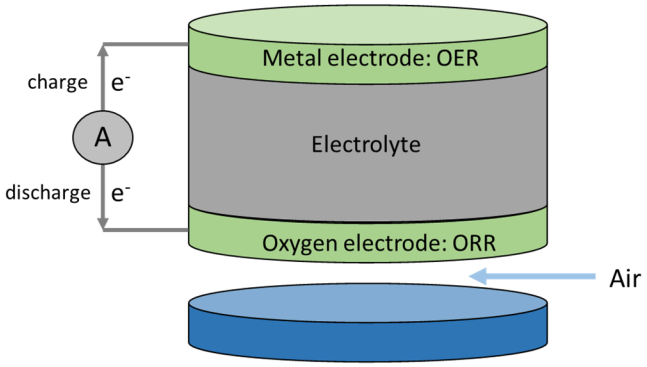

Scheme 2A.1. Schematic representation of a metal-air battery based on a bifunctional ORR/OER electrode.

Nonetheless, the kinetics of both processes is inherently sluggish, and very active catalysts based on noble metals (such as Ir and Pt) are generally required.[11,12] Fortunately, over the last years, different perovskite-based catalysts have proven to be highly efficient for both, OER and ORR, reaching activities that are, in some cases, superior to those obtained with noble catalysts.[13]

Perovskites are mixed metal oxides of general formula ABO_3, where A and B are the largest and smallest metal cations, respectively. Cation A is usually a lanthanide, alkaline or alkaline–earth element, while B is a transition metal with partially occupied *d* orbitals.[14] The general structure of a perovskite is shown in Figure 2A.1. As depicted in the figure, cation B is 6-fold coordinated by oxygen atoms, being in an octahedral environment; whereas A is 12-fold coordinated. One of the main features of these materials is the easiness to produce structural changes by means of cation substitution and introduction of both, oxygen and cation vacancies. This allows for the modulation of physical and chemical properties, such as the catalytic activity.[15,16] In addition to their rich variety of properties, perovskite-based catalysts constitute a promising alternative for energy technologies due to their high abundance on Earth, economic price and environmental friendliness.[4]

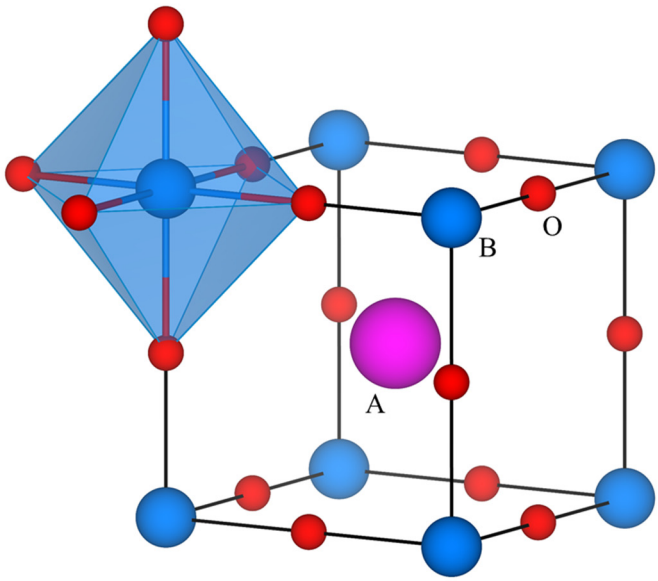

Figure 2A.1. Schematic representation of the structure of an ABO_3 perovskite. Octahedral coordination of cation B is highlighted in blue.

As previously stated, different materials designed on the basis of perovskite structures have proven to be very active for both, OER and ORR, reaching activities that are comparable or even superior to those of "gold standard" noble metal oxides, such as RuO_2 and IrO_2.[13] Due to these promising properties, several studies have been performed with the aim of identifying reactivity descriptors able to guide the design

of novel and more active materials.[17] Nonetheless, studies that take into account the influence of the magnetic state of the catalysts are scarce.[18-20] This lack of information prompted us to in-depth investigate the effect of magnetism and orbital interactions on OER and ORR, as well as their potential use for deriving physically meaningful descriptors for the catalytic activity. For the sake of clarity, the most frequent magnetic orderings that perovskites present are shown in Figure 2A.2. In particular, collinear magnetic structures are generally either ferromagnetic (FM), when all magnetic atoms have their spins aligned in a parallel way, or antiferromagnetic (AFM), when there are the same number of atoms with spins up and down. Notice that AFM structures can present different relative spin orientations: AFM-A, AFM-C and AFM-G, as depicted in Figure 2A.2.[21]

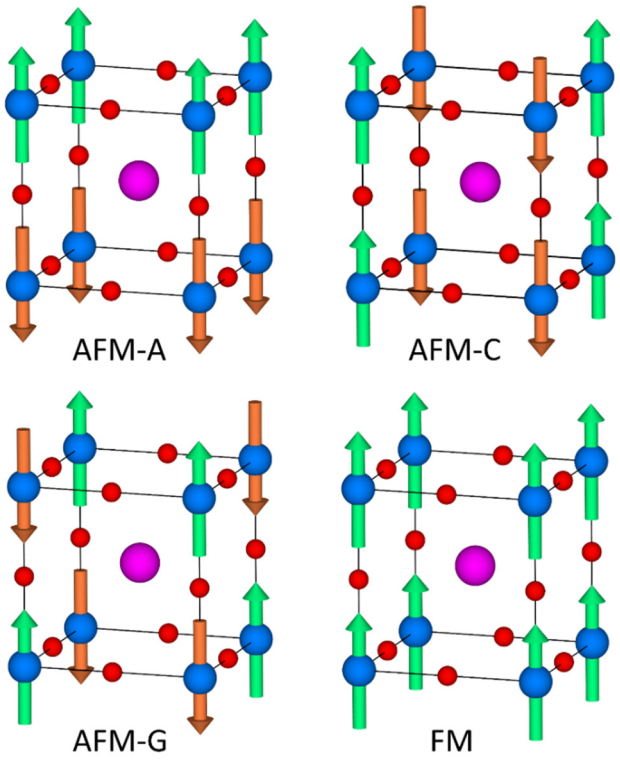

Figure 2A.2. More frequent AFM (A-, C-, and G-type) and FM spin orderings in perovskite-based structures. Arrows indicate the relative orientation of spin angular momenta in magnetic B-cations. Spin up is depicted in green and down in orange.

The different results and its discussion corresponding to this part of the Doctoral Thesis are organized in three subsections. In the first one (section A.2), the effect of magnetic entropy and orbital interactions in the catalytic performance of the most active $LaMnO_3$-based catalysts for ORR reactions is investiagted. In the second (A.3), general rules for the rational design of oxide-based catalysts for OER and ORR are derived from the results obtained from the previous study, as well as from others reported our research group.[18-20] Finally, in the third section (A.4), a working example

of the application of the previous rules is provided. Specifically, the main aims of the performed studies are:

(i) Unravel the effect of orbital interactions and magnetic entropy in $LaMnO_3$-based catalysts for ORR.
(ii) Determine the nature of magnetic interactions stablished between the reagents (O_2) and the catalysts surface.
(iii) Apply the previous information to propose physically meaningful activity descriptors.
(iv) Extend the previous principles to OER reactions and propose a set of rules for enhancing the catalytic activity of perovskite-, and, in general, magnetic oxide-based materials.
(v) Apply these rules to the rational design of more efficient catalysts.

A.2 Analysis of the Magnetic Entropy in Oxygen Reduction Reaction

As previously stated, perovskite manganites relative to $LaMnO_3$ have been reported to present high ORR activities. Among them, compositions with stoichiometry $La_{1-x}Sr_xMnO_3$ perform particularly well.[22] These promising results prompted us to investigate the effect of magnetism on this kind of materials. The different catalysts under study, as well as their relative activities and other relevant characteristics, are shown in Table 2A.1. Notice that the activity of the parent compound, $LaMnO_3$, was taken as a reference.

Table 2A.1. Relative catalytic activity, conductivity and Curie temperature of the $LaMnO_3$-based catalysts studied. The energy difference between FM and AFM magnetic phases have been obtained by means of DFT calculations (see the Methodology chapter). The appropriate references for conductivities and T_C are provided in the text.

Material	Relative Specific Activity			Conductivity	T_C	ΔE_{FM-AFM}
	Ref.[21a]	Ref.[23]	Ref.[13d]	($S \cdot cm^{-1}$)	(K)	(meV/f.u.)
$LaMnO_3$	***1.00***	***1.00***	***1.00****	10^{-5} - 10^{-6}	140	-10
$LaMnO_{3+\delta}$			100.0*	10^{-2} - 10^{-3}	200-260	62
$La_{0.67}Sr_{0.33}MnO_3$	2.10-2.20			10^3	370-380	167
$La_{0.8}Sr_{0.2}MnO_3$	0.90-1.00			10^0 - 10^1	300	91
$La_{0.5}Sr_{0.5}MnO_3$	1.10-1.20			10^0	270	25
$La_{0.6}Ca_{0.4}MnO_3$		0.70-0.80		10^0 - 10^1	270	60
$La_{0.5}Ca_{0.5}MnO_3$			25.4*	10^0 - 10^1	225	29

* Catalyst area was estimated by means of STM measurements.

A.2.1 Magnetic structure analysis

A comprehensive study of the magnetic structure of each compound was carried out. The energy difference between the most stable FM and AFM magnetic couplings is shown in Table 2A.1. Notice that negative values indicate that the magnetic ground state is AFM, while positive ones correspond to FM ground states.

Stoichiometric $LaMnO_3$ was the least active catalyst. However, it presents a moderate activity in absolute terms, despite its reduced bulk conductivity.[24] Remarkably, according to theoretical calculations, this is the only material whose magnetic ground state is AFM, with a band gap of 1.0 eV; in agreement with experimentally reported results (see Figure 2A.3a and b).[25] However, the FM phase is only 10 meV less stable per formula unit (f.u.). This result points towards the possibility of introducing electronic changes by means of stoichiometric changes in the structure.

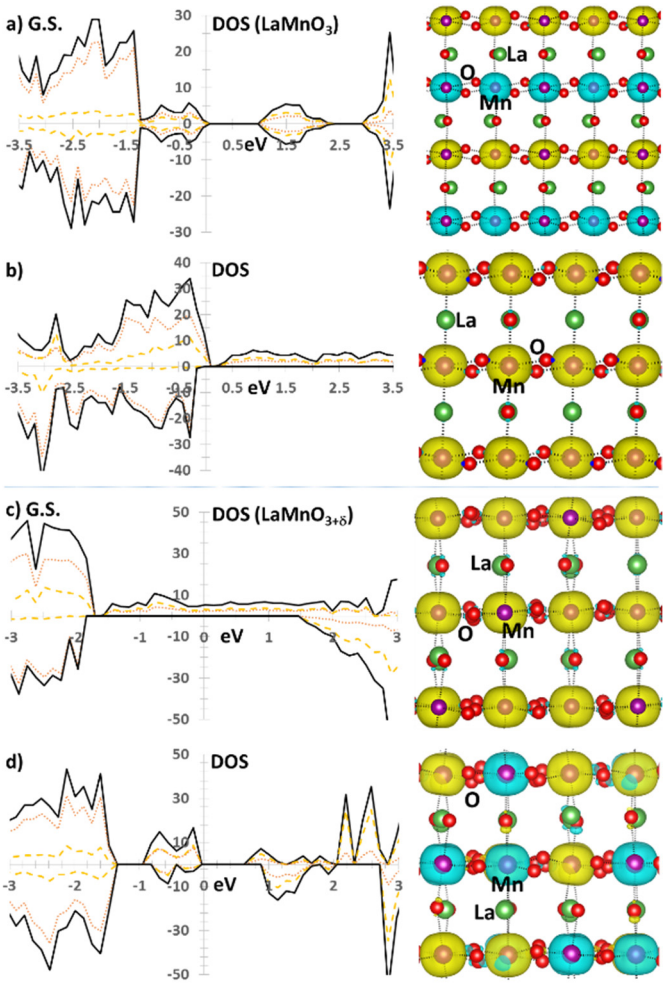

Figure 2A.3. Right: spin density (yellow: up, blue: down) and left: Total DOS (solid), and DOS projected over O (dotted) and Mn (dashed) for a) $LaMnO_3$ (AFM-A ground state), b) $LaMnO_3$ (FM), c) $LaMnO_{3.27}$ (FM ground state) and d) $LaMnO_{3.27}$ (lowest-in-energy AFM ordering).

In this regard, $LaMnO_{3+\delta}$ was analysed in order to evaluate the effect of Mn and La vacancies on the magnetic structure. In particular, a supercell with $La_{11}Mn_{11}O_{36}$ ($LaMnO_{3.27}$) composition was considered. As expected, the structure variation resulted in a change in the most stable magnetic ordering. Specifically, a half-metal FM ground state, 62 meV/f.u. more stable than the closest-in-energy AFM structure was obtained (see Table 2A.1 and Figure 2A.3c and d). Remarkably, the electric conductivity of $LaMnO_{3.27}$ is three orders of magnitude superior to that of stoichiometric $LaMnO_3$; this property being in line with the higher catalytic activity of $LaMnO_{3+\delta}$.[26] This material has been reported to be an outstanding ORR catalyst, with an activity about 100 times that of $LaMnO_3$. Nonetheless, we believe that the relative performance is overestimated as a consequence of the non-comparable estimation of the surface area (calculated on the basis of STM images).

With respect to alkaline-earth-doped catalysts of stoichiometries $La_{1-x}A_xMnO_3$, the most active materials correspond to compositions with x close to 0.33, which also present high conductivities.[27] Interestingly, the most active catalyst, $La_{0.67}Sr_{0.33}MnO_3$ (LSMO), is also the one that presents the highest conductivity and Curie temperature.[28] Moreover, it has a half-metal FM ground state (see Figure 2A.4) with the highest difference between FM and AFM phases. This result points out the influence of magnetism on the catalytic performance, pointing towards FM catalysts are especially active.[18] Notice that FM orientations involve minimum spin magnetic entropy since spin ordering is maximum, as all spins are orientated in the same direction.

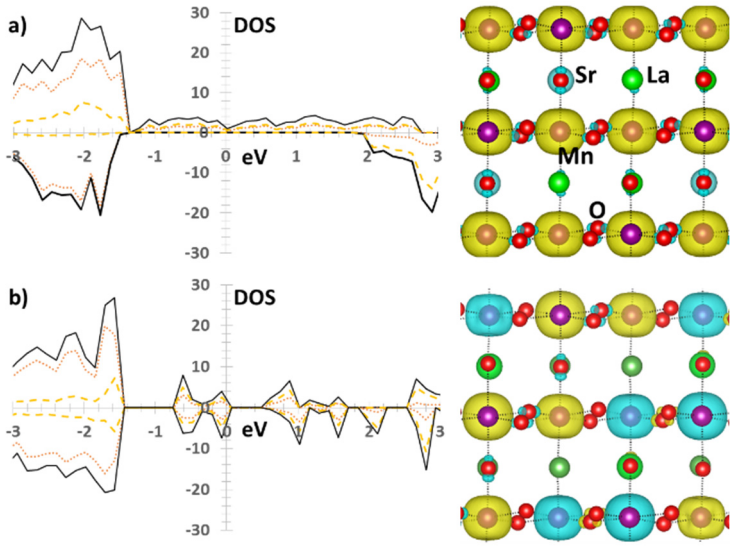

Figure 2A.4. Right: spin density (yellow: up, blue: down) and left: Total DOS (solid), and DOS projected over O (dotted) and Mn (dashed) for LSMO: a) FM ground state, b) lowest-in-energy AFM phase.

In order to obtain a further understanding of the nature of the interactions between the catalysts and the reagents, we computed the adsorption energy of the triplet O_2 molecule on the (001) surface of the most active material, *i. e.* LSMO (see Figure 2A.4 a).[29] Interestingly, O_2 shows preferential adsorption in an AFM manner, that is, it presents spins in the opposite orientation than those in the FM catalyst. In particular, O_2 adsorption in an AFM orientation is 0.4 eV (9.2 kcal·mol^{-1}) more favorable than FM one. This feature has a positive effect on the catalyst performance, since the electrons that are to be transferred from the catalyst surface to π* semi-occupied orbitals of the triplet state O_2 have already the correct orientation. Then, there is no need for the quantum mechanically forbidden spin flipping to match Pauli Exclusion Principle (see Figure 2A.5a).

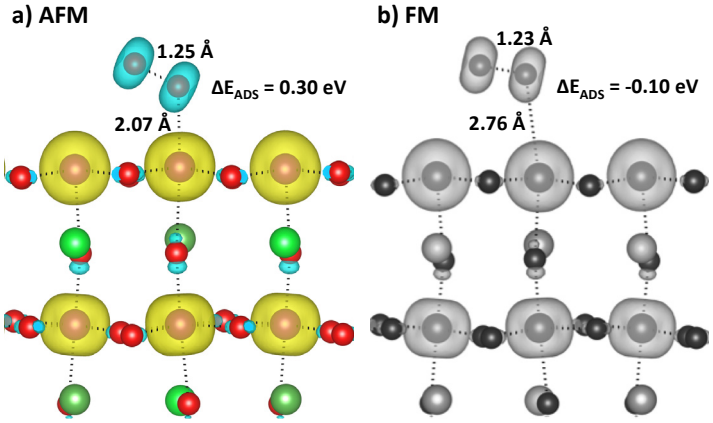

Figure 2A.4. Spin density of O_2 molecule adsorbed on the (001) surface of LSMO: a) AFM relative orientation (yellow: spin up, blue: spin down); b) FM relative orientation. Adsorption energies are defined as the energy difference between the desorbed and the adsorbed products. Hence, positive values correspond to favourable adsorption processes.

A.2.2 Magnetic effects on reaction rates

The initial step of ORR formally involves the transference of an electron from the catalyst to the triplet state of O_2. As previously stated, this electron must have the opposite spin orientation to electrons in O_2, in order to follow the Pauli Exclusion Principle. With the aim of evaluating the rate coefficient of this kind of electron-transfer reactions, we applied eq. 2.4. This approach is similar to others developed by Gerischer[30] and Marcus.[31] In particular, we defined the term E_{BG}^{e-} as the energy required to place an electron with the appropriate spin orientation to be transferred to the O_2 molecule from the catalyst valence band to the conduction band. ΔS_{TS}^{e-} accounts for the electronic entropic variation and E_a' for all the other energy terms that have an influence on the activation energy. Pre-exponential factors are included in k_{st}.

$$K(T) = k_{st} \cdot e^{\frac{-E_a'}{k_B T}} \cdot e^{\frac{-E_{BG}^{e-}}{k_B T}} \cdot e^{\frac{\Delta S_{TS}^{e-}}{k_B}} \qquad (2.4)$$

We will first focus on ΔS_{TS}^{e-}, that is, the entropic variation of transferring an electron from the catalyst to the O_2 molecule. If one compares different ORR catalysts, the reaction pathways that correspond to electron-transfer will have roughly the same translational, rotational and vibrational entropic changes. Thus, the distinctive parameter will be the electronic entropy.

ΔS_{TS}^{e-} can be estimated from the accessible spin states through a Boltzmann distribution: $S_{TS}^{e-} = k_B \ln(g^{e-})$, where g^{e-} is the electronic partition function.[32] The value of g^{e-} depends on the spin degeneracy, that is, the number of equivalent configurations available: the more degenerated a system is, the more spin entropy it has. The spin degeneracy in the transition state equals 1, since the electron has to be transferred in a specific orientation antiparallel to spins in O_2 so as to match Pauli Principle, existing only one possibility. On the contrary, higher degeneracy values can be observed depending on the nature of the catalyst. In particular, in a FM catalyst with long range spin ordering, all spins will have the same orientation. On the contrary, paramagnetic materials (PM) present atoms with spins completely disordered with respect to each other, and thus the system will be largely degenerated ($g^{e-} \gg 1$). Consequently, ΔS_{TS}^{e-} will be roughly 0 for FM materials and significantly negative for PM ones, since much spin disorder is lost (see Figure 2A.5). AFM materials will have negative ΔS_{TS}^{e-} values, between those of FM and PM materials.

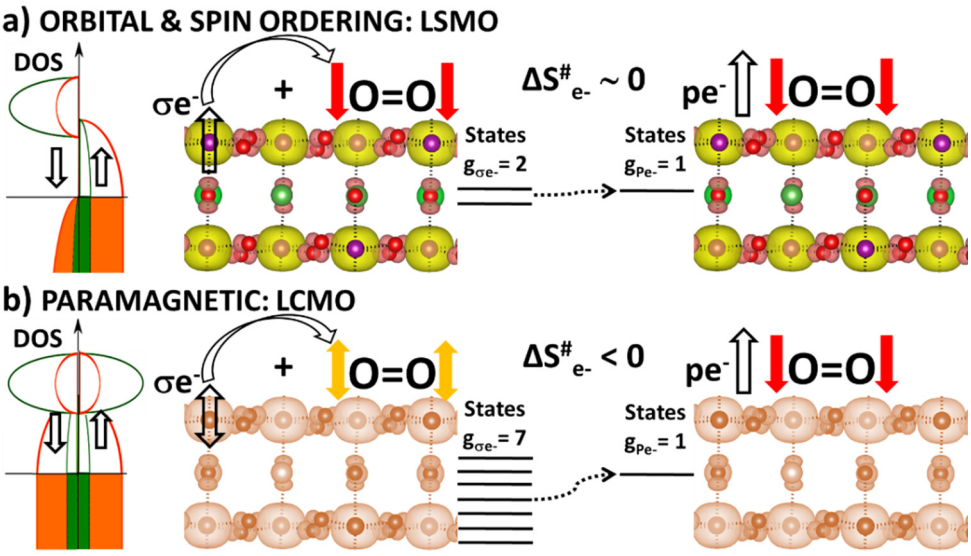

Figure 2A.5. Scheme of the electronic entropy variations of the first electron-transfer step in ORR for LSMO: a) FM; b) PM.

Then, FM materials undergo minimum electronic entropic losses, thus favoring electron-transfer catalytic reactions, as derived from eq. 2.4. This result supports the better performance of FM materials towards ORR. This approach to

ΔS_{TS}^{e-} is only partial, since other effects, such as changes in spin-orbit configurations, are not included. However, it highlights the influence of orbital effects and electronic configuration in heterogeneous catalysis. For those materials at the top of the volcano plots, electronic entropy variation is likely to constitute a discerning descriptor.

Another factor that can affect the catalytic performance according to eq. 2.4 is E_{BG}^{e-}, that is, the energy required to place the electron that is to be transferred in the catalyst conducting band. In this regard, catalysts with a FM ground state present enhanced electron mobility and thus, a reduced band gap. This translates into lower E_{BG}^{e-} and therefore higher reaction rates. This factor explains why, in general, catalysts with high electron conductivity and reduced bang gap are usually associated with good catalytic activities (see Table 2A.1).[18]

On balance, these results remark the importance of considering the catalyst magnetic state and other derived properties, such as spin entropy and transport, in the rational design of novel materials for electron-transfer processes. In the next section, a set of guidelines for the design of efficient magnetic oxides for ORR and OER on the basis of magnetic principles is provided.

A.3 Activity of magnetic oxides towards ORR and OER

As explained in the previous section, the understanding of the catalytic properties of magnetic metal oxides (MMOs), such as perovskites, can only be complete if magnetic properties are taken into account.[18-20,33-35] Within these materials, quantum exchange interactions (QEI) involving metals with 3*d* or 4*f* orbitals are typically relevant, and determine the characteristics of valence and conduction bands, which may have a relevant influence in their catalytic performance.[36] In particular, some FM oxides have proven to be very active catalysts for OER and ORR, such as $A_{1-x}A'_xCo_{1-y}Fe_yO_{3-\delta}$ and $Sm_{1-x}A'_xFe_{1-y}B'_yO_{3-\delta}$ compositions, respectively.[13]

In MMOs, QEI modulate the charge transfer, higher conductivities being observed in FM orderings. On the contrary, spin mobility in AFM phases is more hindered.[25a] This behaviour can be explained by a Heisenberg model Hamiltonian for the magnetic interaction between electrons in the valence band of the catalyst ($\widehat{s_{cat}}$) and the one that has to be promoted to the conduction band during the electron transference to the reagent ($\widehat{s_{e^-}}$) (see eq. 2.5). Δ_{mag} is defined as the magnetic interaction, and J_{exc} is the magnetic coupling. J_{exc} takes a positive value for FM systems and a negative one for AFM compositions. FM systems have $\Delta_{mag} < 0$, indicating that FM exchange interactions reduce electron-electron repulsions (Coulomb integrals), thus favouring charge mobility.[18,37] As a result, electron

transition to the O_2 molecules is easier, and FM catalysts are especially active for ORR and OER.

$$\Delta_{mag} = -J_{exc} \cdot (\widehat{s_{cat}} \cdot \widehat{s_{e^-}}) \quad (2.5)$$

On the basis of the previous principles, a set of rules for predicting and ranging catalytic activity in MMOs (with special focus on perovskites) are provided below.

Rule 1. *"The spin angular momentum is conserved during all the steps of the electron transfer processes."*

Description. In general, the transition probability of an electron from a catalytic interface to the reagents depends on the overlapping between the wavefunctions of the initial and final states. In particular, the electron has to be transferred from the valence to the conduction band and from the latter to the reagent (semi-occupied π^* orbitals of the O_2 molecule) in ORR, and *vice versa* in OER (see eqs. 2.6 and 2.7).

$$P_{val \leftrightarrow cond} \propto |\langle \Phi_{val} | \Phi_{cond} \rangle \cdot \langle \chi_{val} | \chi_{cond} \rangle|^2 \quad (2.6)$$

$$P_{cond \leftrightarrow reac} \propto |\langle \Phi_{cond} | \Phi_{reac} \rangle \cdot \langle \chi_{cond} | \chi_{reac} \rangle|^2 \quad (2.7)$$

Where Φ and χ correspond to the spatial and spin parts of the wavefunction, respectively. When there is a change in the spin of the transferred electron, $\langle \chi_{val} | \chi_{cond} \rangle$ and $\langle \chi_{cond} | \chi_{reac} \rangle$ are equal to zero, and, as a result, the transmission probability is close to zero. This analysis also explains why higher conductivity materials typically present enhanced catalytic activity.[26] High conductivity is indicative of high transition probability, as electrons can be easily promoted from the valence to the conduction band.

The Pauli Exclusion Principle imposes additional restrictions to electron transfer reactions, since two electrons with the same spin cannot occupy the same molecular orbital. As a result, spin conservation is necessary but not enough, since the transferred electron must have a spin angular momentum with an opposite orientation than those of the triplet state of the O_2 molecule (see Figure 2A.6). In this regard, in the previous section we reported that the most active $LaMnO_3$-based catalysts for ORR (*i. e.* LSMO) are FM but interactions with the triplet state of O_2 are AFM. As a result, the transferred electron has already the correct spin orientation to match that of the triple state of O_2 Thus, the catalytic activity is enhanced, as the electron transfer-process is faster. This way, FM materials behave as spin filters, selecting the electron that is transferred from the reagent to the catalyst or *vice versa* (see Figures 2A.4 and 2A.6).[38]

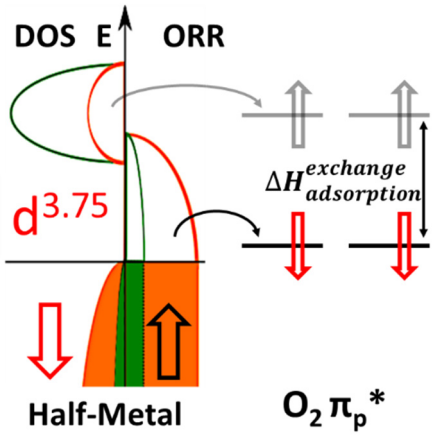

Figure 2A.6. Schematic representation of the electron-transfer process from the catalyst to triplet O_2 molecule.

Rule 2. *"The intra-atomic and inter-atomic exchange interactions in the covalent –B–O–B– framework in the most active catalysts are ferromagnetic."*

Description. Orbital interactions in FM conductors favour electron-spin mobility, as they reduce the value of Coulomb integrals. As a result, the band gap is small (zero in most cases). Thus, electron transference from the valence to the conducting band is very fast. Then, the limiting factor will be the charge transport between the catalyst conducting band and the reagents. This explains why maximum bulk electron conductivity does not always assure optimum catalytic activity: a given catalyst may have very high electron conductivity but not being able to couple with the reagents in the proper manner. The case of LSMO is also quite illustrative: LSMO is FM, hence, electron mobility within the catalyst will be very high. However, AFM catalyst–O_2 coupling is necessary for optimizing electron transfer from the catalyst to O_2. If the –B–O–B– framework is AFM, electron mobility within the catalyst will be limited, a band gap will probably open and electron transfer reactions will be slower.

Rule 3. *"In the active metal atoms on the surface of the catalyst, the d-orbitals oriented towards the reagents must be partially occupied."*

Description. The orbital interactions between the active metal atoms in the catalyst surface and the adsorbed species influence the electron transfer rate.[39] As previously explained, the magnetic interactions between two spin-electrons can be described by means of a Heisenberg Hamiltonian (see eq. 2.5). Magnetic interactions will be more favourable (more negative) when the spin in the metal centre, $\widehat{s_{cat}}$, is maximum, in conjunction with negative J_{exc} (FM systems). $\widehat{s_{cat}}$ will be maximum when the number of unpaired *d* electrons in the active metal centre is maximum, that is, when there is an intermediate number of *d* electrons (the *d*-shell is close to be half-

filled and the overall spin is maximum). Then, the number of *d* electrons can be used as a descriptor for the catalytic activity: compositions with an intermediate number of *d* electrons, will present higher activities. This descriptor can be represented in a Sabatier-like diagram.[40] Notice that we must take into account that the most active catalysts also present a FM ground state (see Figure 2A.7).

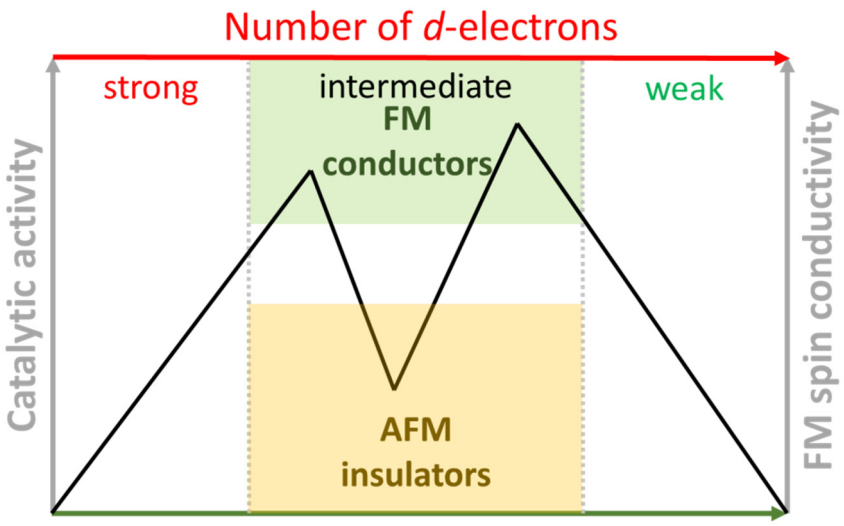

Figure 2A.7. Sabatier diagram for catalytic activity towards ORR and OER with respect to the number of d electrons.

Rule 4. *"The overall reduction of the Coulomb interactions can facilitate the entrance of itinerant charge carriers at working conditions. Defects at the interstitial sites (A) or cations with active 4f or 3d electrons help create active FM orderings."*

Description. The presence of cation vacancies, as well as interstitial cation substitution by metals with semi-occupied 3*d* or 4*f* orbitals enhances the system preference for FM orderings.

Recent studies have shown that the activation energy for electron-transfer processes on perovskite-based materials strongly depends on the magnetic interaction between the catalyst and the reagents.[18] In particular, the activation Gibbs energy can be defined as shown in eq. 2.8.

$$\Delta G^{\#} = \Delta G^{\#\prime} + \Delta_{mag} \tag{2.8}$$

Where $\Delta G^{\#}$ is the total activation energy and $\Delta G^{\#\prime}$ is the activation energy without considering magnetic effects. As a result, magnetic interactions between the catalyst and the reagent can be used to modulate the activation energy. This interaction, Δ_{mag}, will be more favourable (more negative) when the metal *d* orbitals are semi-occupied (higher $\widehat{s_{cat}}$) and the magnetic ordering is FM (J_{exc} is negative); as shown in eqs. 2.5 and 2.8. This finding is supported by the experimental studies of

Iwakura *et al.*, who showed that spinel ferrites diminished the required overvoltage for OER when magnetization increases.[41] Then, among the different descriptors for ORR and OER proposed in the literature, the occupancy of *d* orbitals constitutes a physically meaningful one,[19,36,42] as it is directly related to the origin of QEI and their effects on catalysis. These results also support the use of the Sabatier diagram shown in Figure 2A.7 for catalyst design. This rule will be further explained in the next section by means of a working example.

Rule 5. *"At the Transition State, the active metal centres formally receive or lose electron density. Nonetheless, good electro-catalysts retain the FM exchange ground state."*

Description. Some *p*- and *n*-type semiconductors undergo a large resistance increase when they are exposed to electron donors or acceptors, respectively.[43] On the basis of these results, we state that electron-transfer at the electrocatalyst surface should not alter the FM state so as not to reduce spin transfer facility.

Rule 6. *"The reaction mechanism adapts to the response of the electronic free energy of activation, $\Delta G^{\#}$, towards maximum entropic gains."*

Description. The activity of a given catalyst towards ORR and OER will depend on the value of the total Gibbs activation energy, that is, $\Delta G^{\#} = \Delta H^{\#} - T \cdot \Delta S^{\#}$. As a result, the most active catalysts have minimum $\Delta H^{\#}$ and maximum $\Delta S^{\#}$. $\Delta H^{\#}$ is mainly related to the energy cost of promoting an electron from the catalyst valence band to the conduction band and then to O_2 $\pi*$ orbitals for ORR; the opposite process taking place in OER. This way, $\Delta H^{\#}$ can be expressed as $\Delta H^{\#} = \Delta H^{\#}_{val \leftrightarrow cond} + \Delta H^{\#}_{cond \leftrightarrow reac}$. In optimum FM catalysts, $\Delta H^{\#}_{val \leftrightarrow cond}$ will be roughly zero due to enhanced spin mobility; the limiting factor being $\Delta H^{\#}_{cond \leftrightarrow reac}$. However, it is also necessary to consider the variation of electronic entropy, since it plays an important role in the total value of $\Delta G^{\#}$, as stated in the previous section. In this regard, Nahavavi and co-workers recently reported that electronic entropy maximization enhances the performance of water splitting reactions catalysed by ceria.[44]

In the following section, these principles will be applied to the design of novel perovskite-based catalysts for OER.

A.4 Catalyst design for OER

According to the previous section, the introduction of defects or A-cation substitution by atoms with active *d* or *f* orbitals in the interstitial A-sites in perovskite-based materials assists in the enhancement of FM delocalization, and thus in the increase of the catalytic activity.

Recently, A-defective, stable and non-toxic $La_{1-x}FeO_{3-\delta}$ perovskite-based catalysts have been reported to be as efficient for OER as the best mixed Cobalt-Iron perovskites and "gold standards".[22] In this section, a computational analysis of the effect of oxygen and La vacancies, as well as La substitution, on the magnetic properties and catalytic activity towards OER of $LaFeO_3$ is performed.

Interestingly, stoichiometric $LaFeO_3$ is an insulator with an AFM-G ground state (see Figure 2A.8). As a result, it shows the lowest activity of the $La_{1-x}FeO_{3-\delta}$ series. Similar behaviour is observed for $CaMnO_3$- and $LaMnO_3$-based catalysts: while stoichiometric $CaMnO_3$ and $LaMnO_3$, both with AFM ground states, are poor catalysts, the presence of oxygen vacancies and substitution of A-cations by others with semi-occupied *f* orbitals (such as Yb, $Ca_{0.9}Yb_{0.1}MnO_{3-\delta}$), enormously increases their catalytic activity.[45]

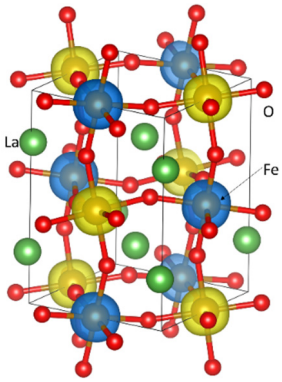

Figure 2A.8. Spin density of AFM-G ground state of stoichiometric $LaFeO_3$; yellow: up, blue: down.

In order to analyse how La^{3+} deficiencies affect the magnetic structure of these materials, we considered a super-cell of composition $La_{12}Fe_{12}O_{36}$ and created La vacancies (selecting in each case the most stable possibility). The inclusion of La vacancies progressively stabilizes the FM ordering with respect to the AFM one. In particular $La_{0.92}FeO_3$ ($La_{11}Fe_{12}O_{36}$) is still AFM-G. However, the energy difference between FM and AFM states significantly decreases with respect to stoichiometric $LaFeO_3$, from 251 to 101 meV/Fe. The same tendency is observed when the number of La vacancies increases until there is a change in the magnetic structure from AFM-G to FM, when going from $La_{0.83}FeO_3$ to $La_{0.75}FeO_3$ (see Figure 2A.9). This fact

involves an increase in the electron mobility, as shown by density of states (DOS) analysis: $La_{0.75}FeO_3$ is a half-metal material without band gap.

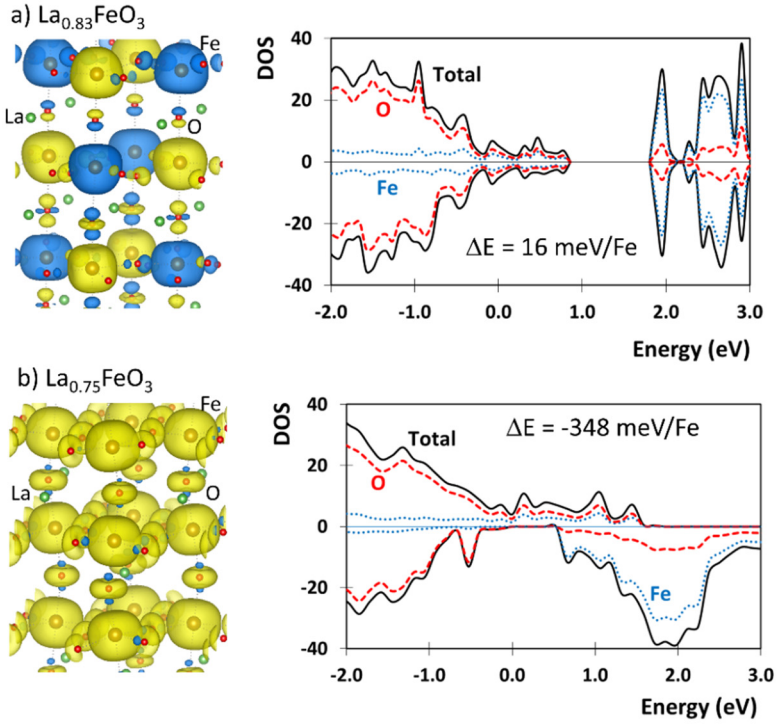

Figure 2A.9. Right: spin density (yellow: up, blue: down) and left: Total DOS (solid), and DOS projected over O (red dashed) and Fe (blue dotted) for a) $La_{0.83}FeO_3$ AFM-G ground state, b) $La_{0.75}FeO_3$ FM ground state. ΔE corresponds to energy difference between FM and AFM-G magnetic phases.

The same analysis was performed considering oxygen vacancies. For that, a $La_{12}Fe_{12}O_{34}$ ($LaFeO_{2.83}$) supercell was used. Noteworthy, the same behaviour was observed: starting with an AFM-G ground state, the FM phase becomes progressively more stable until it becomes the most stable one for a composition of $La_{0.58}FeO_{2.83}$. In Figure 2A.10, the last AFM composition ($La_{0.67}FeO_{2.83}$) and the first one with FM ground state ($La_{0.58}FeO_{2.83}$) are shown.

This study further supports the helpful effect of A-cation vacancies to create FM compositions with enhanced catalytic activity. Interestingly, in both cases, the FM active phase, $La_{0.75}FeO_3$ and $La_{0.58}FeO_{2.83}$, presents Fe atoms with a formal oxidation state very close to +4, +3.75 and +3.9, respectively. This finding is in agreement with the previous studies reported by Zhu and co-workers, in which they correlate catalytic activity in $LaFeO_3$-based materials with the presence of Fe^{4+}.[22]

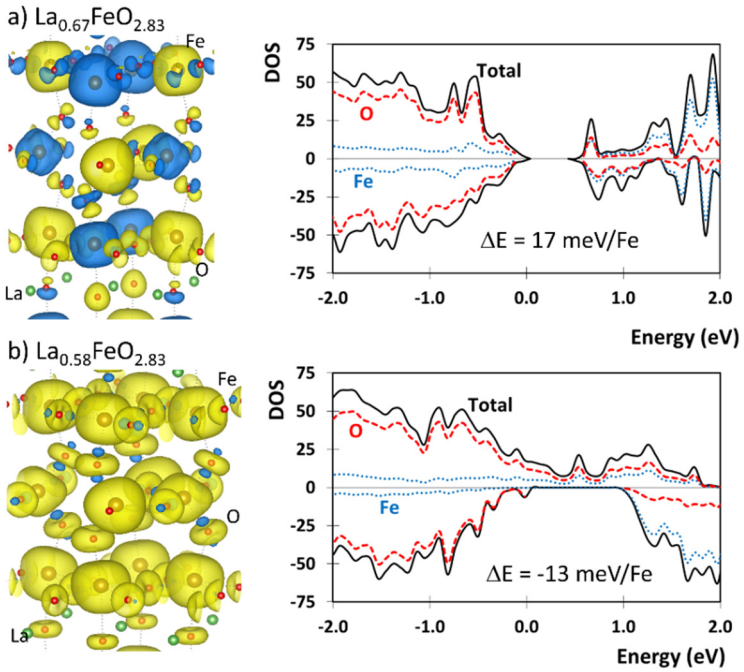

Figure 2A.10. Right: spin density (yellow: up, blue: down) and left: Total DOS (solid), and DOS projected over O (red dashed) and Fe (blue dotted) for a) $La_{0.67}FeO_{2.83}$ AFM-G ground state, b) $La_{0.58}FeO_{2.83}$ FM ground state. ΔE corresponds to energy difference between FM and AFM-G magnetic phases.

As stated in Rule 4, we should be able to improve the catalytic activity by substituting La^{3+} A-cations (without *d* nor *f* unpaired electrons) by others such as Nd^{3+} and Yb^{3+}, with active *f* orbitals. Specifically, La was substituted by Nd in the previous $LaFeO_3$-based perovskites. As expected, the substitution of La by Nd enhances the stability of the FM phase. In particular, the first magnetic transition from AFM-G to FM ground states takes place for $Nd_{0.83}FeO_3$ for the non-oxygen-vacant system, while the La-based perovskite required more La vacancies ($La_{0.75}FeO_3$). The same behaviour is observed for the systems with oxygen vacancies: the magnetic transition takes place for $Nd_{0.67}FeO_{2.83}$ composition, while the La-based system requires $La_{0.58}FeO_{2.83}$ (see Figure 2A.11). This way, we provide further evidence that doping materials with *f* and *d* A-cations help create FM compositions with enhanced catalytic performance.[42b,46] According to our calculations, $Nd_{1-x}FeO_{3-\delta}$ should be more active towards OER than $La_{1-x}FeO_{3-\delta}$. Similar magnetic phase transitions have been experimentally observed for $La_{0.88}MnO_{3-\delta}$ perovskites when changing the concentration of oxygen defects.[47] In addition, the substitution of A-cations by others with *f* or *d* active electrons has been reported to increase the catalytic activity of $La_{1-x}MnO_{3-\delta}$ catalysts.[41b] In future studies, we intend to test the effect of La substitution by Ru, since other ruthenates have been reported to have excellent catalytic activities while being highly stable under acidic conditions.[48]

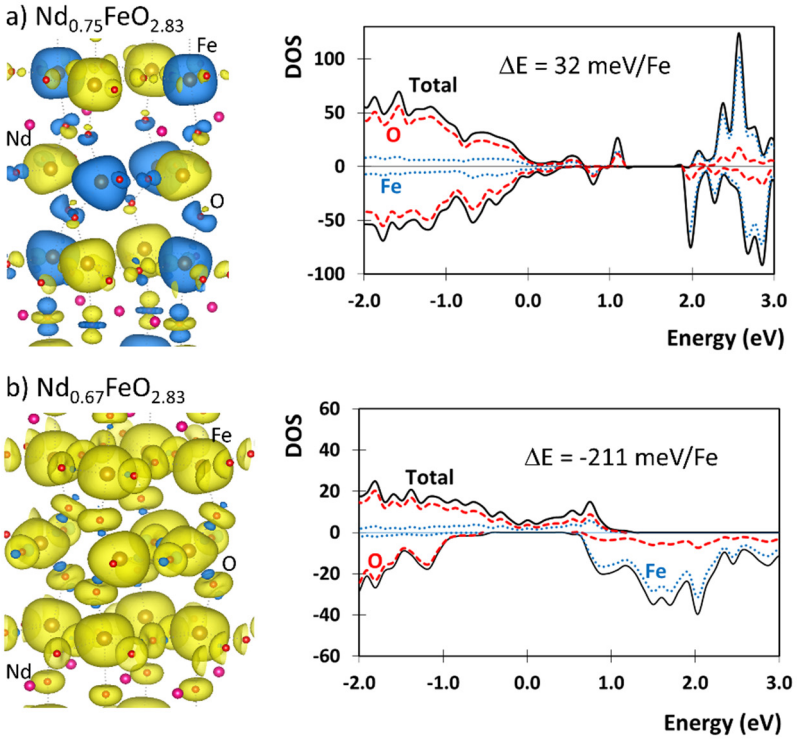

Figure 2A.11. Right: spin density (yellow: up, blue: down) and left: Total DOS (solid), and DOS projected over O (red dashed) and Fe (blue dotted) for a) $Nd_{0.75}FeO_{2.83}$ AFM-G ground state, b) $Nd_{0.67}FeO_{2.83}$ FM ground state. ΔE corresponds to energy difference between FM and AFM-G magnetic phases.

A.5 Summary

In this section of the Doctoral Thesis, the magnetic effects that may have an influence on catalytic performance of perovskites and, in general, magnetic metal oxides, towards OER and ORR have been studied. The main outcomes are presented below:

(a) The effect of magnetic structure of $LaMnO_3$-based materials on their catalytic activity towards ORR has been analysed. Results showed that FM catalysts generally have higher catalytic activity.

(b) The importance of spin entropy variations in ORR has been revealed. In particular, FM catalysts are associated with lower entropic losses when transferring the electrons from the surface catalyst to the O_2 molecule.

(c) The relative interaction with adsorbed O_2 molecules for the most active FM materials studied (LSMO) is AFM. This feature assists the electron

transference from the catalyst to O_2, since there is no need for spin flipping.

(d) A set of principles for determining the relative activity of MMOs towards OER and ORR is presented. In particular, FM compositions are proposed to be especially active.

(e) On the basis of the aforementioned principles, an analysis of the factors that may enhance $LaFeO_{3-\delta}$ performance towards OER was performed. In agreement with experimental available data, calculations showed that the presence of oxygen vacancies and the substitution of La cations by Nd (with active *f* electrons) enhance catalytic activity by favouring FM phases over AFM-G ones.

B. Nitrogen fixation

B.1 Introduction and objectives

As stated in the previous section, fossil fuels depletion in conjunction with the increasing concern for reducing greenhouse effect, has translated into a growing interest to develop new clean and sustainable energy processes.[1] Given this situation, the development of novel environmentally respectful routes for ammonia synthesis play a key role, since they open the door to the sustainable synthesis of fertilizers, plastics, explosives and nitric acid, and allow for the production of energy in ammonia-fed fuel cells.[49,50]

From an industrial point of view, ammonia is obtained almost exclusively *via* the reaction of N_2 with H_2 by means of the Haber-Bosch process. This methodology is very expensive, since it requires high temperatures and pressures (400-500 ºC and up to 170 bar), as well as very pure steams of hydrogen. As a result, the energy cost is very high, about 485 $kJ \cdot mol^{-1}$ overall. The chemical reaction takes place over iron or ruthenium-based heterogeneous catalysts.[51]

On the contrary, nitrogen fixation in nature is achieved under mild conditions *via* an enzymatic reaction catalysed by the so called nitrogenases. Among them, FeMo-nitrogenases have been reported to be the most active. These enzymes present two different subunits that work in tandem: an electron donating iron-protein and a catalytic molybdenum-iron-protein.[52] The energy cost of this process is much lower than that of industrial reactions, about 244 $kJ \cdot mol^{-1}$.[53] Consequently, great research efforts have been made on trying to mimic these "natural" reactions. This has resulted into very interesting advances, such as the synthesis of molybdenum,[54] and iron-based[55] complexes that present high activities towards N_2 fixation.

Important breakthroughs in ammonia synthesis have also been achieved thanks to heterogeneous catalysis.[56] Among them, photocatalytic reactions inspired by the photosynthesis have been remarkably successful.[57] Likewise, the ability of protons to act as a source of hydrogen in biological systems has inspired the electrochemical synthesis of ammonia using solid electrolyte cells. This methodology has the advantage of avoiding the direct use of H_2, obtained from natural gas.[58]

Another relevant approach involves the use of transition metal nitrides (V, Zr, Nb, Cr and Mo nitrides), which are promising heterogeneous electrocatalysts.[59,60] In this regard, ternary nitrides have been reported to present high catalytic performance, with activities following the order: $FeCo_2Mo_3N$ > $Co_3Mo_3N_{1-\delta}$ > $Fe_3Mo_3N_{1-\delta}$ > $Ni_2Mo_3N_{1-\delta}$.[61–64] Both, experimental results and DFT calculations, have shown that nitrogen vacancies of Co_3Mo_3N-derived materials can adsorb and activate the strong triple N–N bond in N_2.[65,66] As a result, some authors have proposed that nitrogen

fixation proceeds through a Mars–van Krevelen (MvK) mechanism, as suggested by experimental results[67] and calculations[68] (see Scheme 2B.1). However, the mechanism has not been fully characterised and the electronic structure of active-site Mo atoms has barely been explored.

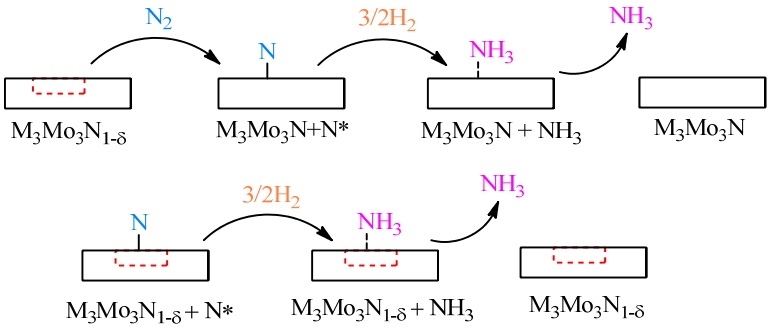

$M_3Mo_3N_{1-\delta} + N_2 \rightarrow M_3Mo_3N + N^*$;
$M_3Mo_3N + N^* + 3/2\ H_2 \rightarrow M_3Mo_3N + NH_3$;
$M_3Mo_3N \rightarrow M_3Mo_3N_{1-\delta} + N^*$;
$M_3Mo_3N_{1-\delta} + N^* + 3/2\ H_2 \rightarrow M_3Mo_3N_{1-\delta} + NH_3$

$M_3Mo_3N_{1-\delta} + N_2 + 3H_2 \rightarrow M_3Mo_3N_{1-\delta} + 2NH_3$

Scheme 2B.1. Schematic representation of the proposed Mars–van Krevelen mechanism for ammonia synthesis on $M_3Mo_3N_{1-\delta}$ catalysts.

In the previous section, we proposed that transition metal oxides with FM ground state are excellent catalysts for oxygen electrochemistry.[18,19] In addition, we stated that the activation energy of this kind of electron transfer reactions decreases proportionally to the strength of the magnetic interactions stablished between the catalyst an the reagents (see eq. 2.8).[35] As a result, catalysts with higher $\widehat{s_{cat}}$ should present the lowest energy barriers. Interestingly, N_2 reduction to NH_3 has many similarities with O_2 reduction (ORR): in both cases, the chemical bonds are activated by incoming electrons that locate in the same kind of π^* molecular orbitals, prior to the immobilization of the protons (see Scheme 2B.2).

To the best of our knowledge, the influence of QEI has not been applied to ammonia synthesis. This lack of information prompted us to apply the same physical principles that were applied to OER and ORR to nitrogen fixation. In particular, the magnetic structure of the aforementioned series of Mo-based nitrides, $FeCo_2Mo_3N_{1-\delta}$ > $Co_3Mo_3N_{1-\delta}$ > $Fe_3Mo_3N_{1-\delta}$ > $Ni_2Mo_3N_{1-\delta}$ (see Figure 2B.1) was studied. The knowledge of magnetic effects that make a difference in the activity of heterogeneous catalysts towards ammonia synthesis would be very helpful in the rational design of new catalysts with enhanced activity.[69]

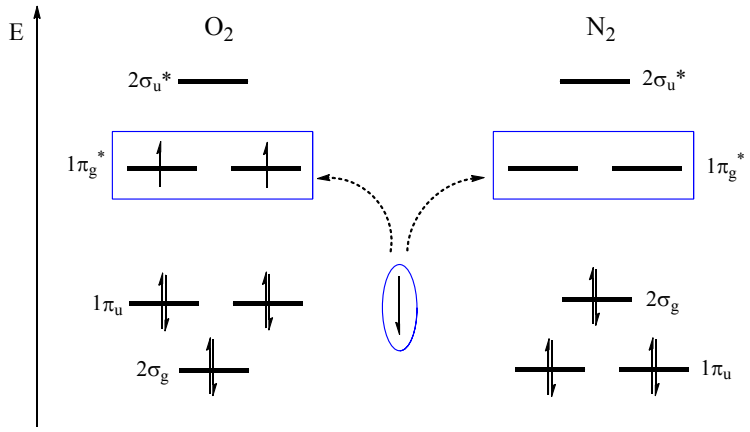

Scheme 2B.2. Schematic comparison of electron transfer from the catalyst to $1\pi_g^*$ orbitals in N_2 and O_2. The energies of Molecular Orbitals are not represented at scale for visual purposes.

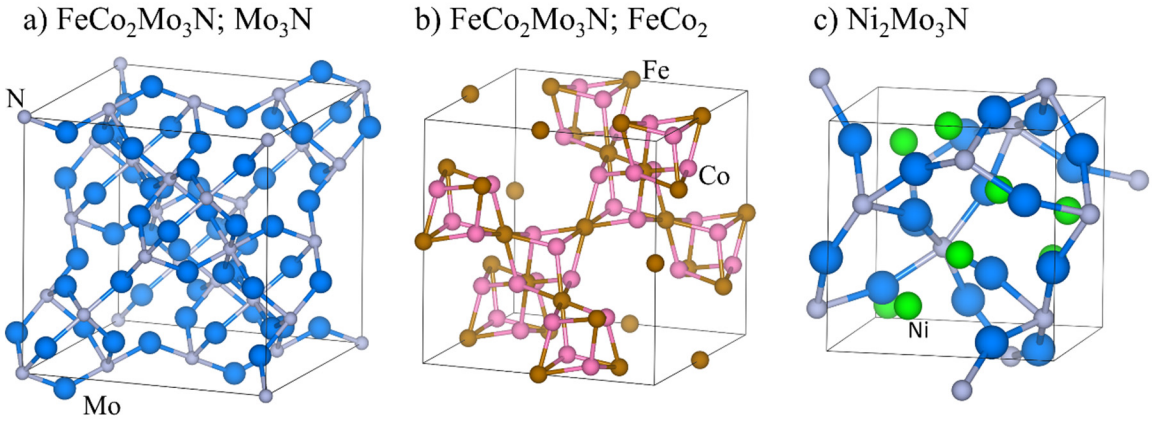

Figure 2B.1. Crystal structure of a) 3D array of Mo_3N and b) 3D array of $FeCo_2$ of $FeCo_2Mo_3N$; and c) Ni_2Mo_3N. $FeCo_2Mo_3N$ is split into two cells for simplicity. Co_3Mo_3N and Fe_3Mo_3N have same crystal structure as $FeCo_2Mo_3$. Crystal structures were extracted from references 69 and 70.

The main goals of the performed DFT studies are the following:

(i) Studying the magnetic structures of Mo-based nitrides with different relative activities towards N_2 fixation. In particular, the magnetic structure of Ni_2Mo_3N, Fe_3Mo_3N, Co_3Mo_3N and $FeCo_2Mo_3N$ with and without N vacancies was analysed.

(ii) Identifying whether there is a relation between the magnetic ground state and the catalytic activity.

(iii) Unravelling the magnetic phases associated to higher catalytic activities.

(iv) Finding a descriptor for the catalytic activity on the basis of magnetic properties.

B.2 Results and discussion

Since the Mo-nitrides under study are known to have nitrogen vacancies under the typical reaction conditions,[55] the analyses were started by studying the N-defective structures. After that, the same kind of studies were performed in non-N-defective systems.

B.2.1 N-defective structures

In order to model the nitrogen defective systems, one of the sixteen N atoms in the unit cells of Fe_3Mo_3N, Co_3Mo_3N and $FeCo_2Mo_3N$ was substracted.[70] Since the unit cell of Ni_2Mo_3N has four times less nitrogen atoms, a (2x2x1) supercell was considered in order to maintain the same Mo/N relation.[71] This way, compositions of the form $M_xMo_3N_{0.94}$ were created.

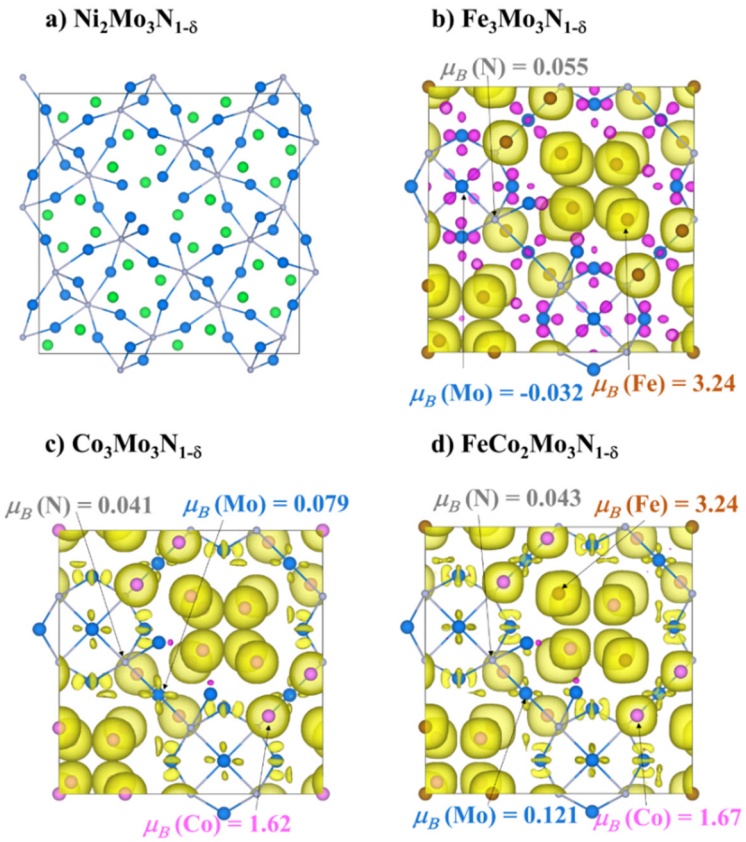

Figure 2B.2. Spin density (yellow: up, purple: down) of the ground state magnetic state of a) $Ni_2Mo_3N_{1-\delta}$, b) $Fe_3Mo_3N_{1-\delta}$, c) $Co_3Mo_3N_{1-\delta}$, and d) $FeCo_2Mo_3N_{1-\delta}$.

Interestingly, $Ni_2Mo_3N_{1-\delta}$, the least active material, is not magnetic, and the following one in activity, $Fe_3Mo_3N_{1-\delta}$, is ferrimagnetic, with Mo and Fe atoms in a relative AFM configuration. The most active ones, $Co_3Mo_3N_{1-\delta}$ and $FeCo_2Mo_3N_{1-\delta}$, are completely FM (see Figure 2B.2). Remarkably, there is a correlation between the relative catalytic activity and the magnetic moment in Mo atoms, which are the catalytically active centres. Specifically, the magnetic moments are: $Ni_2Mo_3N_{1-\delta}$ (0.0 μ_B) < $Fe_3Mo_3N_{1-\delta}$ (-0.032 μ_B) < $Co_3Mo_3N_{1-\delta}$ (0.079 μ_B) < $FeCo_2Mo_3N_{1-\delta}$ (0.121 μ_B). This result suggests a possible dependence of activation energy on the magnetic structure of the material and, especially, on the magnetism accumulated at the active centres.

B.2.2 Non N-defective structures

The same study was carried out on non-N-defective structures. Interestingly, the same magnetic ground states were observed in all cases. Moreover, the spin polarization on Mo atoms follows the same sequence: Ni_2Mo_3N (0.0 μ_B) < Fe_3Mo_3N (0.014 μ_B) < Co_3Mo_3N (0.083 μ_B) < $FeCo_2Mo_3N$ (0.132 μ_B), see Figure 2B.3. Overall, these results show that we can directly use the non-vacant systems in our study, since the magnetic behaviour is maintained in the N-vacant system.

In Fe_3Mo_3N, iron presents a magnetic moment of 3.03 μ_B and a Bader charge of 0.03 a.u. Molybdenum atoms have a magnetic moment that is close to zero (-0.014 μ_B), and a Bader charge of 0.51 a.u. This result is in agreement with the typical low spin state of 4*d*-Mo systems (t_{2g}^6, $S \sim 0$).[72] Iron atoms are ferromagnetically coupled with each other, and antiferromagnetically with respect to Mo. As previously stated, $Ni_2Mo_3N_{1-\delta}$ and $Fe_3Mo_3N_{1-\delta}$ are the least active catalysts. They are the only compositions in which Mo is non-magnetic ($Ni_2Mo_3N_{1-\delta}$), or is AFM coupled with the other metal atoms, $Fe_3Mo_3N_{1-\delta}$. The magnetic moments accumulated in Mo atoms are the lowest of the whole series.

Co atoms in Co_3Mo_3N have a magnetic moment of 1.63 μ_B, and a Bader charge of -0.22 a.u. The magnetic moment of Co in Co_3Mo_3N is smaller than that of Fe in Fe_3Mo_3N, since the 3*d* band is more saturated in Co atoms. Noteworthy, Mo centres are more oxidized in Co_3Mo_3N (Bader charge of 0.73 a.u.) than in Fe_3Mo_3N (0.51 a.u.), as a consequence of the higher electronegativity of Co with respect to Fe. Accumulated magnetism in Mo atoms is 0.083 μ_B, almost six times that in Fe_3Mo_3N. In addition, Co_3Mo_3N is completely FM, that is, all Co–Co, Mo–Mo and Co–Mo exchange interactions are FM. The same magnetic structure is observed in $FeCo_2Mo_3N$, in which all metallic atoms are ferromagnetically coupled. In particular, Fe and Co atoms have magnetic moments of 3.25 μ_B and 1.69 μ_B, respectively. As

previously specified, the magnetism accumulated in Mo atoms is the greatest of the series: 0.132 μ_B.

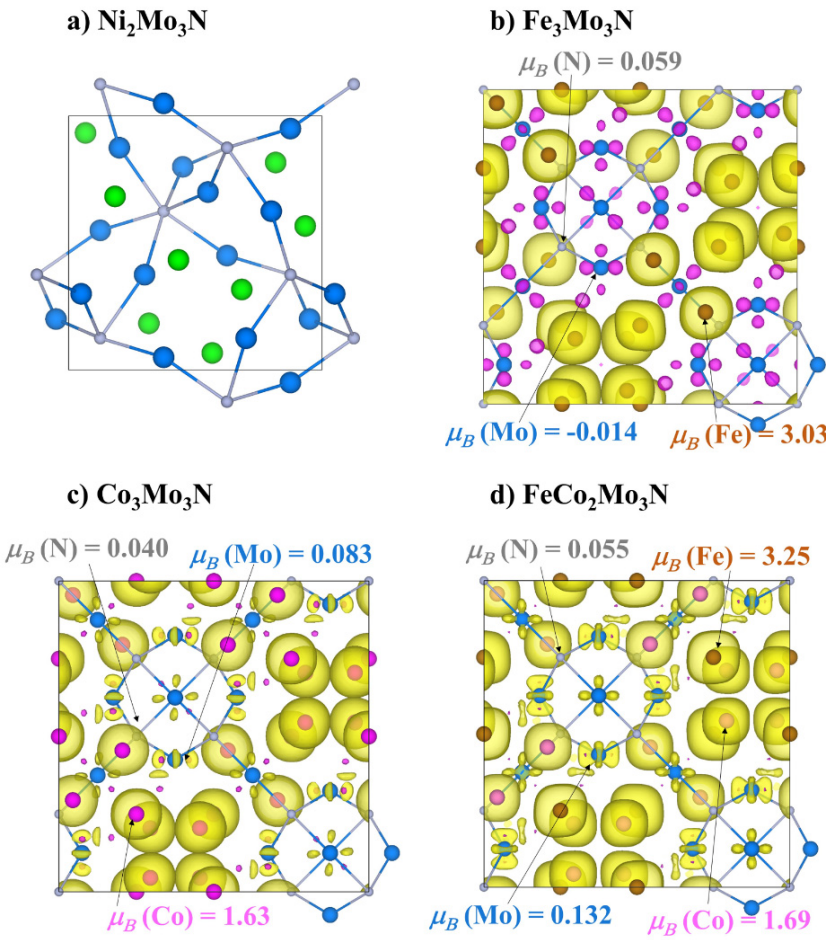

Figure 2B.3. Spin density (yellow: up, purple: down) of the ground state magnetic state of a) Ni_2Mo_3N, b) Fe_3Mo_3N, c) Co_3Mo_3N, and d) $FeCo_2Mo_3N$.

Interestingly, not only the magnetic moment of Mo, but also the Mo–N distance in isostructural materials correlates with the relative activity. Specifically, more active catalysts have shorter Mo–N bonds: *d*(Mo–N) Fe_3Mo_3N > Co_3Mo_3N > $FeCo_2Mo_3N$ (see Table 2B.1). Besides, in a MvK mechanism, the most active systems usually have a formation energy for N-vacancies in the middle zone of a Sabatier diagram.[40] In agreement with this result, in this case, the formation energy of N-vacancies for the most active catalyst, $FeCo_2Mo_3N$, lies between that of Co_3Mo_3N and Ni_2Mo_3N (which interact with the reagents too weakly), and Fe_3Mo_3N (which interacts with N_2 molecules to strongly), see Table 2B.1.

Table 2B.1. Mo magnetic moment and Bader atomic charge, Mo–N distance, N-vacancies formation energy and energy difference between FM and lowest-in-energy AFM phase in the studied nitrides.

Material	***μ* (Mo)** *(a.u.)*	***charge Mo*** *(a.u.)*	***ΔE (FM-AFM)*** *(meV/Mo)*	***d (Mo–N)*** *(Å)*	***ΔE (N vac.)*** *(meV/Mo)*
$FeCo_2Mo_3N$	0.132	0.65	89	2.081	54
Co_3Mo_3N	0.083	0.73	113	2.089	50
Fe_3Mo_3N	-0.014	0.51	138	2.098	63
Ni_2Mo_3N	0.00	0.73	--	2.068	49

Overall, these results provide strong evidence that ammonia synthesis is less optimally catalysed by materials that do not have magnetic Mo atoms (Ni_2Mo_3N). Moreover, the most active catalysts have a complete FM structure, with enhanced accumulated magnetism in Mo atoms. This way, the magnetism of active centres can be used as a physically meaningful descriptor for predicting the catalytic activity of novel materials. Overall, the performed study reveals the importance of magnetic interactions in N_2 fixation processes, opening the door to further and more detailed studies. The good correlation between the bulk results and the experimentally determined relative catalytic performance further supports its use for predicting catalytic properties.

B.3 Summary

The main studies performed in this section of the Doctoral Thesis are summarized in the following lines:

(a) The magnetic structure of different heterogeneous catalysis for N_2 fixation has been computationally studied. In particular, the following Mo-based nitrides were considered: Ni_2Mo_3N, Fe_3Mo_3N, Co_3Mo_3N and $FeCo_2Mo_3N$.

(b) The magnetic ground state is maintained when including N-vacancies within the structures. As a result, it is possible to use fully stoichiometric (non N-defective) systems for predictive purposes.

(c) More active systems have a FM ground state. Besides, there is a correlation between the magnetic moment accumulated in Mo active centres and the relative catalytic activity.

(d) The magnetic moment of Mo atoms can be used as a physically meaningful descriptor for the catalytic activity.

(e) In this kind of materials, the bulk magnetic properties can be used for obtaining predictive catalytic trends.

C. References

[1] Chu, S.; Majumdar, A. Opportunities and challenges for a sustainable energy future. *Nature* **2012**, *488*, 294–303.

[2] Shao, M.; Chang, Q.; Dodelet, J. –P.; Chenitz, R. Recent Advances in electrocatalysis for Oxygen Reduction Reaction. *Chem. Rev.* **2016**, *116*, 3594–3657.

[3] Gupta, S.; Kellogg, W.; Xu, H.; Liu, X.; Cho, J.; Wu, G. Bifunctional Perovskite Oxide Catalysts for Oxygen Reduction and Evolution in Alkaline Media. *Chem. Asian J.* **2016**, *11*, 10–21.

[4] Sapountzi, F. M.; Gracia, J. M.; Weststrate, C. J.; Fredriksson, H. O. A.; Niemantsverdriet, J. W. H. *Prog. Energy Combust. Sci.* **2017**, *58*, 1–35.

[5] Juodkazyte, J.; Seniutinas, G.; Sebeka, B.; Savickaja, I.; Malinauskas, T.; Badokas, K.; Joudkazis, K.; Juodkazis, S. Solar water splitting: Efficiency discussion. *Int. J. Hydrog. Energy* **2016**, *4*, 11941–11948.

[6] Chandran, P.; Ghosh, A.; Ramaprabhu, S. High-performance Platinum-free oxygen reduction reaction and hydrogen oxidation reaction catalyst in polymer electrolyte membrane fuel cell. *Scientific Reports* **2018**, *8*, 3591.

[7] Huang, Z. –F.; Wang, J.; Peng, Y.; Jung, C. –Y.; Fisher, A.; Wang, X. Design of Efficient Bifunctional Oxygen Reduction/Evolution Electrocatalyst: Recent Advances and Perspectives. *Adv. Energy Mater.* **2017**, *7*, 1700544.

[8] Li, Y.; Lu, J. Metal−Air Batteries: Will They Be the Future Electrochemical Energy Storage Device of Choice? *ACS Energy Lett.* **2017**, *2*, 1370−1377.

[9] Armand, M.; Tarascon, J.-M. Building better batteries. *Nature* **2008**, *451*, 652–657.

[10] Strasser, P. Free Electrons to Molecular Bonds and Back: Closing the Energetic Oxygen Reduction (ORR)–Oxygen Evolution (OER) Cycle Using Core–Shell Nanoelectrocatalysts. *Acc. Chem. Res.* **2016**, *49*, 2658–2668.

[11] Guo, S.; Zhang, S.; Sun, S. Tuning nanoparticle catalysis for the oxygen reduction reaction. *Angew. Chem. Int. Ed.* **2013**, *52*, 8526–8544.

[12] Lee, Y.; Suntivich, J.; May, K. J.; Perry, E. E.; Shao-Horn, Y. Synthesis and Activities of Rutile IrO_2 and RuO_2 Nanoparticles for Oxygen Evolution in Acid and Alkaline Solutions. *J. Phys. Chem. Lett.* **2012**, *3*, 399–404.

[13] (a) Grimaud, A.; May, K. J.; Carlton, C. E.; Lee, Y. –L.; Risch, M.; Hong, W. T.; Zhou, J.; Shao-Horn, Y. Double perovskites as a family of highly active catalysts for oxygen evolution in alkaline solution. *Nat. Commun.* **2013**, *4*, 2439. (b) Jung, J. –I.; Jeong, H. Y.; Lee J. S.; Kim, M. G.; Cho, J. A bifunctional perovskite catalyst for oxygen reduction and evolution. *Angew. Chem. Int. Ed.* **2014**, *53*, 4582–4586. (c) Zhao, B.; Zhang, L.; Zhen, D.; Yoo, S.; Ding, Y.; Chen, D.; Chen, Y.; Zhang, Q.; Doyle, B.; Xiong, X.; Liu, M. A tailored double perovskite nanofiber catalyst enables ultrafast oxygen evolution. *Nat. Commun.* **2017**, *8*, 14586. (d) Stoerzinger, K. A.; Risch, M.; Han, B.; Shao-Horn, Y. Recent Insights into Manganese Oxides in Catalyzing Oxygen Reduction Kinetics. *ACS Catal.* **2015**, *5*, 6021–6031.

[14] Tanaka, H.; Misono, M. Advances in designing perovskite catalysts. *Curr. Opin. Solid State Mater. Sci.* **2001**, *5*, 381–387.

[15] (a) Srirapu, V. K. V. P.; Kumar, M.; Awasthi, R.; Singh, R. N.; Sinha, A. S. K. Manganese molybdate and its Fe-substituted products as new efficient electrocatalysts for oxygen evolution in alkaline solutions. *Int. J. Hydrogen Energy* **2013**, *38*, 13587–13595. (b) Wu, G.; Zelenay, P. Nanostructured nonprecious metal catalysts for oxygen reduction reaction. *Acc. Chem. Res.* **2013**, *46*, 1878–1889. (c) May, K. J.; Carlton, C. E.; Stoerzinger, K. A.; Risch, M.; Suntivich, J.; Lee, Y. –L.; Grimaud, A.; Y. Shao-Horn, Y. Influence of Oxygen Evolution during Water Oxidation on the Surface of Perovskite Oxide Catalysts. *J. Phys. Chem. Lett.* **2012**, *3*, 3264–3270. (d) Kim, N. –I.; Sa, Y. J.; Yoo, T. S.; Choi, S. R.; Afzal, R. A.; Choi, T.; Seo, Y. –S.; Lee, K. –S.; Hwang, J. Y.; Choi, W. S.; Joo, S. H.; Park, J. –Y. Oxygen-deficient triple perovskites as highly active and durable bifunctional electrocatalysts for oxygen electrode reactions. *Sci. Adv.* **2018**, *4*, 9360. (e) Hardin, W. G.; Mefford, J. T.; Slanac, D. A.; Patel, B. B.; Wang, X. Q.; Dai, S. ; Zhao, X.; Ruoff, R. S.; Johnston, K. P.; Stevenson, K. J. Tuning the electrocatalytic activity of perovskites through active site variation and support interact ions. *Chem. Mater.* **2014**, *26*, 3368–3376.

[16] (a) Zhang, H.M.; Shimizu, Y.; Miura, N.; Yamazoe, N. Oxygen sorption and catalytic properties of La1−xSrxCo1−yFeyO3 perovskite-type oxides. *J. Catal.* **1990**, *121*, 432–440. (b) Wang, Z. L.; Xu, D.; Xu, J. J.; Zhang, X. B. Oxygen electrocatalysts in metal-air batteries: from aqueous to nonaqueous electrolytes. *Chem. Soc. Rev.* **2014**, *43*, 7746–7786.

[17] (a) Kulkarni, A.; Siahrostami, S.; Patel, A.; Nørskov, J. Understanding Catalytic Activity Trends in the Oxygen Reduction Reaction. *Chem. Rev.* **2018**, *118*, 2302−2312. (b) Ryabova, A. S.; Napolskiy, F. S.; Poux, T.; Istomin, S. Y.; Bonnefont, A.; Antipin, D. M.; Baranchikov, A. Y.; Levin, E. E.; Abakumov, A. M.; Kéranguéven, G.; Antipov, E. V.; Tsirlina, G. A.; Savinova, E. R. Rationalizing the Influence of the Mn(IV)/Mn(III) Red-Ox Transition on the Electrocatalytic Activity of Manganese Oxides in the Oxygen Reduction Reaction. *Electrochim. Acta* **2016**, *187*, 161−172.

[18] Gracia, J. Spin dependent interactions catalyse the oxygen electrochemistry. *Phys. Chem. Chem. Phys.* **2017**, *19*, 20451−20456.

[19] Sharpe, R.; Munarriz, J.; Lim, T.; Jiao, Y.; Niemantsverdriet, J. W.; Polo, V.; Gracia, J. Orbital Physics of Perovskites for the Oxygen Evolution Reaction. *Top. Catal.* **2017**, *61*, 267−275.

[20] (a) Fletcher, S.; Van Dijk, N. J. Supercatalysis by Superexchange. *J. Phys. Chem. C* **2016**, *120*, 26225−26234. (b) Sharpe, R.; Lim, T.; Jiao, Y.; Niemantsverdriet, J. W.; Gracia, J. Oxygen Evolution Reaction on Perovskite Electrocatalysts with Localized Spins and Orbital Rotation Symmetry. *ChemCatChem* **2016**, *8*, 3762–3768.

[21] Korotana, R.; Mallia, G.; Gercsi, Z.; Liborio, L.; Harrison, N. M. Hybrid density functional study of structural, bonding, and electronic properties of the manganite series $La_{1-x}Ca_xMnO_3$ (x = 0,1/4,1). *Phys. Rev. B* **2014**, *89*, 205110.

[22] (a) Tulloch, J.; Donne, S. W. J. Activity of perovskite $La_{1-x}Sr_xMnO_3$ catalysts towards oxygen reduction in alkaline electrolytes. *Power Sources* **2009**, *188*, 359–366. (b) Yunphuttha, C.; Porntheeraphat, S.; Wongchaisuwat, A.; Tangbunsuk, S.; Marr, D. W. M.; Viravathana, P. Characterization of $La_{1-x}Sr_xMnO_3$ perovskite catalysts for hydrogen peroxide reduction. *Phys. Chem. Chem. Phys.* **2016**, *18*, 16786–16793. (c) Stoerzinger, K. A.; Lü, W.; Li, C.; Ariando; Venkatesan, T.; Shoa-Horn, Y. Highly Active Epitaxial $La_{(1-x)}Sr_xMnO_3$ Surfaces for the Oxygen Reduction Reaction: Role of Charge Transfer. *J. Phys. Chem. Lett.* **2015**, *6*, 1435–

1440. (d) Hong, W. T.; Risch, M.; Stoerzinger, K. A.; Grimaud, A.; Suntivich, J.; Shao-Horn, Y. Toward the rational design of non-precious transition metal oxides for oxygen electrocatalysis. *Energy Environ. Sci.* **2015**, *8*, 1404–1427. (e) Stoerzinger, K. A.; Risch, M.; Suntivich, J.; Le, W. M.; Zhou, J.; Biegalski, M. D.; Christen, H. M.; Ariando, Venkatesan, T.; Shao-Horn, Y. Oxygen electrocatalysis on (001)-oriented manganese perovskite films: Mn valency and charge transfer at the nanoscale. *Energy Environ. Sci.* **2013**, *6*, 1582–1588.

[23] Zhu, Y.; Zhou, W.; Yu, J.; Chen, Y.; Liu, M.; Shao, Z. Enhancing Electrocatalytic Activity of Perovskite Oxides by Tuning Cation Deficiency for Oxygen Reduction and Evolution Reactions. *Chem. Mater.* **2016**, *28*, 1691–1697.

[24] (a) Celorrio, V.; Calvillo, L.; Dann, E.; Granozzi, G.; Aguadero, A.; Kramer, D.; Russell, A. E.; Fermín, D. J. Oxygen reduction reaction at $La_xCa_{1-x}MnO_3$ nanostructures: interplay between A-site segregation and B-site valency. *Catal. Sci. Technol.* **2016**, *6*, 7231–7238. (b) Chen, D.; Chen, C.; Baiyee, Z. M.; Shao, Z.; Ciucci, F. Nonstoichiometric Oxides as Low-Cost and Highly-Efficient Oxygen Reduction/Evolution Catalysts for Low-Temperature Electrochemical Devices. *Chem. Rev.* **2015**, *115*, 9869–9921.

[25] Baldini, M.; Struzhkin, V. V.; Goncharov, A. F.; Postorino, P.; Mao, W. L. Persistence of Jahn-Teller Distortion up to the Insulator to Metal Transition in $LaMnO_3$. *Phys. Rev. Lett.* **2011**, *106*, 066402.

[26] Lee, D.-G.; Gwon, O.; Park, H. –S.; Kim, S. H.; Yang, J.; Kwak, S. K.; G. Kim, G.; Song, H. –K. Conductivity-dependent completion of oxygen reduction on oxide catalysts. *Angew. Chem. Int. Ed.* **2015**, *54*, 15730–15733.

[27] (a) Kozuka, H.; Ohbayashi, K.; Koumoto, K. Electronic conduction in La-based perovskite-type oxides. *Sci. Technol. Adv. Mater.* **2015**, *16*, 026001. (b) Van Santen, J. H.; Jonker, G. H. Electrical conductivity of ferromagnetic compounds of manganese with perovskite structure. *Physica* **1950**, *16*, 599–600.

[28] Mellergård, A.; McGreevy, R. L.; Eriksson, S. G. Structural and magnetic disorder in $La_{1-x}Sr_xMnO_3$. *J. Phys. Condens. Matter* **2000**, *12*, 4975–4991.

[29] Stoerzinger, K. A.; Risch, M.; Suntivich, J.; Lü, W. M.; Zhou, J.; Biegalski, M. D.; Christen, H. M.; Ariando, Venkatesandeh, T.; Shao-Horn, Y. Oxygen electrocatalysis on (001)-oriented manganese perovskite films: Mn valency and charge transfer at the nanoscale. *Energy Environ. Sci.* **2013**, *6*, 1582–1588.

[30] Gersicher, H. The impact of semiconductors on the concepts of electrochemistry. *Electrochim. Acta* **1990**, *35*, 1677–1699.

[31] (a) Marcus, R. A. On the Theory of Electron-Transfer Reactions. VI. Unified Treatment for Homogeneous and Electrode Reactions. *J. Chem. Phys.* **1965**, *43*, 679. (b) Truhlar, D. G.; Garret, B. C.; Klippenstein, S. J. Current Status of Transition-State Theory. *J. Phys. Chem.* **1996**, *100*, 12771–12800.

[32] (a) Koshibae, W.; Maekawa, S. Effect of spin and orbital on thermopower in strongly correlated electron systems. *J. Magn. Magn. Mater.* **2003**, 258, 216–218. (b) Hoffmann, R. A Claim on the Development of the Frontier Orbital Explanation of Electrocyclic Reactions. *Angew. Chem. Int. Ed.* **2004**, *43*, 6586–6590.

[33] Goodenough, J. B. Electronic and ionic transport properties and other physical aspects of perovskites. *Rep. Prog. Phys.* **2004**, *67*, 1915–1993.

[34] Lim, T.; Niemantsverdriet, J. W. H.; Gracia, J. Layered antiferromagnetic ordering in the most active perovskite catalysts for the oxygen evolution reaction. *ChemCatChem* **2016**, *8*, 2968–2974.

[35] Jiao, Y.; Sharpe, R.; Lim, T.; Niemantsverdriet, J. W. H.; Gracia, J. Photosystem II acts as a spin-controlled electron gate during oxygen formation and evolution. *J. Am. Chem. Soc.* **2017**, *139*, 16604–16608.

[36] Tokura, Y. Orbital physics in transition-metal oxides. *Science* **2000**, *288*, 462–468. (b) Dagotto, E. Complexity in strongly correlated electronic systems. *Science* **2005**, *309*, 257–262.

[37] de Graaf, C.; Broer, R. *Magnetic Interactions in Molecules and Solids*; Springer International Publishing: Switzerland, 2016.

[38] Aravena, D.; Ruiz, E. Coherent Transport through Spin-Crossover Single Molecules. *J. Am. Chem. Soc.* **2012**, *134*, 777–779.

[39] (a) Bockris, J. O.; Otagawa, T. The electrocatalysis of oxygen evolution on perovskites. *J. Electrochem. Soc.* **1984**, *131*, 290–302. (b) Matsumoto, Y.; Sato, E. Electrocatalytic properties of transition metal oxides for oxygen evolution reaction. *Mater. Chem. Phys.* **1986**, *14*, 397–426.

[40] Medford, A. J.; Vojvodic, A.; Hummelshøj, J. S.; Voss, J.; Pedersen, F. –A.; Studt, F.; Bligaard, T.; Nilsson, A.; Nørskov, J. K. From the Sabatier principle to a predictive theory of transition-metal heterogeneous catalysis. *J. Catal.* **2015**, *328*, 36–42.

[41] Iwakura, C.; Nishioka, M.; Tamura, H. Oxygen Evolution on Spinel-type Ferrite Film Electrodes. *Nippon Kagaku Kaishi* **1982**, *7*, 1136–1140.

[42] (a) Suntivich, J.; May, K. J.; Gasteiger, H. A.; Goodenough, J. B.; Shao-Horn, Y.; A Perovskite Oxide Optimized for Oxygen Evolution Catalysis from Molecular Orbital Principles. *Science* **2011**, *334*, 1383–1385. (b) Suntivich, J.; Gasteiger, H. A.; Yabuuchi, N.; Nakanishi, H.; Goodenough, J. B.; Shao-Horn, Y. Design principles for oxygen-reduction activity on perovskite oxide catalysts for fuel cells and metal–air batteries. *Nat. Chem.* **2011**, *3*, 546–550.

[43] (a) Sahner, K.; Gouma, P.; Moos, R. Electrodeposited and sol-gel precipitated p-type $SrTi_{1-x}Fe_xO_{3-\delta}$ semiconductors for gas sensing. *Sensors* **2007**, *7*, 1871–1886. (b) Akamatsu, T.; Itoh, T.; Izu, N.; Shin, W. NO and NO_2 sensing properties of WO_3 and Co_3O_4 based gas sensors. *Sensors* **2013**, *13*, 12467–12481.

[44] Naghavi, S. S.; Emery, A. A.; Hansen, H. A.; Zhou, F.; Ozolins, V.; Wolverton, C. Giant onsite electronic entropy enhances the performance of ceria for water splitting. *Nat. Commun.* **2017**, *8*, 285.

[45] (a) Du, J.; Zhang, T.; Cheng, F.; Chu, W.; Wu, Z.; Chen, J. Nonstoichiometric Perovskite CaMnO3−δ for Oxygen Electrocatalysis with High Activity. *Inorg. Chem.* **2014**, *53*, 9106–9114. (b) Guo, Y.; Tong, Y.; Chen, P.; Xu, K.; Zhao, J.; Lin, Y.; Chu, W.; Peng, Z.; Wu, C.; Xie, Y. Engineering the Electronic State of a Perovskite Electrocatalyst for Synergistically Enhanced Oxygen Evolution Reaction. *Adv. Mater.* **2015**, *27*, 5989–5994.

[46] Chen, Y.; Wei, Y.; Zhong, H.; Gao, J.; Liu, X.; Meng, G. Synthesis and electrical properties of $Ln_{0.6}Ca_{0.4}FeO_{3-\delta}$ (Ln = Pr, Nd, Sm) as cathode materials for IT-SOFC. *Ceram. Int.* **2007**, *33*, 1237–1241.

[47] Troyanchuk, I.O.; Khomchenko, V.A.; Tovar, M.; Szymczak, H.; Bärner, K. Antiferromagnet-ferromagnet and structural phase transitions in $La_{0.88}MnO_x$ manganites. *Phys. Rev. B* **2004**, *69*, 54432.

[48] (a) Kim, J.; Shih, P. –C.; Tsao, K. –C.; Pan, Y. –T.; Yin, X.; Sun, C. –J.; Yang, H. High-Performance Pyrochlore-Type Yttrium Ruthenate Electrocatalyst for Oxygen Evolution Reaction in Acidic Media. *J. Am. Chem. Soc.* **2017**, *139*, 12076–12083. (b) Parrondo, J.; George, M.; Capuano, C.; Ayers, K. E.; Ramani, V. Pyrochlore electrocatalysts for efficient alkaline water electrolysis. *J. Mater. Chem. A* **2015**, *3*, 10819–10828.

[49] Mekhilef, S.; Saidur, R.; Safari, A. Comparative study of different fuel cell technologies. *Renew. Sustain. Energy Rev.* **2012**, *16*, 981–989.

[50] Afif, A.; Radenahmad, N.; Cheok, Q.; Shams, S.; Kim, J. H.; Azad, A. K. Ammonia-fed fuel cells: A comprehensive review. *Renew. Sustain. Energy Rev.* **2016**, *60*, 822–835.

[51] Appl. M. *Ullmann's Encyclopedia of Industrail Chemistry*; Wiley-VCH Verlag, GmbH & Co. KGaA: Weinheim, 2006.

[52] (a) Shah, V. K.; Brill, W. J. Isolation of an iron-molybdenum cofactor from nitrogenase. *Proc. Natl. Acad. Sci.* **1977**, *74*, 3249–3253. (b) Spatzal, T.; Aksoyoglu, M.; Zhang, L.; Andrade, S. L. A.; Schleicher, E.; Weber, S.; Rees, D. C.; Einsle, O. Evidence for interstitial carbon in nitrogenase FeMo cofactor. *Science* **2011**, *334*, 940. (c) Lancastrer, K. M.; Roemelt, M.; Ettenhuber, P.; Hu, Y.; Ribbe, M. W.; Neese, F.; Bergmann, U.; DeBeer, S. X-ray Emission Spectroscopy Evidences a Central Carbon in the Nitrogenase Iron-Molybdenum Cofactor. *Science* **2011**, *334*, 974–977.

[53] van der Ham, C. J. M.; Koper, M. T. M.; Hetterscheid, D. G. H. Challenges in reduction of dinitrogen by proton and electron transfer. *Chem. Soc. Rev.* **2014**, *43*, 5183–5191.

[54] (a) Arashiba, K.; Miyake, Y.; Nishibayashi, Y. A molybdenum complex bearing PNP-type pincer ligands leads to the catalytic reduction of dinitrogen into ammonia. *Nat. Chem*. **2011**, *3*, 120–125. (b) Yandulov, D. V.; Schrock, R. R. Catalytic reduction of dinitrogen to ammonia at a single molybdenum center. *Science* **2003**, *301*, 76–78.

[55] (a) Anderson, J. S.; Rittle, J.; Peters, J. C. Catalytic conversion of nitrogen to ammonia by an iron model complex. *Nature* **2013**, *501*, 84–88. (b) Kuriyama, S.; Arashiba, K.; Nakajima, K.; Matsuo, Y.; Tanaka, H.; Ishii, K.; Yashizawa, K.; Nishibayashi, Y. Catalytic transformation of dinitrogem into ammonia and hydrazine by iron-dinitrogen complexes bearing pincer ligand. *Nat. Commun.* **2016**, *7*, 1.

[56] (a) Shipman, M. A.; Symes, M. D. Recent progress towards the electrosynthesis of ammonia from sustainable resources. *Catal. Today* **2017**, *286*, 57–68. (b) Manabe, R.; Nakatsubo, H.; Gondo, A.; Murakami, K.; Ogo, S.; Tsuneki, H.; Ikeda, M.; Ishikawa, A.; Nakai, H.; Sekine, Y. Electrocatalytic synthesis of ammonia by Surface proton hopping. *Chem. Sci.* **2017**, *8*, 5434–5439.

[57] (a) Li, H.; Shang, J.; Ai, Z.; Zhang, L. Efficient Visible Light Nitrogen Fixation with BiOBr Nanosheets of Oxygen Vacancies on the Exposed {001} Facets. *J. Am. Chem. Soc.* **2015**, *137*, 6393–6399. (b) Qui, P.; Xu, C.; Zhou, N.; Chen, H.; Jiang, F. Metal-free phosphorus nanosheets-decorated graphitic carbon nitride nanosheets with C-P bonds for excellent photocatalytic nitrogen fixation. *Appl. Catal. B* **2018**, *221*, 27–35.

[58] (a) Kyriakou, V.; Garagounis, I.; Vasileiou, E.; Vourros, A.; Stoukides, M. Progress in the Electrochemical Synthesis of Ammonia. *Catal. Today* **2017**, *286*, 2–13. (b) Ahmed, A.;

Radenahmad, N.; Cheok, Q.; Shams, S.; Kim, J. H.; Azad, A. K. Ammonia-fed fuel cells: a comprehensive review. *Renew. Sust. Energ. Rev.* **2016**, *60*, 822–835.

[59] Abghoui, Y.; Garden, A. L.; Howalt, J. G.; Vegge, T.; Skúlason, E. Electroreduction of N_2 to Ammonia at Ambient Conditions on Mononitrides of Zr, Nb, Cr and V: A DFT Guide for Experiments. *ACS Catal.* **2016**, 6, 635–646.

[60] Jacobsen, C. J. H. Novel Class of Ammonia Synthesis Catalysis. *Chem. Commun.* **2000**, *0*, 1057–1058.

[61] Perret, N.; Alexander, A. -.M; Hunter, S. M.; Chung, P.; Hargreaves, J. S. J.; Howe, R. F.; Keane, M. A. Synthesis, characterisation and hydrogenation performance of ternary nitride catalysts. *Appl. Catal. A* **2014**, *488*, 128–137.

[62] Jacobsen, C. J. H.; Dahl, S.; Clausen, B. S.; Bahn, S.; Logadóttir, A.; Nørskov, J. Catalyst Design by Interpolation in the Periodic Table: Bimetallic Ammonia Synthesis Catalysts. *J. Am. Chem. Soc.* **2001**, *123*, 8404–8405.

[63] Amar, I. A.; Lan, R.; Petit, C. T. G.; Tao, S. Electrochemical Synthesis of Ammonia Using Fe_3Mo_3N Catalyst and Carbonate-Oxide Composite Electrolyte. *Int. J. Electrochem. Sci.* **2015**, *10*, 3757–3766.

[64] Mckay, D.; Hargreaves, J. S. J.; Rico, J. L.; Rivera, J. L.; Sun, X. –L. The influence of phase and morphology of molybdenum nitrides on ammonia synthesis activity and reduction characteristics. *J. Solid State Chem.* **2008**, *181*, 325–333.

[65] McKay, D.; Gregory, D. H.; Hargreaves, J. S. J.; Hunter, S. M.; Sun, X. Towards Nitrogen Transfer Catalysis: Reactive Lattice Nitrogen in Cobalt Molybdenum Nitride. *Chem. Commun.* **2007**, *0*, 3051–3053.

[66] Zeinalipour-Yazdi, C. D.; Hargreaves, J. S. J.; Catlow, C. R. A. DFT-D3 Study of Molecular N_2 and H_2 Activation on Co_3Mo_3N Surfaces. *J. Chem. Phys. C* **2016**, *120*, 21390–21398.

[67] Hunter, S. M.; Gregory, D. H.; Hargreaves, J. S. J.; Richard, M. I.; Duprez, D.; Bion, N. A.; Study of 15N/14N Isotopic Exchange over Cobalt Molybdenum Nitrides. *ACS Catal.* **2013**, *3*, 1719–1725.

[68] (a) Zeinalipour-Yazdi, C. D.; Hargreaves, J. S. J.; Catlow, C. R. A. Nitrogen Activation in a Mars–van Krevelen Mechanism for Ammonia Synthesis on Co_3Mo_3N. *J. Chem. Phys. C* **2015**, *119*, 28368–28376. (b) Zeinalipour-Yazdi, C. D.; Hargreaves, J. S. J.; Catlow, C. R. A. Low-T Mechanism of Ammonia Synthesis on Co_3Mo_3N. *J. Phys. Chem. C* **2018**, *122*, 6078–6082.

[69] Zunger, A. Inverse design in search of materials with target functionalities. *Nat. Chem. Rev.* **2018**, *2*, 0121.

[70] Jackson, S. K.; Layland, R. C.; zur Loye, H. C. The simultaneous powder X-ray and neutron diffraction refinement of two η-carbide type nitrides, Fe_3Mo_3N and Co_3Mo_3N, prepared by ammonolysis and by plasma nitridation of oxide precursors. *J. Alloys Compd.* **1999**, 291, 94–101.

[71] Alconchel, S.; Sapina, F.; Beltran, D.; Beltran, A. Chemistry of interstitial molybdenum ternary nitrides M_nMo_3N (M=Fe, Co, n=3; M=Ni, n=2). *J. Mater. Chem.* **1998**, *8*, 1901–1909.

[72] McNaughton, R. L.; Chin, J. M.; Weare, W. W.; Schrock, R. R.; Hoffman, B. M. EPR Study of the Low-Spin [d^3; S =1/2], Jahn−Teller-Active, Dinitrogen Complex of a Molybdenum Trisamidoamine. *J. Am. Chem. Soc.* **2007**, *129*, 3480–3481.

CONCLUSIONS

The conclusions obtained from each section has been explained along the dissertation. In the following lines, the main conclusions extracted from this Doctoral Thesis are summarized.

i) The electronic factors that determine the kinetics and thermodynamics of the oxidative addition of ammonia into five different Ir(I)-PXP complexes have been revealed.

ii) A reaction mechanism for the silylation of aromatic C–H bonds catalysed by a well-defined Ir(III)-NHC complex has been proposed. This mechanism is in agreement with different stoichiometric experiments. The proposed catalytic cycle highlights the importance of the substrate directing groups in the reaction selectivity and explains the different yields that are observed with and without a hydrogen acceptor.

iii) A plausible reaction mechanism for the dehydrogenation of formic acid to produce molecular hydrogen has been proposed. This mechanism is in agreement with the activation energy experimentally determined, and with the isolation and characterization of the most stable reaction intermediate proposed in the catalytic cycle.

iv) The preparation of carbamates *via* oxidative carbonylation catalysed by a Rh(I) commercial complex was studied. The reaction requires the action of an oxidant, $KHSO_5$, to proceed. The computational study allowed to unravel the reaction mechanism, with special focus on the key role of the oxidant.

v) The relation between the magnetism of $LaMnO_3$-based materials and their catalytic activity towards ORR has been computationally studied. The results revealed the importance of the spin entropy. Moreover, the most active catalysts are associated with ferromagnetic phases.

vi) A set of guidelines for improving the relative activity of magnetic metal oxides towards OER and ORR has been proposed. These rules were applied to the rational design of $LaFeO_3$-based catalysts for OER.

vii) The previous physical principles were extended to N_2 fixation catalysed by different Mo-nitrides. Our analyses showed that the magnetic moment accumulated on Mo atoms can be used as a physically meaningful descriptor for the catalytic activity.

CONCLUSIONES

Las conclusiones extraídas de cada sección se han explicado a los largo de la memoria. A continuación se enumeran las conclusiones más destacables de esta Tesis Doctoral.

i) Se determinaron los factores cinéticos y termodinámicos que gobiernan la adición oxidante de amoníaco en cinco complejos organometálicos Ir(I)-PXP.

ii) Se ha propuesto un mecanismo de reacción para la sililación de enlaces C–H aromáticos catalizada por un complejo de Ir(III)-NHC bien definido. El mecanismo propuesto está de acuerdo con diferentes experimentos estequiométricos. Asimismo, revela la importancia de los grupos directores presentes en el sustrato orgánico en la selectividad de la reacción y explica los diferentes rendimientos observados con y sin aceptor de hidrógeno.

iii) Se ha propuesto un mecanismo de reacción para la generación de H_2 por deshidrogenación del ácido fórmico. Este mecanismo está de acuerdo con la energía de activación determinada experimentalmente. Asimismo, se ha aislado y caracterizado el intermedio de reacción propuesto más estable.

iv) Se estudió la preparación de carbamatos mediante carbonilación oxidante catalizada por un complejo comercial de Rh(I). La reacción requiere la acción de un oxidante, el $KHSO_5$. El estudio computacional permitió determinar el mecanismo de reacción y poner de manifiesto el papel clave del oxidante.

v) Se ha analizado la relación entre magnetismo y actividad catalítica en la reacción de reducción de oxígeno (ORR) catalizada por diferentes materiales basados en $LaMnO_3$. Los estudios demostraron la importancia de la entropía de espín. Asimismo, los catalizadores más activos se asocian a fases magnéticas ferromagnéticas.

vi) Se han propuesto una serie de reglas para mejorar la actividad catalítica de los óxidos metálicos magnéticos en ORR y OER. Estas reglas se aplicaron al diseño de nuevos catalizadores para OER basados en $LaFeO_3$.

vii) Se extendieron los principios físicos anteriores a la fijación de N_2 catalizada por diferentes nitruros de molibdeno. Los estudios realizados mostraron que el momento magnético acumulado en los átomos de Mo puede utilizarse como descriptor de la actividad catalítica.

PCCP

PAPER

View Article Online
View Journal

Cite this: DOI: 10.1039/c7cp07453k

Understanding the reaction mechanism of the oxidative addition of ammonia by (PXP)Ir(I) complexes: the role of the X group†

J. Munarriz, [a] E. Velez, [b] M. A. Casado [c] and V. Polo *[a]

Received 3rd November 2017,
Accepted 30th November 2017

DOI: 10.1039/c7cp07453k

rsc.li/pccp

An analysis of the electronic rearrangements for the oxidative addition of ammonia to a set of five representative (PXP)Ir pincer complexes (X = B, CH, O, N, SiH) is performed. We aim to understand the factors controlling the activation and reaction energies of this process by combining different theoretical strategies based on DFT calculations. Interestingly, complexes featuring higher activation barriers yield more exothermic reactions. The analysis of the reaction path using the bonding evolution theory shows that the main chemical events, N–H bond cleavage and Ir–H bond formation, take place before the transition structure is reached. Metal oxidation implies an electron density transfer from non-shared Ir pairs to the Ir–N bond. This decrement in the atomic charge of the metal provokes different effects in the ionic contribution of the Ir–X bonding depending on the nature of the X atom as shown by the interacting quantum atoms methodology.

Introduction

N–H activation of ammonia by late metal complexes is a topic of current interest in chemistry, especially regarding the context of its catalytic functionalization.[1] This is a challenging task, as ammonia tends to coordinate to metallic centers through the nitrogen lone pair rather than through N–H bond activation, forming stable Werner-type NH_3 adducts which keep away the hydrogen atom from the metal center (see Scheme 1). Hence, the number of reported processes involving the reaction of ammonia with late metallic precursors leading to the formation of amido late metal reactive species is rather limited.[2] Two main mechanistic pathways may be followed for N–H bond activation: (i) the heterolytic mechanism based on metal–ligand cooperation without change in the metal oxidation state (ruthenium(II),[3] iridium(I)[4] and nickel(II)[5]) and (ii) the homolytic mechanism (or inner-sphere) following the oxidative addition of the N–H bond at the metal, among other approaches.[6] The latter approach is particularly attractive since the utilization of robust pincer-like ligand architectures in combination with iridium allows the homolytic activation of the N–H bond of ammonia, rendering hydrido terminal amido species which could open new routes for catalytic pathways for alkene or alkyne hydroamination.[7]

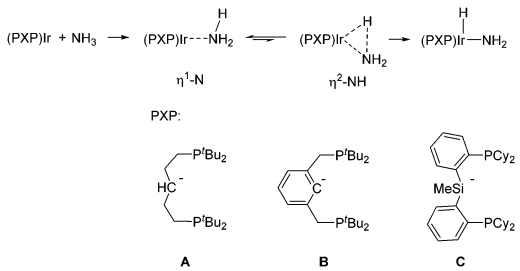

Scheme 1 Oxidative addition of the N–H bond of ammine complexes by (PXP)Ir complexes reported in the literature (**A**–**C**).

Three paradigmatic Ir(PXP) complexes were reported in the literature by the groups of Hartwig (X = CH and Ph) and Turculet (X = Si(Me)) showing that suitable ligands may promote the oxidative addition of the ammonia N–H bond. Encouraged by these results, Leitner *et al.*[8] have evaluated their potential use as molecular catalysts for the intermolecular hydroamination of ethylene with ammonia by means of a detailed theoretical study on the energy profiles of the possible catalytic cycles. Although the energy spans are excessively high for complexes **A** and **C**, after ligand and solvent modifications they can be improved up to turnover frequency (TOF) values of 6.0 h^{-1}, making the process feasible.

Oxidative addition is a characteristic reaction involving transition metal complexes with subtle electronic rearrangements.[9,10] Formally, the metal (M) suffers a two-electron oxidation process

[a] Departamento de Química Física and Instituto de Biocomputación y Física de los Sistemas Complejos (BIFI), Universidad de Zaragoza, 50009, Zaragoza, Spain. E-mail: vipolo@unizar.es
[b] Departamento de Ciencias Básicas, Universidad de Medellín, Medellín, Colombia
[c] Departamento de Química Inorgánica-Instituto de Síntesis Química y Catálisis Homogénea (ISQCH), Universidad de Zaragoza, 50009, Zaragoza, Spain

† Electronic supplementary information (ESI) available: Energetic data, ELF data, geometrical representations and Cartesian coordinates. See DOI: 10.1039/c7cp07453k

being able to cleave the A–B ligand covalent bond, forming two new M–A and M–B bonds with a large degree of covalent character.[11] The importance of electron correlation and the interplay between donation/back-donation interactions between the metal and A–B have been stressed for a long time by different authors.[12,13] Crabtree *et al.* even proposed that oxidative additions in some systems are best interpreted as reductive additions.[14]

Usually, the thermodynamics and kinetics of oxidative additions are favored using ligands with enhanced electron-donating capability,[15–17] whereas reductive eliminations are favored with ligands presenting electron-withdrawing properties.[18–20] However, other authors have claimed that less electron-donating ligands also favor oxidative addition.[21–24] Cundari reported that for the C–H bond oxidative addition of methane to *trans*-$(PH_3)_2IrX$ (X = H, Cl) complexes, the most favorable thermodynamics are found with the least electron-donating ligand considered (Cl).[25] The same behavior has been described for the oxidative addition of H_2 to *trans*-$(PH_3)_2MX$ complexes (X = Cl, Ph; M = Rh, Ir), the thermodynamics being more favorable with the least electron-donating ligand (Ph). Moreover, in a recent assessment of the electronic factors determining the thermodynamics of oxidative addition of C–H and N–H bonds using a wide set of substituents, Goldman *et al.*[26] concluded that the sigma donation of X disfavors N–H (and C–H) oxidative addition to *trans*-$(PH_3)_2IrX$, although the coordination of NH_3 is even more strongly disfavored. Activation energies for NH_3 oxidative addition have been calculated and analyzed for the Ir and Rh complexes pointing out that higher barriers arise from the strong coordination of the ammonia to the metallic center. It has been indicated by Milstein and Schultz that slippage of the bound NH_3 from η^1-N to η^2-NH is necessary for N–H bond activation *via* the donor acceptor interaction model, this reorientation being linked to the activation energies.[27] However, Macgregor in a theoretical study,[23] found no correlation between the strength of the ammine adduct formation and the N–H activation energy proposing that the NH_3 oxidative addition is a two-stage process consisting of: (i) ammine reorientation and (ii) N–H bond activation. The energetic variation in both processes seems to cancel out each other: stronger Lewis acidic metallic fragments difficult ammine reorientation while favoring N–H bond activation.

In the last decade, theoretical methods that offer a clear and unambiguous view of bond transformation have been successfully employed to characterize complete chemical reaction mechanisms by analyzing the transfers of electron density.[28,29] These analyses substantiate the widely and useful "curly arrows" diagrams for the description of reaction mechanisms, which also provide an understanding and rationalization of the electronic and steric factors controlling the activation as well as the reaction energies. In particular, the study of the electron localization function (ELF)[30] allows clear identification of the electron-pairs and even the electron-pair rearrangements taking place along a reaction path by means of bonding evolution theory.[31] This methodology has been applied to elucidate reaction mechanisms of a wide range of organic reactions[32,33] and for some specific organometallic reactions, such as the C–H bond activation of methane by atomic Pd[34] or hydrogen abstraction by an iron complex in cytochrome P450 aromatase.[35] As the ELF focuses on electron-pairs, this study is complemented by an energy decomposition analysis taking into account the ionic character which may be important for metal–ligand interactions. Several approaches have been developed for doing so.[36] One of the most popular decomposition schemes is the "Energy Decomposition Analysis" (EDA).[37] It is an analytical tool that partitions the intermolecular interaction energy into electrostatic, polarization, charge transfer, exchange and correlation components. In this study, due to the pincer structure of the ligand, fragment definition is unclear. As our goal is to understand the interaction between Ir and X atoms, the interacting quantum atoms (IQA)[38] approach extended to B3LYP level[39] has been selected among other schemes. This method separates the total molecular energy into different components from a topological partition as defined by the quantum theory of atoms-in-molecules (QTAIM) methodology. Selection was made on the basis that IQA is a chemically meaningful parameter-free approach, thus providing the method with a high computational rigor. In addition, it presents a demonstrated good performance in the study of a variety of chemical systems. In particular, it has been successfully applied to different organometallic bonding analyses, such as transition metal carbonyls[40] and Zn(II) complexes,[41] as well as in other fields such as hydrogen bonding,[42] hyperconjugation[43] and steric repulsions.[44]

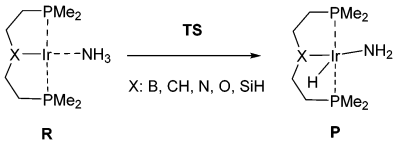

R P

Scheme 2 Complexes considered in this work.

The main goal of this work is (i) to unravel the electronic rearrangements taking place along the reaction path for the N–H oxidative addition of ammonia to a series of Ir(I) complexes and (ii) to clarify the role of the X atom (or group) in PXP Ir complexes in the kinetics and thermodynamics of the process. This information is very relevant in the rational design of new and more efficient organometallic complexes for ammonia N–H bond activation. In this paper, first, a summary of the activation and reaction energies, geometrical data, atomic charges and bond orders for the stationary points of the oxidative addition of N–H to a series of five pincer PXP Ir(I) complexes (X = B, CH, N, O, SiH, see Scheme 2) is presented. Then, we performed an analysis of the electron localization function along the calculated reaction pathway, identifying the chemical events (bond breaking/forming steps). Finally, a deeper understanding of the role of the X atom in the activation energies is provided by using the interacting quantum atoms method.

Results and discussion

Activation and reaction energies for NH_3 activation using (PXP)Ir (X = B, CH, N, O, SiH) complexes

Inspection of the calculated activation and reaction energies for the oxidative addition of the N–H bond to the metal for

complexes **1–5** demonstrates the critical role of X within the PXP pincer complex for this reaction. The energetic values, some selected geometric parameters, atomic charges and bond orders are shown in Table 1 for the stationary points (R, TS and P) and the isolated species (metallic fragment, F, and ammonia).

The formation of the complex between the metallic fragment and ammonia is exothermic (positive complexation energies) in all cases. The most favorable coordination occurs for the cationic complex **4** (X = O), $\Delta E_{complex}$ = 55.8 kcal mol^{-1}, while neutral complexes present energetic values ranging from 15.1 kcal mol^{-1} for complex **1** (X = B) to 29.2 kcal mol^{-1} for complex **3** (X = N). The complexation energy of ammonia can be related to the stronger/weaker Lewis acid character of the (PXP)Ir metallic fragments.[23]

Activation energies vary from values affordable at room temperature for X = N (18.2 kcal mol^{-1}) and CH (21.9 kcal mol^{-1}) up to non-affordable ones for X = SiH (25.5 kcal mol^{-1}), B (27.4 kcal mol^{-1}), and O (29.9 kcal mol^{-1}). The different Lewis acid character of the (PXP)Ir metallic fragments do not show a consistent correlation with the activation energy. Stronger Lewis acids such as (PNP) or (POP) ligands may coordinate better with the ammonia (the complexation energies are 29.2 and 55.8 kcal mol^{-1}, respectively), being more resistant to the slippage and they should activate more easily the σ(N–H) bond but their activation energies are the lowest and highest values within the series. On the other hand, fragments with a weaker Lewis acid character such as (PBP) or (PSiHP) interact worse with ammonia (the complexation energies are 15.1 and 19.1 kcal mol^{-1}, respectively) facilitating the slippage but disfavoring the σ(N–H) bond activation. However, the calculated activation energies are high: 27.4 and 25.5 kcal mol^{-1} for X = B and SiH, respectively. Therefore, for the metallic fragments considered in this work, the cancellation of effects between the η^1-N and η^2-NH slippage of bound ammonia and N–H bond activation is clearly incomplete, or other effects should be taken into account in order to understand the origin of the activation energies for ammonia oxidative addition.

Not only the kinetics but also the thermodynamics of the process is strongly influenced by the nature of X. Exothermic values are found for X = B (−9.9 kcal mol^{-1}), SiH (−6.8 kcal mol^{-1}) and CH (−4.8 kcal mol^{-1}). For X = N the reaction energy is only slightly exothermic (1.1 kcal mol^{-1}) while for X = O the reaction is endothermic (5.2 kcal mol^{-1}). Noteworthily, complex **4** (X = O), the only cationic complex considered, yields the highest activation and reaction energies. Interestingly, among the neutral complexes, **1** (X = B) yields the highest activation energy, being also the most exothermic. In contrast, complex **3** (X = N) gives the lowest activation energy but the highest reaction energy. These observations indicate that the reaction follows an anti-Hammond behavior, suggesting that the transition structure and the product are very dissimilar.

In order to understand the effect of X on reaction energies it is also interesting to analyze the Ir–N distance, which can be employed as a descriptor of the *trans* influence exerted by the X atom, as pointed out by Goldman *et al.*[26] In this case, the reactant is a square planar Ir(I) complex bearing an ammonia ligand and longer *d*(Ir–N) are found for less electronegative atoms such as B and Si. This explanation is in agreement with the work of Ziegler *et al.*[45] which, based on a detailed molecular orbital analysis on square-planar d^8-complexes, concludes that there is an inverse relationship between the *trans*-directing ability of X and its electronegativity (see Scheme 3). Then, for the complexes considered in this work, the Ir–N distances for the reactants follow the order B > SiH > CH > N > O. When the oxidative addition process takes place, the square planar form is lost and the *trans* effect of the X atom no longer applies. Looking for the dependence of reaction energies with the nature of the X atom in the PXP complex, it is interesting to correlate the Ir–N distance at the reactant with the reaction energies as shown in Fig. 1. The good correlation found (R^2 = 0.980) suggests that weaker coordination of ammonia to the metal, as obtained by the labilizing *trans*-influence, exists in order to give more exothermic values for the oxidative addition.

Table 1 B3LYP-D3BJ/def2-TZVP energetic values (in kcal mol^{-1} relative to the corresponding reactants), geometric distances, NBO atomic charges and Wiberg bond order (BO) indexes for isolated fragments (F + NH_3), reactants (R), transition structures (TS) and products (P) for complexes **1–5**

Complex	Structure	*E*	*d*(IrN)	*d*(IrX)	*q*(Ir)	*q*(X)	BO IrN	BO IrX
1	F + NH_3	15.1	—	1.979	−0.73	0.75	—	0.88
(X = B)	R	0.0	2.382	2.023	−0.76	0.65	0.21	0.88
	TS	27.4	2.183	2.059	−0.68	0.61	0.57	0.89
	P	−9.9	2.015	2.027	−0.67	0.72	0.80	0.89
2	F + NH_3	22.3	—	2.069	−0.57	−0.27	—	0.58
(X = CH)	R	0.0	2.267	2.124	−0.62	−0.42	0.29	0.56
	TS	21.9	2.180	2.134	−0.50	−0.46	0.57	0.56
	P	−4.8	1.998	2.145	−0.51	−0.34	0.87	0.70
3	F + NH_3	29.2	—	2.018	−0.43	−0.57	—	0.56
(X = N)	R	0.0	2.185	2.072	−0.55	−0.68	0.37	0.53
	TS	18.2	2.174	2.049	−0.46	−0.68	0.54	0.54
	P	−1.1	1.981	2.131	−0.39	−0.66	0.91	0.62
4	F + NH_3	55.8	—	2.058	−0.10	−0.51	—	0.36
(X = O)	R	0.0	2.089	2.164	−0.39	−0.55	0.52	0.33
	TS	29.9	2.036	2.173	−0.31	−0.56	0.78	0.32
	P	5.2	1.922	2.244	−0.25	−0.56	1.10	0.27
5	F + NH_3	19.1	—	2.274	−0.86	1.25	—	0.81
(X = SiH)	R	0.0	2.309	2.322	−0.88	1.10	0.26	0.82
	TS	25.5	2.170	2.366	−0.78	1.06	0.57	0.76
	P	−6.8	2.011	2.323	−0.83	1.26	0.84	0.75

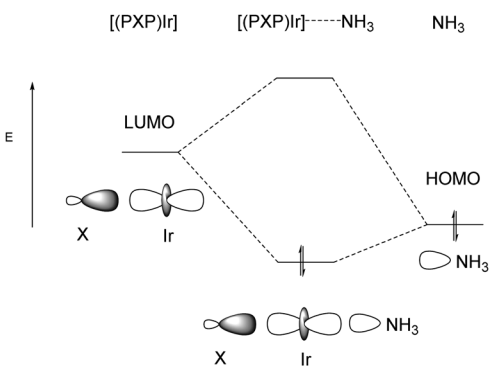

Scheme 3 Orbital diagram representation for the (PXP)Ir–NH_3 interaction.

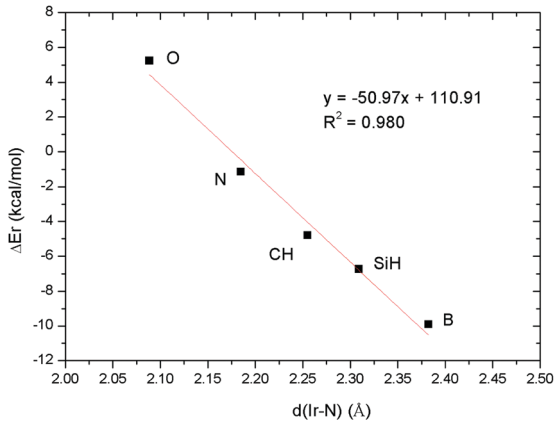

Fig. 1 Plot of reaction energy ΔE_r (in kcal mol^{-1}) *versus* distance (Ir–N) (in Å) for (PXP)IrNH$_3$ complexes (X = B, CH, N, O, SiH).

Remarkably, in all cases, the Ir–N distance decreases substantially upon the oxidative addition of the N–H bond. This change can be attributed to the formation of stronger Ir–N bonds at the transition state, which are even stronger at the product, as indicated by the bond order indexes shown in Table 1. Within the products, the bond orders between Ir and N present similar values to those corresponding to metal carbenes.[46] Therefore, some degree of the Ir = N double bond character is expected for the formed Ir(III) metal amido products. Also the bond order indexes between Ir and X for X = B, SiH indicate some double bond character between the metal and X. This is explained by the availability of empty orbitals at B (of p type) and Si (or d type).

Focusing on the Ir–X distance, it is observed that its variation along the oxidative addition reaction is very small for all complexes. In addition, the values for all complexes are rather similar, except for complex **5**, due to the larger atomic radius of silicon compared to second row atoms. The charges on the metal and X depend strongly on the complex, larger charge separations being found for the less electronegative X atoms (B and Si). It should be noted that the Si–H bond is polarized through the hydride, and then the atomic charge of Si is more positive than B. For all complexes, the metal increases its atomic charge upon the oxidative addition reaction, which is expected for the oxidation of Ir from I to III. Also the X atom increases its charge along the reaction except for the most electronegative atoms (N and O), which do not show any variation.

Bonding evolution analysis of the N–H bond oxidative addition at the (PXP)IrNH$_3$ complexes

Using the ELF, an electronic structure analysis of the stationary points for the oxidative addition of ammonia with (PXP)Ir complexes **1–5** (see Fig. 2 for the representation and values) is first carried out in this section followed by the results of the bonding evolution along the calculated reaction path for complex **2** (X = CH). It should be noted that for all Ir–X, Ir–N and Ir–H bonds there are disynaptic (or hydrogenated) basins connecting both atoms and the integrated electron populations present typical values for bonds with a large covalent character ($>1.5e$). The complexes bearing the less electronegative atoms (B and Si) present a smaller electronic density into the non-shared electron pairs of the metal V(Ir) and the larger electron populations of the V(Ir,B) and V(Ir,Si) basins. This fact supports the formation of some amount of double bond character between Ir and B/Si as suggested by the bond order indexes. Also in agreement with the previous section, the electronic density integrated over the basin populations of the non-shared electron pairs of the metal, V(Ir), decreases significantly at the TS and P (around 1 electron) suggesting that the oxidation of the metal may have already occurred.

It is observed that the V(Ir,N_{NH_3}) disynaptic basin nearly doubles the population when going from R to P. The square planar Ir(I) complex features a single Ir–N_{NH_3} bond with an electron population ranging from 1.77*e* to 1.90*e* which is characteristic of a single bond while the product is an Ir(III) complex with a V(Ir,N_{NH_3}) basin with a total electron density varying from 3.40*e* to 3.67*e*, indicating the existence of the Ir=N double bond character as was pointed out by bond order indices. Therefore, the product can be better described by the two resonance forms shown in Scheme 4.

The behavior of the electron pairs bonding the metal and the atoms of the pincer ligand (PXP) are similar for all complexes.

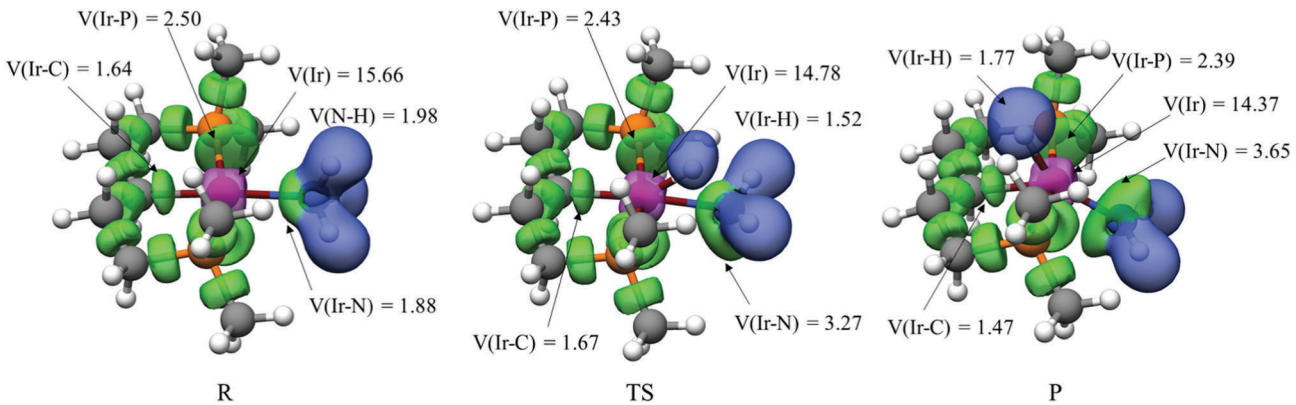

Fig. 2 ELF representation of the reactant (up), transition structure (middle) and product (down) for the oxidative addition of ammonia to complex **1**. Isocontour value of 0.8. Core basins in purple, hydrogenated in blue and disynaptic in green. Hydrogen basins are omitted for simplicity.

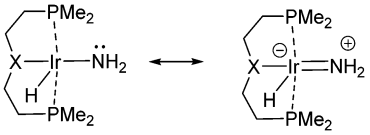

Scheme 4 Proposed resonance structures for Ir(III) product.

The electron populations of V(Ir,X), V(Ir,P_1) and V(Ir,P_2) decrease on going from R and P. This supports the electron-donating role of the PXP ligand, although for X = B, CH and SiH there is an increment of the electronic population of the V(Ir,X) basin at the TS. N–H bond breaking takes place before the transition structure is reached for all complexes, no change being observed in the ELF topology between the TS and P. Therefore, the bond breaking/forming events do not depend on the nature of X. However, different trends are appreciated in the electronic population amounts of the V(Ir,X) and V(Ir,N_{NH_3}) basins which can explain the reported activation and reaction energies.

For all complexes, the variation of the integrated electron density for each ELF basin along the reaction path has been calculated and the changes in the ELF topology have been characterized. In Fig. 3, the reaction paths for complexes **1–3** are shown, indicating the two turning points in ELF topology found. The integrated ELF basin populations along the reaction path for complex **2** is shown in Fig. 4 and the values for the starting and ending points of each associated structural stability domain (SSD) are collected in Table 2 (see ESI† for the other complexes, **1** and **3–5**). The analysis of the basin electron populations allows establishing the curly arrow diagram also depicted in Fig. 3.

The first SSD starts at the reactant and finishes at the transformation of the disynaptic V(N,H_1) basin to a monosynaptic V(H_1) basin through a fold-type catastrophe, according to catastrophe theory. Along this domain, the change is the reorientation

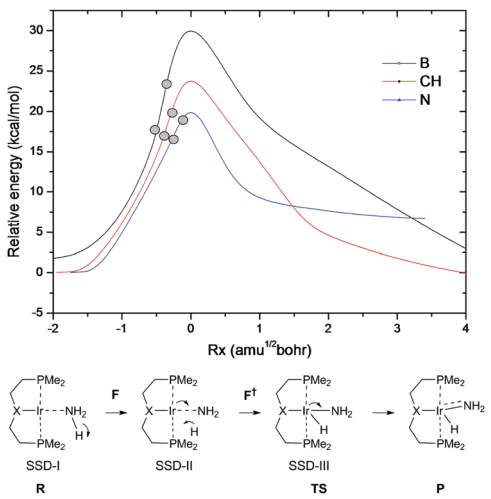

Fig. 3 Energy profiles for the oxidative addition of NH_3 to the (PXP)Ir (X = B, CH, N) fragment calculated at the B3LYP-D3BJ/def2-SVP level. Bifurcation points along the reaction paths are represented by dots. Representation of the electronic rearrangements according to ELF basin populations.

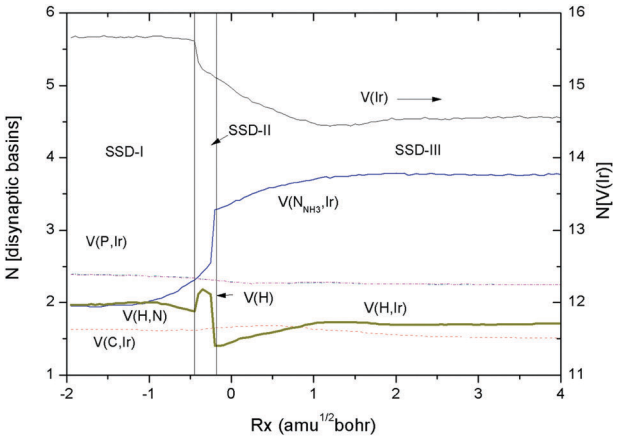

Fig. 4 Integrated electron density for some ELF basins along the calculated IRC path for the oxidative addition of NH_3 to the (PCHP)Ir fragment. Bifurcation points separating the SSDs indicated by vertical lines. Basin populations in electrons. Right axis for V(Ir) basin and left axis for the other basins (disynaptic).

Table 2 Reaction coordinates (IRC, amu$^{1/2}$ Bohr), energy relative to the reactant (*E*, B3LYP-D3BJ/def2-SVP, in kcal mol^{-1}), some geometrical parameters (in Å) and selected ELF basin populations for the initial and final points of the SSDs defined on the reaction path for NH_3 oxidative addition at complex **2**

Complex **2** (X = CH)	SSD-I		SSD-II		SSD-III	
Rx	−1.95	−0.4	−0.35	−0.25	−0.2	4.95
E	0.1	16.7	18.1	20.7	21.8	−1.0
*d*N–H_1	1.022	1.157	1.198	1.294	1.344	3.394
*d*Ir–H_1	2.778	1.765	1.738	1.692	1.672	1.597
*d*Ir–N	2.256	2.185	2.183	2.182	2.181	1.996
*d*IrX	2.123	2.128	2.129	2.131	2.131	2.159
V(Ir,N_{NH_3})	1.97	2.36	2.45	2.58	3.28	3.77
V(Ir,P_1)	2.51	2.4	2.43	2.41	2.42	2.36
V(Ir,P_2)	2.49	2.42	2.46	2.4	2.41	2.37
V(Ir,C_1)	1.68	1.68	1.69	1.69	1.69	1.52
V(H,N)	1.97	1.87	—	—	—	—
V(H_1)	—	—	2.29	2.16	—	—
V(Ir,H_1)	—	—	—	—	1.45	1.8

of the bound ammonia from η^1-N to η^2-NH given by the approximation of the hydrogen to the metal, from 2.778 Å to 1.765 Å. Therefore, the energetic variation of this SSD can be associated to partial decoordination of the ammonia lone pair from the metal and activation of the N–H bond by the metal. As suggested by Macgregor,[23] the stronger/weaker Lewis acid character of the metallic fragment should not affect the energetics of both processes. Inspection of the energetic increments along the first SSD for complexes **1** (17.6 kcal mol^{-1}), **3** (16.1 kcal mol^{-1}), and **5** (17.5 kcal mol^{-1}) confirms this point. The cationic complex **4** presents a higher energy (24.6 kcal mol^{-1}), which can be attributed to the much stronger complexation energy of ammonia to the metal, as compared to the other cases.

The second SSD is very short on the reaction path, being completed when the monosynaptic V(H_1) basin merges with the V(Ir) basin forming the metal-hydride bond V(Ir,H_1). Noteworthily, the V(H_1) basin integrates to slightly more than 2 electrons, therefore it can be considered formally as a hydride transfer

process. Inspection of Fig. 4 shows that the electron density of the V(Ir) basins drops dramatically along this SSD. Therefore, this step can be associated with the metal oxidation process from Ir(I) to Ir(III) which should be facilitated when weaker Lewis acid ligands are employed (B and SiH). Considering the five complexes, the energetic increments along SSD are 5.8 (B), 2.6 (CH), 1.7 (N), 4.1 (O) and 3.2 (SiH) kcal mol^{-1}, which do not agree with the expected trend. However, one should keep in mind that the ionic component of Ir–X bond also has to be taken into account. The analysis of Ir–X bond using a complementary methodology suitable for such ionic interactions will be discussed in the next section.

For all complexes, the third SSD starts shortly before the TS is reached and no more changes in the ELF topology are observed until the final product is obtained. Then, within this SSD there are geometrical changes from a square planar disposition of the ligands around the metal up to a distorted trigonal bipyramid which stabilize the final product. A transference of the electron population from the non-shared V(Ir) basins to the V(Ir,N_{NH_3}) basin is observed. Comparison between different (PXP) ligands reveals that for σ-donor ligands such as those of complexes **1** (X = B) and **5** (X = SiH) another transference from V(Ir,X) to V(Ir) compensates the electronic population of non-shared V(Ir). For more electronegative X groups (N and O), such a transference is not observed.

Analysis of the ionic interactions between Ir and X using IQA methodology

In order to analyze the possible energetic change in the ionic interaction between Ir and X, an energy decomposition analysis is detailed in this section. Within the IQA framework, the interaction energy between two fragments, defined for an atom or a group of atoms, is partitioned into a classical component by adding the V_{en}, V_{ne}, V_{nn}, and the Coulombic part of V_{ee} (V_c^{AB}) and a non-classical, quantum mechanical or exchange correlation term (V_{xc}^{AB}). These two terms, classical and exchange–correlation, can be associated with the traditional chemical concepts of ionicity and covalency.[40] The atomic charges, interaction energies and ionic and covalent terms between Ir and X atoms, calculated with the IQA scheme are reported in Table 3 while the trends for the ionic terms are plotted in Fig. 5.

Looking for insights into the dependence of activation energies on the nature of X on the (PXP)Ir fragment, the interaction energies between the Ir and X atoms at R and TS are analyzed. Interatomic interaction energies cannot be directly related to the total energies because other terms (such as atomic deformation) are not included for simplicity. Hence, when moving from R to TS, complex **1** suffers an energetic destabilization of 0.048 a.u. which is due to the weaker ionic interaction between the Ir and X atoms (0.044 a.u.).

The same behavior, even more pronounced due to the larger positive charge on the Si atom, is observed for complex **5** (X = SiH), 0.115 a.u. Interestingly, the interaction energies between the Ir and C atoms at R and the TS are nearly identical for complex **2**, −0.001 a.u. In this case, the bond energetics are not perturbed by the oxidative addition of the N–H bond.

Table 3 QTAIM integrated properties: interaction E_{int}^{IrX}, classical V_{cl}^{IrX} and exchange–correlation V_{XC}^{IrX} energies, in atomic units between Ir and X atoms for R, TS and P of complexes **1**–**5**. Atomic charges for Ir, q(Ir), and X, q(X), are also included

Complex	Structure	E_{int}^{IrX}	V_{cl}^{IrX}	V_{XC}^{IrX}	q(Ir)	q(X)
1	R	−0.1965	−0.0664	−0.1301	−0.36	1.39
(X = B)	TS	−0.1484	−0.0228	−0.1255	−0.05	1.33
	P	−0.1158	−0.0080	−0.1078	0.12	1.52
2	R	−0.1152	−0.0063	−0.1088	−0.04	−0.07
(X = CH)	TS	−0.1166	−0.0128	−0.1038	0.21	−0.11
	P	−0.1125	−0.0104	−0.1021	0.48	−0.05
3	R	−0.1452	−0.0422	−0.1030	0.07	−1.08
(X = N)	TS	−0.1724	−0.0679	−0.1045	0.28	−1.10
	P	−0.1800	−0.0886	−0.0914	0.58	−1.07
4	R	−0.1005	−0.0409	−0.0596	0.13	−1.03
(X = O)	TS	−0.1176	−0.0605	−0.0571	0.34	−1.04
	P	−0.1293	−0.0802	−0.0491	0.59	−1.04
5	R	−0.4553	−0.3704	−0.0848	−0.80	2.57
(X = SiH)	TS	−0.3404	−0.2538	−0.0866	−0.46	2.47
	P	−0.3149	−0.2427	−0.0722	−0.24	2.64

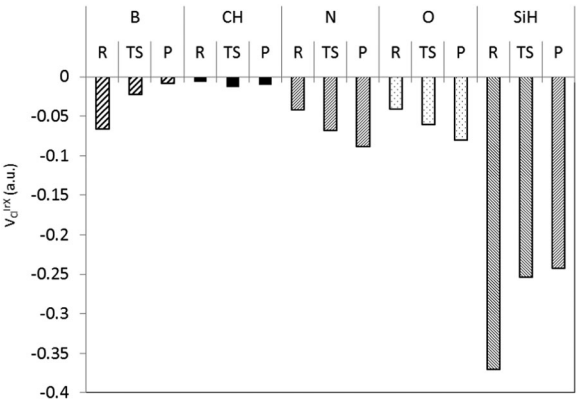

Fig. 5 Plots of the interacting quantum atom values for the classical interaction energy, V_{cl}^{IrX}, between the QTAIM atomic basins of atoms Ir and X (X = B, CH, N, O, SiH) at the stationary points.

The other two remaining complexes, **3** and **4**, show the opposite trend to **1** and **5**. The energetic interaction between the Ir and X atoms is stronger at the TS compared to the R, −0.026 a.u. and −0.020 a.u. for X = N and O, respectively. This energetic stabilization of the TS for complexes **3** and **4** is of electrostatic nature. In Fig. 5, the trends of the ionic interaction energy between Ir and X atoms can be clearly visualized, complexes **1** and **5** increase the activation energy (and the reaction energy). In contrast, complexes **3** and **4** favour both the kinetics and thermodynamics due to the stronger ionic interaction between the Ir and X atoms.

These trends can be rationalized considering the fact that the atomic charges at X are positive for B and Si while negative for C, N and O (see Tables 1 and 3) due to its electronegativity. As revealed by the previous bonding evolution analysis along the reaction path, the oxidation of the metal takes place before the TS and the electronic density from its lone pairs are transferred to the Ir–N and Ir–H bonds. Consequently the atomic charge at the metal shows less negative (or more positive) values. On comparison between R and TS, the complexes containing B and

Si (positive atomic charges) will decrease the electrostatic interaction with the metal (less negative atomic charge) and then the activation barrier will be higher. In the contrast, those complexes with a more negative atomic charge (N and O) will increase the ionic interaction with the metal and consequently the activation barrier will be lowered.

Experimental section

Computational details

All DFT theoretical calculations have been performed using the Gaussian 09 program package.[47] The B3LYP method[48] has been employed including the D3 dispersion correction scheme developed by Grimme[49] using the Becke–Johnson damping[50] for both energies and gradient calculations in conjunction with the ''ultrafine'' grid. The def2-SVP basis set[51] has been selected for all atoms for geometry optimizations, performing single point calculations with the def2-TZVP basis set to refine energy results. The nature of the stationary points has been confirmed by analytical frequency analysis, and the transition states were characterized by calculation of the reaction paths following the intrinsic reaction coordinate. The complexation energies are defined as:

$$\Delta E_{\text{complex}} = E(\text{F}) + E(\text{NH}_3) - E(\text{R}) \quad (1)$$

where R stands for the reactant and F for the metallic fragment.

Atomic charges have been calculated using the natural bond analysis and the QTAIM methodology, while bond orders have been found using the Wiberg approach. The ELF study was performed with the TopMod program[52] using the corresponding monodeterminantal B3LYP-D3BJ/def2-SVP wave functions in a tridimensional grid of 200 points in each direction. The IQA analysis was performed using the AIMAll package.[53] The ELF plots of molecular structures were represented using Chimera software.[54]

Conclusions

The successful design of new organometallic complexes with improved catalytic properties can only be achieved if there is a detailed understating of the electronic effects determining its reactivity. In this work, the activation and reaction energies for the N–H bond activation of ammonia using (PXP)Ir (X = B, CH, N, O and SiH) pincer complexes are calculated showing the crucial impact of the X group. The electronic factors determining the process are explained using theoretical tools based on the topological analysis of the electron localization function and the IQA energy decomposition between Ir and X. These methods are employed in a complementary way; the ELF analyzes in detail the rearrangements of electron pairs while the IQA allows quantifying ionic interaction energies at the stationary points. The following conclusions can be drawn:

(i) The oxidative addition of N–H bond by the (PXP)Ir metallic fragments do not follow the Hammond postulate, the chemical events occurring near the TS and the product are dissimilar as revealed by the bonding evolution theory.

(ii) For the five considered complexes, a correlation is found between the reaction energy and lability of the coordinated ammonia ligand, which is controlled by the *trans*-influence of the X ligand. Strong *trans*-influence ligands favor exothermic reactions.

(iii) Analysis of the electronic rearrangements along the reaction using bonding evolution theory reveals that the two chemical events found take place before the TS for all considered complexes. The first SSD corresponds to the ammonia reorientation followed by N–H bond activation. In the next SSD, the hydride is transferred to the metal center which is then oxidized, and an important transfer of electron density from the Ir non-shared pairs to the Ir–N bond is detected. The final SSD, starts at the TS and concludes at the final product. Along this step, there are geometrical changes and the transfer from the Ir non-shared pairs to the Ir–N bond continues. For X = B and SiH, the non-shared electron pairs of Ir receive electron density from the Ir–X bond.

(iv) Calculated activation energies for NH_3 oxidative addition by (PXP)Ir metallic fragments are strongly dependent on the nature of the X atom. The activation energy depends on three main factors: (i) ammonia reorientation from η^1-N to η^2-NH (involving partial decoordination of ammonia), (ii) N–H bond activation and (iii) the metal oxidation process. The energetic cost of factors (i) and (ii) are similar for complexes containing X = B, CH, N and SiH (around 17 kcal mol^{-1}) while it is larger for X = O (24.6 kcal mol^{-1}) due to the stronger ammonia coordination to a cationic metallic fragment. Metal oxidation decreases its atomic charge and the ionic interactions between Ir and X vary differently for the considered (PXP)Ir fragments depending on the electronegativity of X atom.

Conflicts of interest

There are no conflicts to declare.

Acknowledgements

The authors express their appreciation for the financial support from the MINECO/FEDER project CTQ2015-67366-P, DGA/FSE (group E07) and Vicerrectoría de Investigación, Universidad de Medellin, Project 749, 2015/00017/002. Co-authors J. M., E. V. and V. P. gratefully acknowledge the resources provided by the supercomputers ''Memento'' and ''Terminus'', the technical expertise and assistance provided by the Institute for Biocomputation and the Physics of Complex Systems (BIFI) – Universidad de Zaragoza. J. M. thankfully acknowledges the Spanish MECD for a FPU fellowship (FPU14/06003).

Notes and references

1 (*a*) T. Braun, *Angew. Chem., Int. Ed.*, 2005, **44**, 5012–5014; (*b*) J. I. van der Vlugt, *Chem. Soc. Rev.*, 2010, **39**, 2302–2322; (*c*) J. L. Klinkenberg and J. F. Hartwig, *Angew. Chem., Int. Ed.*,

2011, **50**, 86–95; (*d*) J. Kim, H. J. Kim and S. Chang, *Eur. J. Org. Chem.*, 2013, 3201–3213.

2 (*a*) G. L. Hillhouse and J. E. Bercaw, *J. Am. Chem. Soc.*, 1984, **106**, 5472–5478; (*b*) A. L. Casalnuovo, J. C. Calabrese and D. Milstein, *Inorg. Chem.*, 1987, **26**, 971–973; (*c*) Y. Nakajima, H. Kameo and H. Suzuki, *Angew. Chem., Int. Ed.*, 2006, **45**, 950–952; (*d*) I. Mena, M. A. Casado, P. García-Orduña, V. Polo, F. J. Lahoz, A. Fazal and L. A. Oro, *Angew. Chem., Int. Ed.*, 2011, **50**, 11735–11738; (*e*) E. Velez, M. P. Betoré, M. A. Casado and V. Polo, *Organometallics*, 2015, **34**, 3959–3966; (*f*) M. Álvarez, E. Álvarez, M. R. Fructos, J. Urbano and P. J. Pérez, *Dalton Trans.*, 2016, **45**, 14628–14633; (*g*) G. W. Margulieux, M. J. Bezdek, Z. R. Turner and P. J. Chirik, *J. Am. Chem. Soc.*, 2017, **139**, 6110–6113.

3 E. Khaskin, M. A. Iron, L. J. W. Shimon, J. Zhang and D. Milstein, *J. Am. Chem. Soc.*, 2010, **132**, 8542–8543.

4 (*a*) Y. H. Chang, Y. Nakajima, H. Tanaka, K. Yoshizawa and F. Ozawa, *J. Am. Chem. Soc.*, 2013, **135**, 11791–11794; (*b*) H. O. Taguchi, D. Sasaki, K. Takeuchi, S. Tsujimoto, T. Matsuo, H. Tanaka, K. Yoshizawa and F. Ozawa, *Organometallics*, 2016, **35**, 1526–1533.

5 (*a*) D. V. Gutsulyak, W. E. Piers, J. Borau-Garcia and M. Parvez, *J. Am. Chem. Soc.*, 2013, **135**, 11776–11779; (*b*) R. M. Brown, J. B. Garcia, J. Valjus, C. J. Roberts, H. M. Tuononen, M. Parvez and R. Roesler, *Angew. Chem., Int. Ed.*, 2015, **54**, 6274–6277.

6 (*a*) Y. Kim and S. Park, *C. R. Chim.*, 2016, **19**, 614–629; (*b*) J. Cámpora, P. Palma, D. del Río, M. M. Conejo and E. Alvarez, *Organometallics*, 2004, **23**, 5653–5655; (*c*) D. J. Fox and R. G. Bergman, *J. Am. Chem. Soc.*, 2003, **125**, 8984–8985; (*d*) A. W. Kaplan, J. C. M. Ritter and R. G. Bergman, *J. Am. Chem. Soc.*, 1998, **120**, 6828–6829; (*e*) D. Conner, K. N. Jayaprakash, T. R. Cundari and T. B. Gunnoe, *Organometallics*, 2004, **23**, 2724–2733; (*f*) A. W. Holland and R. G. Bergman, *J. Am. Chem. Soc.*, 2002, **124**, 14684–14695; (*g*) K. N. Jayaprakash, D. Conner and T. B. Gunnoe, *Organometallics*, 2001, **20**, 5254–5256.

7 (*a*) J. Zhao, A. S. Goldman and J. F. Hartwig, *Science*, 2005, **307**, 1080–1082; (*b*) E. Morgan, D. F. MacLean, R. McDonald and L. Turculet, *J. Am. Chem. Soc.*, 2009, **131**, 14234–14236.

8 A. Uhe, M. Hölscher and W. Leitner, *Chem. – Eur. J.*, 2013, **19**, 1020–1027.

9 J. P. Collman, *Acc. Chem. Res.*, 1968, **1**, 136–143.

10 J. A. Labinger, *Organometallics*, 2015, **34**, 4784–4795.

11 J. J. Low and W. A. Goddard, *J. Am. Chem. Soc.*, 1986, **108**, 6115–6128.

12 J. Saillard and R. Hoffmann, *J. Am. Chem. Soc.*, 1984, **106**, 2006–2026.

13 N. Koga and K. Morokuma, *J. Phys. Chem.*, 1990, **94**, 5454–5462.

14 R. H. Crabtree and J. M. Quirk, *J. Organomet. Chem.*, 1980, **199**, 99–106.

15 M. D. Su and S. Y. Chu, *J. Phys. Chem. A*, 1998, **102**, 10159–10166.

16 M. D. Su and S. Y. Chu, *Inorg. Chem.*, 1998, **37**, 3400–3406.

17 R. Fazaeli, A. Ariafard, S. Jamshidi, E. S. Tabatabaie and K. A. Pishro, *J. Organomet. Chem.*, 2007, **692**, 3984–3993.

18 J. F. Hartwig, *Inorg. Chem.*, 2007, **46**, 1936–1947.

19 A. Ariafard and B. F. Yates, *J. Organomet. Chem.*, 2009, **694**, 2075–2084.

20 M. Yamashita, J. V. C. Vicario and J. F. Hartwig, *J. Am. Chem. Soc.*, 2003, **125**, 16347–16360.

21 K. Krogh-Jespersen and A. S. Goldman, in *Transition State Modeling for Catalysis*, ed. D. G. Truhlar and K. Morokuma, American Chemical Society, Washington DC, 1999, pp. 151–162.

22 M. D. Su and S. Y. Chu, *J. Am. Chem. Soc.*, 1997, **119**, 10178–10185.

23 S. A. Macgregor, *Organometallics*, 2001, **20**, 1860–1874.

24 R. A. Diggle, S. A. Macgregor and M. K. Whittlesey, *Organometallics*, 2004, **23**, 1857–1865.

25 T. R. Cundari, *J. Am. Chem. Soc.*, 1994, **116**, 340–347 and references therein.

26 D. Y. Wang, Y. Choliy, M. C. Haibach, J. F. Hartwig, K. Krogh-Jespersen and A. S. Goldman, *J. Am. Chem. Soc.*, 2016, **138**, 149–163.

27 M. Schultz and D. Milstein, *J. Chem. Soc., Chem. Commun.*, 1993, 318–319.

28 G. Knizia and J. E. M. N. Klein, *Angew. Chem., Int. Ed.*, 2015, **54**, 5518–5522.

29 J. Andres, S. Berski and B. Silvi, *Chem. Commun.*, 2016, **52**, 8183–8195.

30 B. Silvi and A. Savin, *Nature*, 1994, **371**, 683–686.

31 X. Krokidis, S. Noury and B. Silvi, *J. Phys. Chem. A*, 1997, **101**, 7277–7282.

32 V. Polo, J. Andres, S. Berski, L. R. Domingo and B. Silvi, *J. Phys. Chem. A*, 2008, **112**, 7128–7136.

33 P. Gonzalez-Navarrete, J. Andres and S. Berski, *J. Phys. Chem. Lett.*, 2012, **3**, 2500–2505.

34 A. S. Nizovtsev, *J. Comput. Chem.*, 2013, **34**, 1917–1924.

35 I. Viciano, P. Gonzalez-Navarrete, J. Andres and S. Marti, *J. Chem. Theory Comput.*, 2015, **11**, 1470–1480.

36 M. J. S. Phipps, T. Fox, C. S. Tautermann and C. K. Skylaris, *Chem. Soc. Rev.*, 2015, **44**, 3177–3211.

37 K. Kitaura and K. Morokuma, *Int. J. Quantum Chem.*, 1976, **10**, 325–331.

38 M. A. Blanco, A. M. Pendas and E. Francisco, *J. Chem. Theory Comput.*, 2005, **1**, 1096–1109.

39 P. Maxwell, A. M. Pendás and P. L. A. Popelier, *Phys. Chem. Chem. Phys.*, 2016, **18**, 20986–21000.

40 D. Tiana, E. Francisco, M. A. Blanco, P. Macchi, A. Sironi and A. M. Pendas, *J. Chem. Theory Comput.*, 2010, **6**, 1064–1074.

41 I. Cukrowski, J. H. de Lange and M. Mitoraj, *Chem. – Eur. J.*, 2014, **20**, 1–13.

42 J. M. Guevara-Vela, R. Chavez-Calvillo, J. Garcia-Revilla, J. Hernandez-Trujillo, O. Christiansen, E. Francisco, A. M. Pendas and T. Rocha-Rinza, *Chem. – Eur. J.*, 2013, **19**, 14304–14315.

43 D. Ferro-Costas and R. A. Mosquera, *Phys. Chem. Chem. Phys.*, 2015, **17**, 7424–7434.

44 A. M. Pendas, M. A. Blanco and E. Franco, *J. Comput. Chem.*, 2009, **30**, 98–109.
45 M. P. Mitoraj, H. Zhu, A. Michalak and T. Ziegler, *Int. J. Quantum Chem.*, 2009, **109**, 3379–3386.
46 G. Frenking, M. Sola and S. F. Vyboishchikov, *J. Organomet. Chem.*, 2005, **680**, 6178–6204.
47 M. J. Frisch, G. W. Trucks, H. B. Schlegel, G. E. Scuseria, M. A. Robb, J. R. Cheeseman, G. Scalmani, V. Barone, B. Mennucci, G. A. Petersson, H. Nakatsuji, M. Caricato, X. Li, H. P. Hratchian, A. F. Izmaylov, J. Bloino, G. Zheng, J. L. Sonnenberg, M. Hada, M. Ehara, K. Toyota, R. Fukuda, J. Hasegawa, M. Ishida, T. Nakajima, Y. Honda, O. Kitao, H. Nakai, T. Vreven, J. A. Montgomery, J. E. Peralta, F. Ogliaro, M. Bearpark, J. J. Heyd, E. Brothers, K. N. Kudin, V. N. Staroverov, R. Kobayashi, J. Normand, K. Raghavachari, A. Rendell, J. C. Burant, S. S. Iyengar, J. Tomasi, M. Cossi, N. Rega, N. J. Millam, M. Klene, J. E. Knox, J. B. Cross, V. Bakken, C. Adamo, J. Jaramillo, R. Gomperts, R. E. Stratmann, O. Yazyev, A. J. Austin, R. Cammi, C. Pomelli, J. W. Ochterski, R. L. Martin, K. Morokuma, V. G. Zakrzewski, G. A. Voth, P. Salvador, J. J. Dannenberg, S. Dapprich, A. D. Daniels, Ö. Farkas, J. B. Foresman, J. V. Ortiz, J. Cioslowski and D. J. Fox, *Gaussian 09, Revision D.01*, Gaussian, Inc., Wallingford CT, 2009.
48 (*a*) C. T. Lee, W. T. Yang and R. G. Parr, *Phys. Rev. B: Condens. Matter Mater. Phys.*, 1988, **37**, 785–789; (*b*) A. D. Becke, *J. Chem. Phys.*, 1993, **98**, 1372–1377; (*c*) A. D. Becke, *J. Chem. Phys.*, 1993, **98**, 5648–5652.
49 S. Grimme, J. Antony, S. Ehrlich and H. Krieg, *J. Chem. Phys.*, 2010, **132**, 154104.
50 E. R. Johnson and A. D. Becke, *J. Chem. Phys.*, 2005, **123**, 024101.
51 F. Weigend and R. Ahlrichs, *Phys. Chem. Chem. Phys.*, 2005, **7**, 3297–3305.
52 S. Noury, X. Krokidis, F. Fuster and B. Silvi, *Comput. Chem.*, 1999, **23**, 597.
53 T. A. Keith, *AIMAll (Version 17. 01.25)*, TK Gristmill Software, Overland Park KS, USA, 2017.
54 (*a*) E. F. Pettersen, T. D. Goddard, C. C. Huang, G. S. Couch, D. M. Greenblatt, E. C. Meng and T. E. Ferrin, *J. Comput. Chem.*, 2004, **25**, 1605–1612; (*b*) T. D. Goddard, C. C. Huang and T. E. Ferrin, *J. Struct. Biol.*, 2007, **157**, 281–287.

Chemical Science

EDGE ARTICLE

Cite this: *Chem. Sci.*, 2017, **8**, 4811

A well-defined NHC–Ir(III) catalyst for the silylation of aromatic C–H bonds: substrate survey and mechanistic insights†

Laura Rubio-Pérez,[a] Manuel Iglesias,*[a] Julen Munárriz,[b] Victor Polo,[b] Vincenzo Passarelli,[ac] Jesús J. Pérez-Torrente[a] and Luis A. Oro*[ad]

Received 4th November 2016
Accepted 3rd April 2017

DOI: 10.1039/c6sc04899d

rsc.li/chemical-science

A well-defined NHC–Ir(III) catalyst, $[Ir(H)_2(IPr)(py)_3][BF_4]$ (IPr = 1,3-bis-(2,6-diisopropylphenyl)imidazol-2-ylidene), that provides access to a wide range of aryl- and heteroaryl-silanes by intermolecular dehydrogenative C–H bond silylation has been prepared and fully characterized. The directed and non-directed functionalisation of C–H bonds has been accomplished successfully using an arene as the limiting reagent and a variety of hydrosilanes in excess, including Et_3SiH, Ph_2MeSiH, $PhMe_2SiH$, Ph_3SiH and $(EtO)_3SiH$. Examples that show unexpected selectivity patterns that stem from the presence of aromatic substituents in hydrosilanes are also presented. The selective bisarylation of bis(hydrosilane)s by directed or non-directed silylation of C–H bonds is also reported herein. Theoretical calculations at the DFT level shed light on the intermediate species in the catalytic cycle and the role played by the ligand system on the Ir(III)/Ir(I) mechanism.

Introduction

Organosilicon compounds are key building blocks in modern organic synthesis, often used as intermediates for complex molecules or monomers for silicone polymers. The synthetic versatility of organosilanes can be attributed to their straightforward functionalisation by various organic transformations, together with the low cost and non-toxic nature of silicon reagents.[1] Moreover, conjugated organosilicon materials are attractive targets *per se* owing to their unique properties, which permit widespread applicability in the fields of organic electronics and photonics.[2,3]

The preparation of organosilanes by catalytic silylation of C–H bonds represents a more atom- and step-efficient alternative to stoichiometric processes[4] and cross-coupling reactions.[5] The silylation of arenes and heteroarenes, in particular, is an important reaction due to the ubiquitous presence of these moieties in natural products and materials. These reactions are typically divided into two main groups: intermolecular and intramolecular. The former requires prefunctionalisation of the (hetero)arene with a hydrosilane moiety, which may be achieved by hydrosilylation or dehydrogenative silylation using di(hydro)silanes.[6] Intermolecular silylations may be classified into directed and undirected reactions. Directed silylations require the presence of a coordinating group in the substrate that reversibly binds to the catalyst. This interaction leaves a C–H bond in the proximity of the active site, which facilitates its activation and defines the selectivity of the process. These reactions mostly use disilanes[7] or hydrosilanes as silicon sources. The latter usually requires the presence of a hydrogen acceptor,[8] although acceptor-less reactions have also been described.[9] Undirected silylation reactions, on the other hand, make use of substrates that lack a coordinating group that is able to direct the reaction. These are more challenging substrates due to their ensuing selectivity issues and low reactivity; however, the scope of this reaction has experienced significant progress[10] since the early reports by Curtis and Berry.[11]

In spite of the prodigious advances that the C–H silylation methodology has experienced in recent years,[12] there is still much room for further development. On the lookout for expanding the synthetic reach of this catalytic process, various improvements may be envisaged: (1) the use of more synthetically useful hydrosilane partners is an unresolved problem.[12a] For instance, the preparation of organotrialkoxysilanes by catalytic C–H bond silylation remains widely unexplored.[13–15] (2) A comprehensive survey of hydro(aryl)silanes would be of interest owing to the potential applicability of these reactions in

[a]*Departamento Química Inorgánica – ISQCH, Universidad de Zaragoza – CSIC, Pedro Cerbuna 12, 50009 Zaragoza, Spain. E-mail: miglesia@unizar.es; oro@unizar.es*
[b]*Departamento Química Física – Instituto de Biocomputación y Física de Sistemas Complejos (BIFI), Universidad de Zaragoza, Pedro Cerbuna 12, 50009 Zaragoza, Spain*
[c]*Centro Universitario de la Defensa, Ctra. Huesca s/n, ES-50090 Zaragoza, Spain*
[d]*King Fahd University of Petroleum & Minerals (KFUPM), Dhahran 31261, Saudi Arabia*

† Electronic supplementary information (ESI) available: Spectroscopic and analytical data. DFT optimized structures and computational details. X-ray crystallographic data for **1**, **2** and **3** (CCDC 1507888, 1507890 and 1507889, respectively). For ESI and crystallographic data in CIF or other electronic format see DOI: 10.1039/c6sc04899d

the synthesis of new materials. Only a limited number of examples has been hitherto reported on this topic.[16,17] (3) The use of an arene as the limiting reagent is of remarkable importance for the synthetic applicability of this reaction since the arene is frequently the most valuable component in these transformations. Examples of non-directed silylation of arenes under this stoichiometry are scarce and a wider substrate scope, especially regarding unactivated substrates, is highly desirable.[18]

Most of the literature on the catalytic dehydrogenative silylation of C–H bonds has focused on the use of "*in situ*" generated catalysts from commercial metal precursors and ligands. However, somewhat less attention has been paid to the development of well-defined organometallic complexes.[16c,19] In this regard, the design of catalysts featuring N-heterocyclic carbenes (NHCs) as ancillary ligands has been surprisingly overlooked,[19b] especially when taking into account their success story in homogeneous catalysis.[20]

We report herein on the synthesis and characterization of a well-defined Ir(III)–NHC complex that behaves as an efficient and versatile catalyst for the dehydrogenative silylation of aromatic C–H bonds for a wide range of hydrosilanes using an arene as the limiting reagent. By means of this catalytic process we have prepared a broad variety of arylsilanes, including examples of the elusive triarylsilanes and trialkoxysilanes. In addition, an experimental and theoretical study on the mechanism that controls this process is discussed here.

In the search for new catalysts for the silylation of C–H bonds, we envisaged an NHC–Ir species featuring labile ligands that would allow for the coordination of substrates and additives[19b,21] while facilitating the C–H and Si–H activation processes thanks to the unique properties of the NHC ligand.[22] On these grounds, complex $[Ir(H)_2(IPr)(py)_3][BF_4]$ (IPr = 1,3-bis-(2,6-diisopropylphenyl)imidazol-2-ylidene) (**1**) would be an excellent candidate for this study since the pyridine ligands can be straightforwardly substituted[23] and the two hydrides may be removed with a hydrogen acceptor or expelled as molecular hydrogen.[24]

Results and discussion

Synthesis and characterization of the pre-catalyst

Complex **1** was prepared in good yield in acetone from [Ir(acetone)(COD)(IPr)][BF_4] (COD = 1,5-cyclooctadiene) in the presence of excess pyridine (py) under a hydrogen atmosphere (Scheme 1).[25]

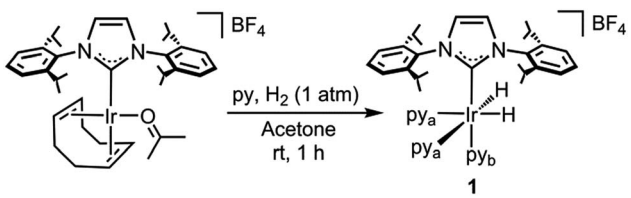

Scheme 1 Synthesis of complex **1**.

Crystals of complex **1** were obtained by the slow diffusion of diethyl ether into a saturated dichloromethane solution. Its global connectivity pattern was confirmed by single crystal X-ray diffraction (Fig. 1). The molecular structure of **1** shows that the iridium centre adopts a slightly distorted octahedral geometry and the two pyridines *cis* to the IPr ligand are visibly displaced from the equatorial plane, probably due to the steric interference of the bulky wingtip groups of the NHC. Remarkably, the two pyridines in the equatorial plane, *trans* to the hydrides, feature longer Ir–N bond lengths compared to that situated in the *trans* position to the IPr ligand.

The ^{1}H NMR spectrum of **1** shows a singlet peak in the high field region at $\delta = -22.48$ ppm for both hydride ligands. The IPr ligand presents one singlet peak for the NC*H* protons at $\delta =$ 7.07 ppm and a septuplet peak for the C*H*Me$_2$ protons of the isopropyl groups at $\delta = 2.87$ ppm, which suggests a fast rotation of the NHC ligand about the Ir–C bond at room temperature.

Variable temperature NMR analysis shows no line broadening at 193 K, which is consistent with a free energy rotation barrier lower than *ca.* 30 kJ mol^{-1}. Two different types of pyridine ligands are observed at $\delta = 8.14$ and 7.84 ppm in a 2 : 1 ratio respectively and are positioned in a facial arrangement. The distinct environments observed for the pyridine ligands (labeled "a" and "b" in Scheme 1) are consistent with pyridine dissociation being slow on the NMR time scale.

The most representative resonance in the ^{13}C NMR spectrum is that corresponding to the carbene carbon at $\delta = 154.7$ ppm. The ^{19}F NMR spectrum confirms the cationic nature of **1** with a peak at $\delta = -155.2$ ppm that is assigned to the BF_4^- counterion.

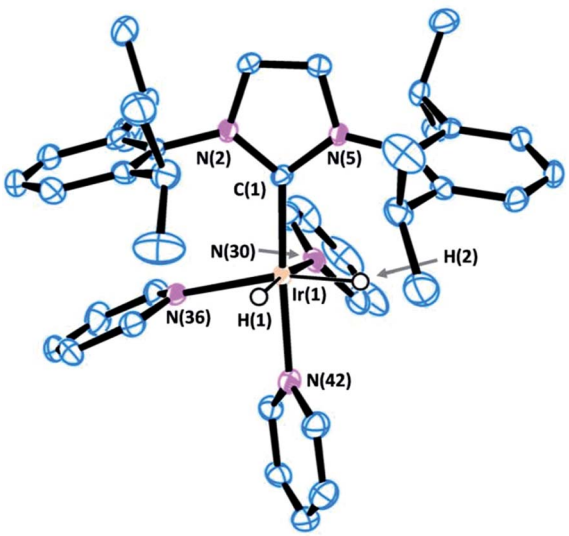

Fig. 1 ORTEP view of the cation $[Ir(H)_2(IPr)(py)_3]^+$ in **1** with a numbering scheme adopted. Most of the hydrogens are omitted for clarity and thermal ellipsoids are at 50% probability. Selected bond lengths (Å) and angles (°): C(1)–N(2) 1.378(4), C(1)–N(5) 1.379(4), C(1)–Ir(1) 1.996(3), N(30)–Ir(1) 2.180(3), N(36)–Ir(1) 2.231(3), N(42)–Ir(1) 2.126(3), N(2)–C(1)–N(5) 102.2(3), C(1)–Ir(1)–N(42) 172.88(13), C(1)–Ir(1)–N(30) 95.39(13), N(42)–Ir(1)–N(30) 89.24(12), C(1)–Ir(1)–N(36) 103.04(13), N(42)–Ir(1)–N(36) 81.93(11), N(30)–Ir(1)–N(36) 94.44(11).

Catalysis

Initial catalytic tests using **1** as a pre-catalyst and 2-(2-thienyl) pyridine as a substrate focused on the optimisation of the reaction conditions and the assessment of whether a hydrogen acceptor would be required. When norbornene was employed as a hydrogen acceptor, a nearly quantitative yield was obtained after 24 h at 110 °C; however, under acceptor-less conditions only a 45% yield was achieved. Other hydrogen acceptors such as cyclohexene or 3,3-dimethyl-1-butene were tested, although somewhat lower yields were obtained.

In order to assess the scope of **1** as a pre-catalyst for the silylation of C–H bonds with different hydrosilanes, a variety of aromatic substrates with and without a directing group (Schemes 2 and 3, respectively) were examined. The catalytic reactions were performed in THF at 110 °C in a sealed flask using a 5 mol% catalyst loading and a hydrosilane/arene ratio of 3 : 1.

The use of **1** as a pre-catalyst permits the silylation of 2-(2-thienyl)pyridine with a wide range of hydrosilanes, namely, Et_3SiH, Ph_2MeSiH, $PhMe_2SiH$, Ph_3SiH and $(EtO)_3SiH$. Remarkably, to the best of our knowledge, these are the only examples of the intermolecular catalytic silylation of aryl C–H bonds that successfully employ triaryl-[17] or trialkoxy-silanes (excluding the boron catalysed silylation of *N*,*N*-dimethylaniline reported by Hou *et al.*[10a] and the silatranes reported by Miyaura *et al.*[13]). However, in the case of the latter, no product was recovered when purification of the crude mixture was attempted by column chromatography. Other substrates featuring nitrogen-containing directing groups, namely, 1-phenylpyrazole, 2-phenylpyridine, and 2-(*p*-tolyl)pyridine, were also successfully converted to the silylated products, except for triethoxysilane (Scheme 2). To our surprise, the silylation of 2-(*p*-tolyl)pyridine showed an unexpected selectivity shift when aromatic silanes were used instead of triethylsilane. In contrast to the previous examples, the directing group, *i.e.* the pyridine moiety, undergoes exclusive silylation of its C5–H bond. This rare selectivity has also been reported recently by Oestreich and co-workers.[26]

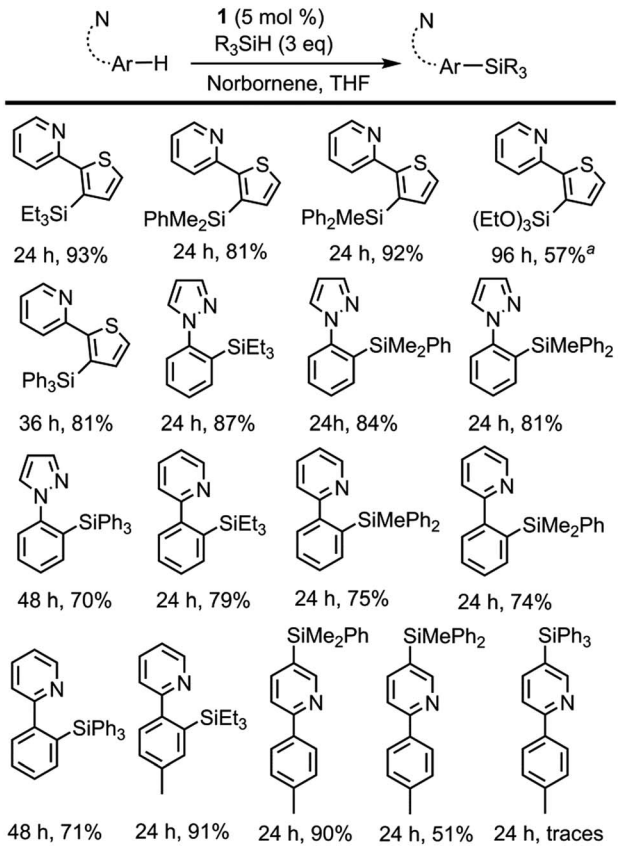

Scheme 2 Directed dehydrogenative silylation of aromatic and heteroaromatic rings. Reaction conditions: cat **1** (5 mol%), norbornene (0.40 mmol), arene (0.13 mmol), R_3SiH (0.40 mmol) in THF (2 mL) at 110 °C. Isolated yields are shown. [a] Yield determined by ^1H NMR using THF-d_8.

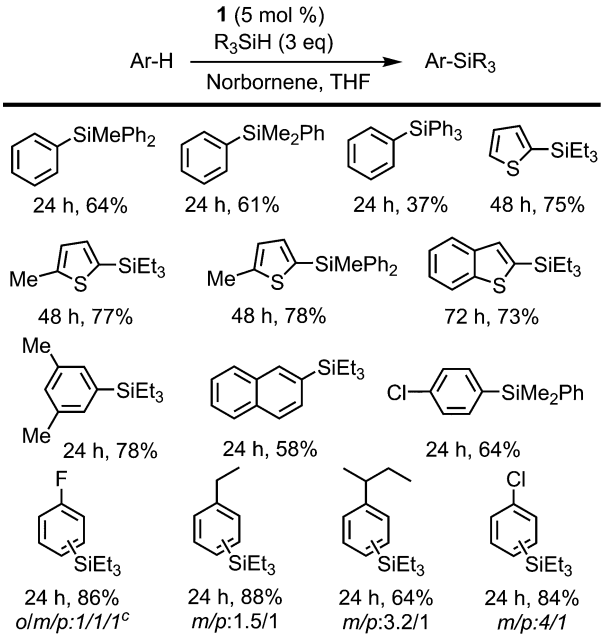

Scheme 3 Non-directed dehydrogenative silylation of aromatic and heteroaromatic rings. Reaction conditions: cat **1** (5 mol%), norbornene (0.40 mmol), arene (0.13 mmol), R_3SiH (0.40 mmol) in THF (2 mL) at 110 °C. Isolated yields are shown. [a] Disilylated product was identified in 7% yield.

The intermolecular non-directed silylation of aromatic and heteroaromatic molecules was also achieved by employing an arene as the limiting reactant (3 equivalents of silane). Among these reactions, the regioselective silylation of naphthalene at the C2-position was also achieved. This is, to the extent of our knowledge, the first example of naphthalene functionalisation by catalytic C–H bond silylation. The silylation of *m*-xylene, thiophene, benzothiophene and 2-methylthiophene was also regioselective, which contrasts to the mixture of regioisomers obtained for fluoro-, chloro-, ethylbenzene and *sec*-butylbenzene using triethylsilane (Scheme 3). To our delight, the selective silylation of chlorobenzene to afford the *para* isomer exclusively was accomplished with $PhMe_2SiH$.

The relative reactivity of the different silanes may be estimated from the results presented in Schemes 2 and 3. The least

reactive silane is $(EtO)_3SiH$ since it only works for the most reactive substrate, 2-thienylpyridine, and requires a reaction time of 96 h. The following hydrosilanes in an ascending order of reactivity would be Ph_3SiH, as longer reaction times are required, then Et_3SiH, Ph_2MeSiH and $PhMe_2SiH$, which usually show similar reactivity.

A competitive experiment was performed using 1 equivalent of 2-phenylpyridine and 1 equivalent of ethylbenzene with Et_3SiH under the reaction conditions described in Scheme 2 in order to assess the relative reactivity of directed and non-directed reactions. Exclusive silylation of 2-phenylpyridine was observed, which supports the expected reactivity boost that stems from the presence of a directing group.

The selective synthesis of bisarylated bis(silanes) was achieved by the reaction of arenes with the bis(hydrosilane)s, employing **1** as a pre-catalyst (Scheme 4). It is worth mentioning that, in contrast to other examples in the literature, no formation of the monoarylated products[10b] was observed in spite of using excess bis(hydrosilane)s. Due to its unique selectivity, this reaction may find application as a method for the chemoselective synthesis of new conjugated organosilicon materials, which have been hitherto prepared by means of stoichiometric reactions[3b,e,f,27] or catalytic silylation from aryl halides.[28]

Mechanistic insights

The mechanistic knowledge of this type of reaction is mainly restricted to the experimental study by Hartwig *et al.*[21] on the Rh(I)-catalyzed silylation of arenes, and the theoretical calculations reported by Murata and co-workers on a Ru-catalysed process.[29] A plausible mechanism for an Ir(III)-catalysed silylation reaction was proposed by Mashima *et al.*,[19b] however, no kinetic or theoretical support for this postulation has been presented so far.

In order to attain a better understanding of the catalytic cycle that operates in these reactions, a computational study at the DFT level was performed using the B3LYP-D3(PCM)/def2TZVP//B3LYP-D3/def2SVP theoretical level which considered the pre-catalyst **1**, 2-phenylpyridine, $HSiMe_3$ as a model for the hydrosilane and NBE (norbornene) as the hydrogen acceptor. The energetic profiles for the directed silylation of 2-phenylpyridine, with and without NBE as the hydrogen acceptor, are shown in Fig. 2 and 3.

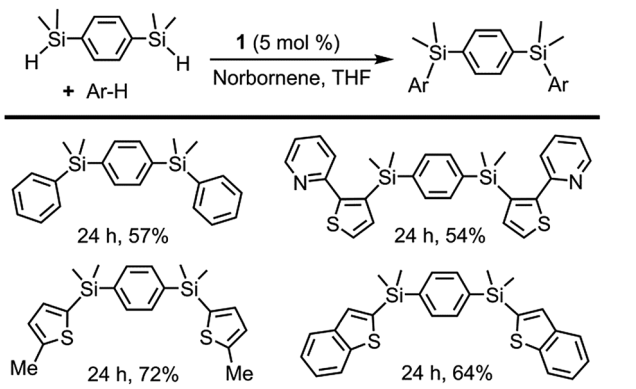

Scheme 4 Directed and non-directed dehydrogenative silylation of aromatic and heteroaromatic rings with bis(hydrosilane)s. Reaction conditions: cat **1** (5 mol%), norbornene (0.40 mmol), arene (0.13 mmol), bis(hydrosilane) (0.40 mmol) in THF (2 mL) at 110 °C. Isolated yields are shown.

The first part of the mechanism involves the dehydrogenation of **1** by the hydrogen acceptor to give a square planar Ir(I) species capable of undergoing cyclometallation with 2-phenylpyridine. The dehydrogenation of **1** with NBE requires the exchange of the pyridine ligand by the olefin followed by the migratory insertion of the double bond into one Ir–H bond *via* $\mathbf{3}^{\ddagger}$ (‡ denotes a transition state) and surmounting an energy barrier of 19.0 kcal mol^{-1}. The alkyl intermediate is thus formed and the remaining hydride ligand undergoes reductive elimination through $\mathbf{5}^{\ddagger}$ to give norbornane (NBA) and the Ir(I) square-planar intermediate **6**. The overall dehydrogenation process is exergonic (−15.2 kcal mol^{-1}) and features an activation energy of 21.0 kcal mol^{-1}. Coordination of 2-phenylpyridine (Phpy) and dissociation of pyridine affords **7**, which subsequently releases a second py ligand and undergoes oxidative addition of the C–H bond adjacent to the pyridine moiety through a barrierless process (ESI†) to yield **8** (−27.0 kcal mol^{-1}). Alternatively, the non-directed *o*-, *m*- and *p*- activations of the Ph ring present remarkably higher activation barriers, and a certain amount of *para* or *meta* product would be expected due to the similar energies of their transition states (see ESI†). Hence, N-coordination of Phpy is required to explain the selectivity of the reaction, which is similar to Morokuma's study.[30]

At this point, coordination of py affords the resting state **9**, which can be isolated by reacting **1** with Phpy (*vide infra*). Coordination of the silane to **8** yields **10**, which undergoes σ-complex assisted metathesis (σ-CAM) between the Ir–C bond of the phenyl moiety and the Si–H bond of the silane *via* transition state $\mathbf{11}^{\ddagger}$, thus yielding the dihydride intermediate **12**.

An alternative Ir(V) pathway has been discarded since no stationary point on the potential energy surface could be found for the hypothetically conceivable Ir(V) intermediate resulting from the oxidative addition of the silane to the cyclometalated species, which agrees with the mechanism proposed by Mashima and co-workers.[19b] Finally, the substitution of the silylated substrate by a pyridine molecule releases the reaction product and regenerates **1**; this process is neatly exergonic by −23.1 kcal mol^{-1}. The effective activation energy for the catalytic cycle is 27.2 kcal mol^{-1} based on the energy span concept,[31] which is defined in this case by the off-cycle species **9** and transition state $\mathbf{11}^{\ddagger}$.

Alternatively, the thermic dehydrogenation of **1** to give **6** is also affordable under the reaction conditions but the overall process is thermodynamically much less favourable (Fig. 3). It is worth noting that no transition structures could be found in the reductive elimination of H_2 from **1** to form **6** plus hydrogen (see ESI†).[32] The thermodynamics for the acceptor and acceptor-less reaction profiles differ by 34.5 kcal mol^{-1}, which is approximately equal to the ΔH° for the hydrogenation of norbornene (33.2 kcal mol^{-1}).[33] In addition, the higher energy span found for this process explains the lower reactivity observed for the acceptor-less reaction (27.2 kcal mol^{-1} and 34.6 kcal mol^{-1} for

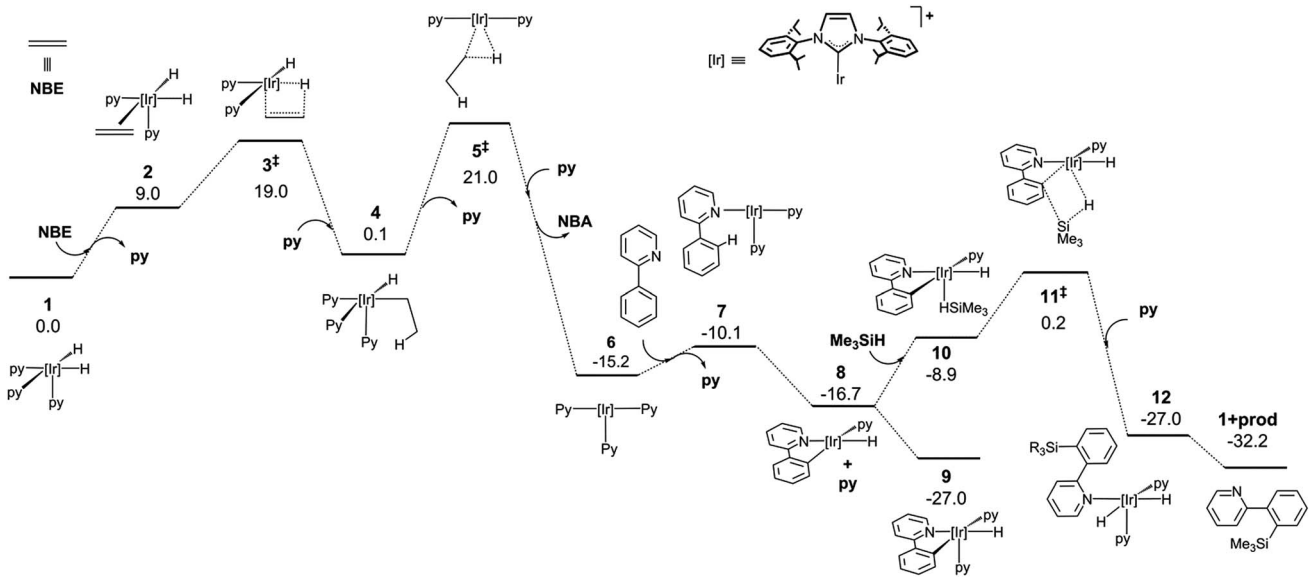

Fig. 2 DFT calculated Gibbs free energy profile at 110 °C and a concentration of 1 M (in kcal mol^{-1} and relative to **1** and the isolated molecules) for the Ir-catalysed silylation of 2-phenylpyridine with a hydrogen acceptor.

the acceptor and acceptor-less processes, respectively). The possibility of oxidative addition of the silane over the NHC–Ir(I) intermediate **7** was also studied; however, the resulting species (**7′**) is 9.3 kcal mol^{-1} less stable than that resulting from the oxidative addition of the C–H bond (**9**) and only 7.7 kcal mol^{-1} more stable than **7**. Therefore, **7′** may be in equilibrium with **7** under the reaction conditions, thus allowing for the transformation of **7′** into **9**.

Reactivity studies

Reactivity of 1. In the search for experimental evidence that would support the mechanism proposed above, several stoichiometric experiments were performed. The reaction of complex **1** at room temperature with 1 equivalent of 2-phenylpyridine (Phpy), 2-thienylpyridine (Thpy), 2-(*p*-tolyl)pyridine (*p*-tolylpy) or 1-phenylimidazole (Phpz), with and without norbornene, afforded the corresponding cyclometalated derivatives: complexes **9** and **13–15** (Scheme 5). In this regard, the sluggish formation of complexes **9** and **13–15** in the presence of norbornene at room temperature, and the concomitant generation of norbornane, agrees with the calculated energy barrier (21.0 kcal mol^{-1}) for the formation of intermediate **9**.

All of the complexes were isolated as air stable solids and fully characterized by multinuclear NMR spectroscopy. In addition, the molecular structures of complexes **9** and **13** were determined by X-ray diffraction analysis on suitable crystals that

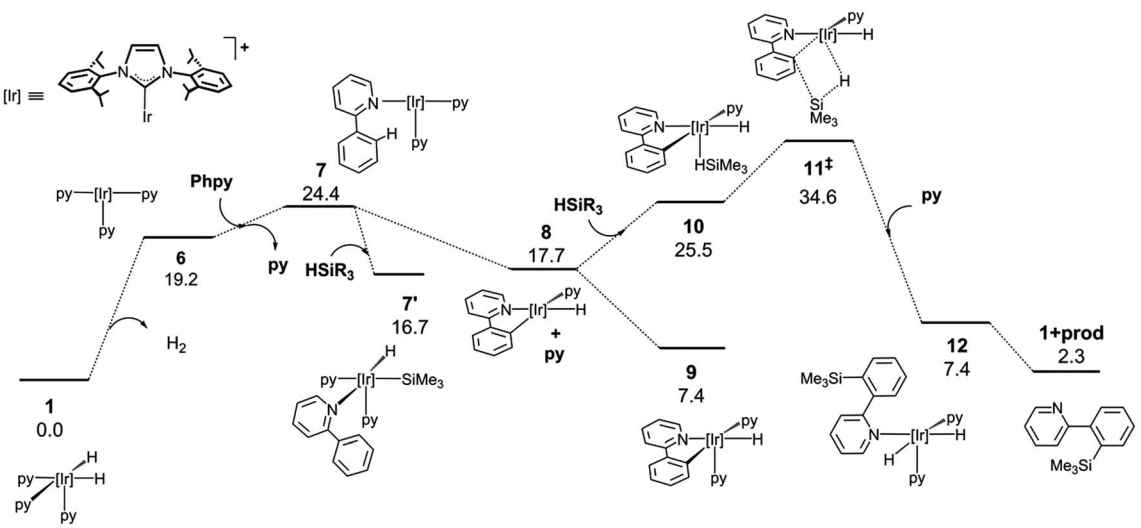

Fig. 3 DFT calculated Gibbs free energy profile at 110 °C and a concentration of 1 M (in kcal mol^{-1} and relative to **1** and the isolated molecules) for the Ir-catalysed silylation of 2-phenylpyridine without a hydrogen acceptor.

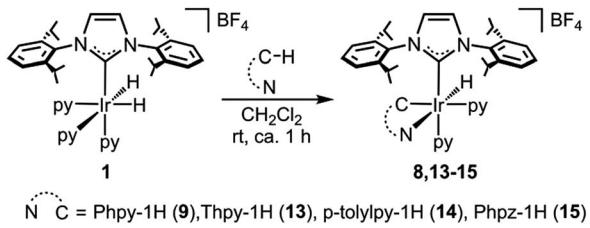

Scheme 5 Synthesis of complexes **9** and **13–15**.

were obtained by slow diffusion of diethyl ether into a solution of the corresponding complex in CH_2Cl_2 (Fig. 4 and 5).

The most representative resonances in the ^{1}H NMR are those in the highfield region, corresponding to the hydrido ligands, which shift upon cyclometallation of the substrate from $\delta = -22.48$ ppm in **1** to $\delta = -18.14$, -19.30, -18.10 and -19.70 ppm in **9**, **13**, **14** and **15**, respectively.

Besides, APT, HSQC and HMBC NMR experiments support the metallation of the corresponding substrates, thereby confirming the directed C–H activation process.

The X-ray diffraction analysis provides valuable information that may shed light into the selectivity patterns observed in directed silylation. In both compounds the Ir(III) centre shows a distorted octahedral geometry with the cyclometalated ligand accommodated in the equatorial plane, *cis* to the IPr ligand. The pyridine moiety in the Phpy-1H and Thpy-1H ligands is situated

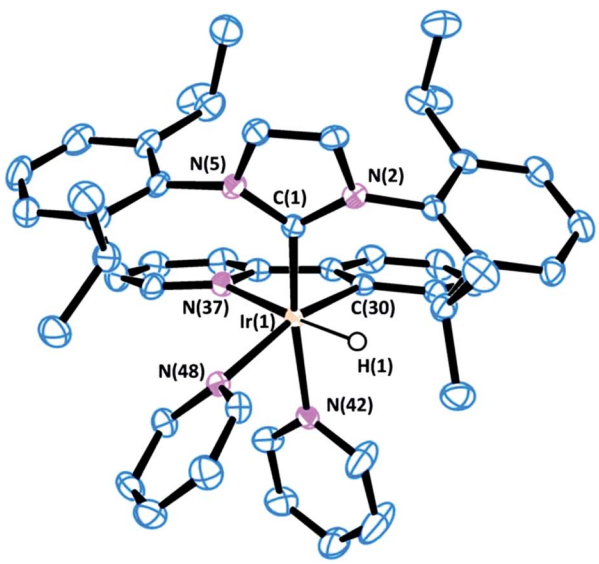

Fig. 4 ORTEP view of the cation $[Ir(H)(IPr)(Phpy\text{-}1H)(py)_2]^+$ in $\mathbf{9}\cdot CH_2Cl_2$ with a numbering scheme adopted. Most of the hydrogens are omitted for clarity and thermal ellipsoids are at 50% probability. Selected bond lengths (Å) and angles (°): C(1)–N(2) 1.375(4), C(1)–N(5) 1.376(4), C(1)–Ir(1) 2.019(4), C(30)–Ir(1) 2.017(3), N(37)–Ir(1) 2.186(3), N(42)–Ir(1) 2.138(3), N(48)–Ir(1) 2.194(3), N(2)–C(1)–N(5) 102.5(3), C(30)–Ir(1)–C(1) 99.60(14), C(30)–Ir(1)–N(42) 82.93(13), C(1)–Ir(1)–N(42) 168.91(12), C(30)–Ir(1)–N(37) 79.42(13), C(1)–Ir(1)–N(37) 101.11(13), N(42)–Ir(1)–N(37) 89.96(12), C(30)–Ir(1)–N(48) 164.74(12), C(1)–Ir(1)–N(48) 95.37(12), N(42)–Ir(1)–N(48) 81.81(11), N(37)–Ir(1)–N(48) 100.63(12).

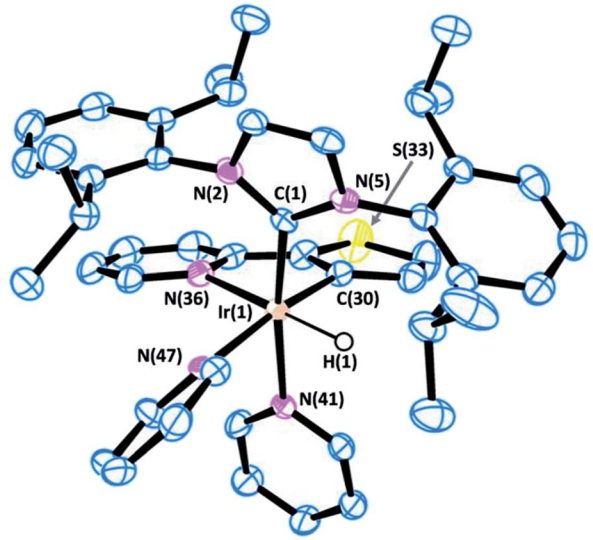

Fig. 5 ORTEP view of the cation $[Ir(H)(IPr)(Thpy\text{-}1H)(py)_2]^+$ in $\mathbf{13}\cdot 1.5\cdot CH_2Cl_2$ with a numbering scheme adopted. Most of the hydrogens are omitted for clarity and thermal ellipsoids are at 50% probability. Selected bond lengths (Å) and angles (°): C(1)–N(2) 1.375(5), C(1)–N(5) 1.382(5), C(1)–Ir(1) 2.007(4), C(30)–Ir(1) 2.013(4), N(36)–Ir(1) 2.195(4), N(41)–Ir(1) 2.146(4), N(47)–Ir(1) 2.176(4), N(2)–C(1)–N(5) 102.8(3), C(1)–Ir(1)–C(30) 97.21(17), C(1)–Ir(1)–N(41) 170.95(15), C(30)–Ir(1)–N(41) 83.69(16), C(1)–Ir(1)–N(47) 92.20(15), C(30)–Ir(1)–N(47) 170.58(16), N(41)–Ir(1)–N(47) 86.97(14), C(1)–Ir(1)–N(36) 100.97(15), C(30)–Ir(1)–N(36) 79.16(17), N(41)–Ir(1)–N(36) 88.05(13), N(47)–Ir(1)–N(36) 99.36(15).

trans to the hydride, thus allowing the two py ligands to sit *trans* to the IPr ligand and the metallated carbon atom.

The distorted geometry of **9** and **13** is attributable to the steric repulsion between the cumbersome side arms of IPr and the cyclometalated ligand. This causes the NHC ligand to move away from Phpy-1H (**9**) or Thpy-1H (**13**) (C(1)–Ir(1)–N(42) 168.91(12) and C(1)–Ir(1)–N(37) 101.11(13) for **9** or C(1)–Ir(1)–N(41) 170.95(15) and C(1)–Ir(1)–N(36) 100.97(15) for **13**) and closer to the apical py ligand (C(30)–Ir(1)–N(42) 82.93(13) for **9** or C(30)–Ir(1)–N(41) 83.69(16) for **13**). Moreover, the geometry of the NHC is also affected: (i) the yaw angle (in plane tilting of the NHC) is *ca.* 10° for **9** and **13**; (ii) the methyl (^{i}Pr) group situated above the py moiety of the cyclometallated ligand shows a dihedral angle $C_{Ar(C-H)}\cdots C_{ipso(C\text{-}iPr)}\cdots C_{CH(iPr)}\cdots C_{Me(iPr)}$ of *ca.* 26°, while the other ^{i}Pr groups feature dihedral angles between 40 and 57°. Both structural parameters are indicative of the steric constraints originating from cyclometallation. On these grounds, an increase in steric hindrance in the system, as is the case for *p*-tolylpy, which would be exacerbated by the use of aromatic silanes, may lead to the de-coordination of the py moiety, reductive elimination and, eventually, oxidative addition of the C–H that affords the least encumbered species. The metallated intermediate that originates from the oxidative addition of the C5–H bond is the one that is situated in the methyl group furthest from the IPr ligand (see the py-silylation products described in Scheme 2).

The reaction of **1** with 1 equivalent of 2,2′-bipyridine (bipy) at room temperature in CH_2Cl_2 affords complex $[Ir(bipy)(H)_2(IPr)(py)][BF_4]$ (**16**) (Scheme 6), which shows no catalytic activity. This suggests that the presence of the chelating ligand, bipy, thwarts the activation of the arene, which consequently inhibits the catalytic activity of the complex. Moreover, the addition of pyridine (10 equivalents) to the reaction of Phpy with Et_3SiH, under the conditions described in Scheme 2, resulted in a significant decrease in catalytic activity. In this case, the ^1H MNR spectrum of the crude mixture shows only a 57% conversion, which contrasts to the example reported in Scheme 2 (without added py) where total conversion was obtained from the crude mixture.

Reactivity of the cyclometalated complexes. The addition of 3 equivalents of triethylsilane to a solution of **9** in CH_2Cl_2 at room temperature renders the starting complex unaltered, which is consistent with the higher temperatures required for the formation of the organosilane and the calculated energy barrier for this process (27.2 kcal mol^{-1} from **9** to **11**‡). Attempts to identify reaction intermediates *in situ* by NMR spectroscopy in 1,1,2,2-tetrachloroethane-d_2 showed that no reaction takes place up to 100 °C.

With the intention of finding support for the calculated mechanism, cyclometalated complexes **9** and **14** were employed as pre-catalysts under the reaction conditions described in Scheme 2. The reaction of Phpy with Et_3SiH catalysed by **9** and the reaction of *p*-tolylpy with Ph_2MeSiH catalysed by **14** gave the silylated products in 81% and 54% yield, respectively (almost identical yields compared to **1**). These experiments, together with the DFT calculations, seem to suggest that **9** may be a resting state that enters the catalytic cycle upon loss of a pyridine ligand.

Moreover, a complex related to **1**, namely $[Ir(CH_3CN)(H)(IPr)(Phpy\text{-}1H)(PPhMe_2)][BF_4]$ (**17**), which presents a $PPhMe_2$ ligand *trans* to the NHC ligand and an acetonitrile ligand *cis* to the hydride ligand, instead of the apical and equatorial pyridine ligands in **1**, was prepared (Scheme 7). When complex **17** was used as a catalyst for the reaction of Phpy with Et_3SiH, under the reaction conditions described in Scheme 2, no silylated product was obtained. The fact that **17** is inactive towards the silylation of Phpy agrees with the proposed mechanism, since a labile position *trans* to the IPr ligand is required for the end-on coordination of the silane. Complex **17** features a strongly coordinating ligand *trans* to the NHC ligand which blocks this coordination site, while the availability of an easily accessible position *cis* to the hydride ligand does not seem to play any role in the reaction, which further supports the calculated mechanism. In this regard, the use of the IPr ligand probably facilitates the dissociation of the *trans* positioned py ligand (NHCs feature stronger trans effects than the ligands usually employed for these transformations),[34] thus generating an available coordination site that may account for the unexpected activity of this system towards less reactive silanes, *e.g.* $(EtO)_3SiH$.

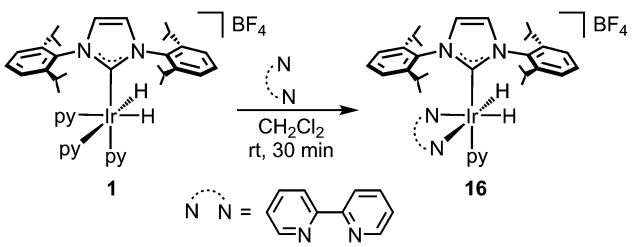

Scheme 6 Synthesis of complex **16**.

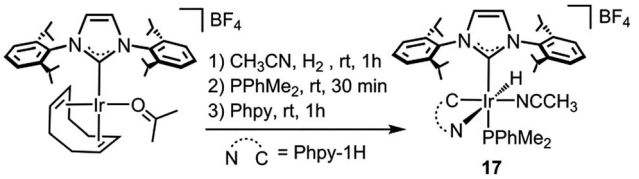

Scheme 7 Synthesis of complex **17**.

In summary, the reactivity shown by complex **1** and the cyclometalated complexes **9** and **13–15** is in accordance with the calculated reaction profile for a variety of reasons: (i) the addition of an arene to **1** gives the corresponding resting states of the catalytic cycle (complexes **9** and **13–15**), which exhibit virtually identical catalytic activity compared to **1**. Furthermore, these species become inactive if the position *trans* to the NHC ligand, where silane coordination should take place, is blocked with a phosphane ligand; (ii) the reaction rates are significantly reduced in the presence of excess py, moreover, when the two coordination sites *trans* to the hydrides in **1** are blocked with bipy, the resulting complex, **16**, is not a competent catalyst for the silylation of Phpy with Et_3SiH; (iii) complex **9** only reacts with the silane at high temperatures to directly afford the silylated product, which is in agreement with the σ-CAM reaction being the rate limiting step followed by a downslope process toward the organosilane **1**.

Additionally, an experiment employing $PhMe_2SiD$ and Phpy showed no deuterium incorporation into the silylated product, which also agrees with the proposed mechanism.

Conclusions

We have prepared a well-defined Ir(III) complex that acts as an efficient pre-catalyst for the intermolecular silylation of a wide variety of arenes and heteroarenes with and without a directing group. Moreover, in view of expanding the synthetic applicability of this reaction the (hetero)arene was successfully employed in all cases as the limiting reagent. This process is compatible with the use of several hydrosilanes, including examples with Et_3SiH, Ph_2MeSiH, $PhMe_2SiH$, Ph_3SiH and $(EtO)_3SiH$. It is worth noting that, in certain cases, the presence of aromatic substituents in the hydrosilanes triggers unprecedented selectivity patterns worthy of a more in-depth study in the future. The use of **1** as a pre-catalyst also permits the efficient bisarylation of bis(hydrosilane)s by directed or non-directed silylation of C–H bonds, which may be utilised as a new tool for the synthesis of conjugated organosilicon materials.

The mechanistic studies performed in this work point towards an Ir(III)/Ir(I) mechanism where the dehydrogenation of the Ir(III) species **1** generates a very electron-rich NHC–Ir(I) intermediate **6** that allows for the facile activation of the arene C–H bond.

Experimental

General considerations

All experiments were carried out under an inert atmosphere using standard Schlenk techniques. The solvents were dried by known procedures and distilled under argon prior to use or obtained oxygen- and water-free from a Solvent Purification System (Innovative Technologies). The starting complex was prepared according to a literature procedure [Ir(COD)(IPr)(acetone)][BF_4].[25f] All other commercially available starting materials were purchased from Sigma-Aldrich, Merck and J. T. Baker and were used without further purification. H_2 gas (>99.5%) was obtained from Infra.

^{1}H, ^{13}C{1H}, ^{19}F, ^{1}H–^{29}Si HMBC, ^{1}H–^{13}C HMBC, ^{1}H–^{13}C HSQC and ^{1}H–^{1}H COSY NMR spectra were recorded either on a Bruker ARX 300 MHz or a Bruker Avance 400 MHz instrument. Chemical shifts (expressed in parts per million) are referenced to residual solvent peaks for ^{1}H and ^{13}C{1H}, and to an external reference of $CFCl_3$ for ^{19}F. Coupling constants, *J*, are given in Hz. Spectral assignments were achieved by combination of ^{1}H–^{1}H COSY, ^{13}C APT and 1H–13C HSQC/HMBC experiments. C, H, and N analyses were carried out in a Perkin-Elmer 2400 CHNS/O analyser. GC-MS spectra were recorded on a Hewlett-Packard GC-MS system. Column chromatography was performed using silica gel (70–230 mesh).

Synthesis and characterization of complexes 9 and 13–17‡

[Ir(H)$_2$(IPr)(py)$_3$][BF_4] (1). A solution of [Ir(COD)(IPr)(acetone)][BF_4] (300 mg, 0.36 mmol) in acetone (10 mL) was reacted with pyridine (0.5 mL) and stirred under a hydrogen atmosphere (1 bar) for 1 h. The resulting pale yellow solution was concentrated to *ca.* 0.5 mL, and treated with diethyl ether to afford a white solid. The solid was separated by decantation, washed with diethyl ether and dried *in vacuo*. A CH_2Cl_2 solution (0.4 mL) of this solid (12 mg) was layered with diethyl ether (5 mL) and stored in a glove box at room temperature to afford crystals suitable for X-ray diffraction. Yield: 72% (234 mg, 0.25 mmol). ^{1}H NMR (300 MHz, CD_2Cl_2, 263 K): δ 8.14 ppm (d, J_{H-H} = 5.0, 4H, $H_{o\text{-py-a}}$); 7.84 (d, J_{H-H} = 5.7, 2H, $H_{o\text{-py-b}}$); 7.71 (t, J_{H-H} = 7.6, 2H, $H_{p\text{-py-a}}$); 7.66 (t, J_{H-H} = 7.5, 1H, $H_{p\text{-py-b}}$); 7.30 (t, J_{H-H} = 7.7, 2H, $H_{p\text{-IPr}}$); 7.11 (d, J_{H-H} = 7.7, 4H, $H_{m\text{-IPr}}$); 7.09 (dd, J_{H-H} = 7.6, 5.0, 4H, $H_{m\text{-py-a}}$); 7.07 (s, 2H, =CHN); 6.96 (dd, J_{H-H} = 7.5, 5.7, 4H, $H_{m\text{-py-b}}$); 2.87 (sept, J_{H-H} = 6.9, 4H, C*H*Me$_{IPr}$); 1.16 and 1.11 (both d, J_{H-H} = 6.9, 24H, CH*Me*$_{IPr}$); −22.48 (s, 2H, Ir–H). ^{13}C{^{1}H}-APT, HSQC and HMBC NMR (75 MHz, CD_2Cl_2, 298 K): δ 155.3 ppm (s, $C_{o\text{-py-b}}$); 154.7 (s, Ir–C_{IPr}); 153.5 (s, $C_{o\text{-py-a}}$); 145.6 (s, $C_{q\text{-IPr}}$); 138.1 (s, C_qN); 136.8 (s, $C_{p\text{-py-b}}$); 136.6 (s, $C_{p\text{-py-a}}$); 129.9 (s, $C_{p\text{-IPr}}$); 125.9 (s, $C_{m\text{-py-a}}$); 125.7 (s, $C_{m\text{-py-b}}$); 123.8 (s, $C_{m\text{-IPr}}$); 28.9 (s, *C*HMe$_{IPr}$); 25.9 and 21.6 (both s, CH*Me*$_{IPr}$). ^{19}F NMR (400 NMR, CD_2Cl_2, 298 K): δ −155.2 ppm (s, BF_4). Anal. calcd. for $C_{42}H_{54}BF_4IrN_5$ (908.40 + CH_2Cl_2): C, 52.02; H, 5.69; N, 7.05%. Found: C, 51.95; H, 5.85; N, 6.85%.

[Ir(H)(IPr)(Phpy-1H)(py)$_2$][BF_4] (9). 2-Phenylpyridine (19 μL, 0.13 mmol) was added to a solution of **1** (120 mg, 0.13 mmol) in 5 mL of dichloromethane and the resulting solution was stirred for 40 min at room temperature. After this time, the resulting light yellow solution was concentrated to *ca.* 0.5 mL and diethyl ether was added to give a white solid. The solid thus formed was separated by decantation, washed with diethyl ether and dried *in vacuo*. Yield: 63% (82 mg, 0.08 mmol). A CH_2Cl_2 solution (0.3 mL) of the solid (10 mg) was layered with diethyl ether (5 mL) and stored in a glove box at room temperature to afford crystals suitable for X-ray diffraction. ^{1}H NMR (300 MHz, CD_2Cl_2, 298 K): δ 8.24 ppm (d, J_{H-H} = 5.1, 2H, $H_{o\text{-py-a}}$); 7.92 (t, J_{H-H} = 6.6, 1H, $H_{p\text{-py-a}}$); 7.91 (d, J_{H-H} = 7.9, 1H, $H_{3\text{-py}}$); 7.72 (dd, J_{H-H} = 7.9, 6.7, 1H, $H_{4\text{-py}}$); 7.55 (d, J_{H-H} = 7.9, 1H, $H_{o\text{-Ph}}$); 7.49 (t, J_{H-H} = 6.7, 1H, $H_{p\text{-py-b}}$); 7.47 (t, J_{H-H} = 6.6, 2H, $H_{p\text{-IPr}}$); 7.40 (d, J_{H-H} = 5.6, 1H, $H_{6\text{-py}}$); 7.37 (d, J_{H-H} = 6.0, 2H, $H_{o\text{-py-b}}$); 7.31 (dd, J_{H-H} = 6.6, 5.1, 2H, $H_{m\text{-py-a}}$); 7.11 (d, J_{H-H} = 6.6, 4H, $H_{m\text{-IPr}}$); 7.09 (s, 2H, =CHN); 6.78 (dd, J_{H-H} = 6.7, 5.6, 1H, $H_{5\text{-py}}$); 6.77 (dd, J_{H-H} = 6.7, 6.0, 2H, $H_{m\text{-py-b}}$); 6.75 (dd, J_{H-H} = 7.9, 7.7, 1H, $H_{m1\text{-Ph}}$); 6.46 (dd, J_{H-H} = 8.2, 7.7, 1H, $H_{p\text{-Ph}}$); 5.97 (d, J_{H-H} = 8.2, 1H, $H_{m2\text{-Ph}}$); 2.87 and 2.25 (both sept, J_{H-H} = 6.6, 4H, C*H*Me$_{IPr}$); 1.11, 1.05, 1.02, and 0.43 (all d, J_{H-H} = 6.6, CH*Me*$_{IPr}$); −18.14 (s, 1H, Ir–H). ^{13}C {^{1}H}-APT, HSQC and HMBC NMR (75 MHz, CD_2Cl_2, 298 K): δ 165.1 ppm (s, $C_{2\text{-py}}$); 153.5 (s, $C_{o\text{-py-a}}$); 152.7 (s, $C_{o\text{-py-b}}$); 150.8 (s, Ir–C_{IPr}); 148.2 (s, $C_{6\text{-py}}$); 146.6 and 146.4 (both s, $C_{q\text{-IPr}}$); 145.3 (s, Ir–C_{Ph}); 143.6 (s, $C_{q\text{-Ph}}$); 143.4 (s, $C_{m2\text{-Ph}}$); 138.0 (s, $C_{p\text{-py-a}}$); 137.1 (s, C_qN); 137.0 (s, $C_{p\text{-py-b}}$); 136.8 (s, $C_{4\text{-py}}$); 130.2 (s, $C_{p\text{-IPr}}$); 129.5 (s, $C_{p\text{-Ph}}$); 126.2 (s, $C_{m\text{-py-a}}$); 125.7 (s, $C_{m\text{-py-b}}$); 125.6 (s, =CHN); 124.4 and 123.7 (both s, $C_{m\text{-IPr}}$); 123.6 (s, $C_{o\text{-Ph}}$); 123.0 (s, $C_{5\text{-py}}$); 121.4 (s, $C_{m1\text{-Ph}}$); 119.9 (s, $C_{3\text{-py}}$); 29.0 and 28.9 (s, *C*HMe$_{IPr}$); 26.9, 26.2, 21.3, and 20.8 (all, s, CH*Me*$_{IPr}$). ^{19}F NMR (400 NMR, CD_2Cl_2, 298 K): δ −152.5 ppm (s, BF_4). Anal. calcd. for $C_{48}H_{55}IrN_5BF_4$ (981.41): C, 58.77; H, 5.65; N, 7.14%. Found: C, 58.70; H, 5.66; N, 7.16%.

[Ir(H)(IPr)(Thpy-1H)(py)$_2$][BF_4] (13). 2-Thienylpyridine (21 mg, 0.13 mmol) was added to a solution of **1** (120 mg, 0.13 mmol) in 5 mL of dichloromethane and the resulting solution was stirred for 40 min at room temperature. After this time, the resulting light yellow solution was concentrated to *ca.* 0.5 mL and diethyl ether was added to give a white solid. The solid thus formed was separated by decantation, washed with diethyl ether and dried *in vacuo*. Yield: 67% (87 mg, 0.09 mmol). ^{1}H NMR (400 MHz, CD_2Cl_2, 283 K): δ 8.27 ppm (d, J_{H-H} = 5.3, 2H, $H_{o\text{-py-a}}$); 7.92 (t, J_{H-H} = 7.8, 1H, $H_{p\text{-py-a}}$); 7.63 (dd, J_{H-H} = 7.9, 6.9, 1H, $H_{4\text{-py}}$); 7.49 (t, J_{H-H} = 7.6, 2H, $H_{p\text{-IPr}}$); 7.48 (d, J_{H-H} = 7.9, 1H, $H_{3\text{-py}}$); 7.47 (t, J_{H-H} = 7.1, 1H, $H_{p\text{-py-b}}$); 7.30 (dd, J_{H-H} = 7.8, 5.3, 2H, $H_{m\text{-py-a}}$); 7.29 (d, J_{H-H} = 6.2, 1H, $H_{o\text{-py-b}}$); 7.25 and 7.13 (both d, J_{H-H} = 7.6, 4H, $H_{m\text{-IPr}}$); 7.20 (d, J_{H-H} = 5.5, 1H, $H_{6\text{-py}}$); 7.11 (s, 2H, =CHN); 6.94 and 5.48 (both d, J_{H-H} = 4.7, 2H, H_{Th}); 6.78 (dd, J_{H-H} = 7.1, 6.2, 2H, $H_{m\text{-py-b}}$); 6.66 (dd, J_{H-H} = 6.9, 5.5, 1H, $H_{5\text{-py}}$); 2.86 and 2.28 (both sept, J_{H-H} = 6.9, 4H, C*H*Me$_{IPr}$); 1.13, 1.06, 1.05, and 0.55 (all d, J_{H-H} = 6.9, 24H, CH*Me*$_{IPr}$); −19.30 (s, 1H, Ir–H). ^{13}C {^{1}H}-APT, HSQC and HMBC NMR (100 MHz, CD_2Cl_2, 298 K): δ 160.9 ppm (s, $C_{2\text{-py}}$); 154.0 (s, $C_{o\text{-py-a}}$); 152.4 (s, $C_{o\text{-py-b}}$); 150.1 (s, Ir–C_{IPr}); 148.5 (s, Ir–C_{Th}); 148.4 (s, $C_{6\text{-py}}$); 146.6 and 146.2 (both s, $C_{q\text{-IPr}}$); 140.0 and 128.0 (both s, C_{Th}); 138.1 (s, $C_{p\text{-py-a}}$); 137.3 (s,

$C_{4\text{-py}}$); 137.1 (s, C_qN); 137.0 (s, $C_{p\text{-py-b}}$); 136.8 (s, $C_{q\text{-Th}}$); 130.3 (s, $C_{p\text{-IPr}}$); 126.3 (s, $C_{m\text{-py-a}}$); 125.5 (s, $C_{m\text{-py-b}}$); 125.4 and 124.3 (both s, $C_{m\text{-IPr}}$); 123.8 (s, =CHN); 120.4 (s, $C_{5\text{-py}}$); 119.2 (s, $C_{3\text{-py}}$); 29.1 and 28.9 (s, *C*HMe$_{IPr}$); 27.0, 26.3, 21.4, and 20.7 (all, s, CH*Me*$_{IPr}$). ^{19}F NMR (400 NMR, CD_2Cl_2, 298 K): δ −153.0 ppm (s, BF_4). Anal. calcd. for $C_{46}H_{53}IrN_5BF_4$ (995.40): C, 55.98; H, 5.41; N, 7.10%. Found: C, 55.93; H, 5.46; N 7.10%.

[Ir(H)(IPr)(py)$_2$(*p*-tolylpy-1H)][BF$_4$] (14). 2-(*p*-Tolyl)pyridine (22 mg, 0.13 mmol) was added to a solution of **1** (120 mg, 0.13 mmol) in 5 mL of dichloromethane and the resulting solution was stirred for 40 min at room temperature. After this time, the resulting light yellow solution was concentrated to *ca.* 0.5 mL and diethyl ether was added to give a light yellow solid. The solid thus formed was separated by decantation, washed with diethyl ether and dried *in vacuo*. Yield: 67% (88 mg, 0.09 mmol). ^{1}H NMR (400 MHz, CD_2Cl_2, 298 K): δ 8.20 ppm (d, J_{H-H} = 5.1, 2H, $H_{o\text{-py-a}}$); 7.93 (t, J_{H-H} = 6.9, 1H, $H_{p\text{-py-a}}$); 7.90 (d, J_{H-H} = 7.6, 1H, $H_{3\text{-py}}$); 7.69 (dd, J_{H-H} = 7.6, 6.9, 1H, $H_{4\text{-py}}$); 7.49 (t, J_{H-H} = 6.9, 1H, $H_{p\text{-py-b}}$); 7.48 (both t, J_{H-H} = 7.9, 2H, $H_{p\text{-IPr}}$); 7.46 (d, J_{H-H} = 8.2, 1H, $H_{o\text{-Ph}}$); 7.36 (br, 2H, $H_{o\text{-py-b}}$); 7.33 (d, J_{H-H} = 5.8, 1H, $H_{6\text{-py}}$); 7.30 (dd, J_{H-H} = 6.9, 5.1, 2H, $H_{m\text{-py-a}}$); 7.23 and 7.09 (both d, J_{H-H} = 7.9, 4H, $H_{m\text{-IPr}}$); 7.22 (s, 2H, =CHN); 6.79 (dd, J_{H-H} = 6.9, 5.3, 2H, $H_{m\text{-py-b}}$); 6.71 (dd, J_{H-H} = 6.9, 5.8, 1H, $H_{5\text{-py}}$); 6.58 (d, J_{H-H} = 8.2, 1H, $H_{m1\text{-Ph}}$); 5.75 (s, 1H, $H_{m2\text{-Ph}}$); 2.91 and 2.20 (both br, 4H, C*H*Me$_{IPr}$); 1.95 (s, 3H, Me), 1.15, 1.04, 1.03, and 0.37 (all d, J_{H-H} = 6.2, 24H, CH*Me*$_{IPr}$); −18.10 (s, Ir–H). ^{13}C {^{1}H}-APT, HSQC and HMBC NMR (100 MHz, CD_2Cl_2, 298 K): δ 165.0 ppm (s, $C_{2\text{-py}}$); 153.5 (s, $C_{o\text{-py-a}}$); 152.4 (s, $C_{o\text{-py-b}}$); 151.2 (s, $C_{IPr\text{-}Ir}$); 147.9 (s, $C_{6\text{-py}}$); 146.5 and 146.4 (both s, $C_{q\text{-IPr}}$); 145.2 (s, Ir–C_{Ph}); 143.9 (s, $C_{m2\text{-Ph}}$); 141.1 (s, $C_{q\text{-Ph}}$); 139.3 (s, $C_{q\text{-Me}}$); 138.1 (s, $C_{p\text{-py-a}}$); 137.0 (s, $C_{p\text{-py-b}}$); 136.9 (s, C_qN); 136.6 (s, $C_{4\text{-py}}$); 130.3 (s, $C_{p\text{-IPr}}$); 126.1 (s, $C_{m\text{-py-a}}$); 125.7 (s, $C_{m\text{-py-b}}$); 125.2 and 124.2 (both s, $C_{m\text{-IPr}}$); 123.7 (s, =CHN); 123.6 (s, $C_{o\text{-Ph}}$); 122.8 (s, $C_{m1\text{-Ph}}$); 122.5 (s, $C_{5\text{-py}}$); 119.7 (s, $C_{3\text{-py}}$); 29.0 and 28.9 (both s, *C*HMe$_{IPr}$); 26.9, 26.2, 21.3, and 20.3 (all s, CH*Me*$_{IPr}$); 21.4 (s, Me). ^{19}F NMR (400 NMR, CD_2Cl_2, 298 K): δ −152.9 ppm (s, BF_4). Anal. calcd. for $C_{49}H_{57}IrN_5BF_4$ (995.43): C, 59.15; H, 5.77; N 7.04%. Found: C, 59.15; H, 5.76; N, 7.10%.

[Ir(H)(IPr)(Phpz-1H)(py)$_2$][BF$_4$] (15). 1-Phenylpyrazole (17 μL, 0.13 mmol) was added to a solution of **1** (120 mg, 0.13 mmol) in 5 mL of dichloromethane and the resulting solution was stirred for 1 h at room temperature. After this time, the resulting light yellow solution was concentrated to *ca.* 0.5 mL and diethyl ether was added to give a white solid. The solid thus formed was separated by decantation, washed with diethyl ether and dried *in vacuo*. Yield: 65% (77 mg, 0.09 mmol). ^{1}H NMR (400 MHz, CD_2Cl_2, 283 K): δ 8.30 ppm (d, J_{H-H} = 5.1, 2H, $H_{o\text{-py-a}}$); 7.81 (d, J_{H-H} = 2.9, 1H, $H_{5\text{-pz}}$); 7.80 (t, J_{H-H} = 6.8, 1H, $H_{p\text{-py-a}}$); 7.44 (t, J_{H-H} = 8.0, 2H, $H_{p\text{-IPr}}$); 7.36 (t, J_{H-H} = 6.9, 1H, $H_{p\text{-py-b}}$); 7.35 (d, J_{H-H} = 5.4, 2H, $H_{o\text{-py-b}}$); 7.21 (dd, J_{H-H} = 6.8, 5.1, 2H, $H_{m\text{-py-a}}$); 7.14 (d, J_{H-H} = 1.9, 1H, $H_{3\text{-pz}}$); 7.08 (s, 2H, =CHN); 7.07 (d, J_{H-H} = 8.0, 4H, $H_{m\text{-IPr}}$); 6.92 (d, J_{H-H} = 7.6, 1H, $H_{o\text{-Ph}}$); 6.79 (dd, J_{H-H} = 7.6, 7.1, 1H, $H_{m1\text{-Ph}}$); 6.76 (d, J_{H-H} = 7.4, 1H, $H_{m2\text{-Ph}}$); 6.71 (dd, J_{H-H} = 6.9, 2H, $H_{m\text{-py-b}}$); 6.69 (dd, J_{H-H} = 7.4, 7.1, 1H, $H_{p\text{-Ph}}$); 6.45 (dd, J_{H-H} = 2.9, 1.9, 1H, $H_{4\text{-pz}}$); 2.85 and 2.49 (both sept, J_{H-H} = 6.9, 4H, C*H*Me$_{IPr}$); 1.12, 1.09, 1.02, and 0.76 (all d, J_{H-H} = 6.9, CH*Me*$_{IPr}$); −19.70 (s, 1H, Ir–H). ^{13}C {^{1}H}-APT, HSQC and HMBC NMR (100 MHz, CD_2Cl_2, 283 K): δ 154.6 ppm (s, $C_{o\text{-py-a}}$); 152.0 (s, $C_{o\text{-py-b}}$); 149.1 (s, Ir–C_{IPr}); 146.4 and 146.0 (both s, $C_{q\text{-IPr}}$); 143.9 (s, Ir–C_{Ph}); 143.0 (s, $C_{m2\text{-Ph}}$); 138.7 (s, $C_{3\text{-pz}}$); 137.6 (s, $C_{p\text{-py-a}}$); 136.9 (s, $C_{p\text{-py-b}}$); 130.0 (s, $C_{p\text{-IPr}}$); 128.5 (s, $C_{q\text{-Ph}}$); 126.4 (s, $C_{5\text{-pz}}$); 126.3 (s, $C_{m\text{-py-a}}$); 126.2 (s, $C_{p\text{-Ph}}$); 125.3 (s, $C_{m\text{-py-b}}$); 125.2 (s, =CHN); 123.8 and 123.6 (both s, $C_{m\text{-IPr}}$); 122.6 (s, $C_{m1\text{-Ph}}$); 111.1 (s, $C_{o\text{-Ph}}$); 107.6 (s, $C_{4\text{-pz}}$); 29.1 and 28.9 (both s, *C*HMe$_{IPr}$); 26.8, 26.3, 21.2, and 21.2 (all s, CH*Me*$_{IPr}$). Anal. calcd. for $C_{46}H_{55}BF_4IrN_6$ (971.41 + 0.5·CH_2Cl_2): C, 55.11; H, 5.57; N, 8.29%. Found: C, 55.08; H, 5.85; N, 8.61%.

[Ir(bipy)(H)$_2$(IPr)(py)]BF$_4$ (16). 2,2′-Bipyridine (16 mg, 0.10 mmol) was added to a solution of **1** (80 mg, 0.10 mmol) in 5 mL of dichloromethane. The resulting solution was stirred for 30 min at room temperature. After this time, the resulting yellow solution was concentrated to *ca.* 0.5 mL and diethyl ether was added to give a yellow solid. The solid was separated by decantation, washed with diethyl ether and dried *in vacuo*. Yield: 79% (69 mg, 0.0764 mmol). ^{1}H NMR (400 MHz, CD_2Cl_2, 298 K): δ 8.67 ppm (d, J_{H-H} = 8.1, 2H, $H_{m2\text{-dipy}}$); 8.56 (d, J_{H-H} = 6.1, 2H, $H_{o\text{-py}}$); 8.42 (dd, J_{H-H} = 8.1, 7.8, 2H, $H_{p\text{-dipy}}$); 8.29 (t, J_{H-H} = 7.6, 2H, $H_{p\text{-IPr}}$); 8.05 (t, J_{H-H} = 7.6, 1H, $H_{p\text{-py}}$); 7.97 (d, J_{H-H} = 7.6, 4H, $H_{m\text{-IPr}}$); 7.80 (d, J_{H-H} = 5.1, 2H, $H_{o\text{-dipy}}$); 7.67 (dd, J_{H-H} = 7.8, 5.1, 2H, $H_{m1\text{-dipy}}$); 7.54 (s, 2H, =CHN); 7.43 (dd, J_{H-H} = 7.6, 6.1, 2H, $H_{m\text{-py}}$); 3.28 (sept, J_{H-H} = 6.9, 4H, CHMe$_{IPr}$); 1.69 and 1.50 (both d, J_{H-H} = 6.9, 24H, CH*Me*$_{IPr}$); −19.80 (s, 2H, Ir–H). ^{13}C {^{1}H}-APT, HSQC and HMBC NMR (75 MHz, CD_2Cl_2, 298 K): δ 156.3 ppm (s, $C_{q\text{-dipy}}$); 155.4 (s, $C_{o\text{-py}}$); 153.0 (s, $C_{o\text{-dipy}}$); 150.5 (s, Ir–C_{IPr}); 147.4 (s, $C_{q\text{-IPr}}$); 137.0 (s, $C_{p\text{-dipy}}$); 136.9 (s, C_qN); 136.7 (s, $C_{p\text{-py}}$); 130.1 (s, $C_{p\text{-IPr}}$); 127.0 (s, $C_{m1\text{-dipy}}$); 125.1 (s, $C_{m\text{-py}}$); 124.5 (s, $C_{m\text{-IPr}}$); 123.5 (s, =CHN); 123.1 (s, $C_{m2\text{-dipy}}$); 28.8 (s, *C*HMe$_{IPr}$); 25.5 and 21.3 (s, CH*Me*$_{IPr}$). ^{19}F NMR (400 NMR, CD_2Cl_2, 298 K): δ −153.1 ppm (s, BF_4). Anal. calcd. for $C_{42}H_{51}BF_4IrN_5$ (905.38): C, 55.75; H, 5.68; N, 7.74%. Found: C, 56.24; H, 5.73; N 7.59%.

[Ir(CH$_3$CN)(H)(IPr)(Phpy-1H)(PPhMe$_2$)][BF$_4$] (17). A solution of [Ir(COD)(IPr)(acetone)][BF_4] (150 mg, 0.18 mmol) in acetonitrile (5 mL) was stirred under a hydrogen atmosphere (1 bar) for 1 h. The solvent was removed under reduced pressure and the remaining pale yellow residue was redissolved in dichloromethane (5 mL). Subsequently, the resulting solution was treated with dimethylphenylphosphine (0.19 mmol, 27 μL) and allowed to react at room temperature for 30 min. Then, 1-phenylpyrazole (25 μL, 0.19 mmol) was added to the solution and stirred at room temperature for 1 h. The resulting pale yellow solution was filtered through Celite, concentrated to *ca.* 0.5 mL and treated with diethyl ether to afford a white solid. The solid was separated by decantation, washed with diethyl ether, and dried *in vacuo*. Yield: 64% (115 mg, 0.11 mmol). ^{1}H NMR (400 MHz, CD_2Cl_2, 298 K): δ 7.86 ppm (d, J_{H-H} = 5.4, 1H, $H_{6\text{-py}}$); 7.53 (d, J_{H-H} = 7.9, 1H, $H_{3\text{-py}}$); 7.47 (dd, J_{H-H} = 7.9, 6.8, 1H, $H_{4\text{-py}}$); 7.46 (d, J_{H-H} = 7.6, 1H, $H_{o\text{-Phpy}}$); 7.45 (t, J_{H-H} = 7.7, 2H, $H_{p\text{-IPr}}$); 7.38 and 7.04 (both d, J_{H-H} = 7.7, 4H, $H_{m\text{-IPr}}$); 7.25 (t, J_{H-H} = 7.2, 1H, $H_{p\text{-Ph}}$); 7.16 (ddd, J_{H-H} = 7.8, 7.2, J_{H-P} = 2.1, 2H, $H_{m\text{-Ph}}$); 7.07 (s, 2H, =CHN); 6.92 (dd, J_{H-H} = 7.6, 7.1, $H_{m1\text{-phpy}}$); 6.81 (dd, J_{H-H} = 7.4, 7.1, 1H, $H_{p\text{-Phpy}}$); 6.72 (dd, J_{H-P} = 9.7, J_{H-H} = 7.8, 2H, $H_{o\text{-Ph}}$); 6.69 (d, J_{H-H} = 7.4, 1H, $H_{o\text{-Phpy}}$); 6.62 (dd, J_{H-H} = 6.8, 5.4, 1H, $H_{5\text{-py}}$); 2.55 and 2.41 (both sept, J_{H-H} = 6.8, 4H, C*H*Me$_{IPr}$); 2.09 (s, 3H, MeCN); 1.35, 1.14, 1.02, and 0.86 (all d, J_{H-H} = 6.8, 24H,

CH*Me*$_{IPr}$); 1.23 and 0.57 (both d, J_{H-P} = 9.7, 6H, PMe); −18.1 (d, J_{H-P} = 17.9, IrH). ^{13}C {^{1}H}-APT, HSQC and HMBC NMR (75 MHz, CD_2Cl_2, 298 K): δ 163.5 ppm (s, $C_{2\text{-py}}$); 163.3 (d, J_{H-P} = 118.7, Ir–C_{IPr}); 149.4 (s, $C_{6\text{-py}}$); 145.9 and 145.2 (both s, $C_{q\text{-IPr}}$); 143.9 (d, J_{H-P} = 2.8, $C_{q\text{-Phpy}}$); 143.0 (s, $C_{m2\text{-Phpy}}$); 142.8 (d, J_{H-P} = 11.7, Ir–C_{Ph}); 137.4 (s, C_qN); 135.5 (s, $C_{4\text{-py}}$); 132.8 (d, J_{H-P} = 48.8, $C_{q\text{-Ph}}$); 130.3 (s, $C_{p\text{-IPr}}$); 129.9 (s, $C_{p\text{-Phpy}}$); 129.1 (d, J_{H-P} = 2.5, $C_{p\text{-Ph}}$); 129.0 (d, J_{H-P} = 8.5, $C_{m\text{-Ph}}$); 128.1 (d, J_{H-P} = 9.2, $C_{o\text{-Ph}}$); 125.2 and 125.1 (both s, =CHN); 123.9 (s, $C_{o\text{-Phpy}}$); 123.9 and 123.4 (both s, $C_{m\text{-IPr}}$); 122.4 (s, $C_{5\text{-py}}$); 120.7 (s, $C_{m1\text{-Phpy}}$); 118.7 (s, Me*C*N); 118.6 (s, $C_{3\text{-py}}$); 28.5 and 28.4 (both s, *C*HMe$_{IPr}$); 26.8, 25.3, 22.8, and 21.5 (all s, CH*Me*$_{IPr}$); 13.8 and 9.3 (both d, J_{H-P} = 41.5, PMe); 3.4 (s, *Me*CN). ^{31}P NMR (100 NMR, CD_2Cl_2, 298 K): δ −28.0 ppm. ^{19}F NMR (400 NMR, CD_2Cl_2, 298 K): δ −152.5 ppm (s, BF_4). Anal. calcd. for $C_{48}H_{60}BF_4IrN_4P$ (1003.42 + CH_2Cl_2): C, 54.10; H, 5.74; N, 5.15%. Found: C, 54.89; H, 6.08; N, 5.62%.

General procedure for the catalytic silylation of C–H bonds

A sealed flask was charged with complex **1** (5 mol%), THF (2.0 mL), an arene (1 eq., 0.13 mmol), norbornene (3 eq., 0.40 mmol) and a hydrosilane (3 eq., 0.40 mmol). The solution was kept at 110 °C in a thermostatic bath for the reaction time described in the article. The progress of the reactions was monitored by ^{1}H NMR spectroscopy and the conversion was determined by integration of the peaks of the starting material with the peaks of the products. At the end of the reaction, the solution was concentrated under reduced pressure to afford the crude residue, which was purified by column chromatography on silica gel using mixtures of hexane/ethyl acetate to isolate the corresponding product.

Acknowledgements

This work was supported by the Spanish Ministry of Economy and Competitiveness (MINECO/FEDER) (CONSOLIDER INGENIO CSD-2009-00050, CTQ-2015-67366-P and CTQ-2013-42532-P projects) and the DGA/FSE-E07. The support from the KFUPM-University of Zaragoza research agreement and the Centre of Research Excellence in Petroleum Refining & KFUPM is gratefully acknowledged. V. P. thankfully acknowledges the resources from the supercomputer "Memento", technical expertise and assistance provided by BIFI-ZCAM (Universidad de Zaragoza). L. R. -P. thanks CONACyT for a postdoctoral fellowship (204033). J. M. acknowledges financial support from the Ministry of Education Culture and Sports (FPU14/06003).

Notes and references

‡ In the NMR characterisation, the terms py-a and py-b refer to the pyridine ligands *cis* and *trans* to the IPr ligand, respectively.

1 (*a*) B. Marciniec, C. Pietraszuk, I. Kownacki and M. Zaidlewicz, in *Comprehensive Organic Functional Group Transformations*, ed. A. R. Katrizky and J. K. Taylor, Elsevier, Oxford, 2005, p. 941; (*b*) Y. Nakao and T. Hiyama, *Chem. Soc. Rev.*, 2011, **40**, 4893–4901; (*c*) I. Ojima, in *The Chemistry of Organic Silicon Compounds*, ed. S. Patai and Z. Rappoport, Wiley, New York, 1989, p. 1479; (*d*) I. Ojima, Z. Li, J. Zhu, in *The Chemistry of Organic Silicon Compounds*, ed. Z. Rappoport and Y. Apeloig, Wiley, New York, 1998, p. 1687; (*e*) G. W. Gribble and J. J. Li, in *Palladium in Heterocyclic Chemistry: a Guide for the Synthetic Chemist*, ed. G. W. Gribble and J. J. Li, Elsevier, Oxford, 2006, p. 12; (*f*) I. Fleming, J. Dunoguès and R. Smithers, in *Organic Reactions*, ed. A. S. Kende, Wiley, New York, 1989, vol. 2, pp. 57–193; (*g*) T.-Y. Luh and S.-T. Liu, in *The Chemistry of Organic Silicon Compounds*, ed. Y. A. Z. Rappoport, Wiley, Chichester, 2003, vol. 2, pp. 1793–1868.

2 S. A. Ponomarenko and S. Kirchmeyer, in *Silicon Polymers*, ed. A. M. Muzafarov, Springer-Verlag, Heidelberg, 2010, pp. 36–110.

3 For examples see: (*a*) R. J. Holmes, B. W. D'Andrade, S. R. Forrest, X. Ren, J. Li and M. E. Thompson, *Appl. Phys. Lett.*, 2003, **83**, 3818–3820; (*b*) X. Ren, J. Li, R. J. Holmes, P. I. Djurovich, S. R. Forrest and M. E. Thompson, *Chem. Mater.*, 2004, **16**, 4743–4747; (*c*) J.-K. Bin, N.-S. Cho and J.-I. Hong, *Adv. Mater.*, 2012, **24**, 2911–2915; (*d*) J.-J. Lin, W.-S. Liao, H.-J. Huang, F.-I. Wu and C.-H. Cheng, *Adv. Funct. Mater.*, 2008, **18**, 485–491; (*e*) M.-H. Tsai, H.-W. Lin, H.-C. Su, T.-H. Ke, C.-c. Wu, F.-C. Fang, Y.-L. Liao, K.-T. Wong and C.-I. Wu, *Adv. Mater.*, 2006, **18**, 1216–1220; (*f*) M.-K. Leung, W.-H. Yang, C.-N. Chuang, J.-H. Lee, C.-F. Lin, M.-K. Wei and Y.-H. Liu, *Org. Lett.*, 2012, **14**, 4986–4989; W.-S. Han, H.-J. Son, K.-R. Wee, K.-T. Min, S. Kwon, I.-H. Suh, S.-H. Choi, D. H Jung and S. O. Kang, *J. Phys. Chem. C*, 2009, **113**, 19686–19693.

4 (*a*) P. D. Lickiss, *Adv. Inorg. Chem.*, 1995, **42**, 147–262; (*b*) S. E. Denmark and L. Neuville, *Org. Lett.*, 2000, **2**, 3221–3224; (*c*) K. Hirabayashi, J.-i. Ando, J. Kawashima, Y. Nishihara, A. Mori and T. Hiyama, *Bull. Chem. Soc. Jpn.*, 2000, **73**, 1409–1417; (*d*) S. E. Denmark and D. Wehrli, *Org. Lett.*, 2000, **2**, 565–568.

5 (*a*) M. Murata, M. Ishikura, M. Nagata, S. Watanabe and Y. Masuda, *Org. Lett.*, 2002, **4**, 1843–1845; (*b*) A. S. Manoso and P. DeShong, *J. Org. Chem.*, 2001, **66**, 7449–7455; (*c*) S. E. Denmark, R. C. Smith, W.-T. T. Chang and J. M. Muhuhi, *J. Am. Chem. Soc.*, 2009, **131**, 3104–3118; (*d*) S. E. Denmark and J. M. Kallemeyn, *J. Am. Chem. Soc.*, 2006, **128**, 15958–15959; (*e*) L. J. Gooßen and A.-R. S. Ferwanah, *Synlett*, 2000, **12**, 1801–1803.

6 For examples of intramolecular silylation see: (*a*) E. M. Simmons and J. F. Hartwig, *J. Am. Chem. Soc.*, 2010, **132**, 17092–17095; (*b*) Q. Li, M. Driess and J. F. Hartwig, *Angew. Chem., Int. Ed.*, 2014, **53**, 8471–8474; (*c*) A. Kuznetsov and V. Gevorgyan, *Org. Lett.*, 2012, **14**, 914–917; (*d*) A. Kuznetsov, Y. Onishi, Y. Inamoto and V. Gevorgyan, *Org. Lett.*, 2013, **15**, 2498–2501.

7 For examples of directed silylation with disilanes see: (*a*) M. Tobisu, Y. Ano and N. Chatani, *Chem.–Asian J.*, 2008, **3**, 1585–1591; (*b*) N. A. Williams, Y. Uchimaru and M. Tanaka, *J. Chem. Soc., Chem. Commun.*, 1995, 1129–1130; (*c*) K. S. Kanyiva, Y. Kuninobu and M. Kanai, *Org. Lett.*, 2014, **16**, 1968–1971.

8 For examples of directed silylation with hydrosilanes in the presence of a hydrogen acceptor see: (*a*) F. Kakiuchi, K. Igi, M. Matsumoto, N. Chatani and S. Murai, *Chem. Lett.*, 2001, **30**, 422–423; (*b*) F. Kakiuchi, K. Igi, M. Matsumoto, T. Hayamizu, N. Chatani and S. Murai, *Chem. Lett.*, 2002, **31**, 396–397; (*c*) H. Ihara and M. Suginome, *J. Am. Chem. Soc.*, 2009, **131**, 7502–7510; (*d*) J. Oyamada, M. Nishiura and Z. Hou, *Angew. Chem., Int. Ed.*, 2011, **50**, 10720–17023.

9 For examples of acceptor-less directed silylation see: T. Sakurai, Y. Matsuoka, T. Hanataka, N. Fukuyama, T. Namikoshi, S. Watanabe and M. Murata, *Chem. Lett.*, 2012, **41**, 374–376.

10 (*a*) Y. Ma, B. Wang, L. Zhang and Z. Hou, *J. Am. Chem. Soc.*, 2016, **138**, 3663–3666; (*b*) A. A. Toutov, W.-B. Liu, K. N. Betz, A. Fedorov, B. M. Stoltz and R. H. Grubbs, *Nature*, 2015, **518**, 80–84.

11 (*a*) K. Ezbiansky, P. I. Djurovich, M. LaForest, D. J. Sinning, R. Zayes and D. H. Berry, *Organometallics*, 1998, **17**, 1455–1457; (*b*) W. A. Gustavson, P. S. Epstein and M. D. Curtis, *Organometallics*, 1982, **1**, 884–885.

12 (*a*) C. Cheng and J. F. Hartwig, *Chem. Rev.*, 2015, **115**, 8946–8975; (*b*) Y. Yang and C. Wang, *Sci. China: Chem.*, 2015, **58**, 1266–1279; (*c*) K. Takada, T. Hanataka, T. Namikoshi, S. Watanabe and M. Murata, *Adv. Synth. Catal.*, 2015, **357**, 2229–2232; (*d*) Y.-J. Liu, Y.-H. Liu, Z.-Z. Zhang, S.-Y. Yan, K. Chen and B.-F. Shi, *Angew. Chem., Int. Ed.*, 2016, **55**, 13859–13862; (*e*) W. Li, X. Huang and J. You, *Org. Lett.*, 2016, **18**, 666–668.

13 For the preparation of silatranes by C–H bond silylation see: T. Ishiyama, T. Saiki, E. Kishida, I. Sasaki, H. Ito and N. Miyaura, *Org. Biomol. Chem.*, 2013, **11**, 8162–8165.

14 For applications of trialkoxysilanes in cross-coupling see: (*a*) P. Y. S. Lam, S. Deudon, K. M. Averill, R. Li, M. Y. He, P. DeShong and C. G. Clark, *J. Am. Chem. Soc.*, 2000, **122**, 7600–7601; (*b*) P. Tang and T. Ritter, *Tetrahedron*, 2011, **67**, 4449–4454; (*c*) S. Riggleman and P. DeShong, *J. Org. Chem.*, 2003, **68**, 8106–8109.

15 For applications of trialkoxysilanes in fluorination and oxidation reactions see: (*a*) T. Furuya and T. Ritter, *Org. Lett.*, 2009, **11**, 2860–2863; (*b*) K. Tamao, N. Ishida, T. Tanaka and M. Kumada, *Organometallics*, 1983, **2**, 1694–1696; (*c*) K. Tamao, N. Ishida and M. Kumada, *J. Org. Chem.*, 1983, **48**, 2120–2122; (*d*) A. Hosomi, S. Iijima and H. Sakurai, *Chem. Lett.*, 1981, **10**, 243–246.

16 (*a*) Y. Uchimaru, A. M. M. E. Sayed and M. Tanaka, *Organometallics*, 1993, **12**, 2065–2069; (*b*) M. Koyanagi, N. Eichenauer, H. Ihara, T. Yamamoto and M. Suginome, *Chem. Lett.*, 2013, **42**, 541–543; (*c*) J. Oyamaga, M. Nishiura and Z. Hou, *Angew. Chem., Int. Ed.*, 2011, **50**, 10720–10723; (*d*) Y. Sunada, H. Soejima and H. Nagashima, *Organometallics*, 2014, **33**, 5936–5939.

17 For precedents of C–H silylation by triarylsilanes see: (*a*) F. Kakiuchi, K. Tsuchiya, M. Matsumoto, E. Mizushima and N. Chatani, *J. Am. Chem. Soc.*, 2004, **126**, 12792–12793; (*b*) D. Leifert and A. Studer, *Org. Lett.*, 2015, **17**, 386–389.

18 (*a*) C. Cheng and J. F. Hartwig, *Science*, 2014, **343**, 853–857; (*b*) C. Cheng and J. F. Hartwig, *J. Am. Chem. Soc.*, 2015, **137**, 592–595; (*c*) B. Lu and J. R. Falck, *Angew. Chem., Int. Ed.*, 2008, **47**, 7508–7510.

19 (*a*) K. Manna, T. Zhang, F. X. Greene and W. Lin, *J. Am. Chem. Soc.*, 2015, **137**, 2665–2673; (*b*) G. Choi, H. Tsurugi and K. Mashima, *J. Am. Chem. Soc.*, 2013, **135**, 13149–13161; (*c*) H. F. T. Klare, M. Oestreich, J.-i. Ito, H. Nishiyama, Y. Ohki and K. Tatsumi, *J. Am. Chem. Soc.*, 2011, **133**, 3312–3315; (*d*) M. Koyanagi, N. Eichenauer, H. Ihara, T. Yamamoto and M. Suginome, *Chem. Lett.*, 2013, **42**, 541–543; (*e*) H. Fang, L. Guo, Y. Zhang, W. Yao and Z. Huang, *Org. Lett.*, 2016, **18**, 5624–5627.

20 (*a*) S. P. Nolan, *N-Heterocyclic Carbenes in Synthesis*, Wiley-VCH, Weinheim, 2006; (*b*) F. E. Hahn and M. C. Jahnke, *Angew. Chem., Int. Ed.*, 2008, **47**, 3122–3172; (*c*) L. A. Adrio and K. K. Hii, in *Organometallic Chemistry*, ed. I. J. S. Fairlamb and J. M. Lynam, RSC Publishing, London, 2009, vol. 35, pp. 62–92; (*d*) C. S. J. Cazin, in *Catalysis by Metal Complexes*, ed. C. Bianchini, D. J. Cole-Hamilton and P. W. N. M. van Leeuwen, Springer Science+Business Media, New York, 2011, vol. 32; (*e*) M. L. Clarke and J. J. R. Frew, in *Organometallic Chemistry*, ed. I. J. S. Fairlamb and J. M. Lynam, RSC Publishing, London, 2009, vol. 35, pp. 19–46; (*f*) A. Poulain, M. Iglesias and M. Albrecht, *Curr. Org. Chem.*, 2011, **15**, 3325–3336.

21 C. Cheng and J. F. Hartwig, *J. Am. Chem. Soc.*, 2014, **136**, 12064–12072.

22 (*a*) M. Albrecht, *Chem. Rev.*, 2010, **110**, 576–623; (*b*) K. R. Jain, W. A. Herrmann and F. E. Kühn, *Curr. Org. Chem.*, 2008, **12**, 1468–1478; (*c*) L. Rubio-Pérez, M. Iglesias, R. Castarlenas, V. Polo, J. J. Pérez-Torrente and L. A. Oro, *ChemCatChem*, 2014, **6**, 3192–3199.

23 (*a*) A. Di Giuseppe, R. Castarlenas, J. J. Pérez-Torrente, M. Crucianelli, V. Polo, R. Sancho, F. J. Lahoz and L. A. Oro, *J. Am. Chem. Soc.*, 2012, **134**, 8171–8183; (*b*) L. Rubio-Perez, E. A. Jaseer, N. García, V. Polo, M. Iglesias and L. A. Oro, *Organometallics*, 2016, **35**, 569–578.

24 M. A. Esteruelas and L. A. Oro, *Chem. Rev.*, 1998, **98**, 577–588.

25 For the preparation of related complexes see: (*a*) M. J. Cowley, R. W. Adams, K. D. Atkinson, M. C. R. Cockett, S. B. Duckett, G. G. R. Green, J. A. B. Lohman, R. Kerssebaum, D. Kilgour and R. E. Mewis, *J. Am. Chem. Soc.*, 2011, **133**, 6134–6137; (*b*) B. J. A. van Weerdenburg, N. Eshuis, M. Tessari, F. P. J. T. Rutjes and M. C. Feiters, *Dalton Trans.*, 2015, **44**, 15387–15390; (*c*) B. J. A. van Weerdenburg, S. Glöggler, N. Eshuis, A. H. J. (Ton) Engwerda, J. M. M. Smits, R. de Gelder, S. Appelt, S. S. Wymenga, M. Tessari, M. C. Feiters, B. Blümich and F. P. J. T. Rutjes, *Chem. Commun.*, 2013, **49**, 7388–7390; (*d*) L. S. Lloyd, A. Asghar, M. J. Burns, A. Charlton, S. Coombes, M. J. Cowley, G. J. Dear, S. B. Duckett, G. R. Genov, G. G. R. Green, L. A. R. Highton, A. J. J. Hooper, M. Khan, I. G. Khazal, R. J. Lewis, R. E. Mewis, A. D. Roberts and A. J. Ruddlesden, *Catal. Sci. Technol.*, 2014, **4**, 3544–3554; (*e*) O. Torres, M. Martín and E. Sola, *Organometallics*, 2009, **28**, 863–870; (*f*) L. Rubio-Pérez, Ma. Iglesias, J. Munárriz,

V. Polo, P. J. Sanz Miguel, J. J. Pérez-Torrentea and L. A. Oro, *Chem. Commun.*, 2015, **51**, 9860–9863.

26 S. Wubbolt and M. Oestreich, *Angew. Chem., Int. Ed.*, 2015, **54**, 15876–15879.

27 (*a*) M. Yoshida, S. Tsuzuki, M. Goto and F. Nakanishi, *J. Chem. Soc., Dalton Trans.*, 2001, 1498–1505; (*b*) A. Naka, Y. Matsumoto, T. Itano, K. Hasegawa, T. Shimamura, J. Ohshita, A. Kunai, T. Takeuchi and M. Ishikawa, *J. Organomet. Chem.*, 2009, **694**, 346–352.

28 (*a*) M.-k. Leung, W.-H. Yang, C.-N. Chuang, J.-H. Lee, C.-F. Lin, M.-K. Wei and Y.-H. Liu, *Eur. J. Org. Chem.*, 2008, 1161–1163; (*b*) M. Murata, H. Yamasaki, K. Uogishi, S. Watanabe and Y. Masuda, *Synthesis*, 2007, 2944–2946; (*c*) Y. Yamanoi, T. Taira, J. Sato, I. Nakamula and H. Hishihara, *Org. Lett.*, 2007, **9**, 4543–4546; (*d*) M. Murata, K. Oka, H. Yamasaki, S. Watanabe and Y. Masuda, *Synlett*, 2007, 1387–1390; (*e*) M. Murata, H. Yamasaki, T. Ueta, M. Nagata, M. Ishikura, S. Watanabe and Y. Masuda, *Tetrahedron*, 2007, **63**, 4087–4094; (*f*) M. Murata, H. Ohara, R. Oiwa, S. Watanabe and Y. Masuda, *Synthesis*, 2006, 1771–1774; (*g*) A. Hamze, O. Provot, M. Alami and J.-D. Brion, *Org. Lett.*, 2006, **8**, 931–934; (*h*) D. Karchtedt, A. T. Bell and T. D. Tilley, *Organometallics*, 2006, **25**, 4471–4482; (*i*) Y. Yamanoi, *J. Org. Chem.*, 2005, **70**, 9607–9609; (*j*) S. E. Denmark and J. M. Kallemeyn, *Org. Lett.*, 2003, **5**, 3483–3486; (*k*) W. Gu, S. Liu and R. B. Silverman, *Org. Lett.*, 2002, **4**, 4171–4174; (*l*) A. S. Manoso and P. J. DeShong, *J. Org. Chem.*, 2001, **66**, 7449–7455; (*m*) M. Murata, K. Suzuki, S. Watanabe and Y. Masuda, *J. Org. Chem.*, 1997, **62**, 8569–8571.

29 K. Kon, H. Suzuki, K. Takada, Y. Kohari, T. Namikoshi, S. Watanabe and M. Murata, *ChemCatChem*, 2016, **8**, 2202–2205.

30 T. Matsubara, N. Koga, D. G. Musaev and K. Morokuma, *J. Am. Chem. Soc.*, 1998, **120**, 12692–12693.

31 S. Kozuch and S. Shaik, *Acc. Chem. Res.*, 2011, **44**, 101–110.

32 (*a*) L. Rubio-Pérez, M. Iglesias, R. Castarlenas, V. Polo, J. J. Pérez-Torrente and L. A. Oro, *ChemCatChem*, 2014, **6**, 3192–3199; (*b*) F. Maseras, A. Lledós, E. Clot and O. Eisenstein, *Chem. Rev.*, 2000, **100**, 601–636.

33 F. J. McQuillin and M. S. Baird, in *Alicyclic Chemistry, Cambridge Texts in Chemistry and Biochemistry*, Cambridge University Press, Cambridge, 2nd edn, 1983.

34 (*a*) J. A. M. Lummiss, C. S. Higman, D. L. Fyson, R. McDonald and D. E. Fogg, *Chem. Sci.*, 2015, **6**, 6739–6746; (*b*) M. S. Sanford, J. A. Love and R. H. Grubbs, *J. Am. Chem. Soc.*, 2001, **123**, 6543–6554.

Green Chemistry

COMMUNICATION

View Article Online
View Journal | View Issue

Cite this: *Green Chem.*, 2018, **20**, 4875

Received 3rd September 2018,
Accepted 3rd October 2018

DOI: 10.1039/c8gc02794c

rsc.li/greenchem

A highly efficient Ir-catalyst for the solventless dehydrogenation of formic acid: the key role of an N-heterocyclic olefin†

Amaia Iturmendi, [a] Manuel Iglesias, *[a] Julen Munarriz, [b] Victor Polo, [b] Vincenzo Passarelli, [c] Jesús J. Pérez-Torrente [a] and Luis A. Oro *[a]

A sturdy iridium complex that features a PCP ligand based on an N-heterocyclic olefin shows remarkable activity for the solventless dehydrogenation of formic acid. Reactivity studies highlight the importance of NHO in the activity of the catalyst. A plausible intermediate has been isolated and the mechanism was substantiated by DFT calculations.

The growth of global energy consumption presents urgent challenges associated with the sustainability and environmental impact of fossil fuels.[1] The energy stored in the chemical bonds of H_2 molecules may be released by electrochemical combustion in fuel cells affording water as the only reaction product. This alternative technology would permit the exploitation of sustainable energy sources such as biomass or water,[2] and the storage of the excess electrical power that renewable energy sources generate off-peak by water electrolysis.[3] The use of hydrogen gas as a sustainable energy vector, however, presents several drawbacks, mainly related to its storage and transportation. The use of liquid organic hydrogen carriers (LOHCs) has been proposed as a viable alternative to bypass the issues that liquefaction or high-pressure storage of H_2 present.[4] In this regard, formic acid (FA) shows several advantages compared to other LOHCs: (i) CO_2 may be hydrogenated to FA to render a carbon-neutral cycle of hydrogen storage, (ii) fuel-cell-grade hydrogen requires levels of CO below 10 ppm, which are achievable by FA dehydrogenation, (iii) the energy density of FA is higher than that of most LOHCs and H_2 and (iv) FA presents fewer toxicity hazards compared to other hydrogen carriers such as ammonia, amine boranes or methanol.[5] The ratio between the amount of H_2 released and the volume of the reaction mixture used in FA dehydrogenation is crucial to the implementation of FA as a hydrogen carrier. The solventless dehydrogenation of FA reduces drastically the volume of the reaction mixture compared to processes that require a solvent, which results in a higher energy density. Moreover, the presence of volatile organic solvents may damage the fuel cell electrode materials. Many outstanding catalysts for FA dehydrogenation have been described since the seminal work by Beller[6] and Laurenczy,[7] the best results being usually obtained in solution.[8] However, examples of homogeneous catalysts that operate efficiently in neat HCOOH are scarce.[9] The iridium complex recently reported by Williams and co-workers, namely $[Ir(COD)(^tBu_2PCH_2(2\text{-py}))]CF_3SO_3$, is the most efficient hitherto reported for the solventless dehydrogenation of FA. Namely, a TOF value of 13 320 h^{-1} (3.7 s^{-1}) and a TON of 12 530 after 13 h were reported for this catalyst in the presence of catalytic amounts of HCOONa and water (10 v%).[10]

Herein we describe a proficient Ir-catalyst for the solventless dehydrogenation of FA, which features a PCP ligand based on an NHO scaffold (NHO = N-heterocyclic olefin). The catalyst $[Ir(PCP)(COD)]BF_4$,[11] (PCP = 1,3-bis(2-(diphenylphosphanyl) ethyl)-2-methyleneimidazoline and cod = 1,5-cyclooctadiene) brings about excellent activities in neat FA, which can be improved in the presence of water.

Initial catalytic tests aimed at exploring the activity of Ir-NHO complexes (**1** and **2**)[11a] in the dehydrogenation of neat FA (Fig. 1). Under unoptimized reaction conditions, 0.016 mol% of the pre-catalyst and 5 mol% of HCOONa at 80 °C, **1** proved to be the most active pre-catalyst. NHO-Ir(III) complex **2** performed significantly worse than **1**, probably due to the fact that one of the coordination positions is blocked by a strongly coordinating carbonyl ligand. Ir(I) complexes related to **1**, namely **3** and **4**,[12] which present a chelating bis-phosphine without an NHO moiety, are noticeably less active than their NHO-containing counterpart.

In order to shed light on the nature of the active species, **1** was dissolved in CH_2Cl_2 and heated to 50 °C in the presence of

[a]*Departamento Química Inorgánica – Instituto Síntesis Química y Catálisis Homogénea (ISQCH), Universidad de Zaragoza – CSIC, C/Pedro Cerbuna 12, 50009 Zaragoza, Spain. E-mail: miglesia@unizar.es, oro@unizar.es*
[b]*Departamento Química Física – Instituto de Biocomputación y Física de Sistemas Complejos (BIFI), Universidad de Zaragoza, Pedro Cerbuna 12, 50009 Zaragoza, Spain*
[c]*Centro Universitario de la Defensa, Ctra. Huesca s/n, ES-50090 Zaragoza, Spain*

†Electronic supplementary information (ESI) available: Experimental data and DFT calculation details. CCDC 1858260 and 1858261. For ESI and crystallographic data in CIF or other electronic format see DOI: 10.1039/c8gc02794c

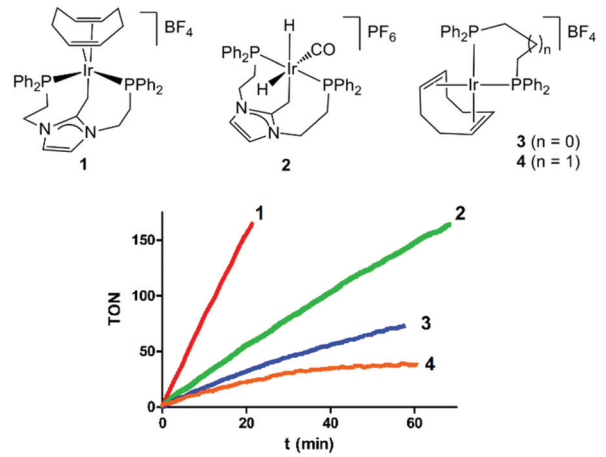

Fig. 1 Depiction of pre-catalysts **1–4** and reaction profiles for the dehydrogenation of neat FA (0.016 mol% of the Ir-catalyst, 5 mol% of HCOONa at 80 °C).

4 equivalents of HCOOH. Interestingly, the reaction does not proceed under strictly anhydrous conditions. The addition of traces of H_2O (30 ppm of H_2O) triggered the formation of a new dihydride species that decomposes upon isolation. Addition of a large excess of pyridine (*ca.* 20 eq.) to the reaction mixture allows the preparation of the new dihydride complex $[Ir(H)_2(PCP)(py)]BF_4$ (**5**) (Scheme 1), which appears always together with small amounts of an unidentified hydride species. When the reaction was performed in CH_3CN, in the presence of HCOONa at 80 °C, the clean formation of the dihydride complex **6** was observed. However, the product decomposed upon purification (ESI†). Addition of excess 3,5-dimethylpyridine (3,5-Me_2py) to a solution of **5** resulted in the formation of the related complex **6** (Scheme 1), which illustrates the facile access to this coordination site.

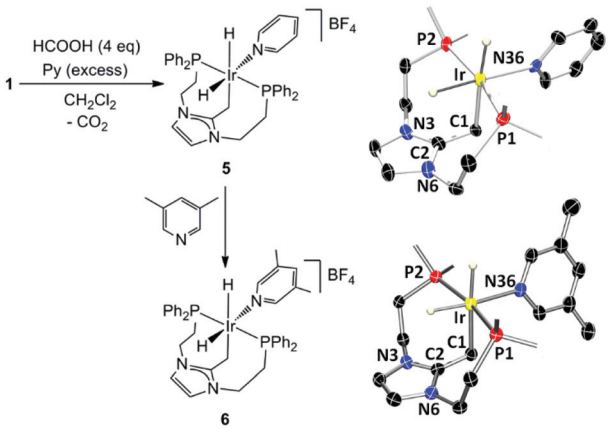

Scheme 1 Synthesis and ORTEP view of **5** and **6** (ellipsoids are drawn at the 50% probability level). The phenyl rings and PF_6^- counterions were omitted for clarity. Selected bond lengths (Å) and angles (°): **5**: Ir–C1 2.258(12), Ir–P1 2.284(3), Ir–P2 2.275(3), Ir–N36 2.196(9), C1–C2 1.434(16), P1–Ir–P2 166.87(12), Ir–C1–C2 100.2(8). **6**: Ir–C1 2.247(6), Ir–P1 2.2751(17), Ir–P2 2.2733(17), Ir–N36 2.190(5), C1–C2 1.430(9), P1–Ir–P2 166.67(6), and Ir–C1–C2 100.9(4).

Crystals of complexes **5** and **6** were obtained by slow diffusion of pentane into a saturated dichloromethane solution of the crude mixture. The molecular structures of cations **5** and **6** (Scheme 1) show a slightly distorted octahedral geometry around the iridium center, in which the PCP ligand occupies three meridional coordination sites, showing a P1–Ir–P2 angle of 166.87(12)° and 166.67(6), respectively. The other three coordination sites are occupied by two hydride ligands (one *trans* to the pyridine ligand pointing towards the NHO moiety and the other *trans* to the ylidic carbon atom) and a py ligand in **5** (Ir–N, 2.196(9) Å) or a 3,5-Me_2py in **6** (Ir–N, 2.190(5) Å).

Diagnostic peaks in the ^{1}H NMR spectrum of **5** are the two doublets of triplets assigned to the two inequivalent hydrides, which appear at δ −15.30 and −23.64 ppm in CD_2Cl_2 ($^2J_{H-P}$ = 15.3 and 20.4 Hz, respectively; $^2J_{H-H}$ = 6.2 Hz). The $^{31}P\{^1H\}$ NMR in CD_2Cl_2 shows a singlet at δ −7.3 ppm that can be assigned to the two equivalent phosphorus atoms of the PCP ligand.

The reaction of **3** or **4** with 4 eq. of HCOOH and 20 eq. of pyridine in CD_2Cl_2 (in the presence or absence of H_2O) led to the formation of a hydride complex that immediately decomposes to give fine black particles. This suggests that, in the absence of the additional stabilization provided by the NHO moiety, the unsaturated species that likely results from the loss of the COD ligand aggregates to give inactive Ir-particles.

In order to explore the reaction mechanism, the catalysis was studied by NMR in DMSO-d_6 (80 °C, 1 mol% of **1**, 10 mol% HCOONa). The ^{1}H NMR spectrum shows the formation of free H_2 and two doublets of triplets ($^2J_{H-P}$ = 17.5 Hz, $^2J_{H-H}$ = 5.7 Hz) at δ −15.29 and −17.38 ppm, which correspond to the only metallic species observed by NMR. Moreover, a singlet at δ −16.7 ppm is observed in the ^{31}P NMR spectrum. These peaks are reminiscent of those present in the NMR spectra of complexes **2** and **5**. It is noteworthy that no traces of NHO-*a*NHC isomerization[11] were observed in the ^{31}P NMR in stoichiometric or catalytic experiments, which supports the key role played by the NHO moiety.

Theoretical calculations predict the dissociation of the 1,5-cyclooctadiene ligand (COD) as a pre-activation step,‡ thus allowing FA coordination (**A** to **B**, Fig. 2). Subsequently, the intramolecular activation of the O–H bond through **TSBC** leads to the monohydride-formate species **C**. The formation of CO_2 from the formate ligand has been often proposed to occur *via* β-hydride elimination[13–15] or hydride abstraction.[14,16] In this case, the β-hydride elimination pathway is more favorable due to the presence of two accessible coordination sites. The coordination of a molecule of FA to **C** yields **D**, which evolves to **E** by deprotonation, thus leading to an energy barrier of 17.8 kcal mol^{-1} for **TSCF**. Elimination of CO_2 from **C** yields the dihydride intermediate **F**, which, upon coordination of formate, affords **G** (−9.7 kcal mol^{-1}). This species can be stabilized by exchange of the formate ligand by pyridine to give **H** (−17.2 kcal mol^{-1}), which agrees with the stoichio-

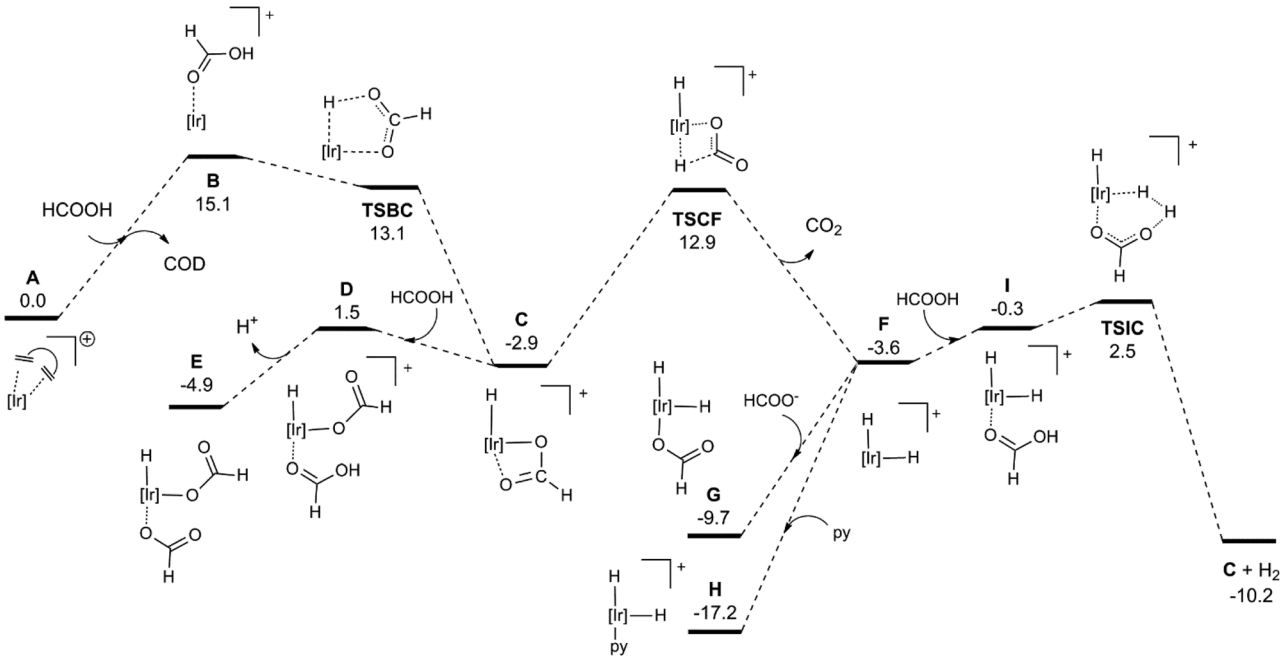

Fig. 2 DFT calculated Gibbs free energy profile (in kcal mol^{-1}) for the dehydrogenation of FA.

metric experiments that afford **5** and the *in operando* NMR experiments described above. Coordination of a molecule of FA to **F** yields **I**, which upon protonation of one of the hydride ligands regenerates **C** and produces a molecule of H_2.

The intermolecular protonation of a hydride ligand by FA has been suggested in the literature.[14,15,17] However, in this case, the vacant coordination site in **F** permits the coordination of FA and the intramolecular protonation of the hydride by a low energy process dictated by **TSIC**.

Pre-activation of the catalysts requires isomerization of the ligand from facial (**A**) to meridional (**C**). Throughout the catalytic cycle the PCP ligand adopts a meridional coordination in Ir(I) and Ir(III) centers. All these species feature an NHO moiety that coordinates end-on by the terminal C atom; however, the Ir–C–C bond angle is, in all cases, *ca.* 100° (similar angles are observed in the crystal structures of **5** and **6**), far from 114° observed for **A** and 109° expected for sp^3 hybridization. This suggests that donation from the π orbital of the olefin is substantial in these species (ESI†).

The positive effect of the addition of catalytic amounts of water on the formation of **5** prompted us to evaluate the impact of H_2O concentration on the dehydrogenation of FA. To our delight, not only was the catalyst stable to water but also its activity improved. The addition of water, from 0 mol% to 150 mol% (0, 5, 10, 30, 50, 70, 100, 120 and 150 mol% values were explored), resulted in a progressive improvement of the activity (Fig. 3). Remarkably, H_2O addition increases the reaction rate until it reaches a plateau at 30 mol%. From 50 mol-% onwards a sharper rise of activity occurs. Above 100 mol% no significant increase was observed upon H_2O addition. This intricate behavior could be ascribed to a combination of different effects: the role that H_2O molecules play in the dissociation of HCOOH, the stabilization of intermediate species of the catalytic cycle or the fact that a significant percentage of the water molecules may engage in hydrogen bonding with HCOOH. By DFT calculations, we were unable to model an alternative mechanism triggered by the presence of water that would lead to a lower energy pathway. In particular, the use of a water molecule as proton shuttle does not reduce the activation energy of the rate-limiting step, the β-hydride elimination (**TSCF**). However, transition state stabilization through hydrogen bonding should not be discarded.[18] Plausibly, the combined effect of several H_2O molecules, involved in second-sphere hydrogen bonding, lowers the activation energy of the process.

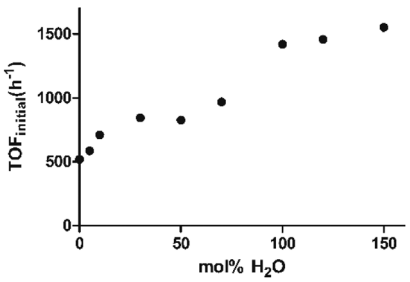

Fig. 3 Effect of H_2O addition on the FA dehydrogenation rate using 5 mol% of HCOONa and 0.016 mol% of **1**.§

In view of the good performance of **1** in the presence of water, its activity in an aqueous solution of FA was also tested in order to broaden its scope. The use of 1 mol% of **1** and 10 mol% of HCOONa at 80 °C in water led to a TOF§ value of 9840 h^{-1}. We were able to recycle the catalyst 14 times,

although activity loss was observed throughout the recycling experiments (ESI†).

Subsequently, we studied the performance of the catalyst at different formate loadings and, consequently, the effects of the pH of the reaction media on the TOF of the reaction. In this regard, a number of reports have proved that the activity of the catalyst depends on the pH of the solution, with optimum values being usually observed between 3 and 4.[15,19]

Fig. 4 shows the TOF values for HCOONa loadings that range from 5 mol% to 100 mol%, with the optimum base concentration being 30 mol% independently of the H_2O concentration (5 mol% or 100% of H_2O). The temperature was optimized using 100 mol% of H_2O and 30 mol% of sodium formate, displaying the best performance at 90 °C (Fig. 5).

The TOF values§ calculated at 60, 70, 80 and 90 °C were 410, 1390, 2580 and 5170 h^{-1}, respectively. The positive effect of the increasing temperature on the catalytic performance suggests that the catalyst is thermally stable in this range of temperatures.[20] In this regard, addition of a drop of mercury to the reaction mixture shows no influence on the reaction rate, which supports the homogeneous nature of the active species.

Remarkably, a TOF§ value of 11 590 h^{-1} and a TON of 8030 (after 5 h) were obtained upon reduction of the catalyst (**1**) loading to 0.001 mol%. Under these conditions, the formation of carbon monoxide was below the detection limit of the infrared spectrum (3 ppm).[3a] The TOF value of 11 590 h^{-1} obtained by us compares well with the highest TOFs so far reported for the solventless dehydrogenation of FA, namely 13 320 h^{-1} and 11 760 h^{-1} reported by Williams *et al.*[10] and Gelman *et al.*,[9b] respectively. At variance with the two excellent catalysts reported by Williams' and Gelman's groups, **1** was proved to work also using water as solvent. Therefore, to the best of our knowledge, this is the only catalyst so far reported to work both in water and under solventless conditions.

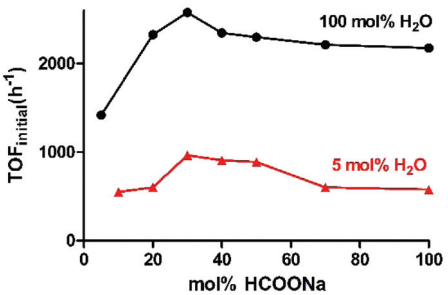

Fig. 4 Effect of HCOONa addition on the FA dehydrogenation rate with 100 mol% and 5 mol% of H_2O, using 0.016 mol% of **1**.§

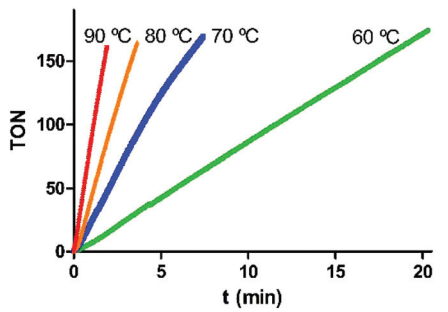

Fig. 5 Reaction profiles for the dehydrogenation of FA in the temperature range 60–90 °C (100 mol% of H_2O, 30 mol% of HCOONa and 0.016 mol% of **1**).

The reaction rates measured at temperatures between 60 and 90 °C allowed the experimental estimation of the activation energy by the Arrhenius plot (E_a = 19.9 ± 0.8 kcal mol^{-1} at 100 mol% of H_2O, 30 mol% of HCOONa and 0.016 mol% of **1**). The activation energy in the absence of H_2O was also calculated under the same experimental conditions (to give a value of 24.5 ± 1.8 kcal mol^{-1}). These E_a values are considerably lower than those reported for FA decomposition by means of a non-catalyzed process.[21]

Taking into consideration the limitations inherent to DFT calculations for the quantitative prediction of activation energies for these types of systems, the theoretical activation energy (17.8 kcal mol^{-1}) agrees well with the experimental energy barrier calculated from the Arrhenius plots (ESI†).

Conclusions

In conclusion, we have demonstrated that **1** is an exceptionally active catalyst for the solventless dehydrogenation of FA. The fact that **1** performs markedly better than complexes **3** and **4** emphasizes the importance of the NHO moiety, which is key to the success of the reaction. The DFT calculations presented here agree with the stoichiometric reactions that lead to compounds **5** and **6**, which are closely related to intermediate **G**. Moreover, the low activity of **2** agrees with the postulated mechanism, which requires a vacant coordination site at the position that the carbonyl ligand occupies. Remarkably, the addition of water to the reaction mixture significantly increases the reaction rates. In fact, **1** also works in an aqueous solution of FA, this being as far as we know the only example of a catalyst that is active under solventless conditions and in water. The effect of water may be related to a decrease of the activation energy by second-sphere hydrogen bonding; however, further investigation is required to understand the nature of these interactions.

Conflicts of interest

There are no conflicts to declare.

Acknowledgements

This work was supported by the Spanish Ministry of Education, Culture and Sports (MECD) (project CTQ2016-75884-P, "Ramón y Cajal" program RYC2016-20864 (M. I.) and FPU14/06003 (J. M.)) and the DGA/E42_17R. J. M. and V. P. gratefully acknowledge the resources from the supercomputer "memento" and technical assistance provided by BIFI-ZCAM.

Notes and references

‡ The dissociation of the COD ligand in Ir-NHO complexes has been previously reported by us (see ref. 11*b*).
§ TOF values were calculated at 1 min reaction time.

1 (*a*) G. W. Huber, S. Iborra and A. Corma, *Chem. Rev.*, 2006, **106**, 4044–4098; (*b*) V. Smil, *Energy at the Crossroads, Global Perspectives and Un-certainties*, MIT Press, Cambridge, 2003.

2 (*a*) D. A. J. Rand and R. M. Dell, *Hydrogen Energy-Challenges and Prospects*, RSC Publishing, Cambridge, 2008; (*b*) *Hydrogen as a Future Energy Carrier*, ed. A. Züttel, A. Borgschulte and L. Schlapbach, Wiley-VCH Verlag GmbH & Co. KgaA, Weinheim, 2008.

3 (*a*) F. Joó, *ChemSusChem*, 2008, **1**, 805–808; (*b*) N. A. Kelly, in *Advances in Hydrogen Production, Storage and Distribution*, ed. A. Basile and A. Iulianelli, Woodhead Publishing, Cambridge, 2014, ch. 6, pp. 159–185.

4 (*a*) P. Preuster, C. Papp and P. Wasserscheid, *Acc. Chem. Res.*, 2017, **50**, 74–85; (*b*) D. Teichmann, W. Arlt and P. Wasserscheid, *Int. J. Hydrogen Energy*, 2012, **37**, 18118–18132.

5 (*a*) J. Eppinger and K.-W. Huang, *ACS Energy Lett.*, 2017, **2**, 188–195; (*b*) *Ullmann's Encyclopedia of Industrial Chemistry*, ed. B. Elvers, S. Hawkings, M. Ravenscroft, F. Rounsaville and G. Schulz, Wiley-VCH, Weinheim, 1989, vol. A12, pp. 13–33.

6 B. Loges, A. Boddien, H. Junge and M. Beller, *Angew. Chem., Int. Ed.*, 2008, **47**, 3962–3965.

7 C. Fellay, P. J. Dyson and G. Laurenczy, *Angew. Chem., Int. Ed.*, 2008, **47**, 3966–3968.

8 K. Sordakis, C. Tang, L. K. Vogt, H. Junge, P. J. Dyson, M. Beller and G. Laurenczy, *Chem. Rev.*, 2018, **118**, 372–433.

9 (*a*) S. Oldenhof, B. de Bruin, M. Lutz, M. A. Siegler, F. W. Patureau, J. I. van der Vlugt and J. N. H. Reek, *Chem. – Eur. J.*, 2013, **19**, 11507–11511; (*b*) S. Cohen, V. Borin, I. Schapiro, S. Musa, S. De-Botton, N. V. Belkova and D. Gelman, *ACS Catal.*, 2017, **7**, 8139–8146.

10 J. J. A. Celaje, Z. Lu, E. A. Kedzie, N. J. Terrile, J. N. Lo and T. J. Williams, *Nat. Commun.*, 2016, **7**, 11308.

11 (*a*) M. Iglesias, A. Iturmendi, P. J. Sanz Miguel, V. Polo, J. J. Pérez-Torrente and L. A. Oro, *Chem. Commun.*, 2015, **51**, 12431–12434; (*b*) A. Iturmendi, N. García, E. A. Jaseer, J. Munárriz, P. J. Sanz Miguel, V. Polo, M. Iglesias and L. A. Oro, *Dalton Trans.*, 2016, **45**, 12835–12845.

12 Complexes **3** and **4** were prepared according to literature procedures: (*a*) M. P. Betore, M. A. Casado, P. García-Orduña, F. J. Lahoz, V. Polo and L. A. Oro, *Organometallics*, 2016, **35**, 720–731; (*b*) T. Makino, Y. Yamamoto and K. Itoh, *Organometallics*, 2004, **23**, 1730–1737; (*c*) W. A. Fordyce and G. A. Crosby, *Inorg. Chem.*, 1982, **21**, 1455–1461.

13 For examples see: (*a*) J. Li, J. Li, D. Zhang and C. Liu, *ACS Catal.*, 2016, **6**, 4746–4754; (*b*) C. Fellay, N. Yan, P. J. Dyson and G. Laurenczy, *Chem. – Eur. J.*, 2009, **15**, 3752–3760; (*c*) L. S. Jongbloed, B. de Bruin, J. N. H. Reek, M. Lutz and J. I. van der Vlugt, *Catal. Sci. Technol.*, 2016, **6**, 1320–1327; (*d*) A. Boddien, D. Mellmann, F. Gärtner, R. Jackstell, H. Junge, P. J. Dyson, G. Laurenczy, R. Ludwig and M. Beller, *Science*, 2011, **333**, 1733–1736.

14 M. Iglesias and L. A. Oro, *Eur. J. Inorg. Chem.*, 2018, 2125–2138.

15 S. Fukuzumi, T. Kobayashi and T. Suenobu, *J. Am. Chem. Soc.*, 2010, **132**, 1496–1497.

16 (*a*) F. J. Fernández-Alvarez, M. Iglesias, L. A. Oro and V. Polo, *ChemCatChem*, 2013, **5**, 3481–3494; (*b*) X. Yang, *Dalton Trans.*, 2013, **42**, 11987–11991; (*c*) T. Zell, B. Butschke, Y. Ben-David and D. Milstein, *Chem. – Eur. J.*, 2013, **19**, 8068–8072; (*d*) E. A. Bielinski, P. O. Lagaditis, Y. Zhang, B. Q. Mercado, C. Würtele, W. H. Bernskoetter, N. Hazari and S. Schneider, *J. Am. Chem. Soc.*, 2014, **136**, 10234–10237.

17 For examples see: (*a*) A. Matsunami, Y. Kayaki and T. Ikariya, *Chem. – Eur. J.*, 2015, **21**, 13513–13517; (*b*) T. Abura, S. Ogo, Y. Watanabe and S. Fukuzumi, *J. Am. Chem. Soc.*, 2003, **125**, 4149–4154; (*c*) A. Boddien, B. Loges, F. Gärtner, C. Torborg, K. Fumino, H. Junge, R. Ludwig and M. Beller, *J. Am. Chem. Soc.*, 2010, **132**, 8924–8934.

18 (*a*) P. J. Dyson and P. G. Jessop, *Catal. Sci. Technol.*, 2016, **6**, 3302–3316; (*b*) K. Leung and S. B. Rempe, *J. Am. Chem. Soc.*, 2004, **126**, 344–351; (*c*) N. Akiya and P. E. Savage, *AIChE J.*, 1998, **44**, 405–415.

19 (*a*) S. Siek, D. B. Burks, D. L. Gerlach, G. Liang, J. M. Tesh, C. R. Thompson, F. Qu, J. E. Shankwitz, R. M. Vasquez, N. Chambers, G. J. Szulczewski, D. B. Grotjahn, C. E. Webster and E. T. Papish, *Organometallics*, 2017, **36**, 1091–1106; (*b*) J. F. Hull, Y. Himeda, W.-H. Wang, B. Hashiguchi, R. Periana, D. J. Szalda, J. T. Muckerman and E. Fujita, *Nat. Chem.*, 2012, **4**, 383–388; (*c*) S. Fukuzumi, T. Kobayashi and T. Suenobu, *ChemSusChem*, 2008, **1**, 827–834; (*d*) Y. Himeda, *Green Chem.*, 2009, **11**, 2018–2022; (*e*) W.-H. Wang, M. Z. Ertem, S. Xu, N. Onishi, Y. Manaka, Y. Suna, H. Kambayashi, J. T. Muckerman, E. Fujita and Y. Himeda, *ACS Catal.*, 2015, **5**, 5496–5504.

20 (*a*) A. Matsunami, S. Kuwata and Y. Kayaki, *ACS Catal.*, 2017, **7**, 4479–4484; (*b*) A. Matsunami, Y. Kayaki and T. Ikariya, *Chem. – Eur. J.*, 2015, **21**, 13513–13517.

21 P. Ruelle, U. W. Kesselring and H. Nam-Tran, *J. Am. Chem. Soc.*, 1986, **108**, 371–375.

ChemComm

COMMUNICATION

Cite this: *Chem. Commun.*, 2017, 53, 404

Received 15th November 2016,
Accepted 6th December 2016

DOI: 10.1039/c6cc09133d

www.rsc.org/chemcomm

Efficient preparation of carbamates by Rh-catalysed oxidative carbonylation: unveiling the role of the oxidant†

Amaia Iturmendi,[a] Manuel Iglesias,*[a] Julen Munárriz,[b] Victor Polo,[b] Jesús J. Pérez-Torrente[a] and Luis A. Oro*[ac]

The synthesis of a wide variety of carbamates from amines, alcohols and carbon monoxide has been achieved by means of a Rh-catalysed oxidative carbonylation reaction that uses Oxone as a stoichiometric oxidant. In-depth studies on the reaction mechanism shed light on the intimate role of Oxone in the catalytic cycle.

The importance of developing new routes that permit a more efficient and straightforward access to organic carbamates is well illustrated by the extensive application of these molecules as pharmaceuticals, agrochemicals or materials in the chemical industry.[1] In addition, carbamates are commonly used as amine protecting groups and are, therefore, important intermediates or starting materials in modern synthetic chemistry.[2]

Classic approaches to the synthesis of carbamates from amines and alcohols usually entail the use of phosgene or its derivatives.[3] Other relevant stoichiometric methods use azides,[4] isocyanates,[5] and CO_2 or carbonates.[6] Several catalysed processes that employ CO_2 as a C1 source, amines and alcohols have also been developed.[7]

The synthesis of carbamates by the oxidative carbonylation of N–H bonds from readily available amines and alcohols has been achieved by means of Pd[8] and Au[9] catalysts under high pressures of CO, usually above 40 bar. Noteworthy exceptions that operate under milder conditions are the methods reported by Orito[10] and Guan.[11] An alternative method for the synthesis of carbamates by carbonylation under low CO pressure requires the use of aromatic and aliphatic azides as starting materials.[12]

The excellent activity of Rh catalysts towards carbonylation reactions[13] prompted us to investigate the activity of commercially available rhodium complexes in the synthesis of carbamates from amines, alcohols and carbon monoxide under mild conditions. Moreover, in order to broaden the synthetic significance and scope of this reaction we assessed Oxone (potassium peroxymonosulfate, $KHSO_5$) as an oxidant, which is an inexpensive, safe and environmentally friendly reagent.[13d]

Initial catalytic tests aimed at evaluating the activity of various commercially available rhodium complexes in the oxidative carbonylation of aniline with 1-hexanol (5 equivalents). The reaction was completed after stirring at 100 °C in toluene for 18 h under a carbon monoxide atmosphere (2 bar) using $[Rh(\mu\text{-Cl})(COD)]_2$, $[Rh(\mu\text{-MeO})(COD)]_2$ or $[Rh(\mu\text{-Cl})(Cl)(Cp^*)]_2$ (COD = cyclooctadiene and Cp* = pentamethylcyclopentadienyl) as catalysts and Oxone as an oxidant (3 equivalents). The Rh(III) catalyst, $[Rh(\mu\text{-Cl})(Cl)(Cp^*)]_2$, led to the formation of carbamate/urea mixtures, while $[Rh(\mu\text{-Cl})(COD)]_2$ and $[Rh(\mu\text{-MeO})(COD)]_2$ afforded exclusively the carbamate in identical isolated yields (75%). Building on these results we decided to explore the scope of $[Rh(\mu\text{-Cl})(COD)]_2$ as a catalyst for this reaction using a variety of amines and alcohols.

Aniline can be efficiently converted into its corresponding carbamates employing a variety of primary and secondary alcohols without the formation of decarboxylation products or ureas (Scheme 1). The compatibility of this methodology with a variety of amines was also tested (Scheme 2).

In view of the potential applicability of this methodology in the synthesis of bioactive molecules, it is significant that the

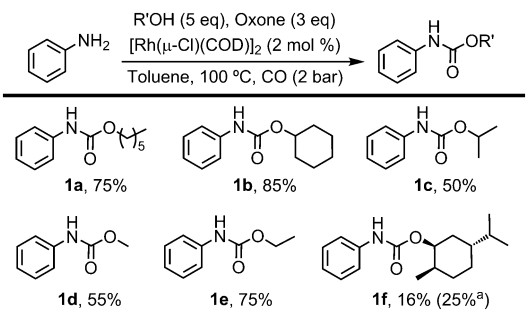

Scheme 1 Oxidative carbonylation of aniline with various alcohols (isolated yields after 16 h).[a]Isolated yield after 5 d.

[a] *Departamento Química Inorgánica – ISQCH, Universidad de Zaragoza – CSIC, 50009 Zaragoza, Spain. E-mail: miglesia@unizar.es, oro@unizar.es*
[b] *Departamento Química Física – Instituto de Biocomputación y Física de Sistemas Complejos (BIFI), Universidad de Zaragoza, 50009 Zaragoza, Spain*
[c] *King Fahd University of Petroleum & Minerals (KFUPM), Dhahran 31261, Saudi Arabia*

† Electronic supplementary information (ESI) available: DFT details. See DOI: 10.1039/c6cc09133d

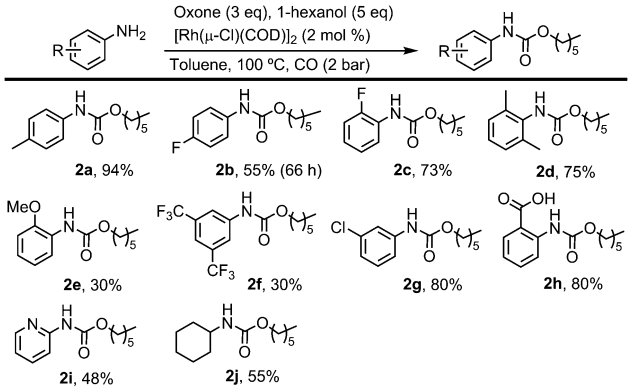

Scheme 2 Oxidative carbonylation of amines with 1-hexanol (isolated yields after 16 h).

presence of carboxylic acids does not seem to thwart the reaction; in fact, **2h** is obtained in excellent yields. In addition, compounds **2i** and **2j** were obtained from 2-aminopyridine and cyclohexylamine, respectively, which demonstrates that the catalyst performs well even with potentially chelating substrates and with aliphatic amines.

In order to assess the scope of this methodology, a secondary alcohol, 2-propanol, was used instead of 1-hexanol (Scheme 3). Except for **3c**, **3e** and **3j,** the expected carbamates were obtained successfully, although the use of a secondary alcohol seems to bring about somewhat lower yields in most cases, probably due to its increased steric hindrance. In fact, bulky amines such as *ortho*-substituted anilines or cyclohexylamine are particularly affected. Remarkably, this methodology permits the phosgene-free preparation of chlorpropham (**3g**), an example of a carbamate-based marketed drug.[3a,12]

The use of imines as starting materials also yields directly the corresponding carbamates without the need for previous transformation into the related amines. Compounds **1a** and **1c** were obtained by the reaction of imines **4** and **5** with 1-hexanol or 2-propanol (Scheme 4). A plausible explanation for this reaction would be that, in the presence of adventitious water, the imines deliver *in situ* the corresponding amines. Subsequently, the formation of the carbamate, concomitant generation of a H_2O

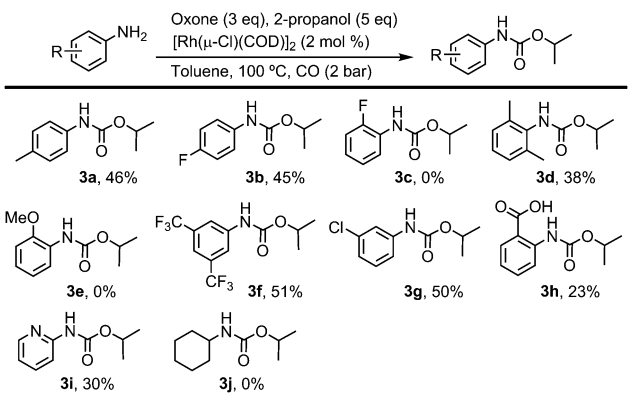

Scheme 3 Oxidative carbonylation of amines with 2-propanol (isolated yields after 16 h).

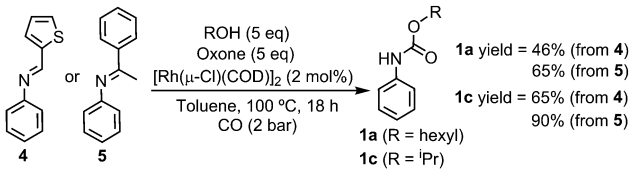

Scheme 4 Direct preparation of carbamates form imines (isolated yields).

molecule and the consumption of free amine from the reaction mixture would drive the hydrolysis equilibrium toward the formation of more amine.

The mechanistic information on Rh-catalysed oxidative-coupling reactions is limited, and the role played by the oxidant is still a source of controversy. Moreover, the studies published so far have focused mainly on Rh(III) catalysts that make use of $Cu(OAc)_2$ as a stoichiometric oxidant.[14,15] Recently, various examples of alkoxycarbonylation of C–H bonds that use Rh(I) catalysts and persulfates as the oxidant have been reported.[16] Two different mechanisms have been postulated for this type of reactions.[17] The first, proposed by Zhang *et al.* for the directed alkoxycarbonylation of arenes, entails the abstraction of a hydrido ligand, formed by previous oxidative addition of the substrate's C–H bond, and the proton of a coordinated alcohol by Oxone (Scheme 5a).[17a] On the other hand, a report by Li and co-workers proposes the oxidation of $[Rh(\mu\text{-}Cl)(COD)]_2$ to a Rh(III) species by $K_2S_2O_8$ as the first step of the catalytic cycle for the non-directed alkoxycarbonylation of indenes (Scheme 5b).[17b]

Prompted by the scarce mechanistic knowledge on this type of oxidations, we set off to study the role played by Oxone in the catalytic cycle and the intimate mechanism through which the complex or substrates interact with the oxidant.

An NMR study showed that a solution of 0.5 equivalents of $[Rh(\mu\text{-}Cl)(COD)]_2$, 1 equivalent of aniline, 1-hexanol and Oxone afforded complex $[Rh(Cl)(CO)_2(aniline)]$[18] under a CO atmosphere at room temperature in CD_2Cl_2. No further reaction was observed upon an increase of the temperature to 50 °C. Attempts to detect CO insertion intermediates *via* the reaction of $[Rh(\mu\text{-}Cl)(COD)]_2$ with aniline or 1-hexanol under a CO atmosphere in toluene-d_8 at 100 °C were unsuccessful. However, when Oxone, 1-hexanol, aniline and 0.5 equivalents of $[Rh(\mu\text{-}Cl)(COD)]_2$ were reacted at 100 °C in toluene under a CO atmosphere, the carbamate and $[Rh(Cl)(CO)_2(aniline)]$ were obtained; conversely, at room temperature no carbamate formation was observed. This suggests that, in this case, Oxone acts before any metal-mediated substrate activation takes place.

In order to shed light on the reaction mechanism, a computational study at the DFT level was performed using

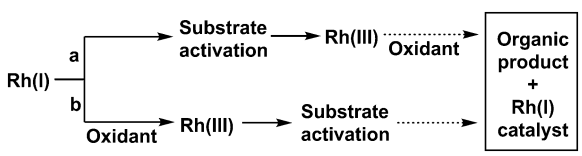

Scheme 5 Differences between the role played by the oxidant in the mechanisms proposed by Zhang and Li.

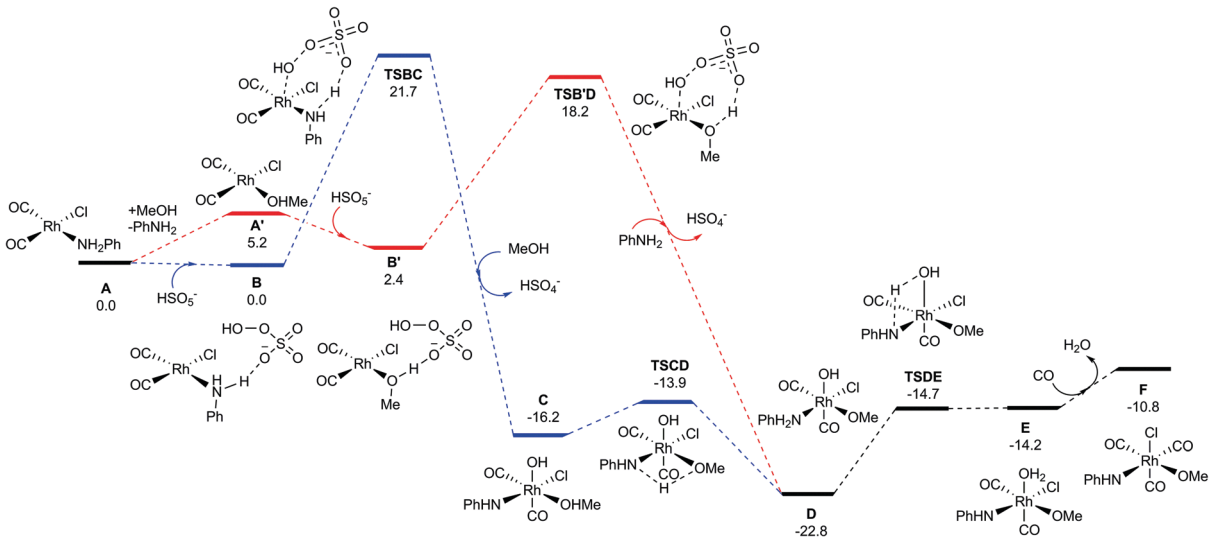

Fig. 1 DFT calculated Gibbs free energy profile (in kcal mol^{-1} and relative to **A** and isolated molecules) for the Rh-catalysed oxidative carbonylation of amines.

the B3LYP-D3 functional, considering [Rh(Cl)(CO)$_2$(aniline)] as the catalyst (**A**) and MeOH as the alcohol. Fig. 1 shows the most plausible mechanism of action of Oxone according to the theoretical calculations and experimental data. Two related pathways can be postulated. In the first, Oxone interacts directly with [Rh(Cl)(CO)$_2$(aniline)] (blue lines) while, in the second, previous substitution of aniline by MeOH is required (red lines). In both cases, the oxidation of the Rh centre and the deprotonation of the substrate (alcohol or aniline) take place according to a concerted mechanism at the beginning of the catalytic cycle,‡ prior to substrate activation or migratory insertion.§ Under the reaction conditions both reaction pathways may occur simultaneously although the second path (red lines) features a slightly lower activation barrier. This mechanism entails that, after the formation of **A′**, the coordinated methanol molecule interacts with Oxone *via* a hydrogen bond to give adduct **B′**. This triggers the oxidation of Rh(I) to Rh(III) by means of a concerted transition state (**TSB'D**) in which Oxone deprotonates the methanol ligand and transfers the hydroxo group to the metal. Simultaneously, the release of HSO_4^- and the formation of **D** upon coordination of aniline take place. The presence of the OH ligand allows for the deprotonation of the coordinated amine, thus affording the aquo-complex **E** *via* **TSDE**, surmounting an energetic barrier of 8.1 kcal mol^{-1}. The carbonylation and isomerisation of **E** give Rh(III)-amido complex **F**. The downslope pathway thereafter (Fig. 2) entails the migratory insertion of the carbonyl ligand into the M–N bond, thus forming intermediate **G**. Finally, the reductive elimination of the carbamoyl (RNHC(O)–) and alkoxo (RO–) ligands, according to the transition state **TSGH**, affords the corresponding carbamate and regenerates the catalyst (**A**) after the exchange of the carbonyl ligand by aniline.

It is noteworthy that the relatively low energy span calculated for the catalytic cycle (23.0 kcal mol^{-1}) from intermediate **D** to the transition state **TSFG** does not seem to justify the high

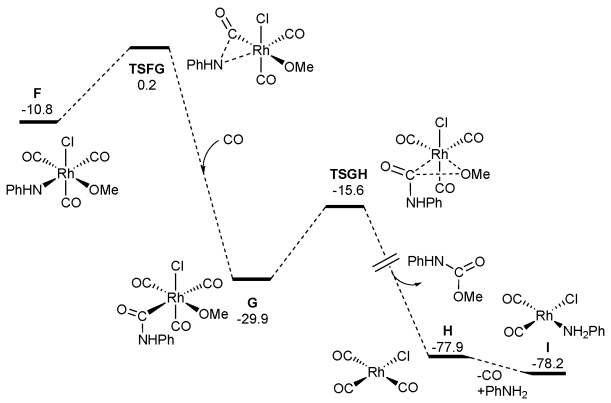

Fig. 2 DFT calculated Gibbs free energy profile (in kcal mol^{-1} and relative to **A** and isolated molecules) for Rh-catalysed oxidative carbonylation of amines.

temperatures required for this reaction. This apparent inconsistency, however, is in accord with the almost negligible solubility of Oxone in organic solvents and the ensuing reactivity problems reported in the literature.[19] Therefore, the reaction rate probably depends on the concentration of Oxone in the solution, which increases at higher temperatures. In this regard, we performed the synthesis of **1a** (Scheme 1) in the presence of a phase transfer catalyst, namely 4 mol% of tetrabutylammonium tetrafluoroborate, which acts as a surfactant that solubilises Oxone. In this case, the reaction takes place at 50 °C; however, *ca.* 40% of aldehyde was obtained as a by-product due to alcohol oxidation.

In conclusion, we have disclosed a Rh(I)-catalysed three-component reaction that allows for the preparation of carbamates from amines (or imines), alcohols and carbon monoxide under mild conditions, affording water and $KHSO_4$ as the only reaction by-products. This process is catalysed by the commercially available complex [Rh(μ-Cl)(COD)]$_2$ in the presence of Oxone. This methodology shows a good tolerance to several functional

groups and is compatible with primary and secondary alcohols. Theoretical and experimental data suggest that Oxone plays a dual role as a base and an oxidant, thus allowing for initial oxidation of the Rh(I) pre-catalyst to a Rh(III) species—this step being essential to achieve substrate activation. Remarkably, this transformation requires previous coordination of the alcohol because its deprotonation and the oxidation of the metal centre occur *via* a concerted mechanism.

This work was supported by the Spanish Ministry of Economy and Competitiveness (MINECO/FEDER) (CONSOLIDER INGENIO CSD2009-0050, CTQ2013-42532-P and CTQ2015-67366-P projects) and the DGA/FSE-E07. The support from the KFUPM-University of Zaragoza research agreement and the Centre of Research Excellence in Petroleum Refining & KFUPM is gratefully acknowledged. V. P. acknowledges the support of BIFI-ZCAM. J. M. thanks the support from the Ministry of Education Culture and Sports (FPU14/06003).

Notes and references

‡ The use of 3-chloroperoxybenzoic acid as an oxidant with or without an external base (K_2SO_4 or DMAP) fails to afford the corresponding carbamates, which suggests that the oxidant and the base act according to a concerted mechanism.

§ Alternative mechanisms where substrate activation precedes Rh(I) → Rh(III) oxidation by Oxone or Rh(I) → Rh(III) oxidation by Oxone occurs without substrate coordination show higher activation energies (see the ESI†).

1 A. K. Ghosh and M. Brindisi, *J. Med. Chem.*, 2015, **58**, 2895–2940.
2 For examples see: (*a*) O. Dangles, F. Guibd and G. Balavoine, *J. Org. Chem.*, 1987, **52**, 4984–4993; (*b*) A. Merzouk, F. Guibé and A. Loffet, *Tetrahedron Lett.*, 1992, **33**, 477–480; (*c*) G. Hancock, I. J. Galpin and B. A. Morgan, *Tetrahedron Lett.*, 1982, **23**, 249–252.
3 For examples see: (*a*) T. A. Unger, in *Pesticides Synthesis Book*, ed. W. Andrew, Noyes Publications, New Jersey, 1996; (*b*) H. Babad and A. G. Zeiler, *Chem. Rev.*, 1973, **73**, 75–91; (*c*) S. M. Rahmathullah, J. E. Hall, B. C. Bender, D. R. McCurdy, R. R. Tidwell and D. W. Boykin, *J. Med. Chem.*, 1999, **42**, 3994–4000; (*d*) N. A. Roberts, J. A. Martin, D. Kinchington, A. V. Broadhurst, J. C. Craig, I. B. Duncan, S. A. Galpin, B. K. Handa, J. Kay, A. Krohn, R. W. Lambert, J. H. Merrett, J. S. Mills, K. E. B. Parkes, S. Redshaw, A. J. Ritchie, D. L. Taylor, G. J. Thomas and P. J. Machin, *Science*, 1990, **248**, 358–361; (*e*) H. Eckert and B. Forster, *Angew. Chem., Int. Ed. Engl.*, 1987, **26**, 894–895.
4 E. F. V. Scriven and K. Turnbull, *Chem. Rev.*, 1988, **88**, 297–368.
5 G. Raspoet and M. T. Nguyen, *J. Org. Chem.*, 1998, **63**, 6878–6885.
6 (*a*) M. Yoshida, Na. Hara and S. Okuyama, *Chem. Commun.*, 2000, 151–152; (*b*) T. Tsuda, K. Watanabe, K. Miyata, H. Yamamoto and T. Saegusa, *Inorg. Chem.*, 1981, **20**, 2728–2730; (*c*) A. Inesi, V. Mucciante and L. Rossi, *J. Org. Chem.*, 1998, **63**, 1337–1338; (*d*) W. D. McGhee, D. P. Riley, M. E. Christ and K. M. Christ, *Organometallics*, 1993, **12**, 1429–1433; (*e*) R. N. Salvatore, J. A. Ledger and K. W. Jung, *Tetrahedron Lett.*, 2001, **42**, 6023–6025.
7 (*a*) M. Abla, J. C. Choi and T. Sakakura, *Chem. Commun.*, 2001, 2238–2239; (*b*) M. Abla, J. C. Choi and T. Sakakura, *Green Chem.*, 2004, **6**, 524–525; (*c*) S. L. Peterson, S. M. Stucka and C. J. Dinsmore, *Org. Lett.*, 2010, **12**, 1340–1343; (*d*) A. Julián, V. Polo, E. A. Jaseer, F. J. Fernández-Alvarez and L. A. Oro, *ChemCatChem*, 2015, **7**, 3895–3902 (preparation of silyl carbamates).
8 (*a*) B. Gabriele, G. Salerno, R. Mancuso and M. Costa, *J. Org. Chem.*, 2004, **69**, 4741–4750; (*b*) F. Shi, Y. Deng, T. SiMa and H. Yang, *J. Catal.*, 2001, **203**, 525–528; (*c*) A. K. Ghosh and M. Brindisi, *J. Med. Chem.*, 2015, **58**, 2895–2940; (*d*) S. Fukuoka, M. Chono and M. Kohno, *J. Org. Chem.*, 1984, **49**, 1458–1460; (*e*) H. Alper and F. W. Hartstock, *J. Chem. Soc., Chem. Commun.*, 1985, 1141–1142; (*f*) S. Fukuoka, M. Chono and M. Kohno, *J. Chem. Soc., Chem. Commun.*, 1984, 399–400; (*g*) B. Gabriele, R. Mancuso, G. Salerno and M. Costa, *Top. Organomet. Chem.*, 2006, **18**, 239–271.
9 F. Shi and Y. Deng, *Chem. Commun.*, 2001, 443–444.
10 K. Orito, M. Miyazawa, T. Nakamura, A. Horibata, H. Ushito, H. Nagasaki, M. Yuguchi, S. Yamashita, T. Yamazaki and M. Tokuda, *J. Org. Chem.*, 2006, **71**, 5951–5958.
11 Z.-H. Guan, H. Lei, M. Chen, Z.-H. Ren, Y. Bai and Y.-Y. Wanga, *Adv. Synth. Catal.*, 2012, **354**, 489–496.
12 L. Rena and N. Jiao, *Chem. Commun.*, 2014, **50**, 3706–3709.
13 (*a*) J. P. Collman, L. S. Hegedus, J. R. Norton and R. G. Finke, *Principles and Applications of Organotransition Metal Chemistry*, University Science Books, Mill Valley, CA, 1978; (*b*) J. F. Hartwig, *Organotransition metal chemistry-from bonding to catalysis*, University Science Books, 2009, vol. 753, pp. 745–825; (*c*) F. J. Fernández-Alvarez, M. Iglesias, L. A. Oro and V. Passarelli, in *Comprehensive Inorganic Chemistry II*, ed. J. Reedijk and K. Poeppelmeier, Elsevier, Oxford, 2013, vol. 8, pp. 399–432; (*d*) Z.-H. Guan, Z.-H. Ren, S. M Spinella, S. Yu, Y.-M. Liang and X. Zhang, *J. Am. Chem. Soc.*, 2009, **131**, 729–733; (*e*) R. Lang, J. Wu, L. Shi, C. Xi and F. Li, *Chem. Commun.*, 2011, **47**, 12553–12555; (*f*) B. Liu, F. Hu and B.-F. Shi, *ACS Catal.*, 2015, **5**, 1863–1881; (*g*) A. Iturmendi, P. J. Sanz Miguel, S. A. Popoola, A. A. Al-Saadi, M. Iglesias and L. A. Oro, *Dalton Trans.*, 2016, **45**, 16955–16965.
14 For computational studies see: (*a*) I. Funes-Ardoiz and F. Maseras, *Angew. Chem., Int. Ed.*, 2016, **55**, 2764–2767; (*b*) L. Xu, Q. Zhu, G. Huang, B. Cheng and Y. Xia, *J. Org. Chem.*, 2012, **77**, 3017–3024; (*c*) N. Quiñones, A. Seoane, R. García-Fandiño, J. L. Mascareñas and M. Gulías, *Chem. Sci.*, 2013, **4**, 2874–2879; (*d*) D. L. Davies, C. E. Ellul, S. A. Macgregor and C. L. McMullin, *J. Am. Chem. Soc.*, 2015, **137**, 9659–9669; (*e*) J. Jiang, R. Ramozzi and K. Morokuma, *Chem. – Eur. J.*, 2015, **21**, 11158–11164.
15 For experimental studies see: (*a*) L. Li, W. W. Brennessel and W. D. Jones, *Organometallics*, 2009, **28**, 3492–3500; (*b*) N. Wang, B. Li, H. Song, S. Xu and B. Wang, *Chem. – Eur. J.*, 2013, **19**, 358–364.
16 B. Liu, F. Hu and B.-F. Shi, *ACS Catal.*, 2015, **5**, 1863–1881.
17 (*a*) Z.-H. Guan, Z.-H. Ren, S. M. Spinella, S. Yu, Y.-M. Liang and X. Zhang, *J. Am. Chem. Soc.*, 2009, **131**, 729–733; (*b*) R. Lang, J. L. Wu, L. J. Shi, C. G. Xia and F. W. Li, *Chem. Commun.*, 2011, **47**, 12553–12555.
18 D. N. Lawson and G. Wilkinson, *J. Chem. Soc.*, 1965, 1900–1907.
19 (*a*) E. P. Bulman Page and B. R. Buckley, in *Mechanisms in Homogeneous and Heterogeneous Epoxidation Catalysis*, ed. S. T. Oyama, Elsevier, Oxford, 2008, pp. 177–217; (*b*) B. M. Trost and R. Braslau, *J. Org. Chem.*, 1988, **53**, 532–537.

ChemPubSoc Europe

DOI: 10.1002/cctc.201700302

CHEMCATCHEM Full Papers

Analysis of the Magnetic Entropy in Oxygen Reduction Reactions Catalysed by Manganite Perovskites

Jose Gracia,*[a] Julen Munarriz,[b] Victor Polo,[b] Ryan Sharpe,[a] Yunzhe Jiao,[a] J. W. (Hans) Niemantsverdriet,[a, c] and Tingbin Lim[a]

Manganese oxides with a half-metallic ground state are particularly active for oxygen reduction reactions (ORR). $La_{0.67}Sr_{0.33}MnO_3$ (LSMO) perovskite is the archetypal example for compositions with a Curie temperature (T_C) above room temperature and with a high intrinsic activity for the partial reduction of triplet-state O_2. The ferromagnetic (FM) character of the superexchange interactions in LSMO facilitates both charge and spin transport below 370 K. Other than the enhanced electronic conductivity, the reduced spin entropy seems to be relevant in oxygen catalysis because the magnetic ordering extends to the surface. The sign of the exchange interactions determines the adsorption of the triplet oxygen molecule with its spin antiparallel to the FM catalysts. Based on the transition-state theory, we report that on LSMO, the hindrance resulting from the magnetic entropy for the initial reduction of O_2 by two antiparallel electrons to diamagnetic intermediates (such H_2O_2) is minimum. On the other hand, the additional reduction of H_2O_2 to H_2O, diamagnetic steps, prefers paramagnetic catalysts with higher magnetic entropy such as $La_{0.4}Sr_{0.6}MnO_3$ to avoid spin accumulation.

Introduction

Oxygen reduction reactions (ORR) allow the generation of electricity in fuel cells to emulate that of organic breathing, that is, O_2 is the acceptor of electrons as shown in Equations (2) and (3) below. However, the kinetics of ORR are not necessarily fast, and a very active cathode is needed to reach a practical usable level in a fuel cell.[1] Numerous studies evaluate manganite perovskites, at ambient temperature and in alkaline solutions, because of their typically excellent activity.[2] The main drive for the renaissance of alkaline cells is actually the use of abundant transition-metal oxides.[3] Work has been performed to understand the ORR mechanism and recognise structure–activity relationships.[4] However, these investigations do not consider the magnetic state of the most active materials, and the subsequent effect on the kinetics of electron-hopping events. The application of perovskite manganites in spin electronics[5,6] and magnetic refrigeration[7] indicates the influence of magnetic entropy in these materials. Of particular interest for the electrochemistry of the triplet state O_2 ($\downarrow O=O\downarrow$) molecule is the thermodynamics, namely the enthalpy and entropy, of the orbital superexchange interactions at the surface of the catalyst. For the complementary oxygen-evolution reaction (OER), we have reported, by first principles simulations, a correlation between delocalised spin passages and activity. However, the best catalysts for H_2O oxidation are in a paramagnetic (PM) phase at working conditions, with dynamical entropic fluctuations of the spin ordering.[8,9]

In addition to good charge conductivity, we propose that magnetic transport promotes the reduction of oriented $\downarrow O=O\downarrow$ molecules by two antiparallel electrons transferred from the catalysts. Nonetheless spin fluctuations are beneficial for the further reduction to H_2O in diamagnetic steps. Eventually, PM conductors such as $LaMnO_{3+\delta}$ or $La_{0.4}Sr_{0.6}MnO_3$, are the optimum catalysts for the complete ORR.[10–12] We formulate, with an adaptation of that transition state theory (TST), the influence of the magnetic entropy on the rate of the different reduction steps.[13]

Results and Discussion

The specific ORR activities for a range of perovskite manganites, relative to $LaMnO_3$ are shown in Table 1 as extracted from the literature. $La_{1-x}Sr_xMnO_3$ compositions with a half-metallic ground state (G.S.) have consistently been reported as oxides with a high intrinsic ORR activity.[11,12,14–16] Intermediate oxidation states must be carefully controlled for the stabilisation of the appropriate electronic–magnetic phase for good activity.[17,18] Ultimately, we find that only compositions with a ferromagnetic (FM) G.S. are excellent ORR catalysts. Nonetheless, experimentally, the composition with the highest intrinsic activity for the total or partial O_2 reduction is still uncertain.

[a] Dr. J. Gracia, Dr. R. Sharpe, Dr. Y. Jiao, Prof. J. W. (. Niemantsverdriet, Dr. T. Lim
SynCat@Beijing
Synfuels China Technology Co. Ltd.
Beijing, 101407 (P.R. China)
E-mail: jose.syngas@outlook.com

[b] J. Munarriz, Dr. V. Polo
Departamento de Química Física and
Instituto de Biocomputación y Física de Sistemas Complejos (BIFI)
Universidad de Zaragoza
Zaragoza (Spain)

[c] Prof. J. W. (. Niemantsverdriet
SynCat@Differ
Syngaschem BV
PO Box 6336, 5600 HH Eindhoven (The Netherlands)

Table 1. Summary of the magnetic properties of the most promising Mn-based oxides for ORR. Specific ORR activities reported at ≈0.8 V vs. reference hydrogen electrode relative to $LaMnO_3$. The appropriate references for conductivities and T_C are given in the text.

Material	Relative specific activity from Ref. [11,12,14]	[11,15,16]	[19]	[2]	Conductivity [S cm^{-1}]	T_C [K]	3d-e_g	ΔE_{FM-AFM} [meV f.u.$^{-1}$]
$LaMnO_{3+\delta}$				100.0[a]	10^{-2}–10^{-3}	200–260	0.70	62
$La_{0.4}Sr_{0.6}MnO_3$	1.5–1.8				4–5×10^2	250	0.4	0
$La_{0.67}Sr_{0.33}MnO_3$	2.1–2.2	1.15–1.25			10^3	370–380	0.67	167
$La_{0.70}Pb_{0.3}MnO_3$					2–3×10^2	361	0.70	163
$La_{0.8}Sr_{0.2}MnO_3$	0.9–1.0	1.2–1.3			10^0–10^1	300	0.80	91
$La_{0.5}Sr_{0.5}MnO_3$	1.1–1.2				10^0	270	0.50	25
$LaMn_{0.5}Ni_{0.5}O_3$				1.0[a]	10^{-5}–10^{-6}	275	1.00	13
$LaMnO_3$	1.0	1.0	1.0	1.0[a]	10^{-5}–10^{-6}	140	1.00	−10
$La_{0.6}Ca_{0.4}MnO_3$			0.7–0.8		10^0–10^1	270	0.60	60
$La_{0.5}Ca_{0.5}MnO_3$				25.4[a]	10^0–10^1	225	0.50	29
$La_{0.37}Ca_{0.63}MnO_3$			0.5–0.6		10^0–10^1	150	0.37	AFM

[a] Surface area was reported from particle size estimation by SEM.

Stoichiometric $LaMnO_3$ is moderately active for O_2 reduction,[20] despite its reduced bulk electrical conductivity (≈10^{-5}–10^{-6} S cm^{-1}). In Figure 1a, the density of states (DOS) shows that in its G.S. $LaMnO_3$ is an antiferromagnetic (AFM) A-type insulator with a band gap of ≈1.0 eV.[21] Electronic alterations in AFM $LaMnO_3$ are easily induced by stoichiometric changes because the FM phase is only slightly less stable (no more than 10 meV per formula unit, (f.u.). For instance, the DOS for $LaMnO_{3+\delta}$ in Figure 1b, for which we strictly use the $La_{11}Mn_{12}O_{36}$ stoichiometry ($Mn^{3.25+}$), indicates that the preferred orbital ordering creates a FM half-metal G.S.; the closest calculated AFM state is less stable by 62 meV f.u.$^{-1}$, see Table 1 ΔE_{FM-AFM}. The reported Curie temperature (T_C) for the $LaMnO_{3+\delta}$ family varies between 200 K and 260 K[22] and the electrical conductivity (at 300 K) of $LaMnO_{3+\delta}$ is approximately three orders of magnitude higher than that $LaMnO_3$, without the material showing pure metallic characteristics.[23] A $LaMnO_{3+\delta}$ composition has been previously reported as a superactive ORR catalyst, see Table 1. We think its relative activity might have been overestimated because of the non-comparable estimation of the surface area. However, despite this, we still believe that $LaMnO_{3+\delta}$ is a good ORR catalyst because it has the properties discussed above.[24]

For the alkaline-earth-doped $La_{1-x}A_xMnO_3$ oxides, the maximum conductivity at room temperature is obtained for compositions close to $x=0.33$.[25,26] $La_{0.67}Sr_{0.33}MnO_3$ (LSMO) is an excellent electronic conductor,[27] with a conductivity of about 10^2–10^3 S cm^{-1}. The catalytic activity of LSMO at least for the initial ↓O=O↓ reduction seems to be among the best.[2,14] LSMO has a half-metallic G.S. (see Figure 2a),[28–30] as does $La_{0.67}Ca_{0.33}MnO_3$ (LCMO, T_C≈260 K).[31,32] The energy difference with the closest AFM state is 167 meV f.u.$^{-1}$ for LSMO, the highest in our calculations, and the T_C is estimated to be between 370 and 380 K.[33] To the best of our knowledge, there are no studies that directly compare LCMO with LSMO for ORR. In any case, the phase diagram of $La_{1-x}Ca_xMnO_3$ at room temperature always indicates insulator phases in a spin-disordered paramagnetic (PM) state.[34]

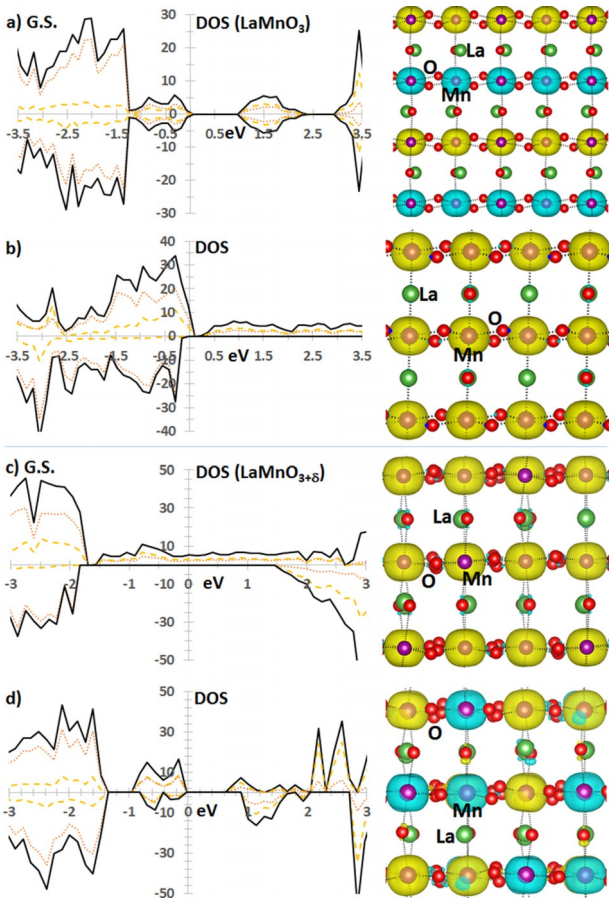

Figure 1. Right: spin density and left: Total DOS (solid lines), O DOS (dotted) and Mn DOS (dashed) for $LaMnO_3$, a) G.S. AFM type-A and b) FM; $La_{11}Mn_{12}O_{36}$, c) G.S. FM, and d) most stable AFM ordering.

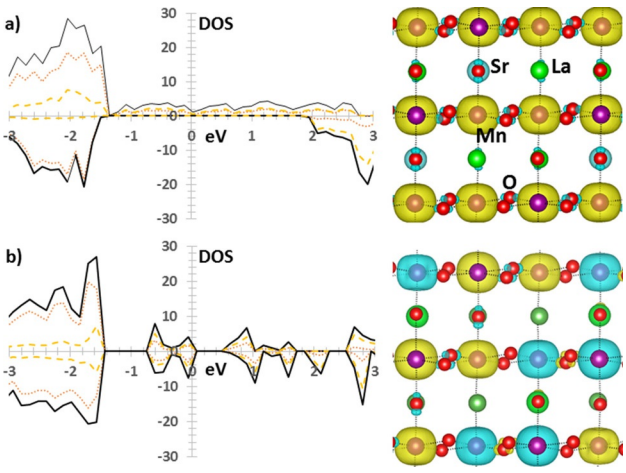

Figure 2. Right: spin density and left: total DOS (Solid), O DOS (Dotted), Mn DOS (Dashed) for $La_{0.67}Sr_{0.33}MnO_3$, a) FM G.S. and b) most stable AFM ordering.

LSMO has a T_C higher than room temperature, in correlation with superior charge mobility, which seems a key difference if compared to $LaMnO_{3+\delta}$ or LCMO. If we discuss in detail the orbital physics that define the electronic properties of LSMO,[35,36] we can actually understand and relate the magnetic transport in the bulk catalysts with O_2 reduction mechanisms beyond the superior charge conductivity. We hope for a better understanding of the nature of the Mn active sites, since the best conductors are not necessarily the most active materials in oxygen electrocatalysis.[20] The number of 3d electrons in the Mn–*O*–Mn framework establishes the strength and sign of exchange interactions that govern the magnetic and electronic properties of manganites.[37] For Mn cations the intra-atomic exchange stabilisation, $\Delta_{intra.ex}$, is superior to the octahedral-field splitting, $\Delta_{C.F.}$, of the 3d orbitals in the perovskite structure; consequently the Mn^{3+} d electrons are in the high-spin (HS) configuration $t_{2g}^3e_g^1$. The three t_{2g} orbitals overlap with the O $2p_\pi$ orbitals creating a π-bond, whilst the two e_g orbitals overlap with the O 2s, and O $2p_\sigma$ orbitals. The anti-bonding states of the σ-bond (e_g) are raised higher in energy than those of a π-bond (t_{2g}) because the σ overlapping is larger. In LSMO the AFM superexchange interactions in the t_{2g}–*O*–t_{2g} band compete with the e_g–*O*–e_g FM interactions. Since the strength of the exchange interactions depends on the overlapping and optimum filling of the orbitals, LSMO has the highest T_C. LCMO shares similar electronic properties with LSMO at low temperatures, and we do not distinguish many alterations but the FM state is relatively less stable, see Table 1, which in part explains the reduced T_C of LCMO. We obtain more tilted octahedra in LCMO; a deeper understanding of the spin–orbital–lattice couplings in this strongly correlated perovskite catalyst will be needed to determine whether or not fluctuations among the electron and lattice degrees of freedom affect the catalytic performance. Besides, the reported relative ORR activity of compositions such as $La_{0.5}Ca_{0.5}MnO_3$ (PM, $T_C = 225$ K) varies between studies from better than $LaMnO_3$,[2,10] to worse, see Table 1,[19] this may result from La_2O_3 segregation to the surface. The electronic properties of $La_{0.5}Ca_{0.5}MnO_3$ are close to $LaMnO_{3+\delta}$ and we do expect comparable activities. On the other hand, the electron transport of LSMO is different because, whilst the intra-atomic exchange interactions are still fixed by the magnetic moment of the localised t_{2g} orbitals, stronger extended superexchange FM interactions in the σ-band, with octahedra tilt angles closer to 180°, maintain the ferromagnetism and the coherent spin conductivity. In thermodynamic terms, below the T_C, a FM half metal has minimum magnetic entropy, or maximum spin ordering. In addition, on the surface of LSMO, the exchange interactions between the Mn e_g band and the half-occupied frontier π* orbitals of an adsorbed ↓O=O↓ molecule prefer an antiferromagnetic arrangement. As indicated in Figure 3, there is a 0.4 eV difference between O_2 adsorbed with spins parallel or antiparallel to the Mn spin centres. Such a preference suggests that electrons transferred from the oxide have the correct spin parity to easily reduce ↓O=O↓.

Initially, ORR always involves the transfer of an itinerant electron from the catalyst with its spin antiparallel to the initial

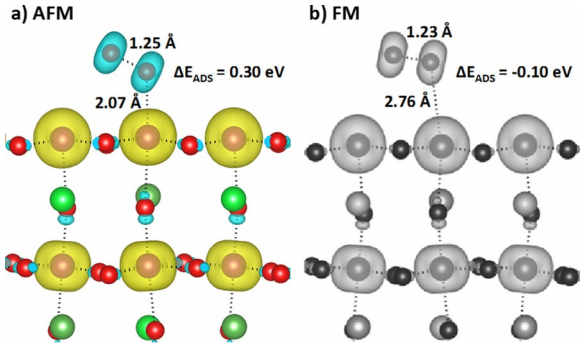

Figure 3. Spin density of an O_2 molecule adsorbed on the LSMO (0 0 1) surface a) AFM or b) FM oriented. The AFM configuration is preferred by 0.4 eV for a single adsorbed O_2 molecule.

triplet state of the ↓O=O↓ molecule to match the Pauli exclusion principle. In this situation of strong electronic coupling of the initial and final valence states, we use equation Equation (1), comparable to other approaches mainly developed by Gerischer,[38] or Marcus,[13,39,40] to evaluate the rate coefficient, $K(T)^-_{STST}$, of heterogeneous electron-transfer reactions. A new term $E^{SPIN}_{T.S.Band.Gap}$ is defined as the energy required to place an electron with the appropriate spin orientation in the conduction band of the catalyst able to form the transition state (T.S.). The relative kinetics of the charge transfer for different catalysts depends on several factors, but we particularly focus on the influence of the spin in the transition-state theory (STST) because it is not usually considered. Equation (1) also shows the entropic contribution (ΔS^{e-}_{STST}) to the Arrhenius equation.

$$K(T)^-_{STST} = k^-_{st} \cdot e^{\frac{\Delta S^{e-}_{STST}}{k_B}} \cdot e^{\frac{-Ea^-_{STST}}{k_B T}} \cdot e^{\frac{-E^{SPIN}_{T.S.Band.Gap}}{k_B T}} \quad (1)$$

For electrocatalytic reactions, the entropic contribution of the electronic partition functions from the reactants to the STST, $e^{\frac{\Delta S^{e-}_{STST}}{k_B}}$ as in usual transition state theory, is largely related to the free-energy change in the electronic states of the reactant–catalyst system. Knowing that the entropy per electron is given by $S^{e-} = k_B \ln g^{e-}$, where $g^{e-} = g^{e-spin} \cdot g^{e-C}$ is the total number of possible states for the transported electron, with g^{e-spin} and g^{e-C} being the spin and configuration degeneracies, respectively.[41] The transfer of spin entropy at the interphase between the 3d band and the ↓O=O↓ *p* shell is one of the factors that contribute to regulate $K(T)^-_{STST}$, and that specifically we want to address in relation to the magnetic state of the catalyst. Before the charge transfer, Figure 4 a and b, the electron is in the catalyst, and spin ordering immediately benefits the starting ↓O=O↓ reduction because of the ordered stable orbital e_g–π* overlapping. In LSMO, spin transport appears through steady FM exchange interactions; extended long-range magnetic interactions implies that $g^{e-spin}_{Reactants} = 1$.

In a two-electron pathway in basic solution, the O_2 reduction to the peroxide radical is optimised by the appropriate relative orientation of the spins, charge carriers and reactants on the surface, as Equations (2) and (3) show:

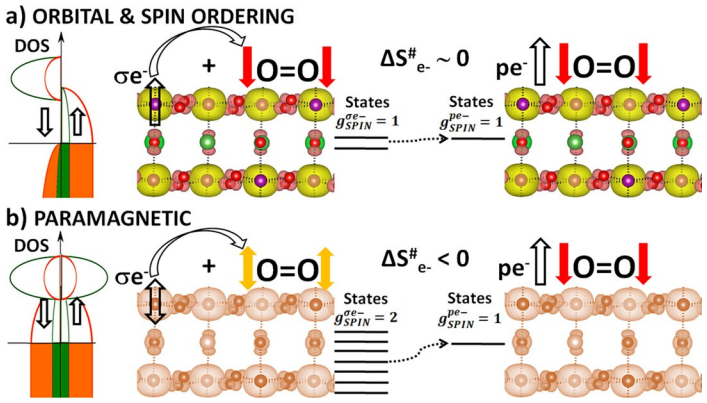

Figure 4. Schematic of the first electron-hopping step on the ORR. The difference between a) low- and b) high-spin entropy per electron in reaching the transition state/products is shown.

$$\downarrow O=O\downarrow \; + \; \uparrow e^- \; + \; H_2O \rightleftharpoons \downarrow O=O\uparrow\downarrow H \; + \; OH^- \qquad (2)$$

$$\downarrow O=O\uparrow\downarrow H + \; \uparrow e^- \; + \; H_2O \rightleftharpoons H\uparrow\downarrow O=O\uparrow\downarrow H \; + \; OH^- \qquad (3)$$

The entropic contribution to the reaction rate depends on the relative values of the partition functions of the reactants and the transition state.[42] ΔS^{e-}_{STST} is the entropy change of the adsorbed reactants if they are electronically excited to form the transition state (TS). If comparing between different ORR catalysts, the reaction pathways during the charge transfers will have largely the same entropy change owing to translational, rotational and vibrational partition functions. We can therefore look particularly at the change in the electron entropy for the electron hopping and at the magnetic contribution, ΔS^{e-spin}_{STST}. ΔS^{e-spin}_{STST} is estimated from the accessible spin states through the Boltzmann equation, $S^{e-spin} = k_B \ln g^{e-spin}$:

The exponential part of the spin prefactor, $\nu_{SPIN} = e^{\Delta S^{e-spin}_{STST}/k_B}$, based on Equation (4), simplifies to $\nu_{SPIN} = g^{e-spin}_{TS} / \left(g^{e-spin}_{Catalyst} \cdot g^{e-spin}_{Reactants} \right)$. The possible values of g^{e-spin}_{TS} are given by the spin degeneracy of the electron acceptor in the electrochemical reaction if we assume that there is no change in the spin-orbit configuration of the active centre during the spin transference. Below 370 K, the spin orientation in LSMO is fixed ($g^{e-spin}_{LSMO} = 1$), as is the orientation of the adsorbed molecules, $\downarrow O=O\downarrow$ $g^{e-spin}_{O_2^{LSMO}} = 1$ ($\Delta E_{ADS}/k_BT \gg 1$ see Figure 3), or HOO↓. This also gives g^{e-spin}_{TS} as 1, since adsorbed, oriented $\downarrow O=O\downarrow$ is the electron acceptor. On the other hand, for LCMO in the PM state, for the limit case $T \gg T_C$, we obtain a value of $g^{e-spin}_{TS} = 2 \cdot 4/3 \cdot 5 \approx 1/2$. Owing to the spin, the rate for the initial reduction of O_2 with LCMO is half the value of LSMO, as expected for the loss of the spin entropy of one electron, spin = 1/2,[43] transferred with spin fixed at the TS ready to proceed towards the products. Similarly, on a diamagnetic (DM) catalyst we should not expect any magnetic preference for the adsorption of triplet state O_2*, $g^{e-spin}_{O_2^{DM}} = 3$, or for reduced OOH*, $g^{e-spin}_{HO_2^{DM}} = 2$, and overall the spin degeneracies disfavour O_2 reduction by $g^{e-spin}_{HO_2^{DM}} / g^{e-spin}_{O_2^{DM}} = 2/3$. We expect the $g^{e-spin}_{Catalyst}$ for diamagnetic catalysts to typically be equal to 1, since the diamagnetism generally precludes any unpaired electrons.

The exchange interactions in the bulk and on the surface of a catalyst might fix the spin orientation of the charge carriers and of the triplet state oxygen molecule; a modest correlation that serves to derive a first specific principle but quite general to consider in ORR: The limited magnetic entropy of the itinerant electrons in the catalyst benefits the initial $\downarrow O=O\downarrow$ reduction to diamagnetic intermediates. Our approximation to ΔS^{e-}_{STST} is partial, but points out at effects due to extended orbital ordering on the overall current possible in the electrocatalytic circuit. Naturally, optimum activation barriers are still needed during electrocatalysis[44] as the enthalpy component exponentially affects the rate of the single events, but for those compositions at the top activity of the volcano plots, the entropy contributes to be a discretising factor.

Another influence of the magnetic state of the catalyst is in the exponential factor: $e^{\frac{-E^{SPIN}_{T.S.Band.Gap}}{k_B T}}$. In addition to initial steps that do not conserve the angular momentum, the complete ORR down to H_2O requires the further reduction of diamagnetic intermediates. As these steps overall conserve the spin, the reduced magnetic entropy in half metals means the electrochemical reaction will be limited by the transference of the electrons with the minority spin (DOWN) if $E^{DOWN}_{Band.Gap} \gg k_BT$. As verified, LSMO ($T_C > 300$ K) will suffer this particular limitation;[12] this constitutes the second general design principle related with the magnetic state of the catalyst as conclusion of this work: If H_2O is the final desired product, essentially PM good conductors such as $La_{0.4}Sr_{0.6}MnO_3$ seem optimum for complete ORR.[11]

Other related charge conductors with FM G.S., such as the $La_{1-x}Ag_xMnO_3$ family, appear to be of interest for O_2 reduction.[45] The A-site substitution by Ag gives rise to various competitions between structural, magnetic and electronic phases, leading to interesting transport properties.[45,46] The charge-carrier density rises with increasing Ag dopant concentration, confirmed by the increased conductivity of about 10^0 S cm^{-1} for $La_{0.85}Ag_{0.15}MnO_3$ (LAMO);[46–48] LAMO exhibits half-metallic ferromagnetism at T_C close to room temperature.[46,49,50] To the best of our knowledge, no literature study has compared the ORR activity of LAMO with LSMO, nor with any of the several FM manganese conductors with perovskite structure with high T_C reported by Jonker and van Santen.[51] However, $La_{0.7}Pb_{0.3}MnO_3$ ($T_C = 361$ K) is ORR active.[52]

The most important Mn-based perovskites discussed in this paper are ordered in Table 1 by their reported activity, T_C, and the computed relative stability of the FM state versus the competing AFM phases. For all the catalysts with a FM half-metal G.S. at comparable experimental conditions, we think that a high T_C correlates with superior initial O_2 reduction.[2] The relative stability of the FM half-metal phase as an ORR descriptor presents a phenomenological understanding, and also shares the predictive advantages of the design principles based on

bulk properties. Cobalt-based catalysts are not broadly considered as highly active for O_2 reduction; however, PM $La_{0.5}Sr_{0.5}CoO_{2.91}$ perovskite is a high-performance catalyst for ORR,[53] and actually shares many of the orbital physics of $La_{0.4}Sr_{0.6}MnO_3$ or $LaMnO_{3+\delta}$. We consider based on our analysis that the oxygen-deficient $Sr_2CoMoO_{6-\delta}$ (SCMO) composition is an entropically capable catalyst.[54,55] SCMO has FM domains characterised by a T_C up to 370 K, and we believe the comparison between LSMO and SCMO is pertinent. Other than perovskites, α-MnO_2 structures show similar magnetic properties to $LaMnO_{3+\delta}$ in alkaline media,[56] and we consider that the preferential FM interactions in the catalyst correlate with its high ORR activity.[57]

Conclusions

Although spin separation in certain conducting oxides is well known,[58] it is still a challenge to prove the effect of magnetism in oxygen electrocatalysis. We have shown that the possibility of a ferromagnetic background can be commonly related with an improvement in the charge conductivity, and then electrocatalytic activity. In addition, minimum spin entropy in the catalysts optimises the kinetics of charge transfer by reducing the entropy losses during the O_2 reduction by just two electrons. Such spin-entropy gains are maximised for a material below its Curie temperature T_C, if the exchange interactions that determine the orbital overlapping between species are well-structured. We have illustrated these principles using the $La_{0.67}Sr_{0.33}MnO_3$ (LSMO) perovskite system, a half metal below its T_C of 370 K, at which spin transport provides for more effective $\uparrow e^- + \downarrow O = O \downarrow$ collisions. These considerations, in combination with our recent work,[8,9] link two new principles towards the prediction and comparison of the best oxygen catalysts: magnetic state and spin transport. In addition to conductivity and activation barriers, probably optimum for noble metals, we believe the consideration of magnetic entropy in oxygen chemistry will open the way to a more complete understanding of the thermodynamic basis of the most active catalysts in this field, as well as other related electrochemically driven reactions.

Experimental Section

All calculations were performed by using periodic density functional theory (DFT) as implemented in the Vienna ab initio simulations package (VASP).[59–61] A plane-wave basis set was used to represent the wave functions. The projected augmented wave (PAW) method developed by Bloch was used to represent the interactions between the core electrons and valence electrons.[62,63] The number of valence electrons are 12, 14, 6, 9 and 12 for La, Ca, Sr, Mn and O atoms, respectively. The exchange–correlation energy was calculated within the generalised gradient approximation using the Perde–Burke–Ernzerhof functional revised for solids.[64] A Monkhorst Pack k-point grid and a plane-wave cut-off of 400 eV was used for all systems. The DFT+U approach was used to account for on-site Coulomb interactions of localised d electrons.[65] All drawings are produced with VESTA.[66]

$LaMnO_3$ and $CaMnO_3$ presented the same *Pnma* orthorhombic crystallographic cell symmetry.[32] In both cases, a KPOINTS grid of (7×7×5) was employed in the calculations. A value of $U=5.5$ reproduced the experimental features of the Mn^{3+} octahedrons for $LaMnO_3$. The calculated lattice parameters in Å for $LaMnO_3$ were $a=5.479$ (5.536), $b=5.649$ (5.730) and $c=7.638$ (7.672), experimental values in parenthesis. The low-temperature phase had an AFM spin ordering A-type; the Mn–O bonds in Å were unequal because of the Jahn–Teller distortion, Mn–O 1.92 (1.91), 1.96 (1.96) and 2.12 (2.18), experimental values in parenthesis.

A value of $U=3.0$ reproduced the experimental features of the Mn^{4+} octahedrons. The calculated lattice parameters in Å for $CaMnO_3$ were $a=5.231$ (5.302), $b=7.359$ (7.505) and $c=5.185$ (5.330), experimental values in parenthesis. The low temperature phase had an AFM spin ordering G-type; the Mn–O bonds were equal, Mn–O 1.88 (1.90), 1.89 (1.90) and 1.89 (1.90), experimental values in parenthesis.

For the rest of the compositions we used an in-between value of $U=4.0$. This better described intermediate $Mn^{(3+x)+}$ states,[67] and allowed us to compare systems. In any case, we checked that the calculations had no spurious results.

The $LaMnO_{3+\delta}$ family was modelled from two compositions, $La_{11}Mn_{12}O_{36}$ and $La_{11}Mn_{11}O_{36}$. Vacancies on A sites or A and B both resulted in the stabilisation of the ferromagnetic phase. We analysed in detail the $La_{11}Mn_{12}O_{36}$ calculations because we thought that $La_{1-\Delta}MnO_{3+\delta}$ will be the most relevant system.[22] We constructed a supercell with lattice parameters in Å: $a=10.8$, $b=10.8$ and $c=6.6$; and a 4×4×6 KPOINTS grid.

Acknowledgements

The authors acknowledge financial support from Synfuels China Technology Co. Ltd. V. P. and J. M. express their appreciation to the financial support of MINECO/FEDER project CTQ2015-67366-P and from the MECD (FPU14/06003), respectively. Also, the resources from the supercomputer "memento", technical expertise and assistance provided by BIFI-ZCAM (Universidad de Zaragoza) are acknowledged.

Conflict of interest

The authors declare no conflict of interest.

Keywords: density functional calculations · magnetism · oxygen · perovskite phases · thermodynamics

[1] S. Guo, S. Zhang, S. Sun, *Angew. Chem. Int. Ed.* **2013**, *52*, 8526–8544; *Angew. Chem.* **2013**, *125*, 8686–8705.
[2] K. A. Stoerzinger, M. Risch, B. Han, Y. Shao-Horn, *ACS Catal.* **2015**, *5*, 6021–6031.
[3] F. Cheng, J. Chen, *Chem. Soc. Rev.* **2012**, *41*, 2172–2192.
[4] A. S. Ryabova, F. S. Napolskiy, T. Poux, S. Y. Istomin, A. Bonnefont, D. M. Antipin, A. Y. Baranchikov, E. E. Levin, A. M. Abakumov, G. Kéranguéven, et al., *Electrochim. Acta* **2016**, *187*, 161–172.
[5] L. Poggini, S. Ninova, P. Graziosi, M. Mannini, V. Lanzilotto, B. Cortigiani, L. Malavolti, F. Borgatti, U. Bardi, F. Totti, et al., *J. Phys. Chem. C* **2014**, *118*, 13631–13637.
[6] C. Felser, G. H. Fecher, B. Balke, *Angew. Chem. Int. Ed.* **2007**, *46*, 668–699; *Angew. Chem.* **2007**, *119*, 680–713.
[7] S. Das, T. K. Dey, *J. Alloys Compd.* **2007**, *440*, 30–35.

[8] T. Lim, J. W. Niemantsverdriet, J. Gracia, *ChemCatChem* **2016**, *8*, 2968 – 2974.
[9] R. Sharpe, T. Lim, Y. Jiao, H. Niemantsverdriet, J. Gracia, *ChemCatChem* **2016**, *8*, 3762 – 3768.
[10] J. Suntivich, H. A. Gasteiger, N. Yabuuchi, H. Nakanishi, J. B. Goodenough, Y. Shao-Horn, *Nature Chem.* **2011**, *3*, 546 – 550.
[11] J. Tulloch, S. W. Donne, *J. Power Sources* **2009**, *188*, 359 – 366.
[12] C. Yunphuttha, S. Porntheeraphat, A. Wongchaisuwat, S. Tangbunsuk, D. W. M. Marr, P. Viravathana, *Phys. Chem. Chem. Phys.* **2016**, *18*, 16786 – 16793.
[13] D. G. Truhlar, B. C. Garrett, S. J. Klippenstein, *J. Phys. Chem.* **1996**, *100*, 12771 – 12800.
[14] K. A. Stoerzinger, W. Lü, C. Li, Ariando, T. Venkatesan, Y. Shao-Horn, *J. Phys. Chem. Lett.* **2015**, *6*, 1435 – 1440.
[15] W. T. Hong, M. Risch, K. A. Stoerzinger, A. Grimaud, J. Suntivich, Y. Shao-Horn, *Energy Environ. Sci.* **2015**, *8*, 1404 – 1427.
[16] K. A. Stoerzinger, M. Risch, J. Suntivich, W. M. Lü, J. Zhou, M. D. Biegalski, H. M. Christen, Ariando, T. Venkatesan, Y. Shao-Horn, *Energy Environ. Sci.* **2013**, *6*, 1582.
[17] Y. Zhu, W. Zhou, Y. Chen, J. Yu, X. Xu, C. Su, M. O. Tadé, Z. Shao, *Chem. Mater.* **2015**, *27*, 3048 – 3054.
[18] Y. Zhu, W. Zhou, J. Yu, Y. Chen, M. Liu, Z. Shao, *Chem. Mater.* **2016**, *28*, 1691 – 1697.
[19] V. Celorrio, L. Calvillo, E. Dann, G. Granozzi, A. Aguadero, D. Kramer, A. E. Russell, D. J. Fermín, *Catal. Sci. Technol.* **2016**, *6*, 7231 – 7238.
[20] D. Chen, C. Chen, Z. M. Baiyee, Z. Shao, F. Ciucci, *Chem. Rev.* **2015**, *115*, 9869 – 9921.
[21] M. Baldini, V. V. Struzhkin, A. F. Goncharov, P. Postorino, W. L. Mao, *Phys. Rev. Lett.* **2011**, *106*, 066402.
[22] A. Maignan, C. Michel, M. Hervieu, B. Raveau, *Solid State Commun.* **1997**, *101*, 277 – 281.
[23] V. S. Zakhvalinskiĭ, R. Laiho, K. G. Lisunov, E. Lähderanta, P. A. Petrenko, Y. P. Stepanov, J. Salminen, V. N. Stamov, *Phys. Solid State* **2006**, *48*, 2300 – 2309.
[24] J. Suntivich, E. E. Perry, H. A. Gasteiger, Y. Shao-Horn, *Electrocatalysis* **2013**, *4*, 49 – 55.
[25] H. Kozuka, K. Ohbayashi, K. Koumoto, *Sci. Technol. Adv. Mater.* **2015**, *16*, 026001.
[26] L. Malavasi, M. Cristina, C. B. Azzoni, G. Chiodelli, G. Flor, I. Unita, C. Fisica, *Solid State Commun.* **2002**, *123*, 321 – 326.
[27] J. H. Van Santen, G. H. Jonker, *Physica* **1950**, *16*, 599 – 600.
[28] T. Ohtani, K. Kuroda, K. Matsugami, D. Katoh, *J. Eur. Ceram. Soc.* **2000**, *20*, 2721 – 2726.
[29] N. Furukawa, *J. Phys. Soc. Jpn.* **2000**, *69*, 1954 – 1957.
[30] T. Geng, N. Zhang, *Phys. Lett. A* **2006**, *351*, 314 – 318.
[31] H. Deng, C. P. Yang, Z. H. Zhou, H. Wang, K. Baerner, I. V. Medvedeva, *J. Phys. Chem. Solids* **2010**, *71*, 1660 – 1663.
[32] R. Korotana, G. Mallia, Z. Gercsi, L. Liborio, N. M. Harrison, *Phys. Rev. B* **2014**, *89*, 205110.
[33] A. Mellergård, R. L. McGreevy, S. G. Eriksson, *J. Phys. Condens. Matter* **2000**, *12*, 4975 – 4991.
[34] P. Schiffer, A. P. Ramirez, W. Bao, S.-W. Cheong, *Phys. Rev. Lett.* **1995**, *75*, 3336 – 3339.
[35] Y. Tokura, *Science* **2000**, *288*, 462 – 468.
[36] J. B. Goodenough, *Phys. Rev.* **1955**, *100*, 564 – 573.
[37] J. B. Goodenough, *Rep. Prog. Phys.* **2004**, *67*, 1915 – 1993.
[38] H. Gerischer, *Electrochim. Acta* **1990**, *35*, 1677 – 1699.
[39] R. A. Marcus, *J. Chem. Phys.* **1965**, *43*, 679.
[40] S. Fletcher, N. J. Van Dijk, *J. Phys. Chem. C* **2016**, *120*, 26225 – 26234.
[41] W. Koshibae, S. Maekawa, *J. Magn. Magn. Mater.* **2003**, *258-259*, 216 – 218.
[42] R. Hoffmann, *Angew. Chem. Int. Ed.* **2004**, *43*, 6586 – 6590; *Angew. Chem.* **2004**, *116*, 6748 – 6752.
[43] Y. Wang, N. S. Rogado, R. J. Cava, N. P. Ong, *Nature* **2003**, *423*, 425 – 428.
[44] I. C. Man, H.-Y. Su, F. Calle-Vallejo, H. A. Hansen, J. I. Martínez, N. G. Inoglu, J. Kitchin, T. F. Jaramillo, J. K. Nørskov, J. Rossmeisl, *ChemCatChem* **2011**, *3*, 1159 – 1165.
[45] Q. Y. Xu, R. P. Wang, Z. Zhang, *Phys. Rev. B* **2005**, *71*, 092401.
[46] O. Y. Gorbenko, O. V. Melnikov, A. R. Kaul, L. I. Koroleva, N. A. Babushkina, A. N. Taldenkov, A. V. Inyushkin, A. Barranco, R. Szymczak, *Thin Solid Films* **2008**, *516*, 3783 – 3790.
[47] Y. M. Baikov, E. I. Nikulin, Y. P. Stepanov, *Phys. Solid State* **2012**, *54*, 140 – 142.
[48] M. W. Shaikh, I. Mansuri, M. A. Dar, D. Varshney, *Mater. Sci. Semicond. Process.* **2015**, *35*, 10 – 21.
[49] M. Kar, S. Ravi, *Mod. Phys. Lett. B* **2004**, *18*, 221 – 231.
[50] T. Tang, Q. Q. Cao, K. M. Gu, H. Y. Xu, S. Y. Zhang, Y. W. Du, *Appl. Phys. Lett.* **2000**, *77*, 723.
[51] G. H. Jonker, J. H. Van Santen, *Physica* **1950**, *16*, 337 – 349.
[52] Y. Matsumoto, E. Sato, *Electrochim. Acta* **1980**, *25*, 585 – 589.
[53] Y. Zhao, L. Xu, L. Mai, C. Han, Q. An, X. Xu, X. Liu, Q. Zhang, *Proc. Natl. Acad. Sci. USA* **2012**, *109*, 19569 – 19574.
[54] M. Cheriti, A. Kahoul, *Mater. Res. Bull.* **2012**, *47*, 135 – 141.
[55] M. C. Viola, M. J. Martínez-Lope, J. A. Alonso, P. Velasco, J. L. Martínez, J. C. Pedregosa, R. E. Carbonio, M. T. Fernández-Díaz, *Chem. Mater.* **2002**, *14*, 812 – 818.
[56] L.-T. Tseng, Y. Lu, H. M. Fan, Y. Wang, X. Luo, T. Liu, P. Munroe, S. Li, J. Yi, *Sci. Rep.* **2015**, *5*, 9094.
[57] G. Chen, J. Sunarso, Y. Zhu, J. Yu, Y. Zhong, W. Zhou, Z. Shao, *ChemElectroChem* **2016**, *3*, 1760 – 1767.
[58] C. Autret, C. Martin, M. Hervieu, A. Maignan, B. Raveau, G. André, F. Bourée, Z. Jirak, *J. Magn. Magn. Mater.* **2004**, *270*, 194 – 202.
[59] G. Kresse, J. Hafner, *Phys. Rev. B* **1994**, *49*, 14251 – 14269.
[60] G. Kresse, J. Hafner, *Phys. Rev. B* **1993**, *47*, 558 – 561.
[61] G. Kresse, *Phys. Rev. B* **1996**, *54*, 11169 – 11186.
[62] P. E. Blöchl, *Phys. Rev. B* **1994**, *50*, 17953 – 17979.
[63] G. Kresse, D. Joubert, *Phys. Rev. B* **1999**, *59*, 1758 – 1775.
[64] J. P. Perdew, A. Ruzsinszky, G. I. Csonka, O. A. Vydrov, G. E. Scuseria, L. A. Constantin, X. Zhou, K. Burke, *Phys. Rev. Lett.* **2008**, *100*, 136406.
[65] S. L. Dudarev, G. A. Botton, S. Y. Savrasov, C. J. Humphreys, A. P. Sutton, *Phys. Rev. B* **1998**, *57*, 1505 – 1509.
[66] K. Momma, F. Izumi, *J. Appl. Crystallogr.* **2011**, *44*, 1272 – 1276.
[67] D. Mierwaldt, S. Mildner, R. Arrigo, A. Knop-Gericke, E. Franke, A. Blumenstein, J. Hoffmann, C. Jooss, *Catalysts* **2014**, *4*, 129 – 145.

Manuscript received: February 15, 2017
Revised manuscript received: April 21, 2017
Accepted manuscript online: April 25, 2017
Version of record online: July 24, 2017

Journal of Catalysis 361 (2018) 331–338

Contents lists available at ScienceDirect

Journal of Catalysis

journal homepage: www.elsevier.com/locate/jcat

Principles determining the activity of magnetic oxides for electron transfer reactions

Jose Gracia [a,b,c,*], Ryan Sharpe [c], Julen Munarriz [d]

[a] Magnetocat S.L., Alicante, Spain
[b] SynCat@Differ, Syngaschem BV, Eindhoven, The Netherlands
[c] SynCat@Beijing, Synfuels China Technology Co., Beijing, China
[d] Departamento de Química Física and Instituto de Biocomputación y Física de Sistemas Complejos (BIFI), Universidad de Zaragoza, Zaragoza, Spain

ARTICLE INFO

Article history:
Received 18 January 2018
Revised 9 March 2018
Accepted 10 March 2018

Keywords:
Electrocatalysis
Electron transfer theory
Spin potentials
Exchange interactions
Ferromagnetism

ABSTRACT

Electrons in covalent oxides are fermions interacting through overlapping atomic orbitals, and quantum exchange interactions incorporate influential spin-dependent potentials in their electrocatalytic properties. The Goodenough-Kanamori rules explain the magnetic coupling between metals connected via ligands, known as super- (or double-) exchange interactions, which regulate their charge transport properties. To describe the electrocatalytic activity of magnetic metal oxides, we must extend their spin-dependent mechanisms of electron tunnelling to catalytic interfaces, because the exchange coupling between orbitals, in the catalysts and with the chemisorbed reactants, influences the kinetics of electron transfer reactions. The principles for developing magnetic coupling rules in electrocatalysis must guarantee spin passages, which are optimum for intrinsically degenerate configurations of the frontier orbitals oriented in the direction of the bonds at both sides of the Fermi level. A continuous energy landscape between the reactants and the catalyst minimizes the overpotentials during coherent redox electron tunnelling. Consequently, in this paper we derive the guidelines of the ferromagnetic (FM) exchange interactions, an extension of the Goodenough-Kanamori rules, to electrocatalytic interfaces, which anticipates minimum Gibbs energy of activation. We focus on the electronic coordinates, targeting reaction conditions where the electrons are the main energy carriers to trigger the steps; nonetheless they are interrelated with the atomic movements. We will use the oxygen evolution and reduction reactions as examples where quantum exchange interactions, a landmark of solid-state magnetism, and the chemistry of the triplet state O_2 molecule, are crucial for optimum kinetics.

One sentence summary: Delocalizing spin potentials facilitate the coherent propagation of electrons at covalent magnetic interfaces; this is a physical principle that links ferromagnetic exchange interactions, antibonding orbitals and optimum viable electrocatalysis: *spintro-catalysis*.

1. Introduction

Some of the most important catalytic reactions for civilisation centre around steps that involve the triplet state O_2 molecule. The best catalysts for the oxygen evolution and oxygen reduction reactions (OER and ORR, respectively), essential for energy technologies, are magnetic mixed oxides (MMOs), the properties of which can only be understood with the consideration of internuclear spin dependent interactions related with electronic mobility [1–5]. Similarly, mixed-valence magnetic complexes are commonly found catalysts in nature for optimum electron-transfer steps; for instance, the oxygen evolution complex during photosynthesis [6], and biological N_2 fixation via molybdenum-iron complexes in proteins, are associated with spin-coupled metals [7–9].

When two antiparallel electrons pile up into the energy levels of Pauli metals, like $LaNiO_3$ or RuO_2, the wavefunction is symmetric in space $\left(\psi^{sym.space}_{Fermi.level}\right)$ and optimizes the classical Coulomb potentials. On the other hand, in MMOs, exchange interactions and strong spin-orbit (s.-o.) coupling for the heavier transition-metals determine the state of the valence and conduction bands [10,11]. Non-magnetic metals maximise the electronic density in between nuclei, charge mobility being due to the overlap of unfilled neighbouring orbitals. $LaNiO_3$ and RuO_2 are excellent charge conductors and good oxygen electro-catalysts [12–16] while ultimately spin-polarized FM oxides without a band gap and with abundant holes

* Corresponding author at: Magnetocat S.L., Alicante, Spain.
E-mail address: magnetocat@outlook.com (J. Gracia).

https://doi.org/10.1016/j.jcat.2018.03.012
0021-9517/

($h^+_\downarrow$) at the Fermi level, like the extensive $A_{1-X}A'_XCo_{1-Y}Fe_YO_{3-\delta}$ perovskite families [17–19] and $Ni_WCo_XFe_YO(OH)_Z$ oxyhydroxides [20], are more active for OER. Equally, FM-metals with conduction bands richer in electrons ($e^-_\uparrow$) than $h^+_\downarrow$ give better rates for ORR [2,21–24]; or even high current efficiency for N_2 reduction, like $Sm_{1-X}A'_XFe_{1-Y}B'_YO_{3-\delta}$ oxides [25,26].

The Pauli exclusion principle leads to an effective coupling between the intrinsic angular momentum of the electrons and the orbital ordering in MMOs, known as quantum exchange energy. The coherent relocation of a fermion from one orbital to the neighbour is only possible if there is not already an electron of the same spin occupying that orbital. Fast ballistic wave-like propagation occurs in a coherent process, referred to as tunnelling, where electrons move from one site to another maintaining a definite phase relationship [27]. On the contrary, hopping is incoherent, a thermally activated process in which an electron moves from one site to another but loses information about its phase. In MMOs, the spin-correlation, exchange or spin-orbit interactions, created on an atom to its neighbours serves to mediate the charge transfer, revealing a more conductive behaviour for dominant FM orderings; whereas materials with intra-plane and inter-plane antiferromagnetic (AFM) coupling require higher thermal activation [28]. Stable AFM insulators, at working conditions, are poor oxygen electrocatalysts; however, activity increases above conventional metallic oxides with increasing FM conductivity [5]. The Goodenough-Kanamori rules explain the dominant magnetic ordering observed in MMOs, see Fig. 1, based on the orbital physics applied to electron transfer between metal atoms carrying a net spin and mediated by shared ions [29–31]. Because $e^-_\uparrow$ transfer in MMOs occurs through a magnetic junction, a review and extension of the FM spin exchange rules in catalysis is pertinent.

In spin-polarized metals with preferential FM interactions, the orbitals of the valence electrons at the active sites are antisymmetric in space $\left(\psi^{anti.space}_{Fermi.level}\right)$, while the spin function is symmetric. As Fig. 1 shows, the spin density of the ferrimagnetic $CaCu_3Fe_4O_{12-\delta}$ (Fe $\boldsymbol{3d\text{-}e_g^{1.25}}$) ground state (G.S) occupies more of the interstitial spaces in between bonds than the AFM type-G $LaCu_3Fe_4O_{12}$ G.S. (Fe $\boldsymbol{3d\text{-}e_g^2}$). The delocalized π-character via orthogonal orbitals at the oxygen atoms in FM orderings contrasts with the localized σ-character of AFM bonds. In this example, archetypal of excellent OER activity but bad for ORR [32], between half-filled $\boldsymbol{3d\text{-}t_{2g}^3e_g^2}$ and hole-rich $\boldsymbol{3d\text{-}t_{2g}^3e_g^{1.25}}$ bands, the sign of the exchange potentials and the free energy of the charge carriers ($e^-_\uparrow$ & $h^+_\downarrow$) fully determines their catalytic differences: no spin-gap n-type excellent OER catalyst versus an insulator with poor activity at ambient conditions [5]. $La_{1-X}Sr_XMnO_{3\pm\delta}$ p-type conductors, associated with FM $e^-_\uparrow$-rich $\boldsymbol{3d\text{-}t_{2g}^3e_g^{0.75}}$ bands, serve as the inverse examples with good ORR activity but poor performance for OER [14]. An overall positive value of the exchange energy between the electrons in the valence and conduction band, in the Heisenberg model $\Delta^{\Psi^\pm_{T.S.}}_{magnetic} = J_{exc.}\cdot(\widehat{s_{Cat.}}\cdot\widehat{s_{e^-}}) > 0$, indicates that FM interactions reduce the classical electronic repulsions ($C_{e^--e^-}$) at the expense of the Coulomb attractions ($C_{n^+-e^-}$) [2]. The less influential the localizing Coulomb interactions are, the more facile the tunnelling of the electrons is.

Founded on previous principles, we extend the rules of quantum FM exchange interactions to catalytic interfaces, where they will serve as guidelines to realise the best compositions for spin-dependent electron transfer reactions. The term "*spin*-electronics" refers to the study of the role played by the spin of the electrons in solid state physics, which specifically exploit spin properties instead of or in addition to charge degrees of freedom. Then, in an analogous terminology, we differentiate with the term "*spintro*-catalysis", where mainly FM exchange interactions, in $\psi^{anti.space}_{Fermi.level}$, set the optimum thermodynamic conditions for spin-assisted electron transfer.

Double-exchange guidelines in *spintro*-catalysis, see Fig. 2[1]:

Rule 1) The spin angular momentum is conserved during an electron transfer in the catalyst and with the reactants.

Description. Overall the electronic transport at a catalytic interface depends on the transition probability, $k^\pm_{ST}\cdot e^{\Delta S^{e^-/h^+}_{T.S.}/k_B}$, associated to the wavefunctions between the reactants and the active sites in the conduction band of the catalyst, Eq. (1), and between atoms in the conduction and valence band, Eq. (2):

$$k^\pm_{ST.reac.\to cond.}\cdot e^{\Delta S^{e^-/h^+}_{T.S.read.\to cond.}/k_B} \propto \left|\left\langle\Phi^{space}_{cat.cond.}|\Phi^{space}_{reac.}\right\rangle\cdot\left\langle\chi^{spin}_{cat.cond.}|\chi^{spin}_{reac.}\right\rangle\right|^2, \quad (1)$$

$$k^\pm_{ST.val.\to cond.}\cdot e^{\Delta S^{e^-/h^+}_{val.\to cond.}/k_B} \propto \left|\left\langle\Phi^{space}_{cat.cond.}|\Phi^{space}_{cat.val.}\right\rangle\cdot\left\langle\chi^{spin}_{cat.cond.}|\chi^{spin}_{cat.val.}\right\rangle\right|^2. \quad (2)$$

Within these equations, Φand χrepresents the spatial and spin parts of the wavefunction, respectively. Subindices *reac.*, *cat.cond.* and *cat.val* refer to the reactants and the catalyst conduction and valence bands, respectively. The spin integrals are zero when there is a change in the angular momentum of electrons, that is, $\left\langle\chi^{spin}_{cat.cond.}|\chi^{spin}_{reac.}\right\rangle$ and $\left\langle\chi^{spin}_{cat.cond.}|\chi^{spin}_{cat.val.}\right\rangle = 0$. Spin tunnelling decays exponentially with potential barriers [33], and via statistical mechanics we can express the oxidation rate ($e^-_\uparrow$ from the reactants) or reduction step ($h^+_\downarrow$ from the reactants) as $K(T)^\pm_{STST} = k^\pm_{ST}\cdot e^{\Delta S^{e^-/h^+}_{T.S.}/k_B}\cdot e^{-\Delta H^{e^-/h^+}_{T.S.}/k_BT}$. The total electronic energy of activation for half-reaction is $\Delta H^{e^-/h^+}_{T.S.} = \Delta H^{e^-/h^+}_{T.S.reac.\to cond.} + \Delta H^{e^-/h^+}_{val.\to cond.}$. In this analysis we are responding from theoretical and physical meaningful principles to the dependence of electrocatalysis on the conductivity [34]; the band gap, $\Delta H^{e^-/h^+}_{val.\to cond.} \geq 0$was similarly included in the outstanding work of Gerischer [35]. Electrocatalysis is still catalysis and the factor $\Delta H^{e^-/h^+}_{T.S.reac.\to cond.}$ represents the activation energies on the catalysts, initiated via the charge transfer.

Accompanying rule 1, the Pauli exclusion principle restricts the transfer of an electron from one orbital to its neighbour if there is already an electron of the same spin occupying that orbital. For instance, during the reduction or evolution of the triplet state oxygen molecule in FM manganites, the tunnelling electrons are antiparallel to the half-filled O_2 π^* orbitals [3,36], see Fig. 3. With this approach we demonstrate the need for consideration of reaction mechanisms including the adsorption of triplet state O_2 on to the active metals .

Rule 2) The ***intra*-**atomic and the ***inter*-**atomic exchange interaction in the covalent ***-B-O-B-O-*** framework are ferromagnetic in oxides with minimum $\Delta G^{e^-/h^+}_{T.S.}$.

Description. The orbitals of FM conductors create an intrinsically degenerate spin-polarized metallic state that optimizes the wavefunction based on the reduction of the electron-electron repulsions, $\psi^{anti.space}_{Fermi.level}$. Magnetic oxides with intermediate valence states can have resonating orbital configurations and $\Delta H^{e^-/h^+}_{val.\to cond.} = 0$, as in conventional metals. This guarantees that the transfer rate of spin-oriented electrons between the conduction band in the bulk and the surface states is fast, represented on the right side of Fig. 2, and the charge transport between the

[1] We use a general nomenclature, like ABO_3 perovskite or $A_2B_2O_7$ pyrochlore oxides, where A refers to the interstitial metals, B to the transition metals at octahedral sites and O to the ligands.

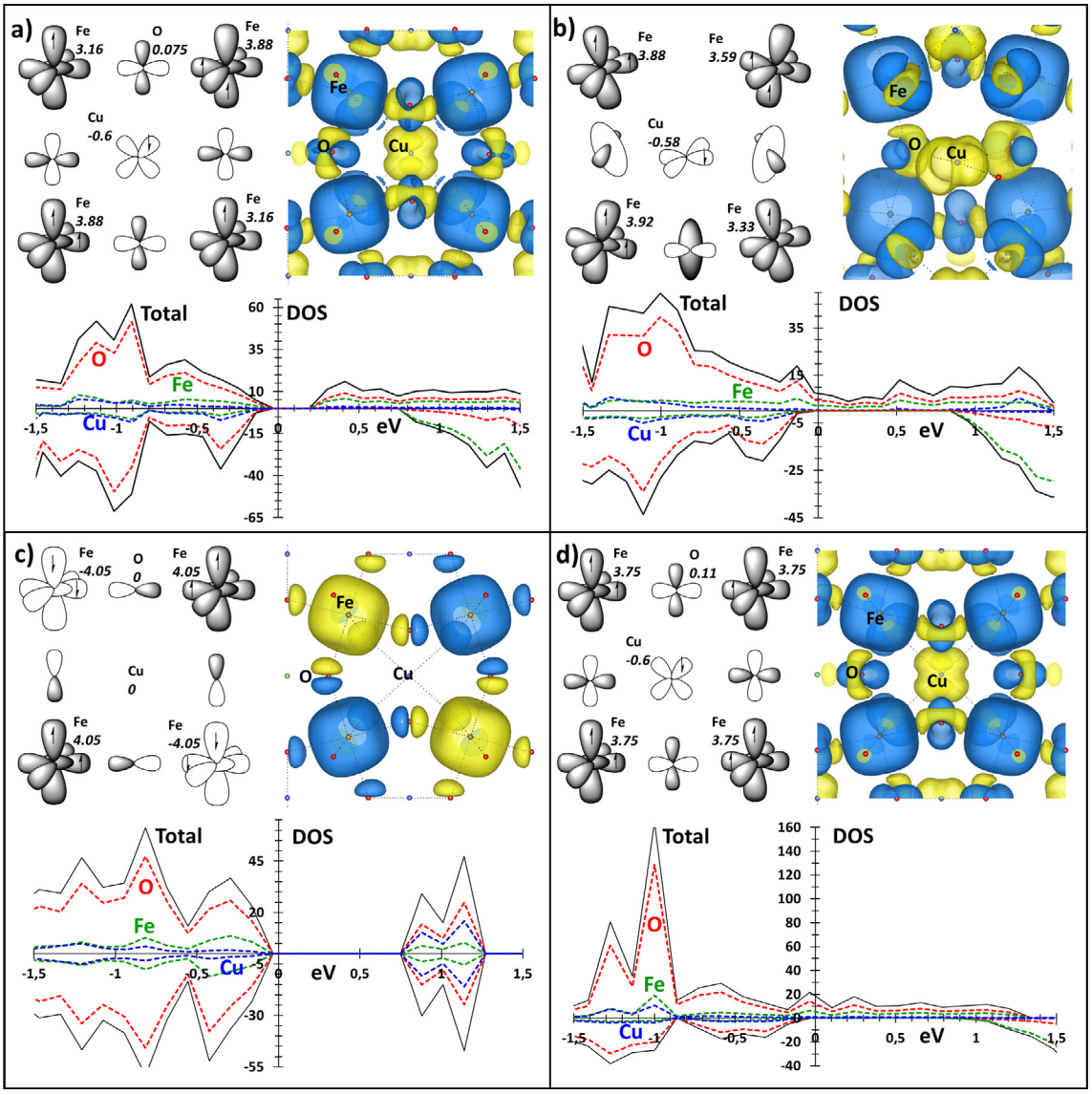

Fig. 1. Goodenough-Kanamori rules for the orbital ordering in $CaCu_3Fe_4O_{12-\delta}$ and $LaCu_3Fe_4O_{12}$ perovskites. (a) and (b) the ferrimagnetic ground state of $CaCu_3Fe_4O_{12}$ and $CaCu_3Fe_4O_{11}$, respectively: spin transfer from a half-filled to an empty orbital between two metal atoms, each carrying a net spin, over shared orbitals centred in the anion with a marked π-character; (c) the ground state of $LaCu_3Fe_4O_{12}$, AFM type-G: a virtual electron transfer between half-filled orbitals, over a shared σ-orbital centred in the anion, is restricted by the Pauli exclusion principle to be antiferromagnetic; and (d) the ferrimagnetic state of $LaCu_3Fe_4O_{12}$: AFM π-interaction between the anion and the interstitial Cu^{2+} cations like $CaCu_3Fe_4O_{12}$ G.S. In (a)–(d), the bottom of each shows the density of states, the top right shows the spin density and the top left shows a simplified schematic of the orbitals forming the spin density. The magnetisation of the atoms is shown in italics and expressed in atomic units.

active metals and the reactants on the surface dominates the reaction path, $\Delta G^{e-/h+}_{T.S.reac.\rightarrow cond.}$. This explains why maximum bulk electronic conductivity does not assure optimum activity. However, activity will be limited if the shells formed by the frontier ***d***-orbitals are half-filled and AFM interactions open a band gap, $\Delta H^{e-/h+}_{val.\rightarrow cond.} > 0$; for instance Mott insulators based on high spin Cr^{3+}, Fe^{3+}, Ni^{2+} or Co^{2+} ions are poor catalysts [4,21].

Rule 3) In the active metal atoms on the surface, the ***d***-orbitals oriented towards the bonds with the reactants, anti-bonding ***d***-orbitals (d-ABO) at the fermi level, must be partially occupied.

Description. The degree of covalent anti-bonding interaction between the orbitals of the active metals at the Fermi level and of the adsorbed species influence the rate of the electron transfer [12,13,37]. In FM metal-oxygen bonds, the ***d***-ABO oriented towards the reactants maximizes the value of the space transfer integrals, $\langle \Phi^{space}_{cat.cond.} | \Phi^{space}_{reac.} \rangle$, and creates intermediate adsorption energies. Consequently, also in agreement with the Sabatier principle, the maximum rate constant occurs at the catalytic interface. FM delocalization, $\Delta^{\Psi^{\pm}_{T.S.}}_{magnetic} = J_{Ex.} \cdot (\widehat{s_{Cat.}} \cdot \widehat{s_{e^-}}) > 0$, reduces the Coulomb interactions versus conventional $\psi^{sym.space}_{Fermi.level}$ metallic bands, $\Delta H^{e-/h+}_{T.S.reac.\rightarrow cond.} \propto \Delta H^{\psi^{sym.space}_{Fermi.level}}_{T.S.reac.\rightarrow cond.} - \Delta^{\Psi^{\pm}_{T.S.}}_{magnetic}$, facilitating charge tunnelling [2].

Rule 4) The overall reduction of the Coulomb interactions can facilitate the entrance of itinerant charge carriers at working conditions. Defects at the interstitial sites (***A***) or cations with occupied ***f***- or ***d***- orbitals, increasing the covalence of the *MMOs* framework, help to create active FM orderings, $\Delta H^{e-/h+}_{T.S.val.\rightarrow cond.} = 0$, adaptable to redox variations and with minimum $\Delta H^{e-/h+}_{T.S.reac.\rightarrow cond.}$.

Description. In the FM $e_g = \pi = e_g = reac.$ bonds with a degenerate orthogonal orbital space between ligand ions and reactants, the Coulomb interactions reduce. The presence of vacancies at **A**-sites,

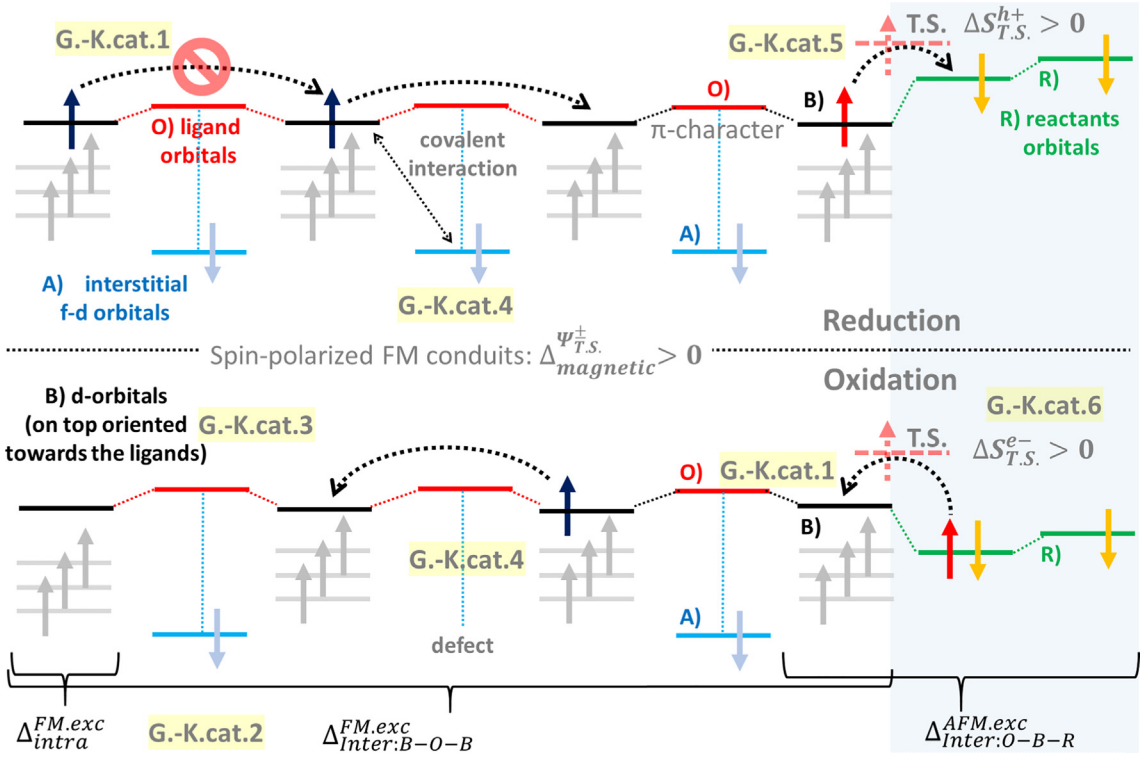

Fig. 2. Representation of the double-exchange guidelines in spintro-catalysis. Every G.K.cat. label corresponds to a rule, carefully described in the text below, associated with the principles of the double-exchange interactions that lead to favourable spin-dependent electron delocalization.

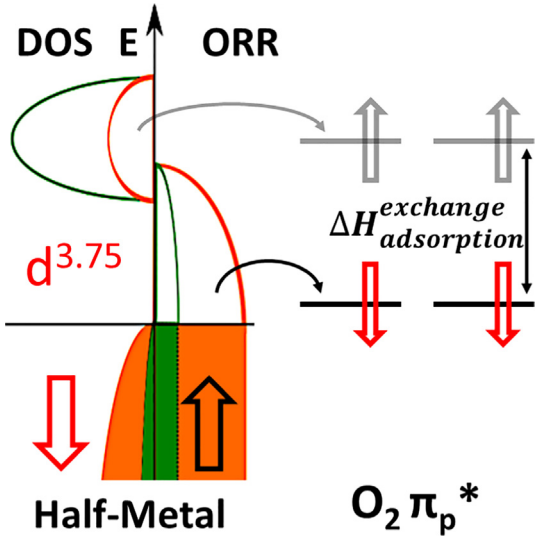

Fig. 3. Schematic representation showing the density of states (left) of FM $La_{1-x}Sr_xMnO_3$ oxides and (right) preferential antiparallel spin orientation of an adsorbed O_2 molecule.

Fig. 2 down, or metals with charge affinity in ***d***- or ***f***-orbitals, Fig. 2 up, that improve the FM covalent spin delocalization also enhance the space transfer integrals, $\langle \Phi^{space}_{cat.cond.} | \Phi^{space}_{reac.} \rangle$, see also Figs. 4 and 6.

Rule 5) At the *Transition State* (T.S.) the active cations on the surface at reaction conditions formally receive or lose electronic density during spin-selective steps with the reactants. Nevertheless good electrocatalysts retain the overall FM exchange delocalization.

Description. In certain p-type ($h^+_{\downarrow}$ are the main charge carriers) and n-type ($e^-_{\uparrow}$ are the majority carriers) semiconductors, their resistance increases when they are exposed to surrounding electron donors or acceptors, respectively [38,39]. In response to the reactants, tunnelling of charge carries ($e^-_{\uparrow}$ or $h^+_{\downarrow}$) at the electrocatalyst interface, which presents FM ordering, should not alter the conductivity, $\Delta H^{e-/h+}_{val.\rightarrow cond.} \approx 0$.

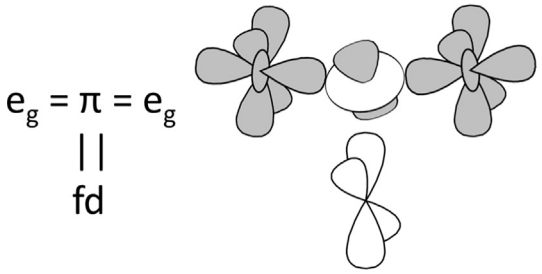

Fig. 4. Schematic showing that the FM resonating space of the antibonding orbitals is optimum in materials with enhanced covalent bonding, limited Coulomb interactions.

Rule 6) The reaction mechanism adapts to the response of the electronic free energy of activation, $\Delta G^{e-/h+}_{T.S.}$, towards maximum entropic gains.

Description. The selectivity towards OER or ORR and the reaction mechanism depends on the minimum free energy of activation, $\Delta G^{e-/h+}_{T.S.} = \Delta H^{e-/h+}_{T.S.} - T\Delta S^{e-/h+}_{T.S.}$. We see optimum electrocatalysts as dynamic redox materials, where the orbital physics adapts to the working conditions, especially to favour conductivity, $\Delta H^{e-/h+}_{val.\rightarrow cond.} \approx 0$, and also the entropy $\Delta S^{e-/h+}_{T.S.} > 0$. These responses associate with the reaction mechanism to minimize $\Delta G^{e-/h+}_{T.S.}$ and define reaction selectivity.

Once the interactions experienced by the electrons significantly depend on the spin magnetic moment, $\psi^{anti.space}_{Fermi.level}$; we depart from

charge transfer reactions in conventional metals, with optimized $\psi^{sym.space}_{Fermi.level}$ Coulomb forces, towards faster spin(-mediated) electron tunnelling. As a distinctive point in *spintro*-catalysis, the rate, $K(T)^{\pm}_{STST} = k^{\pm}_{ST} \cdot e^{-\Delta G^{e-/h+}_{T.S.}/k_B T}$, shows a specific dependence of the activation free energy, $\Delta G^{e-/h+}_{T.S.}$, on the sign of spin-potentials. We then differentiate the specific reduction of the energy needed to reach the T.S. by delocalizing FM spin-potentials: $\Delta G^{e-/h+}_{T.S.reac.\rightarrow cond.} \propto \Delta G^{\psi^{sym.space}_{Fermi.level}}_{T.S.reac.\rightarrow cond.} - \Delta^{\Psi^{\pm}_{T.S.}}_{magnetic}$, ($\Delta^{\Psi^{\pm}_{T.S.}}_{magnetic} = \Delta^{\Psi^{\pm}_{T.S.}}_{exchange}$ or $\Delta^{\Psi^{\pm}_{T.S.}}_{s.o.}$) [2]. Experimentally, Iwakura et al. showed that spinel ferrites diminished the oxygen overvoltage with the increase in magnetization [40].

The FM overlapping of the partially-occupied degenerate ***d***-orbitals of the metal cations via the ***s-p-*** orbitals of the ligands will form ideal π-type tunnelling in MMOs *spintro*-catalysts, $\Delta^{\Psi^{\pm}_{Cat.-T.S.}}_{magnetic} > 0$, associated with a redistribution of the spin density, see Figs. 1 and 6. The transfer of the charge carriers occurs through energy levels based on degenerate orthogonal atomic orbitals, and then separated by minimum changes in energy and space [2].

Fig. 5 illustrates that $\Delta G^{e-/h+}_{T.S.}$ is the core of the activity in any transition state model. Other descriptors proposed in the literature [41] are a partial view of the principles that determine $\Delta G^{e-/h+}_{T.S.}$. The free energy of activation includes the electronic entropy, $\Delta G^{e-/h+}_{T.S.} = \Delta H^{e-/h+}_{T.S.} - T \cdot \Delta S^{e-/h+}_{T.S.}$, usually forgotten. The enthalpy of activation, $\Delta H^{e-/h+}_{T.S.} = \Delta H^{e-/h+}_{T.S.reac.\rightarrow cond.} + \Delta H^{e-/h+}_{val.\rightarrow cond.}$ embraces the band gap of the catalyst, necessary for charge transport, also absent in most theoretical analysis; and the more conventional reaction barriers are in $\Delta H^{e-/h+}_{T.S.reac.\rightarrow cond.}$. This last term can be related with common descriptors in the literature such as ***p- d-*** band centers, bulk formation energies and several others if the exchange interactions are included properly. Of the multiple approaches discussed in literature, the initial occupancy of the ***d***-orbitals oriented towards the ligands is the closest to $\Delta G^{e-/h+}_{T.S.}$ [12–15], because is directly related with the origin of the exchange interactions. We have wanted to provide a complete and interconnected interpretation of the physics behind high activity; and all the excellent compositions we have found follow the FM exchange principles, as the energy flow in electrocatalysis (if $\Delta G^{e-/h+}_{T.S.} \gg k_B T$) mainly depends on electronic mechanisms and not on the thermic activation of the chemical bonds [42].

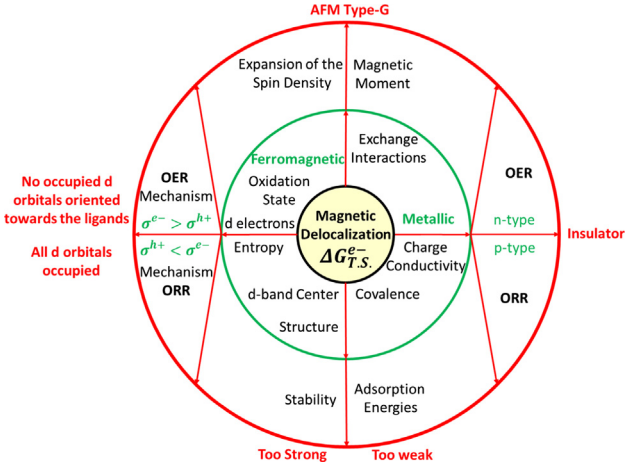

Fig. 5. Excellent oxide electrocatalysts follow the FM exchange principles because $\Delta G^{e-/h+}_{T.S.}$ is minimum, in the centre of the figure. Several of the proposed requirements for high activity are related with the influence of spin-potentials, shown in the inner rings. Compositions with properties outside the peripheral red circle will show low activity.

Electrocatalysis follows the Sabatier's principle from $\Delta H^{e-/h+}_{T.S.reac.\rightarrow cond.}$, and "spintro-catalysis" will guide computational studies in oxygen chemistry based on adsorption energies to include: the spin state of the catalyst, all the reactants and the magnetic nature of the catalytic interphase. Finally, authors can easily include in their studies the band-gap at the interphase as an extra term to the activation barriers, $\Delta H^{e-/h+}_{T.S.} = \Delta H^{e-/h+}_{T.S.reac.\rightarrow cond.} + \Delta H^{e-/h+}_{val.\rightarrow cond.}$. We trust such scheme will help to reduce the uncertainties in most of the actual ab-initio literature.

2. Interrelation between the electronic free energy of activation and the reaction mechanisms

In the best FM oxide catalysts for OER, the lattice oxygen atoms participate in the reaction mechanism, as originally proposed by the group of Stevenson [43]. The step where the O_2 molecule is released seems to be directly linked to a phase with dynamic oxygen vacancies. Fig. 1b shows that for the $CaCu_3Fe_4O_{11}$ stoichiometry, the system has higher magnetisation and conductivity due to the oxygen vacancy. The reduction of the FM *B-O-B* framework in the redox active $CaCu_3Fe_4O_{12}$ perovskite promotes favourable spin transport and entropy towards the catalyst for O_2 evolution; a similar case occurring in the Oxygen Evolution Complex in nature [6].

The reaction mechanism of O_2 formation is guided by the electronic free energy of activation. In fact, once the spin and oxygen mobility cooperate, the evolution of O_2 is not rate limiting [6]. Two electrons of the same spin must be removed from the orthogonal components of the adsorbed O-O π^* orbitals for OER, and this oxidation process has implications for the electronic structure of the catalyst, see Fig. 2-Down. As McGrady and Stranger proposed, the oxidative formation of the π^* orbitals of the triplet state O-O molecule proceeds via a lower-energy pathway in the presence of ferromagnetically coupled metal centres [44].

Fig. 2-Up represents the equivalent requirements for ORR, as we described for $LaMnO_{3+\delta}$ or $La_{1-X}Sr_XMnO_3$ catalysts [3]. In any case, the selectivity of the reaction mechanism adapts towards maximizing electronic entropic gains, as also occurs during thermochemical water splitting on ceria, beautifully explained by Nahvavi et al. [45].

3. Implication of the spin-dependent interactions for the composition of catalysts

The introduction of redox active ***d-*** or ***f-***orbitals at the interstitial ***A-***sites, in addition to the octahedral ***B-***positions, can assist in the enhancement of the FM π-bonding delocalization of the $e^-_{\uparrow}$ or $h^+_{\downarrow}$ in ABO. The introduction of ***d-*** or ***f-*** metals as compensating cations raises the electro-catalytic activity, as long as all the FM exchange principles described above are maintained [17,23,41,46,47]. Analyses should look at the electron transfer between all the redox metals after their adaptation to the working conditions [5].

Catalysts with defects at A-sites, like the stable, non-toxic and dual $La_{1-X}FeO_{3-\delta}$ oxides, can be as efficient for OER as the best mixed cobalt-iron based perovskites and "gold standards", e.g. RuO_2 and IrO_2 [48]. $CaCu_3Fe_4O_{12-\delta}$ has outstanding activity, however, the extreme synthesis conditions required hampers its applicability [18]. $LaFeO_3$ is an AFM type-G insulator; the High Spin Fe^{3+} ions have the ***3d*** orbitals half occupied, $t^3_{2g}e^2_g$, and the exchange interactions are consistently AFM [1]. Not surprisingly, the OER activity of $LaFeO_3$ is the lowest for the A-defective $La_{1-X}FeO_{3-\delta}$ family [48]; as it occurs for the $La_{1-X}Sr_XCoO_{3-\delta}$ family [43]. Likewise, $CaMnO_3$ and $LaMnO_3$ (high spin AFM $t^3_{2g}e^0_g$ and $t^3_{2g}e^1_g$) have a low electrocatalytic activity compared with the dual FM $t^3_{2g}eg^{\sim 0.5}$ $CaMnO_{3-\delta}$ perovskite [49], or the ***f***-doped $Ca_{0.9}Yb_{0.1}MnO_{3-\delta}$ OER cat-

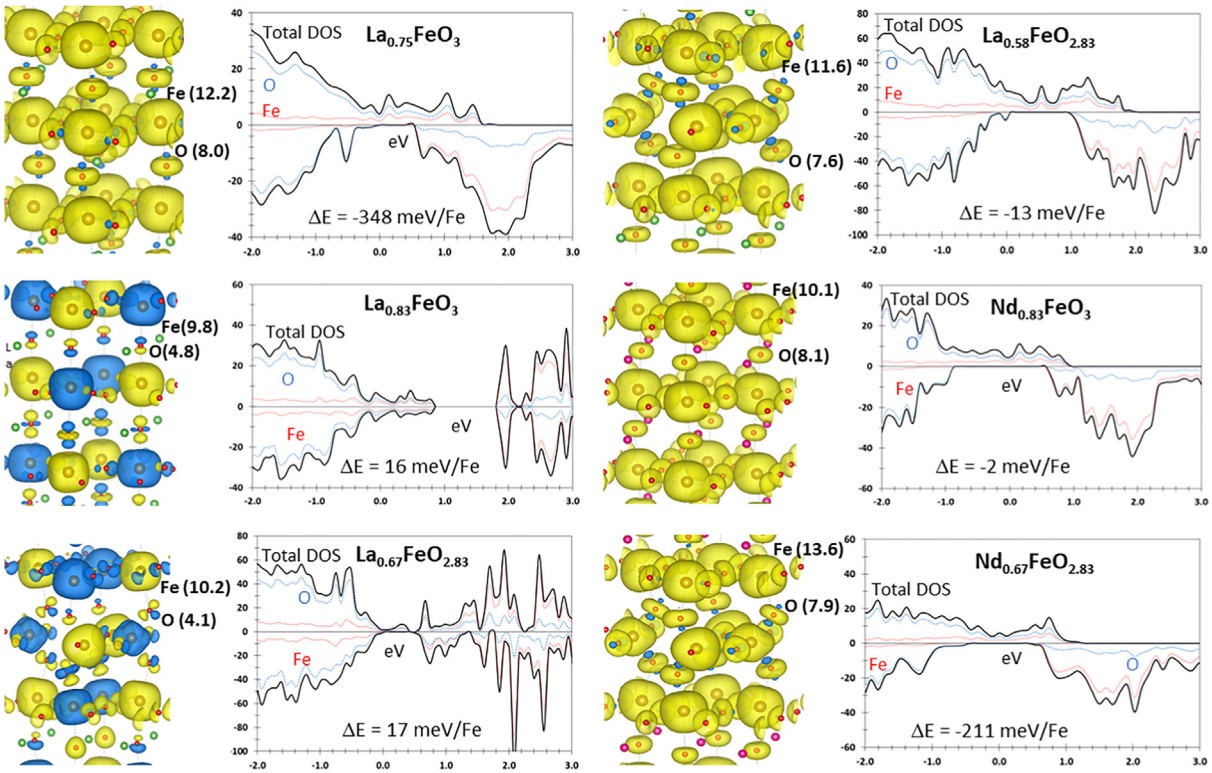

Fig. 6. Role of the compensating orbitals, cation and anion deficiencies in the stabilization of FM catalysts that will exhibit mixed ion-electron conductivity. The labels on the spin density plots indicates the volume, in Å^3, of the spin density for the iron and oxygen atoms. Δ*E* corresponds to energy difference (in meV per iron atom) between FM and AFM-G phases. Hence, negative values correspond to states where the FM phase is the most stable.

alyst [50]. AFM $LaFeO_3$ or $LaCoO_3$ perovskites are orders of magnitude worse electrocatalysts than the best FM oxides [23].

La^{3+} deficiencies destabilize the AFM ordering for $La_{1-X}FeO_{3-\delta}$ compositions, or $A_{1-X}Sr_XCoO_{3-\delta}$ oxides [36]. Fig. 6 shows that with an increasing number of holes a FM G.S. evolves for stoichiometries with ~3/4 Fe^{4+} ions (rule 2), as in $La_{0.75}Fe^{3.75+}O_3$ or $La_{0.58}Fe^{\sim 3.9+}O_{2.83}$. The FM exchange interactions, optimum for $\boldsymbol{3d\text{-}t_{2g}^3e_g^{\sim 1.3}}$ occupations, create delocalized spin-polarized electrons, see Fig. 6. An increase in conductivity and OER activity in particular can be inferred from the electrons/holes ratio, which facilitates incoming spin-density via exchange interactions. We agree with Y. Zhu et al. in correlating the OER activity of $La_{1-X}FeO_{3-\delta}$ perovskites with the presence of Fe^{4+} ions and oxygen vacancies [48].

According to rule 4, we can further improve the activity by substituting La^{3+} with Nd^{3+} or Yb^{3+}. This way, in combination with hole-doping and oxygen vacancies, materials will exhibit the desired mixed ion-electron conductivity [51]. As Fig. 6 indicates, stable FM phases for the $Nd_{1-X}FeO_{3-\delta}$ family need less cation vacancies.

The changes in the electronic states for $La_{1-X}FeO_{3-\delta}$ oxides resemble those reported for $La_{0.88}Mn^{\sim 3.3+}O_{3-\delta}$ manganites [52], but are active for ORR because of the FM ordering corresponding to high electrons/holes ratios. Likewise, $FD_{1-X}MnO_{3-\delta}$ compositions (FD are metals with occupied **f** or **d** orbitals) seem to be an alternative to the excellent ORR $La_{1-X}MnO_{3-\delta}$ catalysts [15]. Previous examples will not be stable in acidic conditions, but without changing the design principles we can improve at the same time the electronic transport and stability in acidic media by introducing Ir or preferably Ru. In view of the excellent dual activity and stability in acidic media of some magnetic mixed-valance ruthenates [53,54], catalysts based on iridium are less stimulating because they are less active and more expensive. Overall, particularly for acidic media, these genuine electronic principles suggest that the $A_{1-X}Ru_{1-Y}B'_YO_{3-\delta}$ or $A_{1-X}A'_XRu_{1-Y}B'_YO_{3-\delta}$ oxide families (A = Nd or Yb, A′ is a 2+ or 1+ metal and B′ are Fe and/or Mn) are excellent electrocatalysts.

4. Conclusions

Exchange coupled mixed-valence spin acceptors or donors, with ferromagnetic delocalization over the orbitals oriented towards the ligands, are excellent electrocatalysts. This applies to both extended and molecular systems, regardless of whether an external potential or photons provide the energy for the reaction to the electrons. Spin-dependent FM potentials, extended to embrace a catalytic interface, allow the understanding of the orbital physics of excellent magnetic oxides for electron transfer reactions. Within these principles, the kinetics of the charge transfer is optimized because the free energy of activations is reduced, applicable at oxidation or reduction potentials. We summarise these effects as "*spintro*-catalysis," as the role played by the spin of the electrons is fundamental to describe the kinetics, enthalpy and entropy of electron transfer reactions.

We foresee the need of applying *spintro-catalysis* in the inspiring work by Fletcher and Van Dijk, "Supercatalysis by Superexchange" [55]. Fletcher has also identified superexchange in the electron flow through an iron(II) d-orbital in photosystem II [56]. The pioneering work in the groups of Naaman and Meijer are showing that spin states, via chiral-selection, play an important role in chemical processes [57–59]; in relation, magnetic potentials are incorporated under the same theoretical principles. Many biologically active molecules are chiral and 10% of the characterized proteins are redox proteins, i.e. they participate in electron transfer; the realization that natural evolution has exploited spin-dependent FM exchange interactions to catalyse vital redox reactions suggests a new specialized field of "*spintro-biocatalysis*".

The exceptional catalytic activity of magnetic oxides for species with unpaired electrons like NO oxidation is related with exchange interactions [60,61]; or in the high-performance oxides exhibiting strong electron correlations associated with emergent applications [62–64].

5. Methods

All calculations were performed using periodic density functional theory (DFT) as implemented in the Vienna *ab initio* simulations package (VASP) [65–67]. A plane-wave basis set was used to represent the wavefunctions. The projected augmented wave (PAW) method developed by Blochl was used to represent the interactions between the core electrons and valence electrons [68,69]. The exchange-correlation energy was calculated within the generalised gradient approximation using the Perde-Burke-Ernzerhof functional revised for solids [70]. A plane-wave cut-off of 400 eV was used for all systems. The DFT+U approach was used to account for on-site Coulomb interactions of localised ***d*** and ***f*** electrons [71]. Unless otherwise mentioned, all elements had a U value of 0. We have kept the U value constant for each metal to be able to accurately compare the spin localisation across each system. All drawings are produced with VESTA [72].

CCF crystallographic information was obtained from Yamada et al. [73] $ACu_3Fe_4O_{12}$ compounds crystallise in a cubic structure at room temperature, with a space group, $Im\bar{3}$. A Monkhorst Pack k-point grid of 6x6x6 was used. A U value of 6.0 and 4.0 was used for Cu [74] and Fe [75] respectively, as described in the literature. $LaFeO_3$ has an orthorhombic Pbnm symmetry at ambient temperatures [76]. We used U = 8.0 eV for Nd [77].

Acknowledgements

J.M. thanks the Spanish Ministry of Education Culture and Sports (FPU14/06003) for a fellowship, as well as support and generous computational resources from BIFI-ZCAM.

References

[1] J.B. Goodenough, Electronic and ionic transport properties and other physical aspects of perovskites, Rep. Prog. Phys. 67 (2004) 1915–1993, https://doi.org/10.1088/0034-4885/67/11/R01.
[2] J. Gracia, Spin dependent interactions catalyse the oxygen electrochemistry, Phys. Chem. Chem. Phys. 19 (2017) 20451–20456, https://doi.org/10.1039/C7CP04289B.
[3] J. Gracia, J. Munarriz, V. Polo, R. Sharpe, Y. Jiao, J.W.H. Niemantsverdriet, T. Lim, Analysis of the magnetic entropy in oxygen reduction reactions catalysed by manganite perovskites, ChemCatChem 9 (2017) 3358–3363, https://doi.org/10.1002/cctc.201700302.
[4] R. Sharpe, T. Lim, Y. Jiao, J.W.H. Niemantsverdriet, J. Gracia, Oxygen evolution reaction on perovskite electrocatalysts with localized spins and orbital rotation symmetry, ChemCatChem 8 (2016) 3762–3768, https://doi.org/10.1002/cctc.201600835.
[5] R. Sharpe, J. Munarriz, T. Lim, Y. Jiao, J.W. Niemantsverdriet, V. Polo, J. Gracia, Orbital physics of perovskites for the oxygen evolution reaction, Top. Catal. (2018), https://doi.org/10.1007/s11244-018-0895-4 (in press).
[6] Y. Jiao, R. Sharpe, T. Lim, J.W.H. Niemantsverdriet, J. Gracia, Photosystem II acts as a spin-controlled electron gate during oxygen formation and evolution, J. Am. Chem. Soc. 139 (2017) 16604–16608, https://doi.org/10.1021/jacs.7b07634.
[7] B.M. Hoffman, D. Lukoyanov, Z. Yang, D.R. Dean, L.C. Seefeldt, Mechanism of nitrogen fixation by nitrogenase: the next stage, Chem. Rev. 114 (2014) 4041–4062, https://doi.org/10.1021/cr400641x.
[8] R. Bjornsson, F.A. Lima, T. Spatzal, T. Weyhermüller, P. Glatzel, E. Bill, O. Einsle, F. Neese, S. DeBeer, Identification of a spin-coupled Mo(III) in the nitrogenase iron–molybdenum cofactor, Chem. Sci. 5 (2014) 3096–3103, https://doi.org/10.1039/C4SC00337C.
[9] D. Lukoyanov, B.M. Barney, D.R. Dean, L.C. Seefeldt, B.M. Hoffman, Connecting nitrogenase intermediates with the kinetic scheme for N2 reduction by a relaxation protocol and identification of the N2 binding state, Proc. Natl. Acad. Sci. 104 (2007) 1451–1455, https://doi.org/10.1073/pnas.0610975104.
[10] Y. Tokura, Orbital physics in transition-metal oxides, Science 288 (2000) 462–468, https://doi.org/10.1126/science.288.5465.462.
[11] E. Dagotto, Complexity in strongly correlated electronic systems, Science 309 (2005) 257–262, https://doi.org/10.1126/science.1107559.
[12] J.O. Bockris, T. Otagawa, The electrocatalysis of oxygen evolution on perovskites, J. Electrochem. Soc. 131 (1984) 290, https://doi.org/10.1149/1.2115565.
[13] Y. Matsumoto, E. Sato, Electrocatalytic properties of transition metal oxides for oxygen evolution reaction, Mater. Chem. Phys. 14 (1986) 397–426, https://doi.org/10.1016/0254-0584(86)90045-3.
[14] J. Suntivich, K.J. May, H.A. Gasteiger, J.B. Goodenough, Y. Shao-Horn, A perovskite oxide optimized for oxygen evolution catalysis from molecular orbital principles, Science 334 (2011) 1383–1385, https://doi.org/10.1126/science.1212858.
[15] J. Suntivich, H.A. Gasteiger, N. Yabuuchi, H. Nakanishi, J.B. Goodenough, Y. Shao-Horn, Design principles for oxygen-reduction activity on perovskite oxide catalysts for fuel cells and metal–air batteries, Nat. Chem. 3 (2011) 546–550, https://doi.org/10.1038/nchem.1069.
[16] Y. Lee, J. Suntivich, K.J. May, E.E. Perry, Y. Shao-Horn, Synthesis and activities of rutile IrO_2 and RuO_2 nanoparticles for oxygen evolution in acid and alkaline solutions, J. Phys. Chem. Lett. 3 (2012) 399–404, https://doi.org/10.1021/jz2016507.
[17] A. Grimaud, K.J. May, C.E. Carlton, Y.-L. Lee, M. Risch, W.T. Hong, J. Zhou, Y. Shao-Horn, Double perovskites as a family of highly active catalysts for oxygen evolution in alkaline solution, Nat. Commun. 4 (2013) 2439, https://doi.org/10.1038/ncomms3439.
[18] S. Yagi, I. Yamada, H. Tsukasaki, A. Seno, M. Murakami, H. Fujii, H. Chen, N. Umezawa, H. Abe, N. Nishiyama, S. Mori, Covalency-reinforced oxygen evolution reaction catalyst, Nat. Commun. 6 (2015) 8249, https://doi.org/10.1038/ncomms9249.
[19] W. Zhou, M. Zhao, F. Liang, S.C. Smith, Z. Zhu, High activity and durability of novel perovskite electrocatalysts for water oxidation, Mater. Horiz. 2 (2015) 495–501, https://doi.org/10.1039/C5MH00096C.
[20] M.S. Burke, S. Zou, L.J. Enman, J.E. Kellon, C.A. Gabor, E. Pledger, S.W. Boettcher, Revised oxygen evolution reaction activity trends for first-row transition-metal (oxy)hydroxides in alkaline media, J. Phys. Chem. Lett. 6 (2015) 3737–3742, https://doi.org/10.1021/acs.jpclett.5b01650.
[21] D.B. Meadowcroft, Low-cost oxygen electrode material, Nature 226 (1970) 847–848, https://doi.org/10.1038/226847a0.
[22] K.A. Stoerzinger, M. Risch, B. Han, Y. Shao-Horn, Recent insights into manganese oxides in catalyzing oxygen reduction kinetics, ACS Catal. 5 (2015) 6021–6031, https://doi.org/10.1021/acscatal.5b01444.
[23] D. Chen, C. Chen, Z.M. Baiyee, Z. Shao, F. Ciucci, Nonstoichiometric oxides as low-cost and highly-efficient oxygen reduction/evolution catalysts for low-temperature electrochemical devices, Chem. Rev. 115 (2015) 9869–9921, https://doi.org/10.1021/acs.chemrev.5b00073.
[24] M. Risch, Perovskite electrocatalysts for the oxygen reduction reaction in alkaline media, Catalysts 7 (2017) 154, https://doi.org/10.3390/catal7050154.
[25] G. Xu, R. Liu, J. Wang, Electrochemical synthesis of ammonia using a cell with a Nafion membrane and $SmFe_{0.7}Cu_{0.3-x}Ni_xO_3$ (x = 0–0.3) cathode at atmospheric pressure and lower temperature, Sci. China Ser. B Chem. 52 (2009) 1171–1175, https://doi.org/10.1007/s11426-009-0135-7.
[26] R. Lan, K.A. Alkhazmi, I.A. Amar, S. Tao, Synthesis of ammonia directly from wet air using $Sm_{0.6}Ba_{0.4}Fe_{0.8}Cu_{0.2}O_{3-\delta}$ as the catalyst, Faraday Discuss. 182 (2015) 353–363, https://doi.org/10.1039/C5FD00033E.
[27] S.A. Wolf, Spintronics: a spin-based electronics vision for the future, Science 294 (2001) 1488–1495, https://doi.org/10.1126/science.1065389.
[28] H. Kozuka, K. Ohbayashi, K. Koumoto, Electronic conduction in La-based perovskite-type oxides, Sci. Technol. Adv. Mater. 16 (2015) 26001, https://doi.org/10.1088/1468-6996/16/2/026001.
[29] J.B. Goodenough, Theory of the role of covalence in the perovskite-type manganites [La, M(II)]MnO3, Phys. Rev. 100 (1955) 564–573, https://doi.org/10.1103/PhysRev. 100.564.
[30] J.B. Goodenough, An interpretation of the magnetic properties of the perovskite-type mixed crystals $La_{1-x}Sr_xCoO_{3-\lambda}$, J. Phys. Chem. Solids 6 (1958) 287–297, https://doi.org/10.1016/0022-3697(58)90107-0.
[31] J. Kanamori, Superexchange interaction and symmetry properties of electron orbitals, J. Phys. Chem. Solids 10 (1959) 87–98, https://doi.org/10.1016/0022-3697(59)90061-7.
[32] I. Yamada, H. Fujii, A. Takamatsu, H. Ikeno, K. Wada, H. Tsukasaki, S. Kawaguchi, S. Mori, S. Yagi, Bifunctional oxygen reaction catalysis of quadruple manganese perovskites, Adv. Mater. 29 (2017) 1603004, https://doi.org/10.1002/adma.201603004.
[33] T.S. Santos, J.S. Lee, P. Migdal, I.C. Lekshmi, B. Satpati, J.S. Moodera, Room-temperature tunnel magnetoresistance and spin-polarized tunneling through an organic semiconductor barrier, Phys. Rev. Lett. 98 (2007) 16601, https://doi.org/10.1103/PhysRevLett. 98.016601.
[34] D.-G. Lee, O. Gwon, H.-S. Park, S.H. Kim, J. Yang, S.K. Kwak, G. Kim, H.-K. Song, Conductivity-dependent completion of oxygen reduction on oxide catalysts, Angew. Chem. Int. Ed. 54 (2015) 15730–15733, https://doi.org/10.1002/anie.201508129.
[35] H. Gerischer, Electron-transfer kinetics of redox reactions at the semiconductor/electrolyte contact. A new approach, J. Phys. Chem. 95 (1991) 1356–1359, https://doi.org/10.1021/j100156a060.
[36] T. Lim, J.W.H. Niemantsverdriet, J. Gracia, Layered antiferromagnetic ordering in the most active perovskite catalysts for the oxygen evolution reaction, ChemCatChem 8 (2016) 2968–2974, https://doi.org/10.1002/cctc.201600611.

[37] R.R. Dogonadze, Y.A. Chizmadzev, The kinetics of some electrochemical redox reactions on metals, Dokl. Akad. Nauk SSSR 145 (1962) 849–852.
[38] K. Sahner, P. Gouma, R. Moos, Electrodeposited and sol-gel precipitated p-type $SrTi_{1-x}Fe_xO_{3-\delta}$ semiconductors for gas sensing, Sensors 7 (2007) 1871–1886, https://doi.org/10.3390/s7091871.
[39] T. Akamatsu, T. Itoh, N. Izu, W. Shin, NO and NO_2 sensing properties of WO_3 and Co_3O_4 based gas sensors, Sensors 13 (2013) 12467–12481, https://doi.org/10.3390/s130912467.
[40] C. Iwakura, M. Nishioka, H. Tamura, Oxygen evolution on spinel-type ferrite film electrodes, Nippon Kagaku Kaishi (1982) 1136–1140, https://doi.org/10.1246/nikkashi.1982.1136.
[41] W.T. Hong, R.E. Welsch, Y. Shao-Horn, Descriptors of oxygen-evolution activity for oxides: a statistical evaluation, J. Phys. Chem. C 120 (2016) 78–86, https://doi.org/10.1021/acs.jpcc.5b10071.
[42] S. Fletcher, The theory of electron transfer, J. Solid State Electrochem. 14 (2010) 705–739, https://doi.org/10.1007/s10008-009-0994-z.
[43] J.T. Mefford, X. Rong, A.M. Abakumov, W.G. Hardin, S. Dai, A.M. Kolpak, K.P. Johnston, K.J. Stevenson, Water electrolysis on $La_{1-x}Sr_xCoO_{3-\delta}$ perovskite electrocatalysts, Nat. Commun. 7 (2016) 11053, https://doi.org/10.1038/ncomms11053.
[44] J.E. McGrady, R. Stranger, Redox-induced formation and cleavage of O−O σ and π bonds in a peroxo-bridged manganese dimer: a density functional study, Inorg. Chem. 38 (1999) 550–558, https://doi.org/10.1021/ic981253k.
[45] S.S. Naghavi, A.A. Emery, H.A. Hansen, F. Zhou, V. Ozolins, C. Wolverton, Giant onsite electronic entropy enhances the performance of ceria for water splitting, Nat. Commun. 8 (2017) 285, https://doi.org/10.1038/s41467-017-00381-2.
[46] V. Kyriakou, I. Garagounis, E. Vasileiou, A. Vourros, M. Stoukides, Progress in the electrochemical synthesis of ammonia, Catal. Today 286 (2017) 2–13, https://doi.org/10.1016/j.cattod.2016.06.014.
[47] Y. Zhu, W. Zhou, Z.-G. Chen, Y. Chen, C. Su, M.O. Tadé, Z. Shao, $SrNb_{0.1}Co_{0.7}Fe_{0.2}O_{3-\delta}$ perovskite as a next-generation electrocatalyst for oxygen evolution in alkaline solution, Angew. Chem. Int. Ed. 54 (2015) 3897–3901, https://doi.org/10.1002/anie.201408998.
[48] Y. Zhu, W. Zhou, J. Yu, Y. Chen, M. Liu, Z. Shao, Enhancing electrocatalytic activity of perovskite oxides by tuning cation deficiency for oxygen reduction and evolution reactions, Chem. Mater. 28 (2016) 1691–1697, https://doi.org/10.1021/acs.chemmater.5b04457.
[49] J. Du, T. Zhang, F. Cheng, W. Chu, Z. Wu, J. Chen, Nonstoichiometric perovskite $CaMnO_{3-\delta}$ for oxygen electrocatalysis with high activity, Inorg. Chem. 53 (2014) 9106–9114, https://doi.org/10.1021/ic501631h.
[50] Y. Guo, Y. Tong, P. Chen, K. Xu, J. Zhao, Y. Lin, W. Chu, Z. Peng, C. Wu, Y. Xie, Engineering the electronic state of a perovskite electrocatalyst for synergistically enhanced oxygen evolution reaction, Adv. Mater. 27 (2015) 5989–5994, https://doi.org/10.1002/adma.201502024.
[51] Y. Chen, Y. Wei, H. Zhong, J. Gao, X. Liu, G. Meng, Synthesis and electrical properties of $Ln_{0.6}Ca_{0.4}FeO_{3-\delta}$ (Ln = Pr, Nd, Sm) as cathode materials for IT-SOFC, Ceram. Int. 33 (2007) 1237–1241, https://doi.org/10.1016/j.ceramint.2006.03.035.
[52] I.O. Troyanchuk, V.A. Khomchenko, M. Tovar, H. Szymczak, K. Bärner, Antiferromagnet-ferromagnet and structural phase transitions in $La_{0.88}MnO_x$ manganites, Phys. Rev. B 69 (2004) 54432, https://doi.org/10.1103/PhysRevB.69.054432.
[53] J. Kim, P.-C. Shih, K.-C. Tsao, Y.-T. Pan, X. Yin, C.-J. Sun, H. Yang, High-performance pyrochlore-type yttrium ruthenate electrocatalyst for oxygen evolution reaction in acidic media, J. Am. Chem. Soc. 139 (2017) 12076–12083, https://doi.org/10.1021/jacs.7b06808.
[54] J. Parrondo, M. George, C. Capuano, K.E. Ayers, V. Ramani, Pyrochlore electrocatalysts for efficient alkaline water electrolysis, J. Mater. Chem. A 3 (2015) 10819–10828, https://doi.org/10.1039/C5TA01771H.
[55] S. Fletcher, N.J. Van Dijk, Supercatalysis by superexchange, J. Phys. Chem. C 120 (2016) 26225–26234, https://doi.org/10.1021/acs.jpcc.6b09099.
[56] S. Fletcher, Discovery of a single molecule transistor in photosystem II, J. Solid State Electrochem. 19 (2015) 241–250, https://doi.org/10.1007/s10008-014-2567-z.
[57] W. Mtangi, F. Tassinari, K. Vankayala, A. Vargas Jentzsch, B. Adelizzi, A.R.A. Palmans, C. Fontanesi, E.W. Meijer, R. Naaman, Control of electrons' spin eliminates hydrogen peroxide formation during water splitting, J. Am. Chem. Soc. 139 (2017) 2794–2798, https://doi.org/10.1021/jacs.6b12971.
[58] F. Tassinari, K. Banerjee-Ghosh, F. Parenti, V. Kiran, A. Mucci, R. Naaman, Enhanced hydrogen production with chiral conductive polymer-based electrodes, J. Phys. Chem. C 121 (2017) 15777–15783, https://doi.org/10.1021/acs.jpcc.7b04194.
[59] A. Kumar, E. Capua, K. Vankayala, C. Fontanesi, R. Naaman, Magnetless device for conducting three-dimensional spin-specific electrochemistry, Angew. Chem. Int. Ed. 56 (2017) 14587–14590, https://doi.org/10.1002/anie.201708829.
[60] W. Wang, G. McCool, N. Kapur, G. Yuan, B. Shan, M. Nguyen, U.M. Graham, B.H. Davis, G. Jacobs, K. Cho, X. Hao, Mixed-phase oxide catalyst based on Mn-mullite (Sm, Gd)Mn_2O_5 for NO oxidation in diesel exhaust, Science 337 (2012) 832–835, https://doi.org/10.1126/science.1225091.
[61] C.H. Kim, G. Qi, K. Dahlberg, W. Li, Strontium-doped perovskites rival platinum catalysts for treating NOx in simulated diesel exhaust, Science 327 (2010) 1624–1627, https://doi.org/10.1126/science.1184087.
[62] Y. Zhou, X. Guan, H. Zhou, K. Ramadoss, S. Adam, H. Liu, S. Lee, J. Shi, M. Tsuchiya, D.D. Fong, S. Ramanathan, Strongly correlated perovskite fuel cells, Nature 534 (2016) 231–234, https://doi.org/10.1038/nature17653.
[63] I. Grinberg, D.V. West, M. Torres, G. Gou, D.M. Stein, L. Wu, G. Chen, E.M. Gallo, A.R. Akbashev, P.K. Davies, J.E. Spanier, A.M. Rappe, Perovskite oxides for visible-light-absorbing ferroelectric and photovoltaic materials, Nature 503 (2013) 509–512, https://doi.org/10.1038/nature12622.
[64] J. Gracia, M. Escuin, R. Mallada, N. Navascues, J. Santamaria, Nano-heaters: new insights on the outstanding deposition of dielectric energy on perovskite nanoparticles, Nano Energy 20 (2016) 20–28, https://doi.org/10.1016/j.nanoen.2015.11.040.
[65] G. Kresse, J. Hafner, Ab initio molecular-dynamics simulation of the liquid-metal–amorphous-semiconductor transition in germanium, Phys. Rev. B 49 (1994) 14251–14269, https://doi.org/10.1103/PhysRevB.49.14251.
[66] G. Kresse, J. Hafner, Ab initio molecular dynamics for liquid metals, Phys. Rev. B 47 (1993) 558–561, https://doi.org/10.1103/PhysRevB.47.558.
[67] G. Kresse, J. Furthmüller, Efficient iterative schemes for ab initio total-energy calculations using a plane-wave basis set, Phys. Rev. B – Condens. Matter Mater. Phys. 54 (1996) 11169–11186, https://doi.org/10.1103/PhysRevB.54.11169.
[68] P.E. Blöchl, Projector augmented-wave method, Phys. Rev. B 50 (1994) 17953–17979, https://doi.org/10.1103/PhysRevB.50.17953.
[69] G. Kresse, D. Joubert, From ultrasoft pseudopotentials to the projector augmented-wave method, Phys. Rev. B 59 (1999) 1758–1775, https://doi.org/10.1103/PhysRevB.59.1758.
[70] J.P. Perdew, A. Ruzsinszky, G.I. Csonka, O.A. Vydrov, G.E. Scuseria, L.A. Constantin, X. Zhou, K. Burke, Restoring the density-gradient expansion for exchange in solids and surfaces, Phys. Rev. Lett. 100 (2008) 136406, https://doi.org/10.1103/PhysRevLett. 100.136406.
[71] S.L. Dudarev, G.A. Botton, S.Y. Savrasov, C.J. Humphreys, A.P. Sutton, Electron-energy-loss spectra and the structural stability of nickel oxide: an LSDA+U study, Phys. Rev. B – Condens. Matter Mater. Phys. 57 (1998) 1505–1509, https://doi.org/10.1103/PhysRevB.57.1505.
[72] K. Momma, F. Izumi, VESTA 3 for three-dimensional visualization of crystal, volumetric and morphology data, J. Appl. Crystallogr. 44 (2011) 1272–1276, https://doi.org/10.1107/S0021889811038970.
[73] I. Yamada, K. Shiro, H. Etani, S. Marukawa, N. Hayashi, M. Mizumaki, Y. Kusano, S. Ueda, H. Abe, T. Irifune, Valence transitions in negative thermal expansion material $SrCu_3Fe_4O_{12}$, Inorg. Chem. 53 (2014) 10563–10569, https://doi.org/10.1021/ic501665c.
[74] Z. Li, J.S. Tse, S. You, C.Q. Jin, T. Itaka, Electronic and magnetic structure of the high pressure phase of Li_2CuO_2, Int. J. Mod. Phys. B 25 (2011) 3409–3414, https://doi.org/10.1142/S0217979211101909.
[75] L. Wang, T. Maxisch, G. Ceder, Oxidation energies of transition metal oxides within the GGA + U framework, Phys. Rev. B 73 (2006) 195107, https://doi.org/10.1103/PhysRevB.73.195107.
[76] S.M. Selbach, J.R. Tolchard, A. Fossdal, T. Grande, Non-linear thermal evolution of the crystal structure and phase transitions of $LaFeO_3$ investigated by high temperature X-ray diffraction, J. Solid State Chem. 196 (2012) 249–254, https://doi.org/10.1016/j.jssc.2012.06.023.
[77] B. Bouadjemi, S. Bentata, A. Abbad, W. Benstaali, Ab-initio study of optoelectronic and magnetic properties of the orthorhombic $NdMnO_3$ perovskite, Solid State Commun. 207 (2015) 9–15, https://doi.org/10.1016/j.ssc.2015.02.001.

ChemPubSoc Europe

DOI: 10.1002/cphc.201800633

CHEMPHYSCHEM Communications

On the Role of Ferromagnetic Interactions in Highly Active Mo-Based Catalysts for Ammonia Synthesis

Julen Munarriz,*[a] Victor Polo,[a] and Jose Gracia*[b]

Reactions involving nitrogen fixation and transfer are of great industrial interest. In this regard, unveiling all the physical principles that determine their activity would be enormously beneficial for the rational design of novel catalysts with improved performance. Within this context, this work explores the activity of bulk molybdenum-based transition metal nitrides in ammonia synthesis. Our results highlight that the most active compositions show increasing ferromagnetism in the metal–nitrogen bonds, which constitute the active sites. We observe that the total spin accumulated in the bonds at the active sites is a physically meaningful descriptor to discriminate optimum catalysts. Higher activities are associated with ferromagnetic phases, and the underlying reason is an enhanced overlapping of the electronic wavefunctions; which also make the reaction steps spin-sensitive. These finding provides strong evidence of the general influence of electrons magnetic moment in catalysis, being part of the specific field of spintro-catalysis.

Spin-dependent potentials are decisive for the kinetics of electron transfer reactions at magnetic interphases.[1,2] Catalysts with preferential ferromagnetic (FM) exchange interactions are optimized on the basis of energy shells antisymmetric in space, $\psi_{antisym}$, being distinguished as "spintro-catalysts".[3] The studies performed so far on magnetic catalysts have focused on oxygen electrochemistry, revealing the importance of quantum exchange interactions (QEI),[4–5] as well as their implications for the understanding and developing of efficient energy technologies. However, the interest and applicability of novel concepts like FM enhanced covalent bonds,[3] reduced Coulomb interactions[1] and spin-sensitive reaction steps in compositions with $\psi_{antisym}$ is wider, and might be extended to other relevant chemical processes, as it is the case of nitrogen fixation to produce ammonia.[6]

The progressive fossil fuels depletion and the need for reducing environmental pollution has resulted in a growing interest to develop new renewable energetic processes, [7] looking for geopolitically stable alternatives. Within this context, ammonia plays a key role for the maintenance of a steady sustainable economy, as it allows the clean synthesis of fertilizers, having also significant applications in the production of plastics, nitric acid and in fuel cells.[8,9] On an industrial scale, ammonia is obtained almost exclusively via the reduction of nitrogen with hydrogen through the Haber Bosch process. This synthesis is expensive, requiring high temperatures and pressures, as well as very pure streams of gases. The reaction takes place over iron or ruthenium-based heterogeneous catalysts and requires about 485 kJ mol^{-1} overall.[10] On the other hand, nitrogen fixation in nature is achieved under mild conditions via an enzymatic reaction catalyzed by the so called nitrogenases. Among them, FeMo-nitrogenases are reported to be the most active.[11,12] On balance, the process requires 244 kJ mol^{-1}, almost half than in industry.[13] Researchers have tried to mimic this "natural" catalyst; what has resulted into stimulating advances, as the synthesis of efficient molybdenum[14] and iron-based[15,16] complexes with high activity. Another relevant approach uses complex transition metal nitrides as heterogeneous catalysts;[17–19] with activities for the ternary nitrides following the order $Co_3Mo_3N_{1-\delta} > Fe_3Mo_3N_{1-\delta} > Ni_2Mo_3N_{1-\delta}$.[17,18] Both, experimental results and ab-initio calculations, show that the number of nitrogen vacancies present on Co_3Mo_3N-based materials can adsorb and activate the strong N≡N triple bond.[20,21] As a result, some authors have proposed that nitrogen fixation occurs via a Mars–van Krevelen (MvK) mechanism, as shown in Scheme 1.[22,23] However, the influence

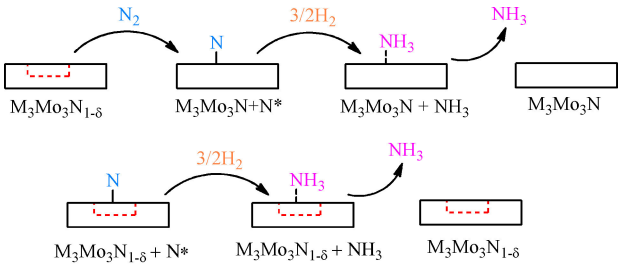

$$M_3Mo_3N_{1-\delta} + N_2 \rightarrow M_3Mo_3N + N^*;$$
$$M_3Mo_3N + N^* + 3/2\ H_2 \rightarrow M_3Mo_3N + NH_3;$$
$$M_3Mo_3N \rightarrow M_3Mo_3N_{1-\delta} + N^*;$$
$$M_3Mo_3N_{1-\delta} + N^* + 3/2\ H_2 \rightarrow M_3Mo_3N_{1-\delta} + NH_3$$

$$M_3Mo_3N_{1-\delta} + N_2 + 3H_2 \rightarrow M_3Mo_3N_{1-\delta} + 2NH_3$$

Scheme 1. Schematic representation of Mars–van Krevelen mechanism for ammonia synthesis on $M_3Mo_3N_{1-\delta}$ catalysts.

[a] J. Munarriz, Dr. V. Polo
Departamento de Química Física and Instituto de Biocomputación y Física de Sistemas Complejos (BIFI)
Universidad de Zaragoza, Zaragoza, Spain, 50009
E-mail: julen@unizar.es
[b] Dr. J. Gracia
Magnetocat SL
General Polavieja 9 3I, Alicante, Spain, 03012
E-mail: magnetocat@outlook.com

of the electronic and magnetic structure of Mo-based transition metal nitrides in their catalytic activity have barely been explored.

Transition metal oxides with preferential FM spin delocalization are excellent catalysts for oxygen electrochemistry.[1,6,24] The explanation lies on the fact that augmented QEI in spin-polarized conductors assists the electron transfer and spin selection.[1,5] In addition, oxygen vacancies are also a crucial part of their reaction mechanisms.[25] Within this context, we aim to apply the same physical principles that work for oxygen electrochemistry to understand the importance of spin exchange potentials in nitrogen hydrogenation. For that, we have theoretically studied the magnetic structure of the related $FeCo_2Mo_3N_{1-\delta}$, $Co_3Mo_3N_{1-\delta}$, $Fe_3Mo_3N_{1-\delta}$ and $Ni_2Mo_3N_{1-\delta}$ catalysts, see Figure 1, focusing on the orbital physics responsible of their activity. The principles presented herein should be general for catalytic N_2 activation and can be used for the "rational design" of optimum compositions.[26]

The magnetic structure of the nitrides was studied by means of periodic DFT calculations. Fe and Co-based nitrides were found to present a FM metallic ground state (G.S.)[27,28] while Ni_2Mo_3N is nonmagnetic, as reported by other authors.[29,30] These kind of compositions are also active for oxygen reduction;[3] and nitrogen fixation has similarities with O_2 reduction as the double bond in oxygen molecule must be activated by incoming electrons in a similar way as the triple bond of nitrogen molecule. In both cases, electrons are to be incorporated into π^* molecular orbitals prior to the immobilization of protons. It is also known that FM potentials reduce the influence of the Coulomb interactions, and intermediates overall present a reaction mechanism with optimum activation energies for electron transfer in oxygen electrochemistry.[1] In this regard, one of the fingerprints in spintro-catalysis is the general reduction of the free activation energies by a quantity that is proportional to the FM spin-moment of the active sites. Within this correlation, we have used the Heisenberg Hamiltonian to quantify the QEI; that is: $H_{QEI} = \triangle J_{QEI} \cdot \boldsymbol{S}_{cat}$ where, $\triangle J_{QEI}$ is a catalytic exchange coupling constant and $\boldsymbol{S}_{cat}$ is the average spin moment at the active sites.[31]

We start the analysis from nitrogen defective unit cells, as the active catalysts present nitrogen vacancies at reaction conditions.[25] For that, we subtracted one of the sixteen nitrogen atoms in the unit cell of Fe_3Mo_3N, Co_3Mo_3N and $FeCo_2Mo_3N$,[32] as well as in an equivalent (with respect to the number of nitrogen atoms) Ni_2Mo_3N supercell ($2\times2\times1$);[33] thus making stoichiometries of the form $M_xMo_3N_{0.94}$. As shown in Table 1, all the structures, but slightly antiferromagnetic (AFM)

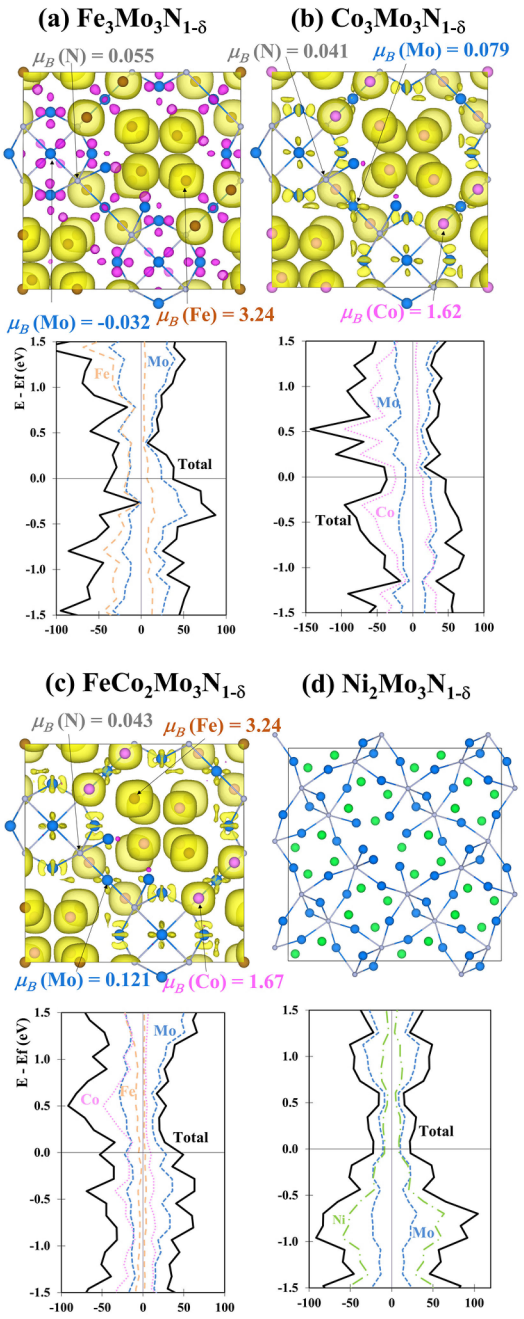

Figure 1. Spin density (yellow: up; purple: down; spin majority in the positive side, isovalue of 0.01 e^- Å^{-3}), density of states, and magnetic moments (in a.u.) for the most stable magnetic phase of nitrogen defective: a) $Fe_3Mo_3N_{1-\delta}$, b) Co3Mo3 $N_{1-\delta}$, c) $FeCo_2Mo_3N_{1-\delta}$, and d) $Ni_2Mo_3N_{1-\delta}$.

Table 1. Energy difference between FM G.S. and the most stable AFM one for defective and non-defective structures, in meV per Mo atom. Energy of formation of the vacancies versus N_2 gas in meV per Mo, relative stability per electron in eV and Mo–N distance in Å.

	N defective FM–AFM	E_e/n_{e^-}	d (Mo–N)	Non-N-defective *FM-AFM*	E_e/n_{e^-}	*d (Mo–N)*	Energy of formation N vacancies
$FeCo_2Mo_3N_{1-\delta}$	86	0.864	2.083	89	0.870	2.081	54
$Co_3Mo_3N_{1-\delta}$	115	0.853	2.090	113	0.860	2.089	50
$Fe_3Mo_3N_{1-\delta}$	134	0.877	2.102	138	0.883	2.098	63
$Ni_2Mo_3N_{1-\delta}$	–	0.758	2.075	–	0.764	2.068	49

$Ni_2Mo_3N_{0.94}$, have FM G.S.; and they keep the same magnetic structure as the fully stoichiometric compounds, as will be explained later on in the text. In the bulk, Mo–N bonds represent the active centers for N_2 hydrogenation, and, noteworthy, the overall increase in the magnetic moments on these bonds agrees with the enhanced catalytic activity (cf. Figure 1): $Ni_2Mo_3N_{1-\delta}$ (0.0 μ_B) < $Fe_3Mo_3N_{1-\delta}$ (0.023 μ_B) < $Co_3Mo_3N_{1-\delta}$ (0.120 μ_B) < $FeCo_2Mo_3N_{1-\delta}$ (0.164 μ_B); the maximum activity of the $FeCo_2Mo_3N_{1-\delta}$ structure results as a theoretical prediction of our study. To rationalize this correlation, consider H_{QEI} as a perturbation that reduces the energy of the system by an increment in the number of unpaired electrons. As a consequence, there is a change in the spatial symmetry that decreases Coulomb potentials and enhance covalent interactions. This way, ferromagnetism anticipates at least the possibility of lowering the activation barriers of the rate limiting step upon spin polarization.

For non-vacant systems, the spin polarization in the Mo–N bonds follows again the sequence: Ni_2Mo_3N (0.0 μ_B) < Fe_3Mo_3N (0.045 μ_B) < Co_3Mo_3N (0.123 μ_B) < $FeCo_2Mo_3N$ (0.187 μ_B), see Figure 2 and Table 2. The increment in the magnetic moment is due to the additional oxidation provided by the extra nitrogen atoms. FM holes located at the Mo–N bonds, in conjunction with the magnetization of these bonds, indicate the ability of the catalysts to polarize spin-density from the *2p*-orbitals of the nitrogen atoms. In other words, the magnetic moment in the Mo–N bonds is an indication of the ability of the catalyst to overlap with the *2p*-orbitals of the intermediate nitrogenates during NH_3 synthesis.

In Fe_3Mo_3N, the iron's magnetic moment is 3.03 μ_B, while the molybdenum atoms have a magnetic moment close to 0, associated with the typical low spin (L.S.) states of *4d*-Mo systems.[34] The molybdenum magnetic moment, although small, presents the opposite orientation (negative sign) with respect to iron atoms, which prefer a FM orientation with respect to each other, see Table 2. In the iron atoms, the strong intra-atomic FM exchange interactions in the *3d*-orbitals polarize the electronic density, and since there are enough empty orbitals at the Fermi level, the inter-atomic exchange interactions between the polarized iron atoms become also FM. The iron atoms are the least electronegative of the *3d*-metals and the bigger *4d*-orbitals are only slightly polarized. $Ni_2Mo_3N_{1-\delta}$ and $Fe_3Mo_3N_{1-\delta}$ are the least active catalysts and result to be the compositions in which the Mo atoms have no spin-polarization or which are somewhat AFM with respect to the rest of the metallic atoms (in $Fe_3Mo_3N_{1-\delta}$ Fe atoms are FM with respect to themselves, but AFM with respect to slightly magnetic polarized Mo atoms). As a result, the Mo–N bond distances are longer, Fermi heaps, the formation energy of nitrogen vacancies is higher, the system is more rigid as shown by the highest FM–AFM energy differences, and the *d*-metal orbitals participate less in the conduction band near the Fermi level. In $Co_3Mo_3N_{1-\delta}$, the cobalt cations present an average magnetic moment of 1.63 μ_B, smaller than those of iron atoms, indicating that the antibonding *3d*-band is more saturated. The cobalt *3d*-orbitals spill-over the magnetic moment towards the Mo cations by oxidizing them, as indicated by the lower Bader atomic charge

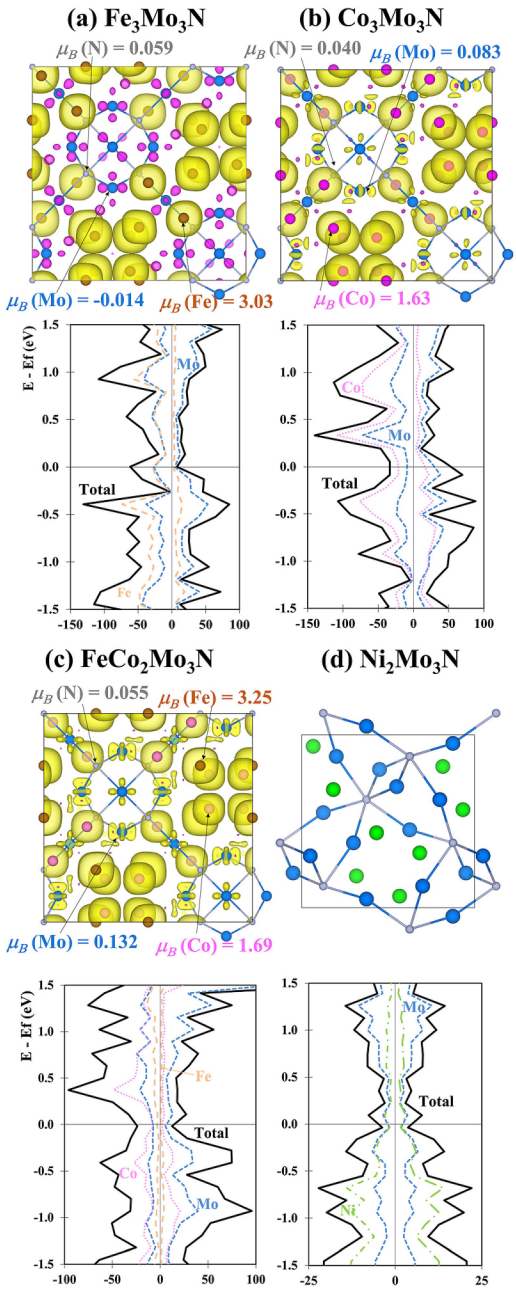

Figure 2. Spin density (yellow: up; purple: down; spin majority in the positive side, isovalue of 0.01 e^- Å^{-3}), density of states, and magnetic moments (in a.u.) for the most stable magnetic phase of nitrogen defective: a) Fe_3Mo_3N, b) Co3Mo3 N, c) $FeCo_2Mo_3N$, and d) Ni_2Mo_3N.

of Mo in $Co_3Mo_3N_{1-\delta}$ with respect to $Fe_3Mo_3N_{1-\delta}$, see Table 2; the magnetism accumulated in the Mo–N bonds in $Co_3Mo_3N_{1-\delta}$ is about three times the values in $Fe_3Mo_3N_{1-\delta}$. In this case, as well as in $FeCo_2Mo_3N_{1-\delta}$, all atoms are in an overall FM state. In $FeCo_2Mo_3N_{1-\delta}$, the iron atoms present a magnetic moment of 3.25 μ_B, while the value for cobalt ions is 1.69 μ_B; the spin polarization of the Mo–N bonds is significantly the greatest of the considered materials, as also shown by shortest bond distance, Fermi holes, see Table 2. There is a crucial transfer of electron density mediated by QEI from the Fe to the Co ions that maximizes the spin-moment in both metals.

Table 2. Average magnetic moment, Bader atomic charge (both in a.u.) and Mo–N distances (in Å) for FM (G. S.) and AFM $FeCo_2Mo_3N$, FM Co_3Mo_3N and Fe_3Mo_3N and diamagnetic Ni_2Mo_3N.

	Co		Fe		Ni		Mo		N		*d* (Mo–N)	
	μ_B	charge	μ_B	charge	μ_B	charge	μ_B	charge	μ_B	charge	G.S.	AFM
$FeCo_2Mo_3N$	1.69	−0.39	3.25	0.34	–	–	0.132	0.65	0.055	−1.53	2.081	–
$FeCo_2Mo_3N$ (AFM)	−1.59	−0.38	−0.06	0.33	–	–	−0.142	0.65	−0.04	−1.51	–	2.074–2.099
Co_3Mo_3N	1.63	−0.22	–	–	–	–	0.083	0.73	0.040	−1.53	2.089	2.066–2.106
Fe_3Mo_3N	–	–	3.03	0.03	–	–	−0.014	0.51	0.059	−1.51	2.098	2.099–2.116
Ni_2Mo_3N	–	–	–	–	0.0	−0.32	0.0	0.73	0.0	−1.46	2.068	–

Overall, we observe that when moving from $Ni_2Mo_3N_{1-\delta}$ and $X_3Mo_3N_{1-\delta}$ (X=Fe, Co) to $FeCo_2Mo_3N_{1-\delta}$, there is an increase in the magnetic moment of all the metal atoms. As shown in Figure 2 and Table 2, the increasing magnetization of the Mo–N bonds shorten them, (non-classical) spin quantum mechanical effects of bonding, and spin-oscillations are easier, as $FeCo_2Mo_3N_{1-\delta}$ compositions have the smaller energy difference between FM and AFM phases. The relative electronic stability of the systems was perused by means of the relation: total electronic energy/number of electrons, E_e/n_e. In relation with the Sabatier's principle,[35] in a MvK mechanism the energy of formation of the N-vacancies is in the middle zone for $FeCo_2Mo_3N_{1-\delta}$; in this respect, $Fe_3Mo_3N_{1-\delta}$ is too ionic, while $Co_3Mo_3N_{1-\delta}$ and $Ni_2Mo_3N_{1-\delta}$ interact with the ligands more weakly.

Ammonia synthesis is clearly less optimal for catalysts that do not present magnetic Mo–N bonds, which do not present FM QEI as part of the stabilizing forces in the orbitals. The magnetic structure seems one amongst many factors controlling catalytic activity; the best catalysts present increasing FM interactions at the active sites, and there is thus a connection between FM G.S., formation of vacancies and shorter Mo–N bonds.

We observe that the enhanced catalytic activity in FM $X_3Mo_3N_{1-\delta}$ compositions is due to similar electronic and magnetic factors as previously anticipated in strongly correlated oxides.[3] The principles of *spintro-catalysis* seem to be valid and applicable to all catalysts including earth-abundant *3d*-magnetic metals. In optimum catalysts for ammonia synthesis, there are spin polarized Mo–N bonds, where the minority spin is easier to extract from the partially occupied AB-orbitals and QEI facilitate nitrogen fixation, as the average distance between AB-electrons will be larger. The studied systems have no band-gap for any of the spins, what allows to maintain the total spin required for ammonia synthesis. Consequently, the increasing magnetic moment in shorter Mo–N bonds is a physically meaningful descriptor for the catalytic activity associated to FM spin-channels at the Fermi level. We propose again that the extra freedom provided by the QEI are effectively described by a Heisenberg Hamiltonian. Finally, we clarified that for these opening studies in relation with the influence of the spin-interactions in catalysis, a deep study of the bulk properties is enough for obtaining predictive trends.

Experimental Section

All calculations were performed using periodic density functional theory (DFT) as implemented in the Vienna ab initio simulations package (VASP).[36–38] The Projector Augmented Wave (PAW) method developed by Blochl was used to represent interactions between core and valence electrons.[39,40] A plane wave cutoff of 400 eV was used for all the elements, in conjunction with Monkhorst-Pack k-point meshes of $11\times11\times11$. The Perde-Burke-Ernzerhof exchange-correlation DFT functional revised for solids was used for all calculations.[41] In order to properly describe on-site Coulomb interactions of localised d electrons, DFT+U methodology was used,[42] with values of U=2.0 for Co and 4.0 for Fe, as previously reported.[3,43] Images were produced with VESTA.[44]

Acknowledgements

J.M. And V.P. Express their appreciation for the financial support from MINECO/FEDER project CTQ2015-67366-P and DGA/FSE (group E07). J.M. acknowledges the financial support provided by the Spanish "Ministerio de Educación Cultura y Deporte" (FPU14/06003). In addition, the resources from the supercomputer "memento", technical expertise and assistance provided by BIFI-ZCAM (Universidad de Zaragoza) are acknowledged. MagnetoCat SL gratefully acknowledge significant funding from Syngaschem BV, Eindhoven (Netherlands), and Synfuels China Technology Co LTD, Beijing (China).

Conflict of Interest

The authors declare no conflict of interest.

Keywords: Ammonia synthesis · nitrogen fixation · Quantum Exchange Interactions · spin-dependent chemistry · Spintro-catalysis

[1] J. Gracia, *Phys. Chem. Chem. Phys.* **2017**, *19*, 20451–20456.
[2] R. Sharpe, T. Lim, Y. Jiao, J. W. H. Niemantsverdriet, J. Gracia, *ChemCatChem* **2016**, *8*, 3762–3768.
[3] J. Gracia, R. Sharpe, J. Munarriz, *J. Catal.* **2018**, *361*, 331–338.
[4] J. B. Goodenough, *Rep. Prog. Phys.* **2004**, *67*, 1915–1993.
[5] R. Sharpe, J. Munarriz, T. Lim, Y. Jiao, J. W. H. Niemantsverdriet, V. Polo, J. Gracia, *Top. Catal.*, **2018**, *61*, 267–275.
[6] X.-L. Ma, J.-C. Liu, H. Xiao, J. Li, *J. Am. Chem. Soc.* **2018**, *140*, 46–49.
[7] S. Chu, A. Majumdar, *Nature* **2012**, *488*, 294–303.
[8] S. Mekhilef, R. Saidur, A. Safari, *Renewable Sustainable Energy Rev.* **2012**, *16*, 981–989.

[9] A. Afif, N. Radenahmad, Q. Cheok, S. Shams, J. H. Kim, A. K. Azad, *Renewable Sustainable Energy Rev.* **2016**, *60*, 822–835.
[10] M. Appl, *Ullmann's Encyclopedia of Industrial Chemistry*, Wiley-VCH Weinheim, **2006**.
[11] T. Spatzal, M. Aksoyoglu, L. Zhang, S. L. A. Andrade, E. Schleicher, S. Weber, D. C. Rees, O. Einsle, *Science* **2011**, *334*, 940.
[12] K. M. Lancastrer, M. Roemelt, P. Ettenhuber, Y. Hu, M. W. Ribbe, F. Neese, U. Bergmann, S. DeBeer, *Science* **2011**, *334*, 974–977.
[13] C. J. M. van der Ham, M. T. M. Koper, D. G. H. Hetterscheid, *Chem. Soc. Rev.* **2014**, *43*, 5183–5191.
[14] K. Arashiba, Y. Miyake, Y. Nishibayashi, *Nat. Chem.* **2011**, *3*, 120–125.
[15] J. S. Anderson, J. Rittle, J. C. Peters, *Nature* **2013**, *501*, 84–88.
[16] S. Kuriyama, K. Arashiba, K. Nakajima, Y. Matsuo, H. Tanaka, K. Ishii, K. Yashizawa, Y. Nishibayashi, *Nat. Commun.* **2016**, *7*, 1.
[17] C. J. H. Jacobsen, *Chem. Commun.* **2000**, *12*, 1057–1058
[18] N. Perret, A. –M. Alexander, S. M. Hunter, P. Chung, J. S. J. Hargreaves, R. F. Howe, M. A. Keane, M. A. *Appl. Catal. A* **2014**, *488*, 128–137.
[19] D. Mckay, J. S. J. Hargreaves, J. L. Rico, J. L. Rivera, X. –L. Sun, *J. Solid State Chem.* **2008**, *181*, 325–333.
[20] D. McKay, D. H. Gregory, J. S. J. Hargreaves, S. M. Hunter, X. Sun, *Chem. Commun.* **2007**, *0*, 3051–3053.
[21] C. D. Zeinalipour-Yazdi, J. S. J. Hargreaves, C. R. A. Catlow, *J. Chem. Phys.* **2016**, *120*, 21390–21398.
[22] S. M. Hunter, D. H. Gregory, J. S. J. Hargreaves, M. I. Richard, D. Duprez, N. A. Bion, *ACS Catal.* **2013**, *3*, 1719–1725.
[23] C. D. Zeinalipour-Yazdi, J. S. J. Hargreaves, C. R. A. Catlow, *J. Chem. Phys.* **2018**, *122*, 6078–6082.
[24] J. Gracia, J. Munarriz, V. Polo, R. Sharpe, Y. Jiao, J. W. H. Niemantsverdriet, T. Lim, *ChemCatChem* **2017**, *9*, 3358–3363.
[25] J. T. Mefford, X. Rong, A. M. Abakumov, W. G. Hardin, S. Dai, *Nat. Commun.* **2016**, *7*, 11053.
[26] A. Zunger, *Nat. Rev. Chem.* **2018**, *2*, 0121.
[27] T. Waki, S. TerazawaY. Tabata, K. Sato, A. Kondo, K. Kindo, H. Nakamura, *Phys. Rev. B* **2014**, *90*, 014416.
[28] L. A. Sviridov, P. D. Battle, F. Grandjean, G. J. Long, T. J. Prior, *Inorg. Chem.* **2010**, *49*, 1133–1143.
[29] E. Haque, A. Hossain, *J. Alloys Compd.* **2018**, *748*, 117–126.
[30] K. S. Weil, P. N. Kumta, J. Grins, *J. Solid State Chem.* **1999**, *146*, 22–35.
[31] Y. Z. Jiao, R. Sharpe, T. Lim, J. W. H. Niemantsverdriet, J. Gracia, *J. Am. Chem. Soc.* **2017**, *139*, 16604–16608.
[32] S. K. Jackson, R. C. Layland, H. C. zur Loye, *J. Alloys Compd.* **1999**, *291*, 94–101.
[33] S. Alconchel, F. Sapina, D. Beltran, A. Beltran, *J. Mater. Chem.* **1998**, *8*, 1901–1909.
[34] R. L. McNaughton, J. M. Chin, W. W. Weare, R. R. Schrock, B. M. Hoffman, *J. Am. Chem. Soc.* **2007**, *129*, 3480–3481.
[35] A. J. Medford, A. Vojvodic, J. S. Hummelshøj, J. Voss, F.-A. Pedersen, F. Studt, T. Bligaard, A. Nilsson, J. K. Nørskovz *J. Catal.* **2015**, *328*, 36–42.
[36] G. Kresse, J. Hafner, *Phys. Rev. B* **1993**, *47*, 558–561.
[37] G. Kresse, J. Hafner, *Phys. Rev. B* **1994**, *49*, 14251–14269.
[38] G. Kresse, J. Furthmüller, *Phys. Rev. B* **1996**, *54*, 11169–11186.
[39] P. E. Blöchl, *Phys. Rev. B* **1994**, *50*, 17953–17979.
[40] G. Kresse, D. Joubert, *Phys. Rev. B* **1999**, *59*, 1758–1775.
[41] J. P. Perdew, A. Ruzsinsky, G. I. Csonka, O. A. Vydrov, G. E. Scuseria, L. A. Constantin, X. Zhou, K. Burke, *Phys. Rev. Lett.* **2008**, *100*, 136406.
[42] S. L. Dudarev, G. A. Botton, S. Y. Savrasov, C. J. Humphreys, A. P. Sutton, *Phys. Rev. B* **1998**, *57*, 1505–1509.
[43] M. Aykol, S. Kim, C. Wolverton, *J. Chem. Phys.* **2015**, *119*, 19053–1908.
[44] K. Momma, F. Izumi, *J. Appl. Crystallogr.* **2011**, *44*, 1272–1276.

Manuscript received: July 3, 2018
Accepted Article published: August 23, 2018
Version of record online: September 19, 2018

APPENDIX

The Impact Factor (included in the Journal of Citations Report, JCR), the JCR thematic areas and the journal position, as well as the author contribution to each of the seven articles that constitute this Ph.D. Thesis are provided in this appendix. All the articles were published in 2017 and 2018. Since the impact factors corresponding to 2018 are not available, all the impact factor provided in this appendix correspond to 2017.

All the co-authors hold a Ph.D. degree except Ms. Amaia Iturmendi, who is co-author in articles 3 and 4. Attached with this memory is her explicit renounce to include these articles as part of another Ph.D. Thesis published as a compendium of publications.

1. Journal: Physical Chemistry Chemical Physics

   Publication year: 2018

   Impact factor: 3.906

   JCR Category: Chemistry, Physical: 46/147

   Physics, Atomic, Molecular & Chemical: 9/37

   Reference:

   Munárriz, J.; Velez, E.; Casado, M. A.; Polo, V. Understanding the reaction mechanism of the oxidative addition of ammonia by (PXP)Ir(I) complexes: the role of the X group. *Phys. Chem. Chem. Phys.* **2018**, *20*, 1105–1113.

   Within this article, the applicant performed all the theoretical calculations and wrote the first version of the manuscript

2. Journal: Chemical Science

   Publication year: 2017

   Impact factor: 9.063

   JCR Category: Chemistry, Multidisciplinary: 18/171

   Reference:

   Rubio-Pérez, L.; Iglesias, M.; Munárriz, J.; Polo, V.; Passarelli, V.; Pérez-Torrente, J. J.; Oro, L. A. A well-defined NHC-Ir(III) catalyst for the silylation of aromatic C–H bonds: substrate survey and mechanistic insights. *Chem. Sci.* **2017**, *8*, 4811–4822.

   The applicant performed all the theoretical calculations of this article and wrote the computational part. In addition, he helped in the interpretation of the experimental results and actively participated in the design and analysis of the reactivity experiments carried out to confirm the reaction mechanism.

3. Journal: Green Chemistry

   Publication year: 2018

   Impact factor: 8.586

   JCR Category: Chemistry, Multidisciplinary: 21/171

   Green & Sustainable Science & Technology: 2/33

   Reference:

   Iturmendi, A.; Iglesias, M.; Munárriz, J.; Polo, V.; Passarelli, V.; Pérez-Torrente, J. J.; Oro, L. A. Highly Efficient Ir-Catalyst for the Solventless Dehydrogenation of Formic Acid: The Key Role of an N-heterocyclic Olefin. Green Chem. 2018, 20, 4875–4879

   The applicant carried out and wrote all the computational part of the article and participated actively in the interpretation of the experimental results and the writing of the whole paper.

4. Journal: Chemical Communications

   Publication year: 2017

   Impact factor: 6.290

   JCR Category: Chemistry, Multidisciplinary: 28/171

   Reference:

   Iturmendi, A.; Iglesias, M.; Munárriz, J.; Polo, V.; Pérez-Torrente, J. J.; Oro, L. A. Efficient preparation of carbamates by Rh-catalysed oxidative carbonylation: unveiling the role of the oxidant. *Chem. Commun.* **2017**, *53*, 404–407.

   The applicant performed all the theoretical calculations included as part of the article, wrote the entire computational part and participated in the writing and revision of the whole article.

5. Journal: ChemCatChem

   Publication year: 2017

   Impact factor: 4.674

   JCR Category: Chemistry, Physical: 34/147

   Reference:

   Gracia, J.; Munárriz, J.; Polo, V. Sharpe, R.; Jiao, Y.; Niemantsverdriet, J. W. H.; Lim, T. Analysis of the Magnetic Entropy in Oxygen Reduction Reactions Catalysed by Manganite Perovskites. *ChemCatChem* **2017**, *9*, 3358–3363.

   The author of this dissertation performed all the computational calculations of the Mn-perovskites including La, Ca and Sr cations. In addition, he actively participated in the writing of the article and the analysis of the results.

6. Journal: Journal of Catalysis

   Publication year: 2018

   Impact factor: 6.759

   JCR Category: Chemistry, Physical: 27/147

Engineering, Chemical: 6/137

Reference:

Gracia, J.; Sharpe, R.; Munárriz, J. Principles determining the activity of magnetic oxides for electron transfer reactions. *J. Catal.* **2018**, *361*, 331–338.

The author of this Doctoral Thesis performed all the calculations corresponding to the $LaFeO_3$-based systems, participated actively in the proposal of the set of rules for the catalytic activity and wrote the main part of the article.

7. Journal: ChemPhysChem

Publication year: 2018

Impact factor: 2.947

JCR Category: Chemistry, Physical: 62/147

Physics, Atomic, Molecular & Chemical: 11/37

Reference:

Munárriz, J.; Polo, V.; Gracia, J. On the Role of Ferromagnetic Interactions in Highly Active Mo-based Catalysts for Ammonia Synthesis. *ChemPhysChem.* **2018**, *19*, 2843–2847.

The applicant performed all the calculations, wrote the first manuscript and revised the paper.